First-principles calculations of NMR parameters for materials applications

Charlotte Isabella Lynch

Trinity College

University of Oxford

A thesis submitted for the degree of

Doctor of Philosophy

Hilary 2017

First-principles calculations of NMR parameters for materials applications

Charlotte Isabella Lynch
Trinity College
University of Oxford
A thesis submitted for the degree of
Doctor of Philosophy
Hilary 2017

Abstract

Nuclear magnetic resonance (NMR) is a powerful experimental technique for probing the local environment of nuclei in materials. However, it can be difficult to separate the large number of interactions that are recorded in the resulting spectra. First-principles calculations based on quantum mechanics therefore provide much-needed support for interpreting experimental spectra. In this way, the underlying mechanisms recorded in experimental spectra can be investigated on an atomic level, and trends can be noted with which to guide the direction of future experiments. This thesis presents two cases in which first-principles calculations do just that. The first is an investigation of the perovskite structures of $NaNbO_3$, $KNbO_3$, $LiNbO_3$ and the related solid solutions of $Na_xK_{1-x}NbO_3$, $K_xNa_{1-x}NbO_3$ and $Li_xNa_{1-x}NbO_3$ in order to study how structural disorder affects their NMR parameters. The second investigation involves the calculation of the Knight shift in platinum, palladium and rhodium—in their elemental bulk forms and in a set of surface structures. The Knight shift is a systematic shift in the NMR frequencies of metallic systems. It arises from the hyperfine interaction between the nuclear spins and the spins of the unpaired conduction electrons. When calculating the Knight shift, it is found that the Brillouin zone must be very finely sampled. A discussion of core polarisation is also presented. This is the polarisation of core electrons as a result of their interaction with valence electrons. In the case of Curie paramagnets, core polarisation can have a significant effect on the calculation of hyperfine parameters.

Acknowledgements

First of all I would like to thank my supervisor Jonathan for all his support and guidance over the years. I'd also like to thank Bi-Ching for many Knight shift discussions and for reading those chapters through. To the wider community in the MML, thank you for the strong academic environment, many enjoyable conversations and much cake.

I'd like to thank all my Trinity friends, and those from further afield, for their companionship and many lunchtimes spent discussing the woes of a DPhil student. In particular, thank you Abi for many late night tea-drinking sessions, and to Putu and Claudia for their unfailing enthusiasm towards everything.

I thank my parents, my brother Lawrence and the rest of my family for all their love and encouragement. Finally I would like to thank my boyfriend Alex for his never-ending support and patience during our studies at Oxford together.

I dedicate this thesis to my grandparents, Deirdre Constance and Peter John Horn.

Contents

Chapter 1

Introduction

Nuclear magnetic resonance (NMR) is a powerful tool for investigating the structure, disorder and dynamics of a material. It uses nuclear spins to probe the local environment in which each nucleus is situated. Experimentally, this is achieved by first applying an external magnetic field to the sample in question. In doing so the degeneracy of the nuclear spins is removed. Second, a range of radiofrequency pulses is applied in order to excite the nuclear spins into a higher energy state. The response of the nuclear spins to these radiofrequency pulses is then recorded. The sensitivity of the nuclear spin-states to their local environment has a measurable effect on the recorded spectra.

The degree of detail that can be obtained in this way on the numerous, and often subtle, interactions in a material is astounding. Information on the types of nuclei present, their geometrical arrangements, their bonding environments, and the dynamics within the structure can all be obtained. This enables us to build up a picture of the material so that we can understand its properties—what they are in the first instance, how they arise and how they can be manipulated—and ultimately leverage these properties for materials applications.

However, a lot of information is contained within experimental spectra, which makes them very difficult to decode. First-principles calculations are an invaluable, if not essential, aid to spectral interpretation because they are capable of isolating individual interactions—whether by type or structural location. The calculations also help to explain experimental observations to a level of detail presently impossible to obtain experimentally, and provide an efficient means of predicting materials properties to guide future experiments.

The methodology for calculating the NMR parameters in diamagnetic solids is well-established and has been used for a range of materials applications [1]. In the context of my thesis, I have used this methodology to study the $NaNbO_3$, $KNbO_3$ and $LiNbO_3$ perovskite structures, and a set of related disordered structures in order to investigate the effect of structural distortions on their NMR parameters. This research provides valuable information on the structural characterisation of these materials, which in turn will aid the development of lead-free alternatives to commercially-used piezoelectric materials.

The calculation of NMR parameters relating to paramagnetic materials is more involved and has yet to be fully developed. Paramagnetic systems contain unpaired electrons, the spins of which interact with the nuclear spins via a hyperfine interaction. Calculating this hyperfine interaction is problematic because the valence electrons induce a spin polarisation on the core electrons which cannot be fully modelled with existing methodologies for solid systems.

The hyperfine interaction also affects perturbed systems. In metallic systems, hyperfine interactions are induced in the course of the NMR ex-

periment due to the induced spin polarisation of the conduction electrons interacting with the nuclear spins. As a result, there is an observable shift in the resonance frequencies in experimental spectra known as the Knight shift [2]. A complete first-principles methodology for calculating Knight shifts, which circumvents the calculation of core polarisation, has been developed [3]. In this thesis, this methodology has been used for the first time to calculate the Knight shift in platinum, palladium and rhodium. These metals are commonly used as catalysts, for example as catalytic converters for automobiles and in fuel cells. The magnitude of the Knight shift across a set of platinum, palladium and rhodium surface structures has therefore also been investigated. This provides valuable insight into the electronic interactions on a catalyst's surface which in turn can be used to inform research into increasing their catalytic efficiency.

All calculations in this thesis have been performed using the state-of-the-art methodologies contained in the CASTEP code [4]. The significant parallelised computing resources required for the calculations were provided by the ARCHER UK National Supercomputing Service and the clusters managed by the Materials Modelling Laboratory of the Department of Materials, University of Oxford. On ARCHER, a typical Knight shift calculation for a bulk metal required 200–960 computing hours and 320 GB of memory. In the case of some of the largest perovskite structures (240 atoms per supercell), geometry optimisation calculations took up to 7680 computing hours with 512 GB of memory; the NMR calculations on the resulting structures took up to 3072 computing hours with 512 GB of memory.

My thesis is organised as follows. Chapters 2–4 explain the theory upon which my research is based. Chapter 2 provides an introduction on the the-

ory of experimental NMR, including discussions of the interactions relevant to the rest of the thesis and an overview of experimental solid-state NMR techniques. Chapter 3 explains the underlying theory of first-principles calculations, including discussions of the numerical approximations required to realistically implement them. Chapter 4 discusses the theory specifically required for the calculation of NMR parameters—including magnetic shielding, electric field gradients and Knight shifts.

In chapters 5–8 I present the results of my calculations. Chapter 5 is an in-depth study of the NMR parameters in $NaNbO_3$, $KNbO_3$ and $LiNbO_3$ perovskite structures, and the related solid solutions of $Na_xK_{1-x}NbO_3$, $K_xNa_{1-x}NbO_3$ and $Li_xNa_{1-x}NbO_3$. This is an investigation into how the NMR parameters are affected by structural disorder. Chapter 6 presents calculations of the Knight shift in the bulk structures of platinum, palladium and rhodium. It also investigates whether core polarisation has an effect on the Knight shift. Chapter 7 extends the study of the Knight shift in platinum, palladium and rhodium to surface structures so as to make a direct link to the surfaces and nanoparticles used in catalysis. Chapter 8 describes a novel method for including the effects of core polarisation in ground-state hyperfine calculations. Finally, chapter 9 contains a summary of the major findings resulting from my work and gives suggestions for further research.

Chapter 2

Nuclear magnetic resonance

In this chapter we shall cover the basic principle of nuclear magnetic resonance (NMR) and the interactions relevant to the calculations presented in later chapters. NMR can be conducted on solutions or solid samples. The former is comparatively straightforward to interpret as the anisotropy of the interactions is averaged out due to molecular tumbling. By contrast, solid-state NMR spectra are subject to large line broadenings because a sample will contain a range of static orientation-dependent interactions that are not averaged out. These interactions could originate from nuclear or electronic interactions or, on a larger length scale, from atomic or even crystal orientations. It is possible to remove some of the anisotropy in solid-state spectra through a technique known as magic angle spinning (MAS).

2.1 The principle of magnetic resonance

Nuclei possess an intrinsic spin angular momentum, $\mathbf{I}$, and with it an associated spin magnetic dipole moment $\boldsymbol{\mu}_I$ according to

$$\boldsymbol{\mu}_I = \gamma \mathbf{I}, \tag{2.1}$$

where γ is the gyromagnetic ratio for a nucleus and is specific to each isotope.

When there is no external magnetic field, all nuclear spin **I** orientations are degenerate. The application of an external magnetic field, $\mathbf{B}_0$, however removes this degeneracy according to the Zeeman interaction, such that the energy, E, of a certain spin-state is given by

$$E = -\boldsymbol{\mu}_I.\mathbf{B}, \tag{2.2}$$

where **B** is the magnetic field experienced by a certain nucleus. The energy difference, ΔE, between two spin-states increases according to

$$\Delta E = \Delta m \gamma |\mathbf{B}|, \tag{2.3}$$

where m is the magnetic quantum number—the quantum number for the orientation of **I** with respect to an arbitrarily chosen z-axis (usually selected to be parallel to $\mathbf{B}_0$).

Under the influence of the external magnetic field, the nuclei distribute themselves across the $2I+1$ energy levels according to Boltzmann statistics. In the case of spin-$\frac{1}{2}$ nuclei (for example ^{1}H or ^{13}C) the number of nuclei in the higher energy state n_{high} to that in the lower energy state n_{low} is given by

$$\frac{n_{\text{high}}}{n_{\text{low}}} = e^{-\Delta E/kT}, \tag{2.4}$$

where ΔE is the energy difference between the two energy levels, k is the Boltzmann constant and T is the temperature. For a system of one million ^{13}C nuclei in a 9.4 T field at room temperature, there are approximately only nine more nuclei in the lower energy state than in the upper energy state [5, p. 18]. There are two related points to make about this. First, measured NMR signals are recorded from the sample as a whole (i.e. from an ensemble of nuclei), whereas the signals from other spectroscopies can be obtained at

near atomic resolution.[1] Second, the ratio of the number of nuclei that have the potential to be recorded by a measurement compared to the total number of nuclei in the sample is much smaller than with other spectroscopies.[2] This results in NMR being a relatively insensitive form of spectroscopy. In order to boost the signal, high external magnetic fields, high gyromagnetic ratios and low temperatures are favoured. In the case of nuclei with low natural abundances, for example ^{13}C or ^{17}O, samples are sometimes enriched with the required magnetic isotope prior to measurement, or cross-polarisation techniques are employed.[3]

In order to probe the range of energies, an external pulse of electromagnetic radiation of frequency ν is applied to the sample. This will excite a spin-state into a higher energy spin-state, provided that the resonance condition, $\Delta E = h\nu$ (where h is Planck's constant), and the transition selection rule, $\Delta m = \pm 1$, are satisfied. Thus the frequency of the radiation required for nuclear magnetic resonance, called the Larmor frequency, is

$$\nu = \frac{\gamma|\mathbf{B}|}{2\pi}. \tag{2.5}$$

Note that equations 2.2 to 2.5 contain the local magnetic field experienced by the nucleus or electron, $\mathbf{B}$, which differs from the external magnetic

[1] An example of a near-atomic resolution spectroscopic technique is electron energy loss spectroscopy (EELS) in which an electron beam is passed through a thin sample. The incident electrons interact with the sample via various mechanisms, losing energy in the process. The subsequent range of energies of the exiting electrons is then analysed to obtain information on the structure and bonding of the sample.

[2] To continue the comparison of NMR with EELS: in EELS, information is obtained on the entirety of the sample volume through which the electrons pass. Whilst the electron beam only passes through a small volume of the sample (hence the near-atomic resolution), the rest of the sample also has the potential to be examined if the electron beam is directed towards a different part of the sample. By contrast, in NMR the whole sample is 'illuminated' by the spectrometer but only a tiny portion of the sample will be able to interact with it.

[3] Cross-polarisation techniques are able to transfer the magnetisation of abundant nuclei onto less abundant nuclei, for example from ^{1}H to ^{13}C.

field, $\mathbf{B}_0$. $\mathbf{B}_0$ induces current loops in the surrounding electrons which in turn induce an additional local magnetic field which is also experienced by the nuclear magnetic moment. This leads to a chemical shift, δ_{iso}, in the resonance frequencies which is specific to the chemical environment, thus enabling valuable information to be deduced about the structure and bonding of a sample.

Experimentally, δ_{iso} is measured as a ratio of frequencies between the frequency of the nuclei being measured, ν, and that of the reference, ν_{ref}, such that

$$\delta_{\text{iso}} = 10^6 \times \frac{(\nu - \nu_{\text{ref}})}{\nu_{\text{ref}}}. \tag{2.6}$$

Common references include the ^{1}H, ^{13}C and ^{29}Si resonances in tetramethylsilane ($Si(CH_3)_4$).

The resonances appear as a set of peaks—for example figure 2.1 shows the first ^{1}H NMR spectrum for ethanol recorded by Arnold *et al.* in 1951. The area under each peak is proportional to the number of nuclei in that chemical environment.

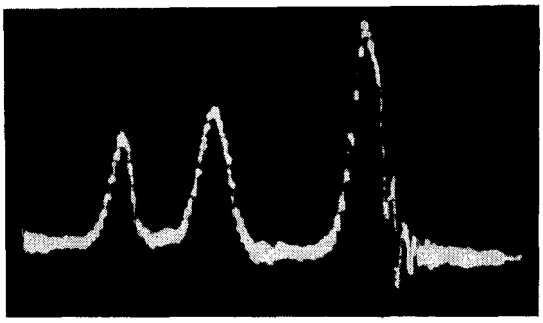

Figure 2.1: The first ^{1}H NMR spectrum for ethanol, CH_3CH_2OH, recorded by Arnold *et al.* in 1951. From left to right the peaks correspond to ^{1}H resonances in OH, CH_2 and CH_3 environments. [Reprinted from [6], with the permission of AIP Publishing.]

Early NMR spectra were recorded by keeping the frequency of the in-

cident radiation constant and varying the magnetic field or vice versa. In modern practices, the magnetic field strength is kept constant and a series of pulses containing a range of frequencies is applied to the specimen so that multiple resonances are excited simultaneously. Additional information can be obtained by measuring how long it takes for the nuclei to re-establish thermal equilibrium as a function of time (section 2.2.5).

The appearance of an NMR spectrum—the position of the resonance peaks and their associated broadenings—is governed by a number of physical phenomena. These include magnetic shielding, spin-spin coupling (which can be decomposed into a sum of dipolar coupling and J-coupling), quadrupolar coupling and relaxation mechanisms. The spectra of metallic samples also exhibit an additional shift in the resonance frequencies, known as the Knight shift.

2.2 Magnetic shielding

The induced local magnetic field, $\mathbf{B}_{\text{in}}$, is related to the applied magnetic field $\mathbf{B}_0$ by a dimensionless rank-2 tensor, $\underline{\underline{\sigma}}$, known as the absolute magnetic shielding tensor, such that

$$\mathbf{B}_{\text{in}} = -\underline{\underline{\sigma}}\mathbf{B}_0. \tag{2.7}$$

The total magnetic field, $\mathbf{B}$, experienced by a nucleus is therefore

$$\mathbf{B} = \mathbf{B}_0 + \mathbf{B}_{\text{in}} = (1 - \underline{\underline{\sigma}})\mathbf{B}_0. \tag{2.8}$$

Under isotropic conditions, such as in solution-based NMR or solid-state NMR under magic angle spinning (see section 2.2.6), the anisotropic components average out so that the key interaction measured is the isotropic

magnetic shielding, σ_{iso}:

$$\sigma_{\text{iso}} = \frac{1}{3}\text{Tr}[\underline{\underline{\sigma}}]. \tag{2.9}$$

Experimentally, σ_{iso} is measured as a chemical shift, δ_{iso}, which is expressed in relation to a reference shielding, σ_{ref}, of the chosen reference compound. δ_{iso} from equation 2.6 can therefore also be expressed in parts per million (ppm) as

$$\delta_{\text{iso}} = \frac{(\sigma_{\text{ref}} - \sigma_{\text{iso}})}{1 - \sigma_{\text{ref}}}. \tag{2.10}$$

Unless very heavy elements are being considered, $|\sigma_{\text{ref}}| \ll 1$ such that equation 2.10 is taken as

$$\delta_{\text{iso}} \approx (\sigma_{\text{ref}} - \sigma_{\text{iso}}). \tag{2.11}$$

The sign and magnitude of the magnetic shielding depends on the behaviour of the electrons surrounding the nuclei. Diamagnetic current loops oppose $\mathbf{B}_0$ and therefore increase the magnetic shielding around the nucleus. Conversely, paramagnetic current loops augment $\mathbf{B}_0$, and therefore decrease the magnetic shielding [7, p. 13].

The magnetic shielding tensor can be decomposed into symmetric and antisymmetric components. The antisymmetric parts have a negligible contribution to NMR spectra as they only affect properties to the second order, however they do affect relaxation times such as T_1 (section 2.2.5) [8, 9]. By diagonalising the symmetric part, the three principal components, σ_{11}, σ_{22} and σ_{33} are obtained. Similarly, the principal components of the chemical shift tensor are $\delta_{11} = \sigma_{\text{ref}} - \sigma_{11}$, $\delta_{22} = \sigma_{\text{ref}} - \sigma_{22}$ and $\delta_{33} = \sigma_{\text{ref}} - \sigma_{33}$. A popular convention, known as the Haeberlen convention, assigns the eigenvalues in the order

$$|\sigma_{33} - \sigma_{\text{iso}}| \geq |\sigma_{11} - \sigma_{\text{iso}}| \geq |\sigma_{22} - \sigma_{\text{iso}}| \tag{2.12}$$

as presented by Apperley *et al.* [5, p. 20].

The values of these three eigenvalues are very important for solid-state NMR because they determine the magnitude of the magnetic shielding along the principal axes. They define the 'chemical shift anisotropy' (CSA) of the sample. In a crystal with a single chemical environment, the CSA would result in the position of the resonance peak changing as a function of crystal orientation. In powder samples which contain crystals at all orientations, the CSA broadens this single peak into a distinctive line shape of the form shown in figure 2.2. By convention there are two common parameters used for the interpretation of this line shape: the (reduced) anisotropy, ζ, which is measured in ppm, and the asymmetry, η, which is dimensionless and takes a value between 0 and 1. These may be expressed as

$$\zeta = \sigma_{33} - \sigma_{\text{iso}} \tag{2.13}$$

and

$$\eta = \frac{\sigma_{22} - \sigma_{11}}{\zeta}. \tag{2.14}$$

The magnetic shielding tensor, $\underline{\underline{\sigma}}$, defined by equation 2.7 can also be expressed as the second derivative of the total energy, E, of the system with respect to the nuclear magnetic moment, $\boldsymbol{\mu}_I$, and the external magnetic field, $\mathbf{B}_0$, according to

$$\underline{\underline{\sigma}} = \frac{\partial^2 E}{\partial \boldsymbol{\mu}_I \partial \mathbf{B}_0}. \tag{2.15}$$

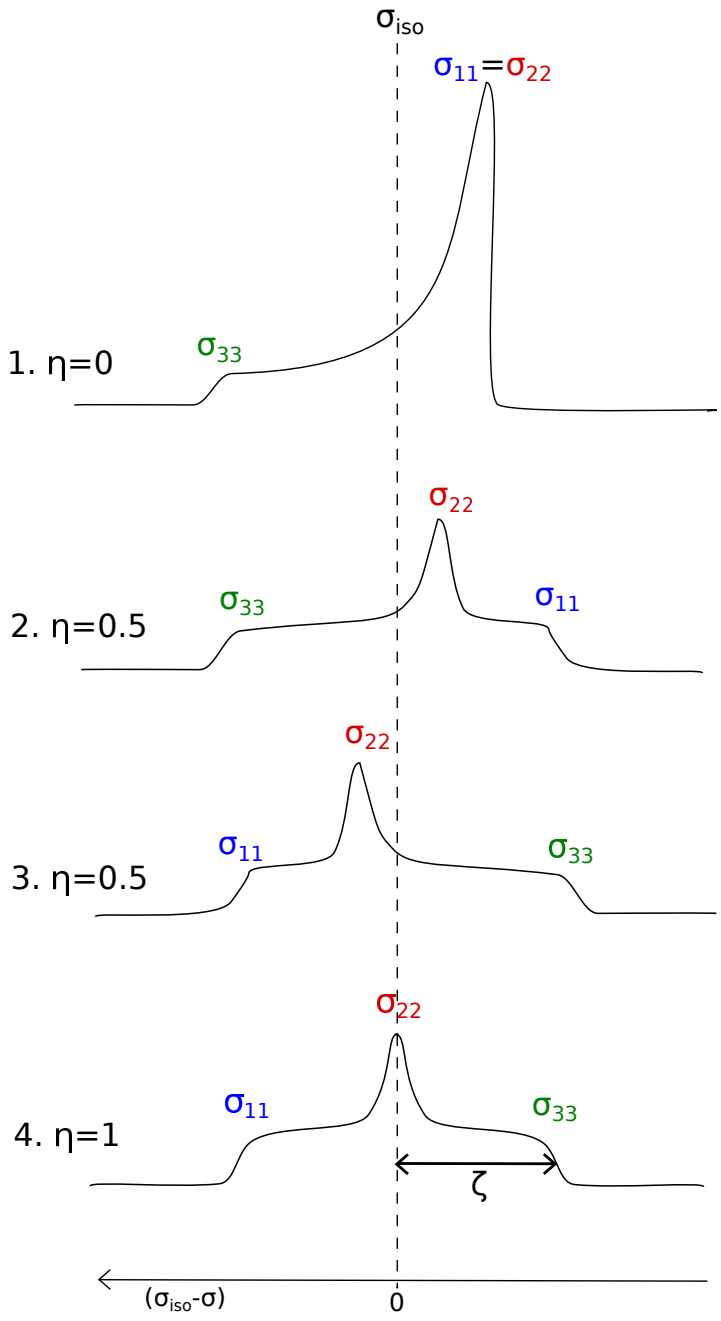

Figure 2.2: The effect of chemical shift anisotropy in powdered samples. Line shape 1 is an example in which $\sigma_{11} = \sigma_{22}$ and $\eta = 0$. Line shapes 2 and 3 both have $\eta = 0.5$ but equal and opposite anisotropies: ζ is negative for line shape 2 and positive for line shape 3. In line shape 4 $\eta = 1$ and ζ is positive (a reverse assignment of σ_{11} and σ_{33} would lead to ζ being negative).

2.2.1 Spin-spin coupling

In addition to the magnetic field induced by the orbital motion of the surrounding electrons, nuclear spins will interact with each other either directly through space or as an interaction mediated by the electrons. The former is known as direct dipolar coupling and is represented by a traceless rank-2 tensor $\underline{\underline{D}}_{KL}$. The latter is known as indirect coupling (often referred to as J-coupling) represented by the rank-2 tensor $\underline{\underline{J}}_{KL}$.

For two nuclear spins, $\mathbf{I}_K$ and $\mathbf{I}_L$, the overall Hamiltonian is given by

$$\hat{H} = \mathbf{I}_K(\underline{\underline{D}}_{KL} + \underline{\underline{J}}_{KL})\mathbf{I}_L. \tag{2.16}$$

The direct dipolar coupling, $\underline{\underline{D}}_{KL}$, is the interaction between the magnetic field generated by one nuclear spin (or nuclear magnetic moment) and a neighbouring nuclear spin (or nuclear magnetic moment). It is of the form (presented in the review paper by Bonhomme *et al.* [1]):

$$\underline{\underline{D}}_{KL} = -\frac{\hbar}{2\pi}\frac{\mu_0\gamma_K\gamma_L}{4\pi}\frac{3\mathbf{r}_{KL}\mathbf{r}_{KL}^{\mathrm{T}} - \underline{\underline{1}}|\mathbf{r}_{KL}|^2}{|\mathbf{r}_{KL}|^5}, \tag{2.17}$$

where μ_0 is the vacuum permeability, $\underline{\underline{1}}$ is the identity matrix, and $\mathbf{r}_{KL}$ is the separation between $\mathbf{I}_K$ and $\mathbf{I}_L$. The direct dipolar interaction is mediated through space, but only depends on the magnitude of the nuclear magnetic moments, not their direction.

By contrast, the indirect coupling, $\underline{\underline{J}}_{KL}$, is the interaction between the spins that is mediated through electrons. It can be expressed as the second derivative of the energy with respect to the magnetic moments of the nuclei K and L according to

$$\underline{\underline{J}}_{KL} = \frac{\hbar\gamma_K\gamma_L}{2\pi}\frac{\partial^2 E}{\partial\boldsymbol{\mu}_K\partial\boldsymbol{\mu}_L}. \tag{2.18}$$

Alternatively, the indirect coupling can be described as the magnetic field generated by the nucleus L which is in turn experienced by nucleus K:

$$\mathbf{B}(\mathbf{R}_K) = \frac{2\pi}{\hbar\gamma_K\gamma_L}\underline{\underline{J}}_{KL}.\boldsymbol{\mu}_L, \tag{2.19}$$

where $\mathbf{R}_K$ is the position of nucleus K.

The magnetic field experienced by nucleus K can be further decomposed into components arising from the orbital and spin moments of the electrons. The magnetic moment of nucleus L induces an orbital current $\mathbf{j}(\mathbf{r})$ which in turn generates a magnetic field experienced by nucleus K. The magnetic moment of nucleus L will also interact with the spin of the electrons, which generates an electronic spin polarisation and which in turn interacts with the magnetic moment of nucleus K. This is expressed as

$$\begin{aligned}\mathbf{B}(\mathbf{R}_K) =& \frac{\mu_0}{4\pi}\int \mathbf{j}(\mathbf{r}) \times \frac{\mathbf{r}_K}{|\mathbf{r}_K|^3}\mathrm{d}^3r \\ &+ \frac{\mu_0}{4\pi}\int \mathbf{m}(\mathbf{r}).\left[\frac{3\mathbf{r}_K\mathbf{r}_K^{\mathrm{T}} - \underline{\underline{1}}|\mathbf{r}_K|^2}{|\mathbf{r}_K|^5}\right]\mathrm{d}^3r \\ &+ \frac{\mu_0}{4\pi}\frac{8\pi}{3}\int \mathbf{m}(\mathbf{r})\delta(\mathbf{r}_K)\mathrm{d}^3r,\end{aligned} \tag{2.20}$$

where $\mathbf{m}(\mathbf{r})$ is the electronic magnetisation of the system and $\mathbf{r}_K = \mathbf{r} - \mathbf{R}_K$. The first term is the orbital contribution, and the second and third terms are the spin contributions. The first term can be further decomposed into diamagnetic and paramagnetic contributions.[4] The second term is the spin-dipolar contribution (and is of a very similar form to equation 2.17) and the third is the Fermi-contact term. The latter two terms are forms of hyperfine interaction (discussed in section 2.2.3). The spin-dipolar and Fermi-contact terms are the anisotropic and isotropic components of the hyperfine interaction respectively.

[4]The decomposition depends on the gauge, though the sum of the parts is not affected. It is natural to set the gauge origin on the atom.

2.2.2 Quadrupolar coupling and electric field gradients

For nuclei with spin $I > \frac{1}{2}$, the charge distribution of the nucleus is not spherical and therefore the nucleus possesses a quadrupole moment, eQ. This quadrupole moment interacts with the electric field gradient (EFG) of the surrounding electrons and ions. Note that quadrupolar coupling is purely electric in origin; it is not magnetic. Nevertheless, it affects spin energies and therefore affects NMR.

The rank-2 EFG tensor, $G_{\alpha\beta}(\mathbf{r})$, is defined by

$$G_{\alpha\beta}(\mathbf{r}) = \frac{\partial E_\alpha(\mathbf{r})}{\partial r_\beta} - \frac{1}{3}\delta_{\alpha\beta}\sum_\gamma \frac{\partial E_\gamma(\mathbf{r})}{\partial r_\gamma}, \tag{2.21}$$

where α, β and γ represent Cartesian coordinates and $E_\alpha(\mathbf{r})$ is the component α of the local electric field at position $\mathbf{r}$ [1]. This tensor is symmetric and traceless. Once diagonalised, the tensor may be characterised by two parameters: the nuclear quadrupolar coupling constant, C_Q, and the asymmetry, η_Q. If the tensor's eigenvalues, V_{xx}, V_{yy} and V_{zz} are assigned such that $|V_{zz}| > |V_{yy}| > |V_{xx}|$ (adopting the convention in CASTEP), the nuclear quadrupolar coupling constant is defined as

$$C_Q = \frac{eV_{zz}Q}{h} \tag{2.22}$$

and the asymmetry as

$$\eta_Q = \frac{V_{xx} - V_{yy}}{V_{zz}}. \tag{2.23}$$

The strength of the quadrupolar coupling is therefore dependent both on the strength of the EFG (characterised by the largest principal component, V_{zz}) and the quadrupole moment of the nucleus, eQ. Since the EFG tensor is traceless, quadrupolar coupling does not affect the resonance frequencies

of solution-based NMR. However, it still affects relaxation processes and therefore line broadening.

Quadrupolar coupling leads to significant line broadening in solid-state NMR. The number of peaks in the spectrum are determined by the number of transitions between the possible nuclear-spin states. The shape of the profile is determined by η_Q and the width of the profile is determined by C_Q. Figure 2.3 shows a set of example spectra for a spin-1 nucleus in different η_Q environments.[5] Experimentally, η_Q and C_Q are obtained by fitting experimental spectra to empirical simulations, for example using Dmfit [10]. It is not possible to determine the sign of C_Q.

If the quadrupolar interaction is particularly large, the second order perturbations to the Zeeman energy will be large enough to have a noticable effect on experimental spectra. This will manifest as additional anisotropic line broadenings and shifts. In situations where these second-order quadrupolar interactions are significant, the quadrupolar product, P_Q, is commonly used:

$$P_Q = C_Q(1 + \eta_Q^2/3)^{1/2}. \tag{2.24}$$

Methods for removing first- and second-order quadrupolar broadening from solid-state spectra are discussed in section 2.2.6.

2.2.3 The hyperfine interaction

In the field of magnetic resonance, the hyperfine interaction is defined as the interaction between the spin of the nucleus, **I**, and the spin of the electron,

[5] In the case of odd multiples of spin-$\frac{1}{2}$ nuclei, the line shapes will consist of a large central peak corresponding to the $I = \frac{1}{2} \leftrightarrow -\frac{1}{2}$ transition, known as the central transition. This will be surrounded by a series of smaller peaks corresponding to the other allowed spin transitions, known as side transitions. In the case of even multiples of spin-$\frac{1}{2}$ nuclei, the two central peaks will correspond to central transitions of equal intensity.

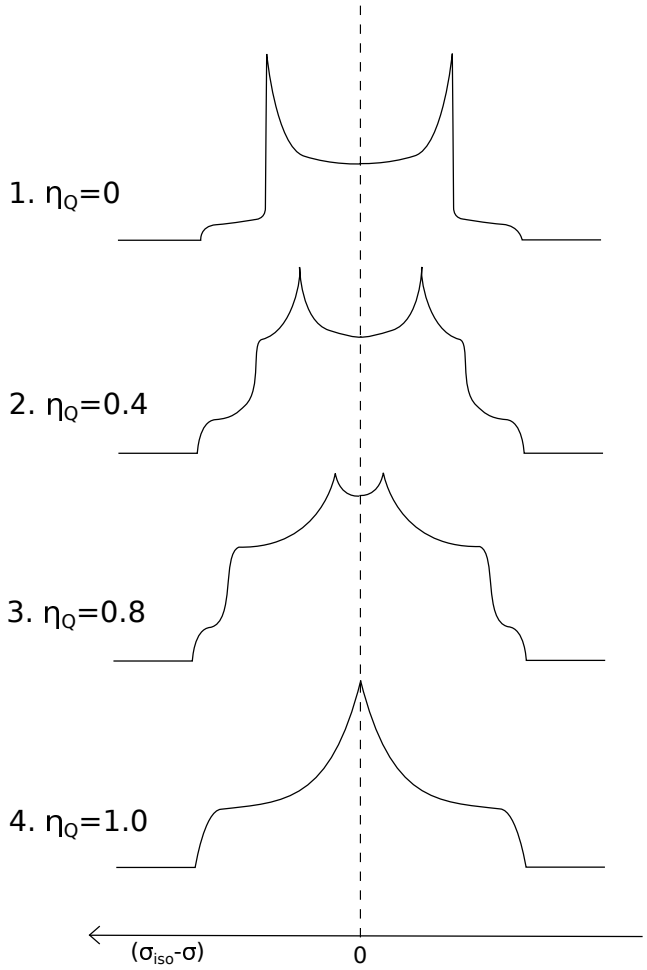

Figure 2.3: Example NMR line-shapes for a spin $I = 1$ nucleus across a range of different η_Q values.

S ([5, p. 211] and [11, p. 97]).

The Hamiltonian for hyperfine coupling, $\hat{H}_{\mathrm{HF}}$, can be expressed as the interaction between the magnetic dipole moment, $\boldsymbol{\mu}_I$, of the nucleus with the magnetic field generated by the atomic electrons, $\mathbf{B}_e$, according to

$$\hat{H}_{\mathrm{HF}} = -\boldsymbol{\mu}_I.\mathbf{B}_e. \tag{2.25}$$

Since the nuclear spin magnetic dipole moment $\boldsymbol{\mu}_I$ is directly proportional to **I** (equation 2.1), and $\mathbf{B}_e$ is directly proportional to the total angular

momentum of the electron **J** ([11, p. 97-101]), equation 2.25 becomes

$$\hat{H}_{\mathrm{HF}} = A\mathbf{I}.\mathbf{J}, \tag{2.26}$$

where A is a constant. For light elements, relativistic effects do not have a measurable effect on the hyperfine interaction [12, 13]. In these cases spin-orbit effects can be excluded and the hyperfine Hamiltonian can be expressed as

$$\hat{H}_{\mathrm{HF}} = A\mathbf{I}.\mathbf{S}. \tag{2.27}$$

Incorporating into the hyperfine Hamiltonian the interaction between the electron and M nuclear spins $\mathbf{I}_l$, where l denotes the l^{th} nucleus at position $\mathbf{R}_l$, equation 2.27 becomes

$$\hat{H}_{\mathrm{HF}} = \sum_{l=1,M} \mathbf{S}^{\mathrm{T}} \underline{\underline{A}}^{(l)} \mathbf{I}_l, \tag{2.28}$$

where $\underline{\underline{A}}^{(l)}$ is the hyperfine coupling tensor for the l^{th} nucleus [14]. This can be separated into two parts corresponding to the isotropic Fermi-contact interaction and the anisotropic spin-dipolar interaction according to

$$A_{ij}^{(l)} = a^{(l)}\delta_{ij} + b_{ij}^{(l)}, \tag{2.29}$$

where $a^{(l)}$ is the isotropic hyperfine (Fermi-contact) interaction, $b_{ij}^{(l)}$ is the anisotropic hyperfine (spin-dipolar) interaction, δ_{ij} is the Kronecker delta and i and j are Cartesian axes.

Physically the Fermi-contact interaction is the magnetic (spin-spin) interaction between the electron and the nucleus when the electron is inside the nucleus. The strength of the Fermi-contact interaction is directly proportional to $\gamma_e\gamma\mathbf{I}.\mathbf{S}$ [15, p. 465] and can therefore be expressed in atomic units as

$$a^{(l)} = \frac{8\pi}{3} g_s \mu_B \gamma_l \mu_N \rho_s(\mathbf{R}_l), \tag{2.30}$$

where $\rho_s(\mathbf{R}_l)$ is the electron spin density ($\rho_s = \rho_\uparrow - \rho_\downarrow$) at the centre of the l^{th} nucleus, γ_l is the gyromagnetic ratio for the l^{th} nucleus, g_s is the dimensionless g-factor for a free electron, γ_e is the gyromagnetic ratio for a free electron, μ_B is the Bohr magneton and μ_N is the nuclear magneton [14]. Since ρ_s is directly proportional to the square of the electron wavefunction at the centre of the nucleus, $|\Psi(\mathbf{R}_l)|^2$, the Fermi-contact interaction is only affected by s-like electrons, because only s-like wavefunctions are non-zero at the nucleus.

By contrast, the spin-dipolar interaction is caused by non s-like electrons, for example those with p or d symmetries. In atomic units, the spin-dipolar interaction is

$$b_{ij}^{(l)} = g_s \mu_B \gamma_l \mu_N \int \frac{3r_i r_j - r^2 \delta_{ij}}{r^5} \mathrm{d}^3 r, \tag{2.31}$$

where $\mathbf{r}$ is expressed in relation to the position of the nucleus at $\mathbf{R}_l$ and $r = |\mathbf{r}|$ [14].

In paramagnetic materials, the ground-state electronic spin density causes a hyperfine interaction which can be measured with NMR or electron paramagnetic resonance (EPR).[6] In diamagnetic and paramagnetic materials the hyperfine interaction can also be induced by the nuclear spin, resulting in J-couplings. In metallic systems the hyperfine interaction induced by $\mathbf{B}_0$ also causes a 'Knight shift' in NMR spectra.

2.2.4 The Knight shift

First observed by Knight in 1949 [2], this is a systematic shift in the resonance frequencies of metallic systems which is not observed in the resonance frequencies of the same element in non-metallic systems. To a first approx-

[6] EPR is similar to NMR but it measures the resonance of unpaired electron spins instead of nuclear spins.

imation, this shift occurs because an external magnetic field will induce a magnetisation, M, in the material. The magnetisation arises from the unequal change in energy of the conduction electrons (those close to the Fermi energy, E_F) between those with spin $= \frac{1}{2}$ and those with spin $= -\frac{1}{2}$. Thus the material acquires a magnetisation, characterised by the average spin of the conduction electrons $\langle S_z \rangle$ or by the Pauli spin susceptibility χ_s, where $M = g_s N \mu_B \langle S_z \rangle = \chi_s |\mathbf{B}_0|$ (where g_s is the free electron g-factor and N is Avogadro's number). This net electron spin creates a magnetic field, additional to $\mathbf{B}_0$, which interacts with the nuclear spin magnetic moment via the hyperfine interaction. This produces a shift in energy levels which manifests as a shift in resonance frequencies. The Knight shift, K, is defined as [16, p. 478]

$$K = -\frac{|\Delta \mathbf{B}|}{|\mathbf{B}_0|} = \frac{a^{(l)} \chi_s}{g_s N \mu_B \gamma_l \hbar}, \tag{2.32}$$

where $a^{(l)}$ is the Fermi-contact constant as defined for the l^{th} nucleus in equation 2.30. Thus K is proportional to the value of the electron spin density at the nucleus according to

$$K \approx \frac{\chi_s |\Psi(\mathbf{R}_l)|^2}{N}. \tag{2.33}$$

The theoretical evaluation of $|\Psi(\mathbf{R}_l)|^2$ poses some difficulties as discussed in section 4.3.1.

The magnitude of the Knight shift at each crystallographically distinct nucleus in a sample will differ. Since a sample will contain several environments (for example those of the bulk and surface), the range of Knight shifts will result in inhomogeneous broadening of the NMR spectra.

2.2.5 Spin-lattice relaxation and the spin-lattice relaxation time, T_1

Spin-lattice relaxation occurs due to the interaction between the nuclear spins and the surrounding lattice. When a sample is placed in an external magnetic field the degeneracy of the spin-states is instantaneously lowered. However, it takes time for the spins to respond and reorient themselves in such a way as to re-establish a Boltzmann equilibrium. This occurs due to multiple mechanisms, for example dipolar coupling between the nuclei and the motion of surrounding nuclei or quadrupolar interactions [17].

In the case of spin-$\frac{1}{2}$ nuclei, assuming the time-dependence of the system re-establishing Boltzmann equilibrium is exponential (which is appropriate in most cases), the difference in the $m = \frac{1}{2}$ and $m = -\frac{1}{2}$ populations is given by

$$\Delta n(t) = \Delta n_{eq}[1 - e^{-t/T_1}], \tag{2.34}$$

where $\Delta n(t)$ is the difference in the two spin populations for a total of n spins, Δn_{eq} is the difference in the spin populations at equilibrium, t is the time after the initial application of the external magnetic field and T_1 is the spin-lattice relaxation time [7, p. 56]. In this way T_1 is the time it takes for the spin population difference to reach 63% of its value at equilibrium. The energy absorbed or emitted due to nuclear spins changing spin-states is taken from or released into the motion of the lattice.

Spin-lattice relaxation tends to be most efficient when the mean component of the molecular motion coincides with the Larmor frequency of the spins (of the order of MHz for nuclei). In the case of liquid samples, the tumbling motion of the molecules results in it being fairly likely that a component frequency of this motion coincides with the Larmor frequency of the

nuclei and thus for spin-$\frac{1}{2}$ nuclei T_1 is usually of the order of seconds [7, p. 56]. In solids, however, the motions tend to be predominantly vibrational and thus of higher frequency than the Larmor frequency. Thus a smaller fraction of the motion coincides with the Larmor frequency, resulting in higher T_1 values of the order of seconds to kiloseconds [5, p. 36].

The spin-lattice relaxation time T_1 affects the time between recording spectra as time should be allowed for the system to establish equilibrium (and thus maximum magnetisation) before applying radiofrequency pulses. It also affects the degree of line broadening of the spectral peaks due to the Heisenberg Uncertainty Principle. Most importantly, in the context of this thesis, T_1 can be used to probe the local density of states at the Fermi level (E_f-LDOS) via the Korringa relation (see chapter 7).

2.2.6 Experimental solid-state NMR

As discussed above, experimental solid-state NMR spectra contain large amounts of line broadening due to the inherent anisotropy of the solid samples. This leads to difficulties pertaining to the sensitivity and resolution of spectra. Notable anisotropic interactions include chemical shift anisotropy (CSA), dipolar coupling and quadrupolar coupling [5, p. 28]. Whilst it may be desirable to remove these interactions from spectra to aid interpretation, the interactions themselves can provide further valuable information about the sample. Dipolar coupling provides information on the distances between nuclei and atomic structure, CSA can provide structural information and J-coupling can provide information on chemical bonding and geometry. There therefore exist methods for selectively reintroducing interactions in spectra. An overview of the experimental methods to both remove and reintroduce

interactions is presented in the extensive review paper by Bonhomme *et al.* [1].

The most common technique for removing broadening due to CSA, dipolar coupling and quadrupolar coupling is magic angle spinning (MAS) [18, 19]. These interactions involve a dependency on the orientation of the crystal relative to the applied magnetic field of the form $3\cos^2\theta - 1$, where θ is the angle between the crystallographic principal axis and the applied magnetic field. When $\theta = 54.736°$, $3\cos^2\theta - 1 = 0$. Associated broadening can therefore be removed by rapidly spinning the sample at the 'magic angle' of 54.736° to the applied magnetic field. Figure 2.4 illustrates how anisotropic interactions are gradually removed with increasing rotation rate. Depending on the strength of the interactions present it is not always possible to spin the specimen fast enough to achieve isotropic conditions. Rotation rates tend to be 5-70 kHz [1], however rates of up to 110 kHz may be used [20]. In the case of paramagnetic materials, where there are unpaired electrons present, the anisotropy associated with the hyperfine interaction can be very large and therefore very high rotation rates are required in order to achieve spectra of a suitable resolution [5, p. 213].

For quadrupolar nuclei, MAS can remove the broadening associated with first-order quadrupolar interactions, however additional techniques are required to remove second- and higher-order effects. Double rotation (DOR) experiments, in which the sample is rotated about two angles simultaneously, can be used to average out second-order quadrupolar interactions. However, the samples cannot be rotated at such high rates as are used in MAS, resulting in a large number of sidebands which may hinder interpretation [5, p. 161]. Multiple quantum magic-angle spinning (MQMAS) experi-

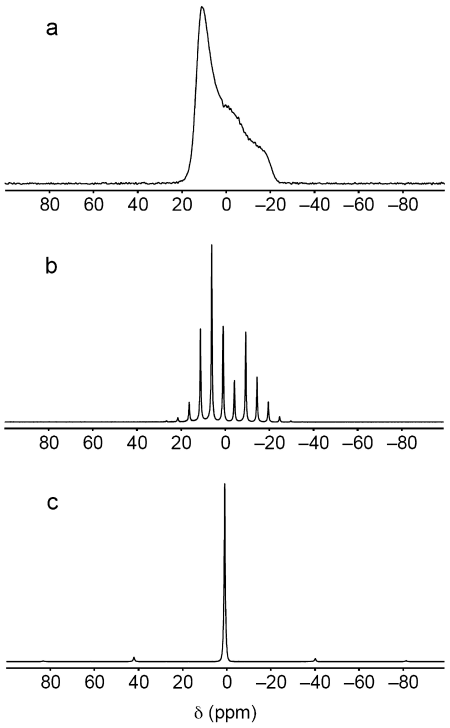

Figure 2.4: NMR spectra for ^{31}P nuclei ($I = \frac{1}{2}$) in ammonium dihydrogen phosphate. Part a shows the broadened resonance peak recorded under static conditions. At a low rotation MAS rate (here 1.25 kHz) this peak resolves into a set of sharp sidebands (part b). As the rotation rate increases (in this case to 10 kHz) these sidebands resolve into the spectrum obtained under isotropic conditions—in this case there is only one resonance (part c). [Reprinted (adapted) with permission from [1]. Copyright 2012 American Chemical Society.]

ments are the most common method for removing or studying second- and higher-order effects. The sample is spun at a single angle, and a sequence of radiofrequency pulses is applied to selectively excite certain transitions. A good introduction into this diverse technique is given by Apperley *et al.* [5, p. 163].

Despite the plethora of different techniques available for probing the structure, interactions and chemical environments in solids, the experiments

are time-consuming and restricted to certain systems, and it can be difficult to acquire spectra of sufficient resolution for analysis. Theoretical calculations of relevant NMR parameters therefore provide a much-needed, if not essential, aid for the prediction and interpretation of experimental spectra, and offer valuable insight into the active mechanisms in a system.

Chapter 3

First-principles methodologies

3.1 First-principles calculations

A first-principles approach is one which is founded only on the basic laws of physics. No extra parameters should be introduced to fit the model to experimental data. Since the mechanisms involved in NMR are quantum mechanical in origin, it is most appropriate to calculate their relevant parameters using quantum theory.

For a system containing electrons and nuclei, the time-independent non-relativistic Schrödinger equation, $\hat{H}\Psi = E\Psi$, can be expressed as

$$\begin{aligned}\Bigg[&-\sum_i \frac{\hbar^2}{2m_e}\nabla_i^2 - \sum_I \frac{\hbar^2}{2M_I}\nabla_I^2 - \sum_{i,I} \frac{e^2}{4\pi\epsilon_0}\frac{Z_I}{|\mathbf{r}_i - \mathbf{R}_I|} \\ &+ \frac{1}{2}\sum_{I\neq J} \frac{e^2}{4\pi\epsilon_0}\frac{Z_I Z_J}{|\mathbf{R}_I - \mathbf{R}_J|} + \frac{1}{2}\sum_{i\neq j} \frac{e^2}{4\pi\epsilon_0}\frac{1}{|\mathbf{r}_i - \mathbf{r}_j|}\Bigg]\Psi_{\text{tot}} = E_{\text{tot}}\Psi_{\text{tot}},\end{aligned} \tag{3.1}$$

where $\mathbf{r}_i$ and $\mathbf{R}_I$ are the spatial coordinates of the electrons and nuclei respectively, M_I is the mass of the nucleus, m_e the mass of the electron, Z_I the absolute charge of the nucleus, ϵ_0 the permittivity of free space and e the charge of the electron ([21, p. 22] and [22, p. 52]). Since the nuclei have a much greater mass than the electrons, the nuclei can be treated as static

with respect to the motion of the electrons. The nuclear kinetic energy is therefore taken to be zero (or treated classically in some situations where nuclear motion is significant), and the nuclear-nuclear potential energy is a constant. Furthermore, the total wavefunction, Ψ_{tot}, can be rewritten as a product of the fully electronic and fully nuclear wavefunctions, such that $\Psi_{\text{tot}} = \Psi(\mathbf{r}_1, \mathbf{r}_2, \ldots, \mathbf{r}_N)\Phi(\mathbf{R}_1, \mathbf{R}_2, \ldots, \mathbf{R}_M)$, where N and M are the total number of electrons and nuclei respectively. The nuclear components of equation 3.1 can therefore be decoupled from the electronic components in accordance with the Born-Oppenheimer approximation [21, p. 52–54]. The Schrödinger equation for the electrons is therefore:

$$\left[-\sum_i \frac{\hbar^2}{2m_e}\nabla_i^2 - \sum_{i,I} \frac{e^2}{4\pi\epsilon_0}\frac{Z_I}{|\mathbf{r}_i - \mathbf{R}_I|} + \frac{1}{2}\sum_{i\neq j} \frac{e^2}{4\pi\epsilon_0}\frac{1}{|\mathbf{r}_i - \mathbf{r}_j|} \right]\Psi = E\Psi, \quad (3.2)$$

where E is the total electronic energy and Ψ is the electronic wavefunction.

Solving equation 3.2 for more than one electron is computationally challenging. The difficulty lies with the calculation of the electron-electron interactions. The computational power required scales to the power of $3N$, where N is the number of electrons. Many methods have been developed to make equation 3.2 computationally viable. A commonly used example is the Hartree-Fock method which treats the interaction between electrons as an interaction between a single electron and the mean field of all the other electrons [23]. Whilst this method can be practically applied to small molecules, it is computationally expensive for solid systems. Density functional theory is a significantly cheaper alternative and has been widely adopted by theoretical and experimental communities for calculating NMR parameters [1].

3.1.1 Density functional theory (DFT)

The DFT formalism begins with the premise that the total ground state energy, E_0, of a system is a unique functional of the total electron density, ρ, of the system, as formally proved by Hohenberg and Kohn in 1964 [24]:

$$E_0 = E_0[\rho]. \tag{3.3}$$

Unfortunately the functional $E_0[\rho]$ is not known exactly. In 1965 Kohn and Sham developed a method that circumvented this by supposing that there existed a system of fictitious non-interacting single electrons whose density was identical to that of the original ground state density of the interacting system [25]. In atomic units, the set of Schrödinger equations for the electrons, i, can be expressed as ([21, p. 40]):

$$\left[-\frac{1}{2}\nabla^2 + V_n(\mathbf{r}) + V_H(\mathbf{r}) + V_{xc}(\mathbf{r}) \right] \psi_i(\mathbf{r}) = \varepsilon_i \psi_i(\mathbf{r}). \tag{3.4}$$

The kinetic energy of the electron is expressed by $-\frac{1}{2}\nabla^2$. $V_n(\mathbf{r})$ is the potential of the nuclei. $V_H(\mathbf{r})$ is known as the Hartree potential: it is the Coulomb interaction between the electron and the mean field of all the electrons. $\psi_i(\mathbf{r})$ are the single electron wavefunctions and ε_i are the corresponding single electron eigenvalues.

The unknown many-body interactions are placed in the exchange-correlation potential $V_{xc}(\mathbf{r})$. The unknown contribution to the energy is therefore confined to a small fraction (approximately 10%) of the total energy, in contrast to equation 3.2 where the unknown interactions were present throughout the whole equation. The total energy for the whole system, E, is now expressed

as [21, p. 39-40]:

$$\begin{aligned} E =& E_{kin} + E_n + E_H[\rho] + E_{xc}[\rho] \\ =& -\sum_i \int \psi_i^*(\mathbf{r}) \frac{\nabla^2}{2} \psi_i(\mathbf{r}) \mathrm{d}^3 r \\ &+ \int \rho(\mathbf{r}) V_n(\mathbf{r}) \mathrm{d}^3 r + \frac{1}{2} \iint \frac{\rho(\mathbf{r})\rho(\mathbf{r}')}{|\mathbf{r}-\mathbf{r}'|} \mathrm{d}^3 r \mathrm{d}^3 r' + E_{xc}[\rho], \end{aligned} \tag{3.5}$$

where the exchange-correlation energy, $E_{xc}[\rho]$, is related to $V_{xc}(\mathbf{r})$ via:

$$V_{xc}(\mathbf{r}) = \left. \frac{\delta E_{xc}[\rho]}{\delta \rho} \right|_{\rho(\mathbf{r})}. \tag{3.6}$$

Equation 3.2 therefore becomes a set of single electron equations which are coupled together through the electron charge density $\rho(\mathbf{r})$ via:

$$\rho(\mathbf{r}) = \sum_i |\psi_i(\mathbf{r})|^2. \tag{3.7}$$

These equations can be solved iteratively in a set of self-consistent (SCF) cycles (see figure 3.1). However, to begin with, $E_{xc}[\rho]$ still has to be approximated.

3.2 Exchange-correlation functionals

The simplest approximation for $E_{xc}[\rho]$ is the 'local density approximation' (LDA) [27, 28]. This assumes that $E_{xc}[\rho]$ depends only on the charge density at each point and is of the form

$$E_{xc}^{LDA}[\rho] = \int \epsilon_{xc}^{LDA}(\rho(\mathbf{r})) \mathrm{d}^3 r, \tag{3.8}$$

where ϵ_{xc}^{LDA} is the exchange-correlation energy per unit volume [29]. Usually the exchange-correlation energy at each point is taken to be that of a homogeneous electron gas of the same charge density present at that point. In this case the exchange part of ϵ_{xc}^{LDA} is $\epsilon_x^{LDA} = -(3/4)(3/\pi)^{1/3}\rho^{4/3}$ [29]. The

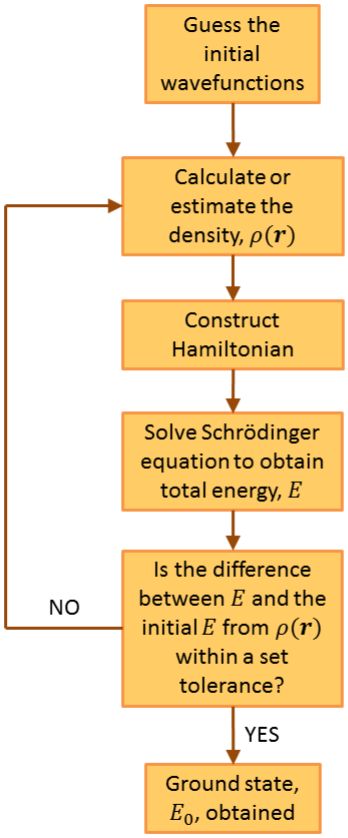

Figure 3.1: The iterative solving of the Kohn-Sham equations for the total energy, E. Self-consistency is reached when the difference in E between a set number of successive iterations is within a set tolerance. [Reprinted with permission from [26].]

correlation component cannot be expressed analytically, however a form has been obtained using Quantum Monte Carlo methods [27]. There have also been several parameterisations of the correlation energy, of which the most commonly used is by Perdew and Zunger [28].

By additionally taking into account the gradient at each point more advanced 'generalised gradient approximation' (GGA) exchange-correlation

functionals are obtained which are of the form [29]

$$E_{xc}^{GGA}[\rho] = \int \epsilon_{xc}^{GGA}(\rho(\mathbf{r}), \nabla\rho(\mathbf{r}))\mathrm{d}^3r. \tag{3.9}$$

The most commonly used exchange-correlation functional used for calculating NMR parameters in solids is the GGA functional formulated by Perdew, Burke and Ernzerhof (PBE) [30]. Calculated NMR parameters are extremely sensitive to lattice constants and therefore require lattice constants to be obtained with high accuracy. LDA is found to underestimate lattice constants by approximately 1%, whereas PBE overestimates them by the same degree. The PBEsol functional is a more recent varient of PBE that has been developed to calculate more accurately the properties of solids [31]. In a small study of simple metals, semiconductors, ionic solids and transition metals, PBEsol was found to reduce the lattice parameter mean error to approximately a quarter of that obtained when using PBE [31].

3.3 Practical implementation of Density Functional Theory

In order to solve equation 3.5 in practice a set of numerical approximations need to be made.

3.3.1 Basis set

The wavefunction needs to be expressed as a set of functions constructed in linear combination. This 'basis' could be a set of localised atom-centred orbitals, for example the Gaussian-type orbitals used in the CRYSTAL [32, 33] and SIESTA [34] codes. Another possibility is a set of planewaves as

used in the CASTEP code [4]:

$$\psi_{\mathbf{k}}(\mathbf{r}) = \sum_{\mathbf{G}=0}^{\mathbf{G}_{max}} c_{\mathbf{k}+\mathbf{G}} \frac{1}{\sqrt{\Omega}} e^{i(\mathbf{k}+\mathbf{G}).\mathbf{r}}, \tag{3.10}$$

where $\mathbf{k}$ is an electron wavevector in the first Brillouin zone, $\mathbf{G}$ is a reciprocal lattice vector and Ω is the volume of the primitive cell. Calculations using a planewave basis are also easily parallelised across multiple computer processors [35].

The size of the basis set must be carefully chosen. The highest component plane-wave is determined by an energy 'cut-off', $\epsilon_{cut-off}$, such that

$$\frac{1}{2}|\mathbf{k} + \mathbf{G}_{max}|^2 \leq \epsilon_{cut-off}. \tag{3.11}$$

Increasing the number of planewaves increases the accuracy of the calculations but at the expense of requiring increased computational power. A set of calculations over a range of energy cut-offs is therefore conducted. As the energy cut-off is increased, the property being calculated converges to a single value—for example, as in figure 3.2. The final chosen energy cut-off is taken to be that for which the property is converged within a required tolerance.

3.3.2 Periodicity of the structures

In order to reduce the number of atoms in the solid-state system to a computationally realistic level, the periodicity of the crystal lattice is exploited using Bloch's theorem [16, p. 163]:

$$|\psi_{\mathbf{k}}(\mathbf{r} + \mathbf{L})|^2 = |\psi_{\mathbf{k}}(\mathbf{r})|^2, \tag{3.12}$$

where $\mathbf{L}$ is the real space lattice vector. In this way the wavefunction is expressed as

$$\psi_{\mathbf{k}}(\mathbf{r}) = e^{i\mathbf{k}.\mathbf{r}} u_{\mathbf{k}}(\mathbf{r}), \tag{3.13}$$

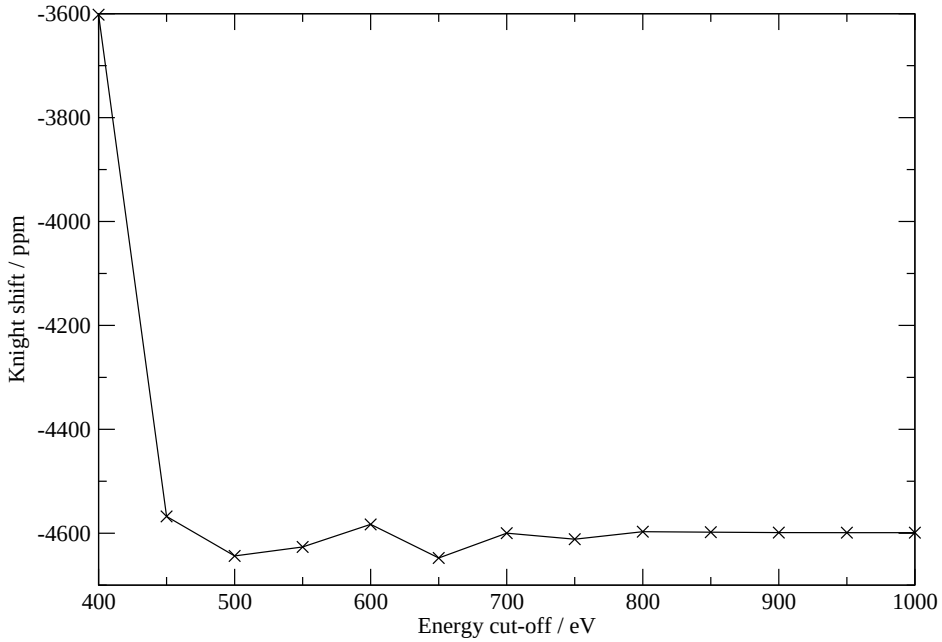

Figure 3.2: Convergence of the Knight shift in bulk Pd with respect to energy cut-off.

where $e^{i\mathbf{k}.\mathbf{r}}$ is the spatial phase factor and $u_{\mathbf{k}}(\mathbf{r})$ is a periodic function. Consequently, only the unit cell needs to be considered.

When investigating non-periodic structures using methodologies which employ periodicity, the structure must be made periodic by containing all the structural information of interest in a supercell. This might be the case for investigations of defects in solids, surfaces or single molecules (see figure 3.3). In the latter two cases, a vacuum region needs to be incorporated in the supercell. A set of convergence calculations must be conducted with increasing supercell size until there is no interaction between the periodic images as this would be non-physical.

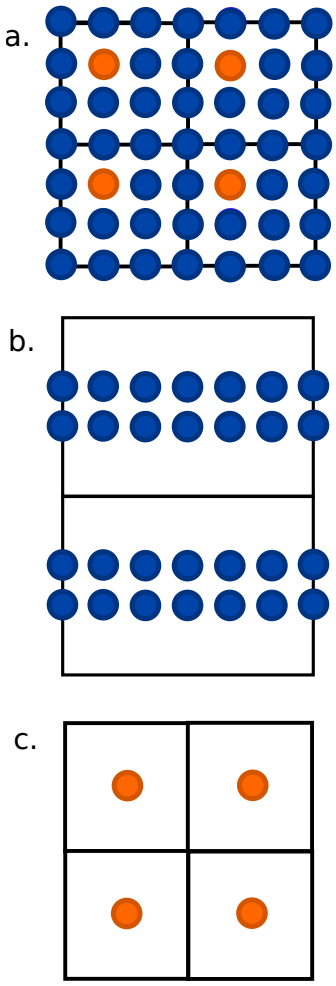

Figure 3.3: Schematic periodic supercells for a. a defect, b. a surface and c. a molecule.

3.3.3 Sampling of k-points

The charge density must be sampled at a set of discrete points in the Brillouin zone. If the number, $N_{\mathbf{k}}$, of these **k**-points is sufficiently large, the sum of the charge densities will be sufficiently close to the total charge density:

$$\rho(\mathbf{r}) \approx \frac{1}{N_{\mathbf{k}}} \sum_{\mathbf{k}i} |\psi_{\mathbf{k}i}(\mathbf{r})|^2. \tag{3.14}$$

These **k**-points are typically chosen to form a grid as developed by Monkhorst and Pack [36]. The total number of **k**-points used in a cal-

culation may be reduced by accounting for symmetry. The computing time scales linearly with the number of **k**-points.

The **k**-point densities between different unit cells are often quoted as a **k**-point spacing.[1] The CASTEP code, in accordance with crystallographic convention, uses the definition of reciprocal lattice vectors which includes a factor of 2π.[2] To reflect this, the **k**-point spacings in this thesis are quoted in units of $2\pi\text{Å}^{-1}$.

3.3.4 Pseudopotentials

Valence wavefunctions oscillate rapidly near the nucleus and therefore require high energy cut-offs in order to be accurately described. To reduce the energy cut-off, and thus increase computational efficiency, the potential close to the nucleus, defined within a radius r_c, is smoothed. This results in a pseudopotential and a correspondingly smoothed pseudowavefunction, as shown in figure 3.4. Crucially, the energy eigenvalues are not affected. This is known as the 'pseudopotential approximation'.

There are many types of pseudopotentials: the two used in this thesis are 'norm-conserving' pseudopotentials and 'ultrasoft' pseudopotentials. Norm-conserving pseudopotentials are easier to incorporate into quantum mechanical codes but may still require high energy cut-offs—they are therefore said to be 'hard'. The 'norm-conserving' constraint means that the total charge density within r_c must be the same for the real wavefunctions and pseudowavefunctions. Commonly used smooth norm-conserving pseudopotentials include those developed by Troullier and Martins [37]. Vander-

[1] Unless otherwise stated, **k**-point spacings are assumed to be the same along all three reciprocal lattice vectors.

[2] For example, if the real space lattice vectors are denoted as **a**, **b** and **c**, the reciprocal lattice vector $\mathbf{a}^*$ is defined as $2\pi\frac{\mathbf{b}\times\mathbf{c}}{\mathbf{a}.\mathbf{b}\times\mathbf{c}}$.

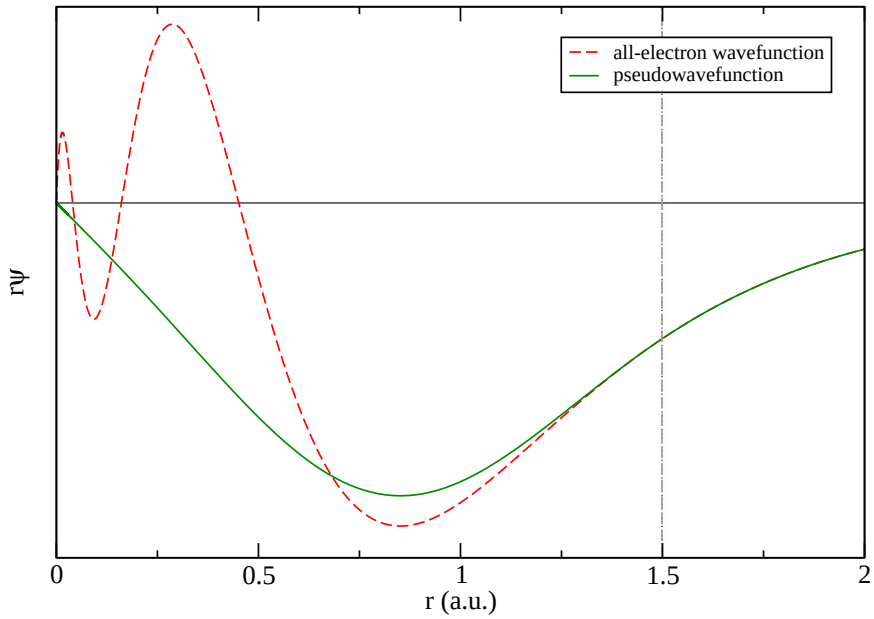

Figure 3.4: The $4s$ wavefunction (red dotted line) and corresponding pseudowavefunction (green line) for Pd using a norm-conserving pseudopotential (the $4p$, $4d$ and $5s$ wavefunctions are similarly pseudised in the full pseudopotential). The cut-off radius, r_c, is marked by the dotted brown line. Note how the wavefunction and pseudowavefunction are the same above r_c.

bilt developed a methodology for relaxing the norm-conserving constraint without sacrificing computational accuracy, thus producing much smoother pseudopotentials [38]. The removed charge is reincorporated at a later stage in the calculation.[3] In doing so the energy cut-off can be substantially lowered. These 'ultrasoft' pseudopotentials are more difficult to incorporate in quantum mechanical codes, though they are commonly used in the CASTEP code.

[3]The removed charge is known as the 'augmentation charge' and is stored on a grid which is finer than the grid used to store the basis functions. This augmentation charge grid is known as the 'fine grid'. In CASTEP it is set by default to being 1.75 times finer than the 'standard grid' used for the basis functions. The cut-off radius, r_c, for the ultrasoft region of the pseudopotential is often set to being lower than the cut-off radius for the overall pseudopotential.

In most cases the pseudopotential approximation is only applied to the valence electrons. The orbitals for the core electrons, since they are not involved in bonding, are assumed to be the same as those in an isolated atom and therefore can be easily calculated without the need for pseudopotentials. This is known as the 'frozen core approximation'. Whilst the frozen core approximation is valid for the calculation of magnetic shieldings [39], it is not appropriate for hyperfine parameters which are highly influenced by core polarisation. Alternative methodologies to the frozen core approximation for hyperfine calculations will be discussed in section 4.3.1 and in chapter 8. In order to obtain accurate results, it is sometimes necessary to use pseudopotentials for outer 'core' electrons, for example the $4s$ and $4p$ states in Rh and Pd, and the $4f$, $5s$ and $5p$ states in Pt (chapters 6 and 7). These states are known as 'semi-core' states.

In the case of NMR parameters, which by nature involve quantum mechanical interactions in the vicinity of the nucleus, the use of pseudopotentials for valence electrons is problematic because the valence pseudowavefunctions are non-physical within r_c. This is corrected by the 'Projector Augmented Wave method'.

Projector Augmented Wave method (PAW)

The true all-electron non-pseudised wavefunction for valence electrons can be recreated from the pseudowavefunction within the core region, as developed by Blöchl [40, 41]. The pseudowavefunction $|\tilde{\psi}\rangle$ is mapped onto the all-electron wavefunction $|\psi\rangle$ by the operator $\hat{\mathcal{T}}$ according to

$$|\psi\rangle = \hat{\mathcal{T}}|\tilde{\psi}\rangle, \tag{3.15}$$

where

$$\hat{\mathcal{T}} = 1 + \sum_n (|\phi_n\rangle - |\tilde{\phi}_n\rangle)\langle\tilde{p}_n|. \tag{3.16}$$

Within the core region (bounded by r_c), the pseudowavefunction is composed of a linear combination of pseudo atomic-states $|\tilde{\phi}_n\rangle$. Equation 3.16 therefore corresponds to removing the section of $|\tilde{\phi}_n\rangle$ located within r_c and replacing it with the equivalent all-electron atomic-states $|\phi_n\rangle$. $|\tilde{p}_n\rangle$ is a function strongly localised within r_c and is therefore used to ensure that only the section of $|\tilde{\psi}\rangle$ within r_c is altered. A pictorial representation of equation 3.16 is given in figure 3.5 [35].

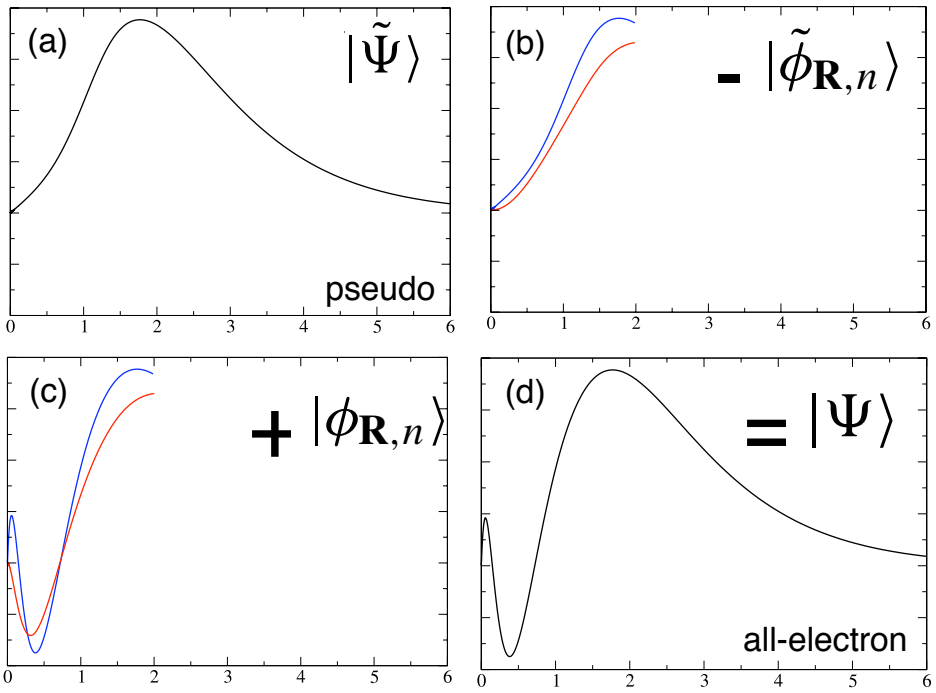

Figure 3.5: Schematic of the PAW method [35]. The horizontal axis signifies the radial distance from the nucleus. Figure (a) represents the initial pseudowavefunction $|\tilde{\psi}\rangle$. Figure (b) represents two separate pseudo atomic-states $|\tilde{\phi}_n\rangle$. Figure (c) represents two corresponding all-electron atomic-states $|\phi_n\rangle$. Figure (d) represents the final reconstructed all-electron wavefunction $|\psi\rangle$. [Reprinted with permission from [35]. Copyright © 2010 John Wiley & Sons, Ltd.]

All-electron (AE) methodologies

Many codes used by the quantum chemistry community do not use pseudopotentials but instead use the full electron wavefunctions. In some cases, however, the core electrons are replaced with those of an isolated atom.

The GAUSSIAN codes [42] use localised Gaussian functions as a basis set and can compute a large number of NMR parameters. They are, however, limited to isolated systems. Gaussian functions can be used to calculate the NMR parameters of solids in codes such as CRYSTAL [32, 33]. CRYSTAL can be used to calculate hyperfine parameters and electric field gradients as these are ground-state properties. However, it is not capable of calculating response properties, for example magnetic shieldings, Knight shifts and J-couplings. The reason for this is that CRYSTAL becomes very unstable when using the large basis sets that would be required to converge the values of the response properties.

3.4 Metals

The treatment of metallic systems requires additional care. In a metal, the bands near the Fermi surface are partially occupied and so there are a different number of occupied bands at each **k**-point. A (slightly) larger number of bands is required than for insulators in order to make sure that all bands crossing the Fermi level are accounted for.

The Fermi surface is also recalculated during each SCF cycle. This will result in bands entering or exiting the sum of occupied states with each SCF iteration if the Brillouin zone is not sampled finely enough. The number of **k**-points required to overcome this numerical instability will be too large to be computationally practical [43, p. 136]. In order to reduce the number

of **k**-points required to a realistic level, a smearing function is applied to each band [44, 45, 3]. This could take the form of a Gaussian [46], Hermite polynomials or a Fermi function, to name a few.[4] Gaussian smearing is the most stable and is therefore used in my calculations. The width of the smearing function must be investigated carefully for each calculated property. As noted by d'Avezac *et al.*, convergence with respect to smearing width may be very slow [3].

Even with the application of smearing schemes, the **k**-point densities required are still significantly higher for metals than for insulators—see figure 3.6. Therefore **k**-point spacings must be very carefully converged as illustrated in chapters 6 and 7.

3.5 Geometry optimisations

Before the properties of a structure are calculated, the structure should first be relaxed. This helps to remove any inconsistencies from a starting structure that may have been obtained via experiment or are contained within a structure that has yet to be experimentally verified. Sometimes the structure may involve a defect or some other detail that cannot be revealed via experiment in sufficient detail. For example, X-ray diffraction can only record the average crystallography of a sample. In these cases geometry optimisations provide insight into the atomic arrangement around a defect site.

A geometry optimisation calculation runs as follows. The energy, forces and stresses in the unit cell are calculated. These are then used to generate

[4]The Fermi distribution can also be employed to simulate the effect of finite temperature on electrons, however in the context of accurate Fermi surface sampling the 'temperature' is purely numerical and has no physical meaning.

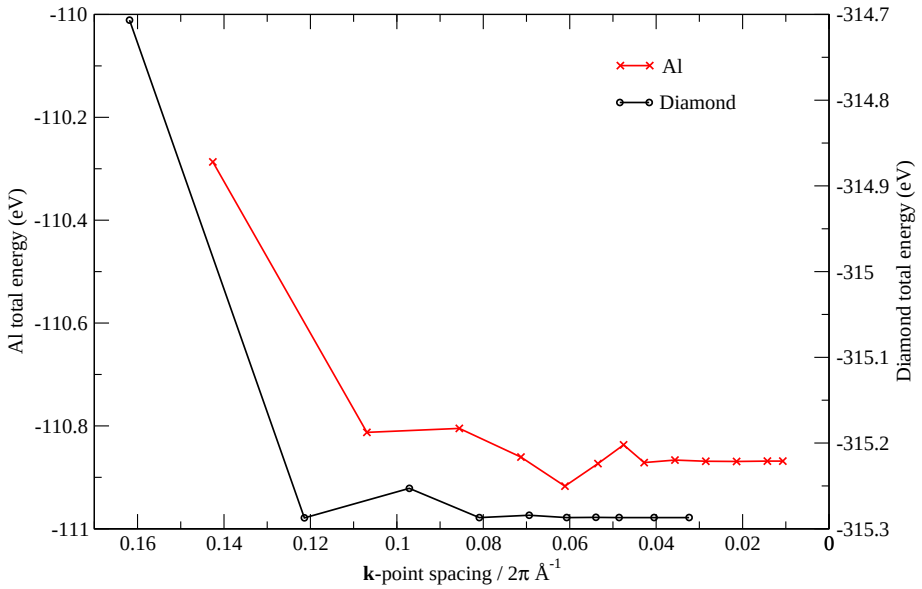

Figure 3.6: Convergence of the total energy with respect to **k**-point spacing for diamond (a typical insulator) and aluminium (a typical metal).

a new unit cell of lower enthalpy. For the calculations in this thesis, the minimising algorithm used for this process was the BFGS minimiser [47]. The algorithm then iterates through a series of unit cell geometries of decreasing enthalpy until a set of specified convergence criteria are satisfied. In CASTEP 8 the default convergence criteria are: the change in the total energy must fall below 2×10^{-5} eV/atom, the atomic displacement must be below 0.001 Å, the forces on the atoms must fall below 0.05 eV/Å and the stress on the unit cell must fall below 0.1 GPa. These tolerances can be made more stringent if required.

Additionally, certain constraints may be placed on the unit cell by the user: the angles and lengths of the unit cell may be held constant or the positions of the ions may be fixed. Supercells involving large amounts of

vacuum are one example in which it is beneficial to fix the vacuum spacing so that the periodic images do not move away or towards one another.

NMR parameters are particularly sensitive to structural changes. Structures therefore require careful relaxation before the NMR paramaters can be calculated. By way of example, figure 3.7 shows a set of ^{93}Nb σ_{iso} values calculated before and after a geometry optimisation. The structure is a perovskite $KNbO_3$ supercell into which a sodium atom has been substituted onto a potassium site. Relaxing the structure changes both the distances between the ^{93}Nb and ^{23}Na nuclei and has a significant effect on the ^{93}Nb σ_{iso} values.

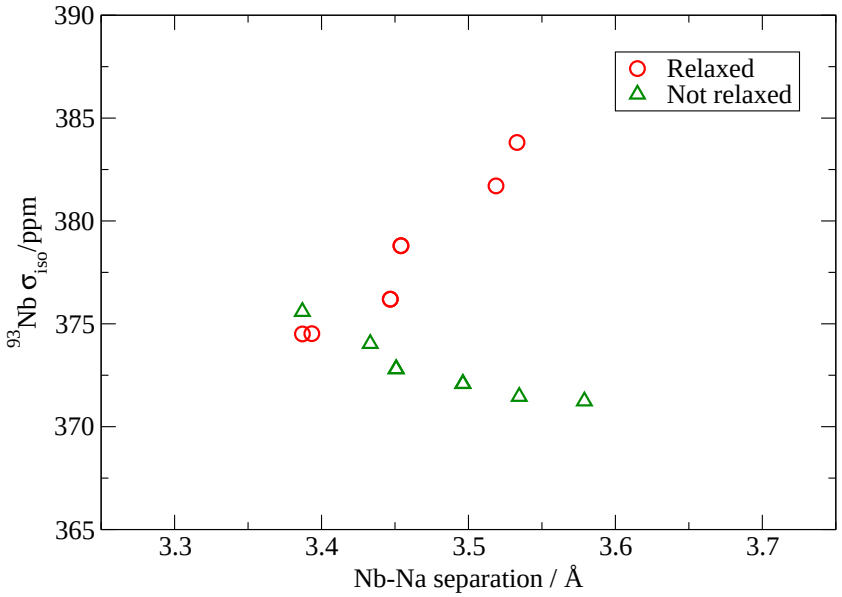

Figure 3.7: The effect of relaxing the structures on ^{93}Nb σ_{iso} for a 2×2×2 supercell of $KNbO_3$ in which a Na atom has been substituted onto a K site.

3.6 Convergence, precision and accuracy

There are two types of approximations used in first-principles methodologies: numerical and physical approximations. Numerical approximations relate to the values chosen by the user for computational parameters such as the planewave cut-off, **k**-point sampling, the supercell size and smearing width. A further numerical approximation is the type of pseudopotential used because it is a non-physical parameter which affects the final result.

It is extremely important to ensure that calculations are sufficiently converged with respect to these parameters if meaningful results are to be obtained. Common sense should determine how rigorously results should be converged. There is little to be gained wasting computational resources by significantly over-converging results if equivalent experimental measurements have large margins of error, or if the errors inherent to the model outweigh those of convergence.

Physical approximations are those which are inherent to the model. These include the type of exchange-correlation functional used, relativistic effects, whether the frozen core approximation is used and whether thermal effects are taken into account. These approximations determine how closely a methodology replicates experiment. In the context of my calculations, I have included scalar-relativistic corrections (which do not take into account spin-orbit coupling). No thermal simulations have been included, with the exception of the fictitious 'electronic temperature' due to smearing at the Fermi surface.

This leads us to think about how to quantify the quality of a calculation. 'Precision' is a measure of how a calculation compares to an equivalent

calculation obtained using different numerical parameters (i.e. during convergence tests) or obtained using a different code. 'Accuracy' is a measure of how a calculation compares to experiment.

There is no universal procedure for quantifying the precision or accuracy of a calculation. Comparisons with experiment must be made with caution, taking into account experimental errors, and the numerical and physical approximations of the model. When assessing precision, one approach for structural calculations is to compare the result of one methodology (a) with that of another (b) using the Δ gauge:

$$\Delta(a,b) = \sqrt{\frac{\int_{0.94V_0}^{1.06V_0} (E_b(V) - E_a(V))^2 \mathrm{d}V}{0.12V_0}}, \tag{3.17}$$

where V_0 is the equilibrium volume and $E(V)$ is the total energy as a function of volume [48]. In this way, in 2016, Lejaeghere *et al.* assessed the precision of 40 methodologies [49].

Chapter 4

Calculation of NMR parameters

The initial theoretical framework for NMR parameters was developed by Ramsey in the 1950s [50, 51, 52]. Since then computational methods pertaining to the NMR parameters for diamagnetic materials have been developed including the magnetic shielding tensor [53, 54], electric field gradients [55] and J-coupling [56]. For metallic systems, progress has been made in the calculation of magnetic shielding tensors and Knight shifts [3]. In terms of hyperfine parameters, early qualitative attempts to calculate Fermi-contact shifts involved calculations on molecular solids using Hartree-Fock and DFT [57, 58, 59, 60]. There is also wide interest in calculating the hyperfine interaction for single molecules [23, p. 209][61, 62, 63]. This chapter will cover the relevant methodologies for calculating those parameters covered in the subsequent results chapters.

4.1 Magnetic shielding in diamagnetic systems

As discussed in chapter 2, an applied magnetic field induces current loops in the electrons surrounding a nucleus. These currents in turn induce a local

magnetic field which shields (or deshields) the nuclear magnetic moment from the applied magnetic field. The nuclear magnetic moment therefore experiences the sum of the applied and local magnetic fields as expressed by equation 2.8.

Calculating the magnetic shielding tensor, $\underline{\underline{\sigma}}$, is therefore a matter of calculating the induced current, $\mathbf{j}^{(1)}(\mathbf{r})$, and the induced magnetic field at the nucleus, $B_{in}(\mathbf{R})$, where $\mathbf{r}$ and $\mathbf{R}$ are the position vectors of the electron current and the nucleus respectively.

The relation between $B_{in}(\mathbf{R})$ and $\mathbf{j}^{(1)}(\mathbf{r})$ is given by the Biot-Savart law:

$$B_{in}(\mathbf{R}) = \frac{\mu_0}{4\pi} \int \mathbf{j}^{(1)}(\mathbf{r}) \times \frac{(\mathbf{r} - \mathbf{R})}{|\mathbf{r} - \mathbf{R}|^3} \mathrm{d}^3 r. \tag{4.1}$$

Within the formalism of quantum mechanics, the current density is expressed (in atomic units) as

$$\mathbf{j}(\mathbf{r}) = \psi^* \hat{\mathbf{p}} \psi + \psi \hat{\mathbf{p}} \psi^*. \tag{4.2}$$

In the presence of an external magnetic field, the momentum, $\hat{\mathbf{p}}$, should be replaced with the canonical momentum, $\hat{\mathbf{p}} + \frac{1}{c}\hat{\mathbf{A}}$, where $\mathbf{A}$ is the vector potential and $c = 1/\alpha$ where α is the fine structure constant. Equation 4.2 therefore becomes

$$\mathbf{j}(\mathbf{r}) = -\psi^* \hat{\mathbf{p}} \psi + \psi \hat{\mathbf{p}} \psi^* + \frac{1}{c} \hat{\mathbf{A}} \psi^* \psi. \tag{4.3}$$

Under experimentally realistic magnetic fields, the induced current and resulting change in the magnetic field are small. It is therefore reasonable to treat the induced current as a perturbation of the system. The total current, $\mathbf{j}(\mathbf{r})$, is therefore

$$\mathbf{j}(\mathbf{r}) = \mathbf{j}^{(0)}(\mathbf{r}) + \mathbf{j}^{(1)}(\mathbf{r}), \tag{4.4}$$

where $\mathbf{j}^{(0)}(\mathbf{r})$ is the ground-state current and $\mathbf{j}^{(1)}(\mathbf{r})$ is the induced current. The associated current density operator, $\hat{J}$, is therefore

$$\hat{J} = \hat{J}^{(0)} + \hat{J}^{(1)}, \tag{4.5}$$

where $\hat{J}^{(0)}$ is the zeroth order current operator and $\hat{J}^{(1)}$ is the contribution to $\hat{J}$ which is linear in $\mathbf{B}$.

The wavefunction can be expanded to first order in the applied magnetic field, $\mathbf{B}$, as

$$|\psi\rangle = |\psi^{(0)}\rangle + |\psi^{(1)}\rangle + \mathcal{O}(B^2). \tag{4.6}$$

The expectation value for the current density is therefore

$$\begin{aligned}\langle J\rangle =& \langle\psi^{(0)}|\hat{J}^{(0)}|\psi^{(0)}\rangle + \langle\psi^{(1)}|\hat{J}^{(0)}|\psi^{(0)}\rangle \\ &+ \langle\psi^{(0)}|\hat{J}^{(0)}|\psi^{(1)}\rangle + \langle\psi^{(0)}|\hat{J}^{(1)}|\psi^{(0)}\rangle + \mathcal{O}(B^2).\end{aligned} \tag{4.7}$$

The ground-state expectation value is therefore

$$\mathbf{j}^{(0)}(\mathbf{r}) = \langle\psi^{(0)}|\hat{J}^{(0)}|\psi^{(0)}\rangle \tag{4.8}$$

and the expectation value for the induced current is

$$\mathbf{j}^{(1)}(\mathbf{r}) = \langle\psi^{(1)}|\hat{J}^{(0)}|\psi^{(0)}\rangle + \langle\psi^{(0)}|\hat{J}^{(0)}|\psi^{(1)}\rangle + \langle\psi^{(0)}|\hat{J}^{(1)}|\psi^{(0)}\rangle. \tag{4.9}$$

The current operators are expressed as

$$\hat{J}^{(0)} = |\mathbf{r}\rangle\langle\mathbf{r}|\hat{\mathbf{p}} + \hat{\mathbf{p}}|\mathbf{r}\rangle\langle\mathbf{r}| = \hat{J}_p \tag{4.10}$$

and

$$\hat{J}^{(1)} = \frac{1}{c}\hat{\mathbf{A}}|\mathbf{r}\rangle\langle\mathbf{r}| = \hat{J}_d, \tag{4.11}$$

where $\hat{J}_p$ and $\hat{J}_d$ are known as the paramagnetic and diamagnetic contributions respectively.

The expectation value for the induced current, $j^{(1)}(\mathbf{r})$, can be further expressed as

$$j^{(1)}(\mathbf{r}) = 4\sum_{occ} \mathrm{Re}[\langle\psi^{(0)}_{occ}|\hat{J}_p|\psi^{(1)}_{occ}\rangle] + 2\sum_{occ}\langle\psi^{(0)}_{occ}|\hat{J}_d|\psi^{(0)}_{occ}\rangle \tag{4.12}$$

with a factor of 2 accounting for spin. The sum is over all occupied states.

The Coulomb gauge, $\mathbf{A} = \frac{1}{2}\mathbf{B}\times(\mathbf{r}-\mathbf{d})$, is now adopted. $\mathbf{d}$ is a constant known as the gauge origin which is usually set to the origin of the coordinate system ($\mathbf{d} = 0$). Rewriting the charge density as $\sum_{occ}\langle\psi^{(0)}_{occ}|\mathbf{r}\rangle\langle\mathbf{r}|\psi^{(0)}_{occ}\rangle = \rho(\mathbf{r})$ gives

$$j^{(1)}(\mathbf{r}) = 4\sum_{occ} \mathrm{Re}[\langle\psi^{(0)}_{occ}|\hat{J}_p|\psi^{(1)}_{occ}\rangle] + \frac{1}{2c}\mathbf{B}\times\mathbf{r}\rho(\mathbf{r}), \tag{4.13}$$

where the first term is the paramagnetic term and the second term is the diamagnetic term.

$|\psi^{(1)}\rangle$ can be obtained through the relation

$$|\psi^{(1)}_{occ}\rangle = \mathcal{G}(\varepsilon^{(0)}_{occ})\hat{H}^{(1)}|\psi^{(0)}_{occ}\rangle. \tag{4.14}$$

$\mathcal{G}$ is a Green's function, which in this context, is defined as

$$\mathcal{G}(\varepsilon^{(0)}_{occ}) = \sum_{unocc}\frac{|\psi^{(0)}_{unocc}\rangle\langle\psi^{(0)}_{unocc}|}{\varepsilon_{occ}-\varepsilon_{unocc}}, \tag{4.15}$$

where the sum is over all unoccupied states. The Green's function is therefore a sum of the unoccupied ground-state wavefunctions, $|\psi^{(0)}_{unocc}\rangle$. Obtaining these can be extremely computationally expensive. However, fortunately, the calculation of $\mathcal{G}(\varepsilon^{(0)}_{occ})$ can be recast as an iterative problem involving only ground-state wavefunctions [53].

All that remains is to find a suitable expression for $\hat{H}^{(1)}$.

4.1.1 Hamiltonian in a magnetic field

From the standard Hamiltonian $\hat{H} = \frac{1}{2}\hat{\mathbf{p}}^2 + \hat{V}$, we substitute $\hat{\mathbf{p}}$ for $\hat{\mathbf{p}} + \frac{1}{c}\hat{\mathbf{A}}$ to obtain

$$\hat{H} = \frac{1}{2}\hat{\mathbf{p}}^2 + \hat{V} + \frac{1}{2c}(\hat{\mathbf{p}}.\hat{\mathbf{A}} + \hat{\mathbf{A}}.\hat{\mathbf{p}}) + \frac{1}{2c^2}A^2. \tag{4.16}$$

Under the Coulomb gauge $\hat{\mathbf{A}} = \frac{1}{2}\mathbf{B} \times \mathbf{r}$, $\hat{\mathbf{p}}.\hat{\mathbf{A}} = \hat{\mathbf{A}}.\hat{\mathbf{p}}$ so equation 4.16 becomes

$$\hat{H} = \frac{1}{2}\hat{\mathbf{p}}^2 + \hat{V} + \frac{1}{2c}\mathbf{L}.\mathbf{B} + \frac{1}{8c^2}(\mathbf{B} \times \mathbf{r})^2, \tag{4.17}$$

where

$$\hat{H}^{(0)} = \frac{1}{2}\mathbf{p}^2 + \hat{V}, \tag{4.18}$$

$$\hat{H}^{(1)} = \frac{1}{2c}\mathbf{L}.\mathbf{B} = \frac{1}{2c}(\mathbf{p}.\mathbf{B} \times \mathbf{r}) = \frac{1}{2c}(\mathbf{B}.\mathbf{r} \times \mathbf{p}) \tag{4.19}$$

and

$$\hat{H}^{(2)} = \frac{1}{8c^2}(\mathbf{B} \times \mathbf{r})^2. \tag{4.20}$$

4.1.2 Calculating the current in molecules

The current in isolated molecules can be calculated directly from equation 4.13 using quantum chemistry codes with local orbital basis sets [64]. The current should not change depending on the gauge chosen, however this is only true if a complete basis set is used. In practice a basis set cannot be complete which means that the calculated current will change depending on which coordinate system is chosen. The problem is known as the 'gauge origin problem' [23, p. 198–199].

The reason for the gauge origin problem is that the diamagnetic and paramagnetic terms converge at different rates with respect to the size of a Gaussian basis set. In practice, the diamagnetic term is well-converged

whereas the paramagnetic term is not. This means that the computed paramagnetic value is sensitive to the position from the gauge origin. Methodologies to 'restore gauge-invariance' have been developed within quantum chemistry codes [1]. Two common methodologies are 'individual gauges for local orbitals' (IGLO) [65] and the 'gauge-including atomic orbital' (GIAO) [66, 67].

4.1.3 Calculating the current in infinite solids

Directly solving equation 4.13 for an infinite system is problematic because the diamagnetic term clearly diverges with increasing $\mathbf{r}$. Fortunately there is an equal and opposite divergence in the paramagnetic term so that the paramagnetic and diamagnetic terms can be summed to give

$$j^{(1)}(\mathbf{r}) = 4\frac{1}{2c}\sum_{occ}\mathrm{Re}[\langle\psi^{(0)}_{occ}|\hat{J}_p\mathcal{G}(\varepsilon^{(0)}_{occ})(\mathbf{r}-\mathbf{r}')\times\mathbf{p}|\psi^{(0)}_{occ}\rangle]. \tag{4.21}$$

This expression for $j^{(1)}(\mathbf{r})$ is now well-defined for infinite crystals because the absolute positions given by $\mathbf{r}$ have been replaced by relative positions $\mathbf{r}-\mathbf{r}'$. The Green's function is calculated using an equivalent iterative methodology to that implemented for molecules.

Nevertheless, calculating $j^{(1)}(\mathbf{r})$ from equation 4.21 is subject to several computational challenges:

1. $\hat{H}^{(1)}$ is not representable under periodic boundary conditions due to the $\mathbf{r}\times\mathbf{p}$ term in equation 4.19. A solution to this was developed by Mauri, Pfrommer and Louie in which the magnetic field was represented as a sinusoidal function which was taken to the limit of an infinite wavelength [68]. Sebastiani *et al.* developed an alternative approach based on Wannier functions however it is not compatible with pseudopotentials and is therefore only feasible for hydrogen [69, 70].

2. Within the formalism of Mauri *et al.* discussed in point 1, the convergence of the core electron wavefunctions is slow when calculating chemical shifts. Gregor, Mauri and Car found that the core electrons could be treated as if they were in an isolated atom [39]. This significantly improved convergence rates without affecting the values of the calculated chemical shifts.

3. Equation 4.21 should not be affected by the gauge origin problem, however, due to the $\frac{1}{\mathbf{r}^3}$ dependence of the induced magnetic field (see equation 4.1), only the current close to the nucleus has a significant effect on the magnetic shielding. When using pseudopotentials, the wavefunctions close to the nucleus are pseudised and therefore non-physical. The 'true' wavefunction near the nucleus therefore has to be restored using PAW if an accurate value of $j^{(1)}(\mathbf{r})$ is to be obtained. However the localised orbital wavefunctions generated with PAW reintroduce the gauge dependence! Instead, the PAW approach can be replaced with the Gauge Including Projector Augmented Wave method (GIPAW) which once again removes the gauge dependence [53].

4.2 Calculation of electric field gradients

The calculation of electric field gradients is much more straightforward than other NMR parameters as it only requires knowledge of the ground-state charge density. The electric field $E_\alpha(\mathbf{r})$ in equation 2.21 can be obtained by summing the nuclear and electronic charge density, $n(\mathbf{r}')$, according to

$$E_\alpha(\mathbf{r}) = \int \frac{n(\mathbf{r}')}{|\mathbf{r} - \mathbf{r}'|^3}(r_\alpha - r'_\alpha)\mathrm{d}^3r'. \tag{4.22}$$

The electronic component of $n(\mathbf{r}')$, $\rho_c(\mathbf{r}')$, is readily obtained with DFT as outlined in chapter 3. Electric field gradients can also be calculated for paramagnetic materials [71].

4.3 Calculation of NMR parameters for paramagnetic and metallic systems

The methodologies described in section 4.1 are fully developed for diamagnetic materials, however they are not sufficient for paramagnetic and metallic systems. For diamagnetic materials only the orbital contribution to the induced magnetic field needs to be taken into account, however for paramagnetic and metallic systems there are additional contributions arising from the electronic spin magnetisation, $\mathbf{m}(\mathbf{r})$.

The combined effect of the spin and orbital contributions to the induced magnetic field is

$$\begin{aligned} B_{in}(\mathbf{R}) =& \frac{\mu_0}{4\pi}\int \mathbf{j}(\mathbf{r}) \times \frac{(\mathbf{r}-\mathbf{R})}{|\mathbf{r}-\mathbf{R}|^3}\mathrm{d}^3r \\ &+ \frac{\mu_0}{4\pi}\frac{8\pi}{3}\int \mathbf{m}^{(1)}(\mathbf{r})\delta(\mathbf{r}-\mathbf{R})\mathrm{d}^3r \\ &+ \frac{\mu_0}{4\pi}\int \mathbf{m}^{(1)}(\mathbf{r}).\left[\frac{3(\mathbf{r}-\mathbf{R})(\mathbf{r}-\mathbf{R})^T - |(\mathbf{r}-\mathbf{R})|^2}{|(\mathbf{r}-\mathbf{R})|^5}\right]\mathrm{d}^3r, \end{aligned} \tag{4.23}$$

where $\mathbf{m}^{(1)}(\mathbf{r})$ is the response of the electronic magnetisation to first order in the applied field. The methodology for incorporating spin (the second and third terms in equation 4.23) has been developed by d'Avezac, Marzari and Mauri [3]. The density of the spin-'up' states is given, to first order, by

$$\rho_\uparrow^{(1)} = \sum_{occ}\left[\langle\psi_\uparrow^0|\mathbf{r}\rangle\langle\mathbf{r}|\psi_\uparrow^1\rangle + \langle\psi_\uparrow^1|\mathbf{r}\rangle\langle\mathbf{r}|\psi_\uparrow^0\rangle\right], \tag{4.24}$$

and likewise for the density of the spin-'down' states,

$$\rho_\downarrow^{(1)} = \sum_{occ}\left[\langle\psi_\downarrow^0|\mathbf{r}\rangle\langle\mathbf{r}|\psi_\downarrow^1\rangle + \langle\psi_\downarrow^1|\mathbf{r}\rangle\langle\mathbf{r}|\psi_\downarrow^0\rangle\right]. \tag{4.25}$$

The first order change in the spin density is therefore

$$\rho_s^{(1)} = \rho_\uparrow^{(1)} - \rho_\downarrow^{(1)}, \tag{4.26}$$

and the first order change in the charge density is

$$\rho_c^{(1)} = \rho_\uparrow^{(1)} + \rho_\downarrow^{(1)} = 0. \tag{4.27}$$

Therefore the first-order response to $\mathbf{m}(\mathbf{r})$ can be expressed in terms of one spin-state only and doubled to incorporate the other:

$$\mathbf{m}^{(1)}(\mathbf{r}) = 2\sum_{occ}\left[\langle\psi_\uparrow^1|\mathbf{r}\rangle\langle\mathbf{r}|\psi_\uparrow^0\rangle + \langle\psi_\uparrow^0|\mathbf{r}\rangle\langle\mathbf{r}|\psi_\uparrow^1\rangle\right]. \tag{4.28}$$

Equation 4.28 can be solved directly using all-electron codes (these do not employ pseudopotentials). In the case of methodologies which require pseudopotentials, the equivalent pseudowavefunctions can be obtained with PAW. GIPAW is not required because there is no gauge choice. The Hamiltonian incorporating spin is

$$\hat{H} = \frac{1}{2}\mathbf{p}^2 + V + g\mu_B\mathbf{B}.\mathbf{S} = \hat{H}^{(0)} + \hat{H}^{(1)}, \tag{4.29}$$

where g is the Landé g-factor, μ_B is the Bohr magneton, $\mathbf{S}$ is the spin vector incorporating the Pauli spin matrices and $\mathbf{B}$ is the external magnetic field.

In the case of the calculation of the orbital contribution in equation 4.23 for metallic systems, the methodology outlined in section 4.1 for diamagnetic systems can be employed. However the technicalities for metallic systems outlined in section 3.4 must be applied.

There are two possible ways to calculate the Knight shift in metallic systems. The first-order perturbation to the spin magnetic moment can be calculated from equation 4.28 (the linear response approach). This is the methodology used for the calculations in chapters 6 and 7. Alternatively,

the overall spin response (all orders of $\mathbf{m}(\mathbf{r})$) can be calculated by applying an external field in accordance with the $\mathbf{B}.\mathbf{S}$ term in equation 4.29; this is known as the finite field approach.

4.3.1 Hyperfine parameters and core polarisation

The hyperfine interaction depends on the electron spin density at the nucleus ($\rho_s(\mathbf{R})$). Therefore in order to calculate hyperfine parameters for paramagnetic materials, two challenges must be overcome:

1. Within the pseudopotential approximation, the wavefunctions for valence electrons are smoothed pseudowavefunctions within r_c. This leads to non-physical charge densities close to the nucleus and therefore incorrect hyperfine parameters.

2. The wavefunctions for the core electrons are calculated within the frozen core approximation. However the spin of the valence electrons can cause spin polarisation of the core electrons. Because accurately computing the Fermi-contact interaction relies on knowing the spin density at the nucleus exactly, failure to include this core polarisation will lead to significant errors.

The first problem is solved using the Projector Augmented Wave methodology, as outlined in section 3.3.4 [40]. Applying the PAW methodology to the Fermi-contact interaction results in the associated operator [35]:

$$\hat{H}_{\mathrm{FC}} = C \sum_{n,m} |\tilde{p}_n\rangle\langle\phi_n|\delta(\mathbf{R}_l)|\phi_m\rangle\langle\tilde{p}_m|, \tag{4.30}$$

where C is a constant and $\delta(\mathbf{R}_l)$ is the Dirac delta function positioned at the nucleus.

The second problem is more difficult to solve. Progress on accurately modelling core polarisation was begun by Yazyev *et al.* through the core spin-polarisation correction method (CSPC) [72]. The all-electron wavefunction for the core electrons was reconstructed in the presence of the valence electrons with the valence states being approximated to those in an isolated atom. This produced a significant improvement on the Fermi-contact term for a series of small molecules. Declerck *et al.* proposed an alternative hybrid method for the inclusion of core polarisation which combined an all-electron calculation for the atom of interest with a pseudopotential calculation for all the others [73]. Not only could this hybrid method be applied to single atoms and small molecules, it could also be applied to periodic systems. The hyperfine interaction of the *L*-α-alanine $R2$ radical in a crystal of *L*-α-alanine molecules was calculated as an example of this.

Bahramy *et al.* developed a further improvement through calculating the core polarisation using first-order perturbation theory [74, 75]. The method consists of two steps as follows [75]. First, the PAW method of Blöchl is used to reconstruct the all-electron wavefunctions of the core and valence electrons within r_c. Second, these wavefunctions are used to create a perturbing potential, ΔV, based on the local charge densities of single occupied molecular orbitals, ρ^{SOMO}:

$$\Delta V = \Delta V_{\uparrow} - \Delta V_{\downarrow} = -\frac{2}{\pi}\frac{\rho^{SOMO}(\mathbf{r})}{\rho_c^{2/3}(\mathbf{r})}. \tag{4.31}$$

The factor of 2 arises from the inclusion of both spin up and down, the contributions of which differ only in sign. This perturbing potential is used to calculate the spin density of the core electrons, $\rho_s^c(\mathbf{r})$, using first-order

perturbation theory according to

$$\rho_s^c(\mathbf{r}) = \rho^{c\uparrow}(\mathbf{r}) - \rho^{c\downarrow}(\mathbf{r}) = 4\sum_{\lambda} \mathrm{Re}\left[\langle\phi_\lambda|\mathbf{r}\rangle \sum_{\kappa\neq\lambda} C_{\lambda\kappa}\langle\mathbf{r}|\phi_\kappa\rangle\right], \tag{4.32}$$

where ϕ_κ and ϕ_λ are non-spin-polarised eigenstates and

$$C_{\lambda\kappa} = \frac{\langle\phi_\kappa|\Delta V|\phi_\lambda\rangle}{\varepsilon_\lambda - \varepsilon_\kappa}. \tag{4.33}$$

This methodology has been used by Filidou *et al.* to evaluate the hyperfine parameters for small organic molecules and optically excited fullerene derivatives [14]. When compared to values obtained by all-electron methodologies and experiment, the values obtained using the methodology of Bahramy *et al.* are an improvement on those obtained without considering core polarisation. There is still however room for further improving the accuracy of the calculations. Chapter 8 tests an alternative methodology for incorporating core polarisation in which all the electrons are included in the pseudopotential. Due to the difficulty in accurately modelling core polarisation, a complete methodology for calculating NMR parameters for paramagnetic materials has yet to be developed.

4.4 Overview of the applications of calculating NMR parameters

The methodologies outlined above have been a great success for calculating NMR parameters for diamagnetic materials. The calculations have offered invaluable insight into the structure, disorder and dynamics of systems. They have aided the interpretation of experimental solid-state spectra, predicted results and guided future experimental research. For example, the calculation of hyperfine parameters by Carlier *et al.* showed that the

previous assignment of Ni peaks in experimental MAS NMR spectra for $LiNi_{(1-y)}Co_yO_2$ materials should have been reversed [76, 60].

The extensive review paper by Bonhomme *et al.* documents all applications of the GIPAW methodology outlined above from the development of GIPAW to 2011 [53]. These structures include organic molecules such as aromatics and carbohydrates [77], amino acids [78], graphene oxide [79], carbon nanotubes [80, 81], inorganic materials (silicates [55], niobates [82, 83], phosphates [8] and so on), polymers and hybrid materials [84, 85], biomaterials [86], nanoparticles (for example ZnSe nanoparticles [87]), surfaces [88, 89], and disordered structures such as glasses [90, 91].

In the next three chapters I present the results of two investigations. The first (chapter 5) concerns the calculation of NMR parameters for disordered systems of perovskites which employs the methodologies for diamagnetic systems outlined in sections 4.1 and 4.2. The next two chapters (chapters 6 and 7) are an investigation of the Knight shift in Pt, Pd and Rh (in bulk and surface forms) which employs the methodologies outlined in sections 4.3. Finally, chapter 8 presents a further investigation on core polarisation, which builds on the discussion in section 4.3.1.

Chapter 5

NMR parameters of group I niobate perovskites

Perovskites are a set of structures, of general formula ABX_3, which consist of a framework of corner-sharing octahedra of 'X' anions with 'B' cations at their centres and 'A' cations in between them as shown in figure 5.1. They have attracted considerable interest due to their broad range of materials properties, for example ferroelectric or superconducting properties, which emerge as a result of the large number of structural arrangements afforded by the structure.

Structural distortions include displacements of the 'A' cations, and octahedral distortions and tilting. Glazer characterised a set of 23 different tilt systems, based on the assumption that the octahedra were ideal and rigid [92]. Octahedral distortions can be quantified using two parameters [93]. The first is the shear strain, $|\psi|$, which provides a measure of how much the X–B–X bond angle, θ_i, differs from the ideal bond angle, θ_o, of 90°:

$$|\psi| = \sum_i |\tan(\theta_i - \theta_o)|. \tag{5.1}$$

The second is the longitudinal strain, $|\alpha|$. This provides a measure of how much the B–X bond lengths, l_i, differ from the ideal bond lengths, l_o, where

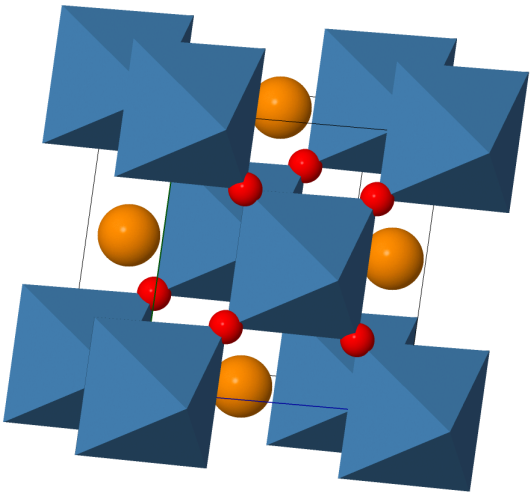

Figure 5.1: A general perovskite structure comprising 'X' anions (red), 'A' cations (orange) and 'B' cations (blue). The structure can be visualised as a framework of corner-sharing octahedra with an 'X' anion at each vertex and a 'B' anion at its centre.

the ideal bond length is defined as the bond length of an ideal octahedron of the same volume as that for the octahedron with bond lengths l_i:

$$|\alpha| = \sum_i \left| \ln\left(\frac{l_i}{l_o}\right) \right|. \tag{5.2}$$

This chapter will focus on the calculation of the NMR parameters of the two most commonly studied room temperature phases of $NaNbO_3$ (*Pbcm* and $P2_1ma$) and the room temperature phases of $KNbO_3$ ($Amm2$) and $LiNbO_3$ ($R3c$). The solid solutions $Na_xK_{1-x}NbO_3$, $K_xNa_{1-x}NbO_3$ and $Li_xNa_{1-x}NbO_3$ ('disordered structures') will also be investigated. ^{23}Na, ^{93}Nb, ^{7}Li, ^{39}K and ^{17}O nuclei are all quadrupolar. ^{93}Nb has spin $\frac{9}{2}$ and ^{17}O has spin $\frac{5}{2}$, whilst the three group I nuclei all have spin $\frac{3}{2}$. Experimental solid-state NMR spectra of these nuclei therefore suffer from a large degree of quadrupolar broadening, particularly ^{93}Nb, ^{23}Na and ^{39}K.[1] First-principles

[1]The degree of quadrupolar broadening pertaining to a nucleus in a given EFG is

calculations are therefore a valuable aid for interpreting these spectra, whilst also offering insight on the reasons for observed spectral trends. The aim of this chapter therefore is to identify how the NMR parameters for these structures are influenced by the geometry and defects.

5.1 Sodium niobate, $NaNbO_3$

Sodium niobate ($NaNbO_3$) is a perovskite well-known for its piezoelectric properties. The pure compound and the related $K_xNa_{1-x}NbO_3$ system have been much studied as a replacement candidate for lead-based piezoelectric materials such as PZT ($Pb(Zr_{1-x}Ti_x)O_3$) [95, 96]. $NaNbO_3$ has a particularly complex phase diagram with multiple phase transitions as a function of temperature and pressure.

There has been much work in characterising these phases. Megaw originally characterised $NaNbO_3$ as having seven phases. These were denoted N, P, R, S, T1, T2 and U in order of ascending temperature, with phase P being stable at room temperature [97]. At the same time there was also known to be an additional 'Q' phase which could be formed at room temperature in the presence of an electric field [98]. Since then, another two phases have been found to exist at room temperature [99, 100]. Peel *et al.* conducted an in-depth investigation on the high temperature R and S phases [101]. Using a combination of X-ray and neutron diffraction and first-principles CASTEP calculations, they presented a model for phase S and two candidate structures for phase R.

---

dictated by the strength of the quadrupole moment of that nucleus. For the nuclei studied in this chapter their quadrupole moments are $^{93}Nb = -320\,mb$, $^{23}Na = 104\,mb$, $^{39}K = 58.5\,mb$, $^{7}Li = -40.1\,mb$ and $^{17}O = -25.6\,mb$. The linewidth of the central peak is given by the second-order quadrupolar broadening factor. For the nuclei in this chapter these are $^{93}Nb = 1.28$, $^{23}Na = 2.64$, $^{39}K = 4.20$, $^{7}Li = 0.228$ and $^{17}O = 0.0640$ relative to ^{27}Al [94, p. 14–16].

5.1.1 The room temperature phases of $NaNbO_3$

The room temperature phases $NaNbO_3$ have been the subject of particular investigation. Which phases are present depend on factors such as the synthesis route, doping and pressure. It is generally stated that phase P is antiferroelectric, with an orthorhombic crystal structure and space group *Pbcm* [102]. However, Darlington and Knight report phase P as possessing a slight monoclinic distortion [103]. A further study by Yuzyuk *et al.*, based on Raman spectroscopy, suggests that there are three variants of phase P: a monoclinic phase between 250–410 K, an incommensurate phase between 410–460 K and an orthorhombic phase between 460–633 K [104].

The other room temperature polymorph of interest, phase Q, is ferroelectric, and is tentatively believed to have an orthorhombic crystal structure and a space group of $P2_1ma$ [83, 105, 106]. However some studies have suggested that it too possesses a slight monoclinic distortion [83]. Recent work on characterising these room temperature phases of $NaNbO_3$ has been conducted using a combination of solid-state NMR, X-ray and neutron diffraction, and first-principles calculations [83, 105, 102].

Characterisation of the room temperature $NaNbO_3$ phases using NMR

Ashbrook *et al.* analysed the crystal structures of two room temperature $NaNbO_3$ samples—one commercially produced, the other formed by a 'low temperature hydrothermal method' [82]. Using a combination of ^{23}Na MQ-MAS NMR experiments and DFT calculations, they concluded that the commercial sample consisted of the *Pbcm* polymorph, whereas the second sample was likely to consist of a combination of *Pbcm* and $P2_1ma$ poly-

morphs.

In a later study, Johnston *et al.* synthesised a range of $NaNbO_3$ samples and characterised them by a combination of MQMAS NMR, X-ray and neutron diffraction, second harmonic generation experiments and CASTEP calculations [83]. A commercial control sample was again found to be of space group *Pbcm*, with two distinct ^{23}Na sites and one ^{93}Nb site, the latter of which exhibited some broadening attributed to slight disorder within the structure. A set of samples synthesised by solid-state and molten salt techniques contained a mixture of two phases (as indicated by four distinct ^{23}Na resonances in the MQMAS NMR spectra): the *Pbcm* phase as found in the commercial sample, and a second undetermined phase. A higher proportion of the *Pbcm* phase was always formed; the authors suggested that this indicated that *Pbcm* was the more thermodynamically stable phase. It was possible to produce an almost pure sample of *Pbcm* via the molten salt method. A final sample, synthesised using sol-gel techniques, was shown to be composed of ∼90% of the 'second phase' and ∼10% of the *Pbcm* phase. Second harmonic generation experiments on the sol-gel sample were therefore used to characterise this 'second phase' as a noncentrosymmetric polar phase. Calculated NMR parameters for a range of candidate structures resulted in $P2_1ma$ providing the best fit to experimental data. It should also be noted that the sol-gel sample had not been placed in an electric field. This indicates that the '$P2_1ma$' structure (considered to be synonymous with the 'phase Q' mentioned earlier) can be synthesised without the presence of an electric field. A re-analysis of subtle peak broadenings in experimental spectra indicated that this '$P2_1ma$' structure was likely to possess a slight monoclinic distortion (i.e. $\beta \neq 90°$).

To shed more light on the problem of characterising the polar phase, Johnston *et al.* conducted a thorough investigation on whether ^{93}Nb NMR could be used to characterise the $NaNbO_3$ phases [105]. Contrary to a previous study by Hanna *et al.* [107], it was shown that the ^{93}Nb resonances for the *Pbcm* and supposed '$P2_1ma$' polymorphs were almost identical. MQMAS, wideline static NMR and MAS NMR spectra were recorded under a range of experimental parameters (magnetic field strengths and sample orientations), all with the same conclusion. By way of example, the MQMAS spectra are shown in figure 5.2.

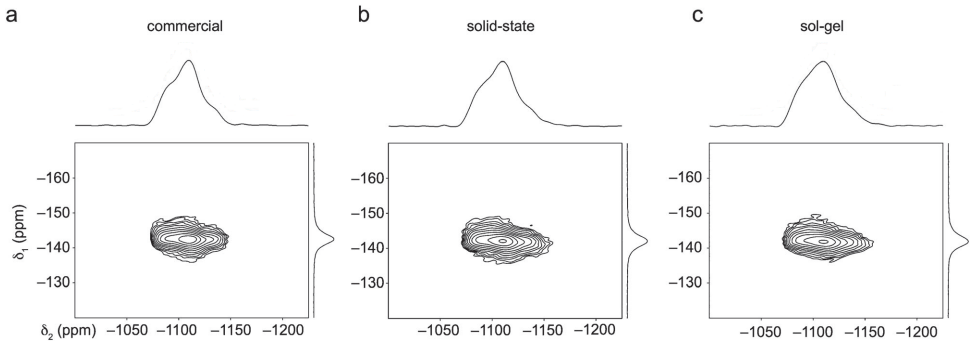

Figure 5.2: ^{93}Nb MQMAS experimental structures for three $NaNbO_3$ samples, recorded by Johnston *et al.* Sample 'a' is almost pure *Pbcm*, sample 'b' is a mixure of *Pbcm* and $P2_1ma$, and sample 'c' is almost pure $P2_1ma$. [Reprinted (adapted) from [105] with permission from the PCCP Owner Societies. http://dx.doi.org/10.1039/C1CP20258H]

Attempts to correlate ^{93}Nb quadrupolar interactions with O_6 octahedral distortions have also been made [107, 105]. Both studies found no correlation between C_Q values and $|\psi|$ nor $|\alpha|$. The study by Hanna *et al.* was conducted over a range of structures [107]. They suggested that the lack of correlation was due to the presence of long range distortions. Johnston *et al.* used a smaller range of structures, but there was still considerable scatter even with similar crystal structures. There was perhaps a weak correlation between

C_Q and $|\psi|$ [105].

5.1.2 $K_xNa_{1-x}NbO_3$ and $Li_xNa_{1-x}NbO_3$ solid solutions

It has been found that phase Q can be obtained if phase P is doped by only 2 molar % of either K or Li [108], as shown by the phase diagram in figure 5.3 and by Rödel *et al.* [96]. The phase diagram of $K_xNa_{1-x}NbO_3$ has been fairly thoroughly investigated [109, 110], however the phase diagram of $Li_xNa_{1-x}NbO_3$ is less well understood.

Preliminary investigations on the $Li_xNa_{1-x}NbO_3$ system have been conducted by Nitta, Zeyfang *et al.* and Jiménez *et al.* [111, 112, 113]. Using a combination of X-ray and neutron diffraction and solid-state NMR, Peel *et al.* conducted a further investigation across the full composition range using a range of synthesis techniques—see figure 5.3 [102]. They also found that, within the 0.05–0.20 molar % Li range, the fraction of phase Q decreased over time whilst the *R*3*c* phase increased.

In contrast to the multiple room temperature phases of $NaNbO_3$, the pure $KNbO_3$ room temperature phase has been well characterised as having an orthorhombic crystal structure and *Amm*2 space group [114]. The pure $LiNbO_3$ has a rhombohedral crystal structure with space group *R*3*c* [115].

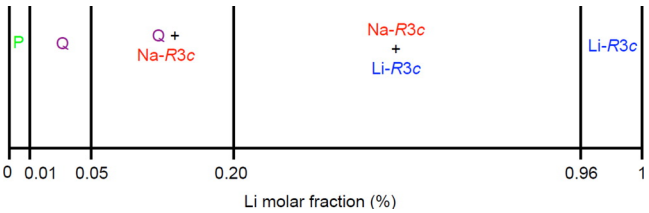

Figure 5.3: The phase diagram of $NaNbO_3$–$LiNbO_3$ constructed by Peel *et al.* [Reprinted (adapted) with permission from [102]. Copyright 2013 American Chemical Society.]

5.2 Calculations on ordered structures

Experimental structures from the ICSD database for $KNbO_3$ *Amm*2 [114], $LiNbO_3$ *R*3*c* [115], $NaNbO_3$ *Pbcm* [116] and $NaNbO_3$ $P2_1ma$ [117] were used as a starting point. The structures were obtained via X-ray diffraction (XRD) and are shown in figures 5.4 and 5.5. The lattice parameters are recorded in table 5.1. All my calculations in this chapter were run using CASTEP version 8.0, with ultrasoft pseudopotentials from the 'OTFG9' set [49]. The isotropic magnetic shielding was converged to within at least ±1 ppm, C_Q to within at least ±0.03 MHz and η to within ±0.01 (or ±0.1 for ^{39}K) using a planewave cut-off of 800 eV and a **k**-point spacing of $0.04\times2\pi$Å^{-1}. Similarly, Johnston *et al.* used a planewave cut-off of 812 eV (60 Ry) and a **k**-point spacing of $0.04\times2\pi$Å^{-1} for their calculations [83, 105].

Structure	a / Å	b / Å	c / Å
$KNbO_3$	3.971	5.697	5.723
$LiNbO_3$	5.142	5.142	13.843
$NaNbO_3$ *Pbcm*	5.506	5.566	15.520
$NaNbO_3$ $P2_1ma$	5.569	7.790	5.518

Table 5.1: Experimental lattice parameters obtained via XRD for the $KNbO_3$, $LiNbO_3$, *Pbcm* $NaNbO_3$ and $P2_1ma$ $NaNbO_3$ perovskite structures [114, 115, 116, 117].

5.2.1 Geometry optimisations

The structures were carefully relaxed until the forces on the atoms were less than 2.5×10^{-2} eV/Å, the stress on the unit cell was less than 0.05 GPa, the total energy change between iterations was less than 1×10^{-5} eV and the change in atomic displacement between successive iterations was less than 5×10^{-4} Å. Both the unit cell and the atomic positions were allowed to move, as also allowed for by Johnston *et al.* in their calculations used to interpret

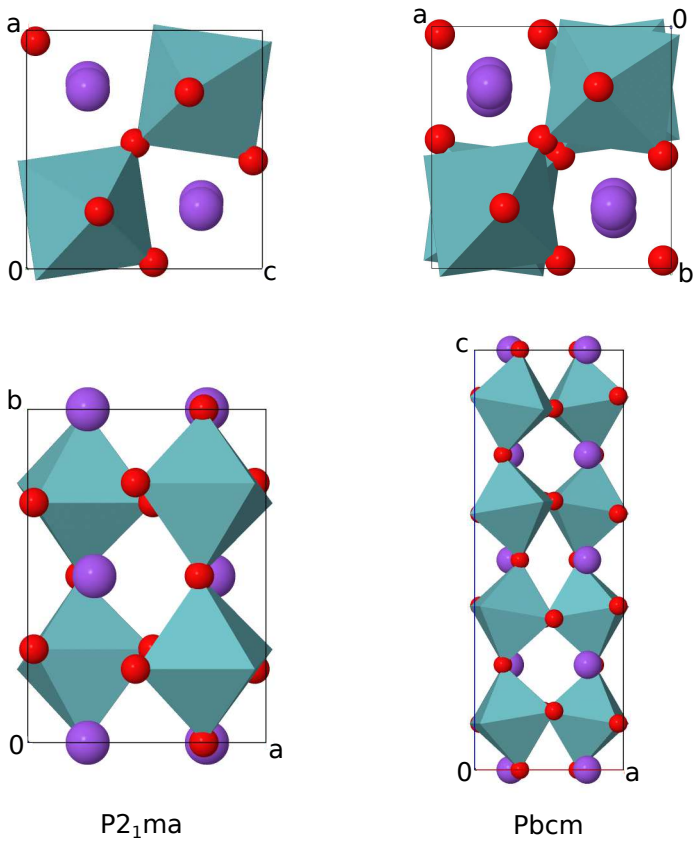

Figure 5.4: The experimental structures for both $NaNbO_3$ polymorphs. Oxygen atoms are shown in red, sodium in purple and the oxygen octahedra encapsulating the niobium atoms in teal.

experimental solid-state NMR spectra [83]. Visually, the relaxed structures are almost identical to the experimental ones.

Forces

As noted in the literature ([101, 105]) the experimental structures contain high forces on some of the atoms, particularly on the Nb and O atoms. The largest force was 2.50 eV/Å for the Nb atoms in the $NaNbO_3$ *Pbcm* structure. Table 5.2 shows the maximum forces in each of the four perovskite structures, calculated using both PBE and PBEsol functionals. After relaxation all forces were reduced to less than 2.50×10^{-2} eV/Å.

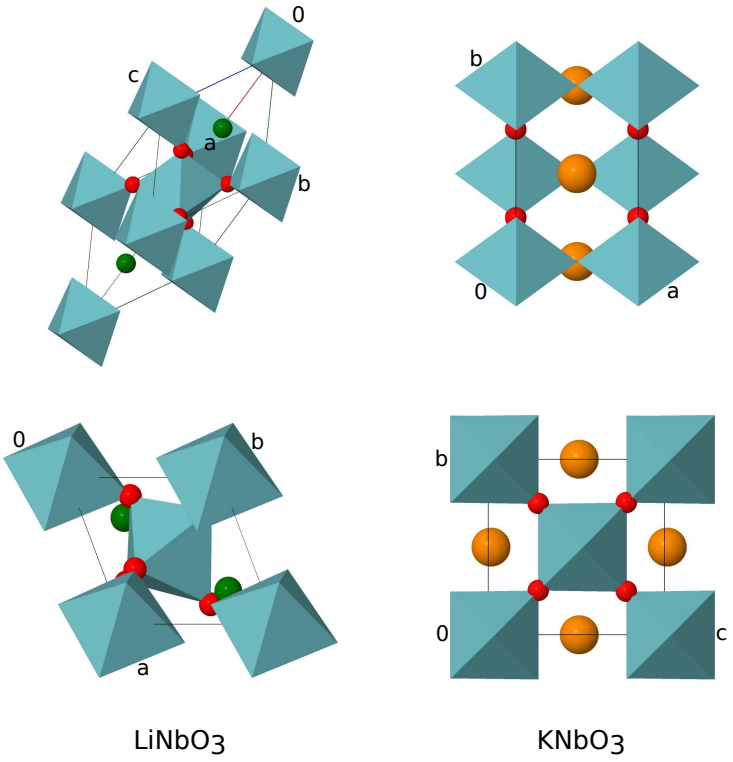

Figure 5.5: The experimental structures for $LiNbO_3$ and $KNbO_3$ perovskite structures. Lithium atoms are shown in green, sodium atoms in orange, oxygen in red and the oxygen octahedra encapsulating the niobium atoms in teal.

	PBE		PBEsol	
	$\|F_{max}\|$(eV/Å)	Atom	$\|F_{max}\|$(eV/Å)	Atom
$NaNbO_3$ *Pbcm*	2.50	Nb	2.48	Nb
$NaNbO_3$ $P2_1ma$	0.194	Nb	0.190	Nb
$LiNbO_3$ *R3c*	0.898	O	0.883	O
$KNbO_3$ *Amm2*	0.184	Nb	0.162	Nb

Table 5.2: Maximum forces on the experimental perovskite structures prior to structural relaxation.

Lattice parameters

Tables 5.3 and 5.4 show the percentage change in the lattice parameters and unit cell volume as a result of relaxing these structures. Geometry optimisations using the PBE functional caused the structures to expand whereas

those using PBEsol caused the structures to contract. Notably, the percentage changes were in general much smaller when using the PBEsol functional (i.e. the relaxed structure did not differ so much from the experimental structure as it did when using PBE). This implies that PBEsol produces a more accurate representation of the perovskite structures.

	Change in lattice parameter/%					
Structure	a(PBE)	b(PBE)	c(PBE)	a(PBEsol)	b(PBEsol)	c(PBEsol)
$KNbO_3$	0.526	1.442	1.612	-0.154	-0.341	-0.509
$LiNbO_3$	0.878	0.878	1.206	-0.214	-0.214	-0.155
$NaNbO_3$ $P2_1ma$	1.530	0.051	1.245	-0.134	-0.551	-0.262
$NaNbO_3$ $Pbcm$	1.171	1.496	0.448	-0.127	-0.091	-0.275

Table 5.3: Percentage change in unit cell axes between the initial experimental and geometry optimised structures. Percentages are expressed with respect to initial unit cell axes.

	Change in cell volume/%	
Structure	PBE	PBEsol
$KNbO_3$	3.619	-1.001
$LiNbO_3$	2.991	-0.581
$NaNbO_3$ $P2_1ma$	2.847	-0.944
$NaNbO_3$ $Pbcm$	3.144	-0.492

Table 5.4: Percentage volume change between the initial experimental and geometry optimised structures. Percentages are expressed with respect to initial volume.

5.2.2 NMR parameters

The magnetic shielding and quadrupolar parameters were calculated before and after the structures were relaxed. In the tables and graphs in this section, calculations on the pre-relaxed structures will be labelled as 'XRD' whilst those on the relaxed structures will be labelled 'OPT'. The NMR parameters reported in this section have been calculated using the same functional as that used for the structural relaxation.

$NaNbO_3$ structures—^{23}Na NMR parameters

Both *Pbcm* and $P2_1ma$ polymorphs have two distinct ^{23}Na resonances, indicating that there are two different Na environments in each structure. Table 5.5 shows the NMR parameters for these two Na nuclei in the *Pbcm* polymorph; table 5.6 shows the equivalent for the two Na nuclei in the $P2_1ma$ polymorph. In all four tables experimental values and the results of CASTEP calculations reported in the literature are shown alongside the results of my own CASTEP calculations. My calculated ^{23}Na σ_{iso} values have been converged to within at least 1 ppm, C_Q values to within 0.01 MHz, and η_Q to within at least 0.01. All ^{23}Na δ_{iso} values are quoted using equation 2.11. The reference magnetic shielding used for the data quoted from Johnston *et al.* [83] was $\sigma_{ref} = 565.84$ ppm [100]. In the case of my calculations I have taken reference shieldings from the y-intercept of the $y = -x + b$ lines of best fit shown in figure 5.6.[2]

Despite the planewave cut-off and **k**-point spacing being almost the same for my calculations and those quoted in the literature (planewave cut-off of 800 eV versus 816 eV and a **k**-point spacing of $0.04 \times 2\pi$Å^{-1} in both cases), there is still a difference in the values of the calculated NMR parameters, with my results being generally closer to the experimental values, particularly in the case of δ_{iso}. Partly this will be due to differences in the pseudopotential: the calculations reported in the literature date back to 2010, and since then the accuracy of ultrasoft pseudopotentials in CASTEP has improved. By way of comparison, the Δ values for the 2010 pseudopotentials and the up-to-date ones used in my calculations are 2.6 meV/atom and

[2]Fitting $y = -x + b$ lines to trends of calculated magnetic shieldings enables a σ_{ref} value to be obtained which is consistent with the level of theory used to obtain the σ_{iso} values in the first place.

0.7 meV/atom respectively [49].[3] Small structural differences in the relaxed unit cells may also have contributed to the differences in the calculated NMR parameters. Johnston *et al.* state that the forces on their relaxed structures were below 0.04 eV/Å [105]. By contrast, the forces on my relaxed structures were below 0.025 eV/Å, indicating that my structures may have been closer to the bottom of the energy minimum than those previously used in the literature.

Tables 5.5 and 5.6 also show that PBE tends to overestimate σ_{iso}, whereas PBEsol underestimates it. The calculated δ_{iso} values for my relaxed structures are closer to the experimental values than are the calculated values for the XRD structures. Furthermore, the PBEsol(OPT) δ_{iso} values are closer to the experimental values than are the PBE(OPT) values. The calculated quadrupolar products are in good agreement with those obtained via experiment. The quadrupolar products for the two Na sites in a given polymorph differ by approximately 1–1.2 MHz, implying that P_Q is a good indicator of the Na site as noted by Peel *et al.* [102].

Figure 5.6 shows my calculated isotropic magnetic shielding values against the experimental chemical shifts corresponding to 'Exp2' in tables 5.5 and 5.6. The figure shows that the relaxed structures produce a more consistent set of magnetic shieldings. This is quantitatively expressed by calculating the root-mean-square deviations from the lines of best fit, as recorded in table 5.7. Structures relaxed using PBEsol produce a gradient that is closer to -1 compared to that for PBE (see figure 5.6) and a RMS deviation for $y = -x + b$ that is much smaller than the corresponding value for PBE (see

[3] The Δ values are quoted as averages over all all-electron methods as presented in table 2 in the paper by Lejaeghere *et al.* [49]. The 2010 pseudopotentials would have been the same as the 'OTFG7' (i.e. 'C7') set, whilst the 'C8' set used for my calculations is the same as the 'OTFG9' ('C9') set quoted in the paper for the elements studied.

a. ^{23}Na1 in $NaNbO_3$ Pbcm

Structure	σ_{iso}/ppm	δ_{iso}/ppm	ζ/ppm	η	$\lvert C_Q\rvert$/MHz	η_Q	$\lvert P_Q\rvert$/MHz
Exp1 [83]	566.44(5)	-0.6(5)	-	-	-	-	2.2(1)
Exp2 [83]	566.34(5)	-0.5(5)	-	-	2.1(1)	0.0(1)	2.1(1)
Calc1 [83]	570.64	-4.8	-	-	2.22	0.17	2.23
Calc2 [83]	570.64	-4.8	-	-	2.27	0.07	2.27
PBE(XRD)	567.3	-1.6	-11.7	0.35	2.04	0.78	2.23
PBEsol(XRD)	565.8	-1.6	-13.5	0.18	1.93	0.79	2.12
PBE(OPT)	567.1	-0.1	-9.7	0.38	2.28	0.07	2.28
PBEsol(OPT)	562.5	-0.6	-15.0	0.25	2.37	0.20	2.38

b. ^{23}Na2 in $NaNbO_3$ Pbcm

Structure	σ_{iso}/ppm	δ_{iso}/ppm	ζ/ppm	η	$\lvert C_Q\rvert$/MHz	η_Q	$\lvert P_Q\rvert$/MHz
Exp1 [83]	570.04(5)	-4.2(5)	-	-	-	-	1.2(2)
Exp2 [83]	570.04(5)	-4.2(5)	-	-	1.0(2)	0.8(1)	1.2(2)
Calc1 [83]	574.84	-9.0	-	-	0.87	0.79	0.96
Calc2 [83]	574.74	-8.9	-	-	0.89	0.71	0.96
PBE(XRD)	570.6	-4.9	14.7	0.31	1.07	0.58	1.13
PBEsol(XRD)	569.1	-4.9	14.4	0.37	1.00	0.52	1.05
PBE(OPT)	571.9	-4.9	15.3	0.45	1.04	0.59	1.09
PBEsol(OPT)	566.5	-4.6	15.3	0.47	1.02	0.60	1.08

Table 5.5: NMR parameters for ^{23}Na1 (**a.**) and ^{23}Na2 (**b.**) in the $NaNbO_3$ *Pbcm* structure. The positions of Na1 and Na2 are shown in figure 5.6. 'Exp1' corresponds to an experimental measurement obtained by Johnston *et al.* on a commercial sample [83]. 'Exp2' corresponds to an experimental measurement obtained by Johnston *et al.* using an external field of 9.4 T on a sample synthesised by solid-state techniques ('Solid-state sample A') [83]. The numbers in the brackets show the uncertainty in the last digit. 'Calc1' and 'Calc2' are the results of CASTEP calculations, using PBE, also conducted by Johnston *et al.* on relaxed structures [83]; the pre-relaxed structures were obtained by experiment by Sakowski-Cowley *et al.* [116] and Johnston *et al.* [83] respectively. For the results obtained in my own calculations, the relaxed (OPT) structures were obtained using the same functional as that used for calculating the NMR parameters. The σ_{ref} values used to obtain δ_{iso} for each of my calculated σ_{iso} values were σ_{ref}[PBE(XRD)]= 565.75 ppm, σ_{ref}[PBEsol(XRD)]= 564.23 ppm, σ_{ref}[PBE(OPT)]= 566.96 ppm and σ_{ref}[PBEsol(OPT)]= 561.91 ppm; these were obtained from the $y = -x + b$ lines of best fit in figure 5.6.

a. ^{23}Na1 in $NaNbO_3$ $P2_1ma$

Structure	σ_{iso}/ppm	δ_{iso}/ppm	ζ/ppm	η	$\lvert C_Q\rvert$/MHz	η_Q	$\lvert P_Q\rvert$/MHz
Exp2 [83]	567.24(5)	-1.4(5)	-	-	2.1(1)	0.9(1)	2.4(1)
Exp3 [83]	567.34(5)	-1.5(5)	-	-	-	-	2.4(1)
Calc3 [83]	570.74	-4.9	-	-	2.33	0.71	2.52
Calc4 [83]	571.54	-5.7	-	-	2.22	0.85	2.47
PBE(XRD)	566.6	-0.9	20.4	0.87	2.27	0.80	2.50
PBEsol(XRD)	564.8	-0.6	19.3	0.98	2.12	0.79	2.33
PBE(OPT)	567.6	-0.6	21.0	0.94	2.48	0.71	2.68
PBEsol(OPT)	562.7	-0.8	-21.7	0.89	2.41	0.63	2.57

b. ^{23}Na2 in $NaNbO_3$ $P2_1ma$

Structure	σ_{iso}/ppm	δ_{iso}/ppm	ζ/ppm	η	$\lvert C_Q\rvert$/MHz	η_Q	$\lvert P_Q\rvert$/MHz
Exp2 [83]	570.94(5)	-5.1(5)	-	-	1.1(2)	0.7(1)	1.2(2)
Exp3 [83]	570.94(5)	-5.1(5)	-	-	-	-	1.2(2)
Calc3 [83]	575.34	-9.5	-	-	1.01	0.8	1.11
Calc4 [83]	575.74	-9.9	-	-	0.80	0.82	0.89
PBE(XRD)	569.7	-4.0	15.4	0.29	1.17	0.72	1.26
PBEsol(XRD)	568.4	-4.2	15.4	0.51	1.09	0.70	1.17
PBE(OPT)	572.5	-5.5	15.1	0.29	1.01	0.79	1.11
PBEsol(OPT)	567.2	-5.3	15.9	0.44	1.02	0.76	1.11

Table 5.6: NMR parameters for ^{23}Na1 (**a.**) and ^{23}Na2 (**b.**) in the $NaNbO_3$ $P2_1ma$ structure. The positions of Na1 and Na2 are shown in figure 5.6. As in table 5.5, 'Exp2' corresponds to an experimental measurement obtained by Johnston *et al.* using an external field of 9.4 T on a sample synthesised by solid-state techniques ('Solid-state sample A') [83]. 'Exp3' corresponds to an experimental measurement also obtained by Johnston *et al.* on a sol-gel sample hypothesised to be the $P2_1ma$ polymorph [83]. The numbers in the brackets show the uncertainty in the last digit. 'Calc3' and 'Calc4' are the results of CASTEP calculations, using PBE, conducted by Johnston *et al.* on relaxed structures; the pre-relaxed structures were experimentally obtained by Shuvaeva *et al.* [117] and Johnston *et al.* [83] respectively. For the results of my own calculations, the relaxed (OPT) structures were obtained using the same functional as was used for calculating the NMR parameters. The σ_{ref} values used to obtain δ_{iso} for each of my calculated σ_{iso} values were σ_{ref}[PBE(XRD)]= 565.75 ppm, σ_{ref}[PBEsol(XRD)]= 564.23 ppm, σ_{ref}[PBE(OPT)]= 566.96 ppm and σ_{ref}[PBEsol(OPT)]= 561.91 ppm; these were obtained from the $y = -x + b$ lines of best fit in figure 5.6.

table 5.7). This implies that PBEsol produces a more accurate representation of the structure.

RMS of residuals	PBE(XRD)	PBEsol(XRD)	PBE(OPT)	PBEsol(OPT)
for initial $y = mx + c$	1.098	1.153	0.4056	0.4390
for $y = -x + b$	1.037	1.011	0.6989	0.4212

Table 5.7: Table showing the root-mean-square deviations from the lines of best fit shown in figure 5.6.

$NaNbO_3$–^{93}Nb NMR parameters

There is a single Nb environment for each of the $NaNbO_3$ *Pbcm* and $P2_1ma$ polymorphs. The NMR parameters for these are shown in table 5.8. Since there were only two σ_{iso} environments from which to obtain a σ_{ref} from my calculations (unlike for ^{23}Na, where there were four), σ_{ref} was taken to be -648.12 ppm, a value obtained by Johnston *et al.* [83] and used for further related work [105]. The blue entries are where I have completed the entries from the literature. For the *Pbcm* structures, my calculated σ_{iso} values are converged to within at least ± 0.2 ppm, C_Q to at least ± 0.02 MHz and η_Q to within ± 0.005. In the case of the $P2_1ma$ structures, σ_{iso} values are converged to within ± 1 ppm, C_Q to ± 0.03 MHz and η_Q to ± 0.005.

As in the case for the ^{23}Na calculations, my calculations are in closer agreement to experiment than are the calculations in the literature [83, 105]. Again, this is probably due to the increased accuracy of the modern pseudopotentials, and in part to the more stringent tolerances placed on my structures during relaxation.

Comparing calculations for my relaxed structures to experiment shows that the PBEsol calculations are in closer agreement to experiment than those with PBE. It can also be seen that, for the relaxed structures, PBEsol

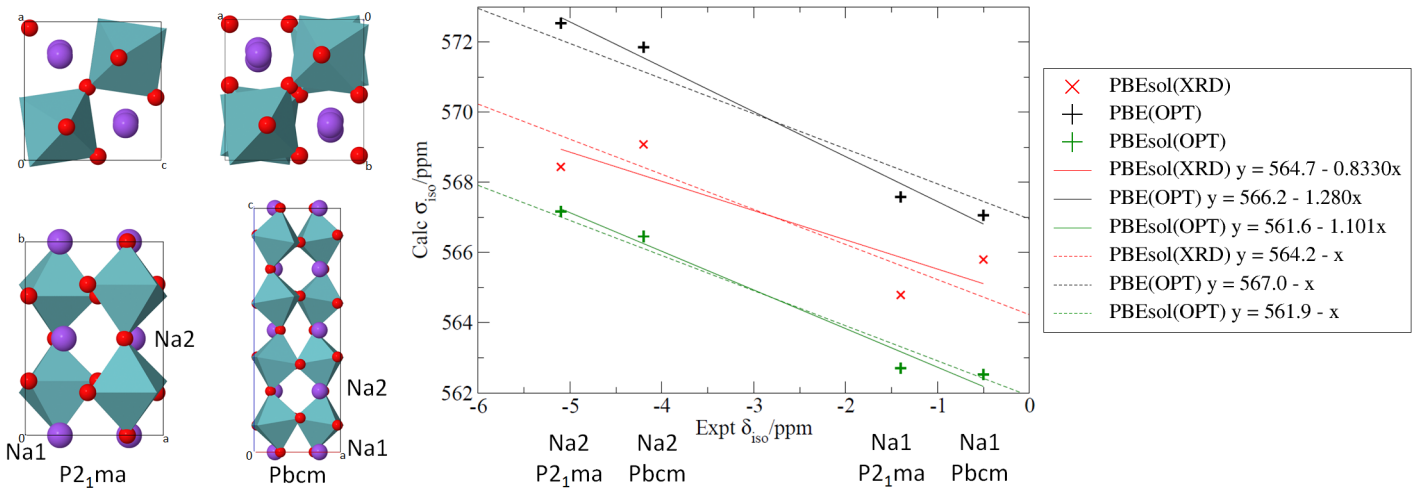

Figure 5.6: Summary of calculated chemical shifts, σ_{iso}, against experimental chemical shifts, δ_{iso}, for Na in the $NaNbO_3$ structures. The δ_{iso} measurements are plotted from 'Exp2' in tables 5.5 and 5.6, which corresponds to the measurements on the two-phase $NaNbO_3$ sample used by Johnston *et al.* [83]. Red crosses represent points for which σ_{iso} corresponds to calculations using the initial (experimental) structures with the PBEsol functional. Black crosses correspond to calculations using the relaxed structure with PBE (geometry optimised also with PBE). Green crosses correspond to calculations using the relaxed structure with PBEsol (geometry optimised also with PBEsol). The straight lines are lines of best fit of the form $\delta_{iso} = -\sigma + \sigma_{ref}$. The dotted lines are the corresponding lines of best fit when imposing a gradient of -1. (PBE(XRD) has been omitted for clarity.)

overestimates σ_{iso} whilst PBE underestimates it, which is the opposite trend to that observed for ^{23}Na. In the case of $|C_Q|$, PBEsol underestimates it whilst PBE overestimates it.

In agreement with the measurements by Johnston *et al.*, my calculations do not indicate that there should be a distinct difference between the ^{93}Nb NMR spectra for the *Pbcm* and $P2_1ma$ structures. This correlates with the earlier calculations of Johnston *et al.*, from which they concluded that the ^{93}Nb NMR parameters could not be used to distinguish the *Pbcm* and $P2_1ma$ polymorphs.

$NaNbO_3$—^{17}O NMR parameters

There are four separate oxygen environments for each $NaNbO_3$ polymorph. The values of σ_{iso} for each of these environments are shown in figure 5.7. Note that the line shapes in figure 5.7 do not take into account any form of physical broadening—quadrupolar or otherwise. The C_Q values at all ^{17}O sites are however small at no more than 1.5 MHz.

To date there have been no published measurements for ^{17}O NMR in $NaNbO_3$. Of the three stable oxygen isotopes (^{16}O, ^{17}O and ^{18}O), only ^{17}O has a non-zero spin. This isotope has a minute natural abundance of 0.037% [94, p. 333]. The only practical way to obtain a sample with a strong enough ^{17}O signal is by enrichment which is extremely expensive. Figure 5.7 shows that the polymorphs have similar ^{17}O magnetic shieldings after the structures have been relaxed (OPT), implying that ^{17}O NMR may not be a good method with which to distinguish between the two polymorphs.

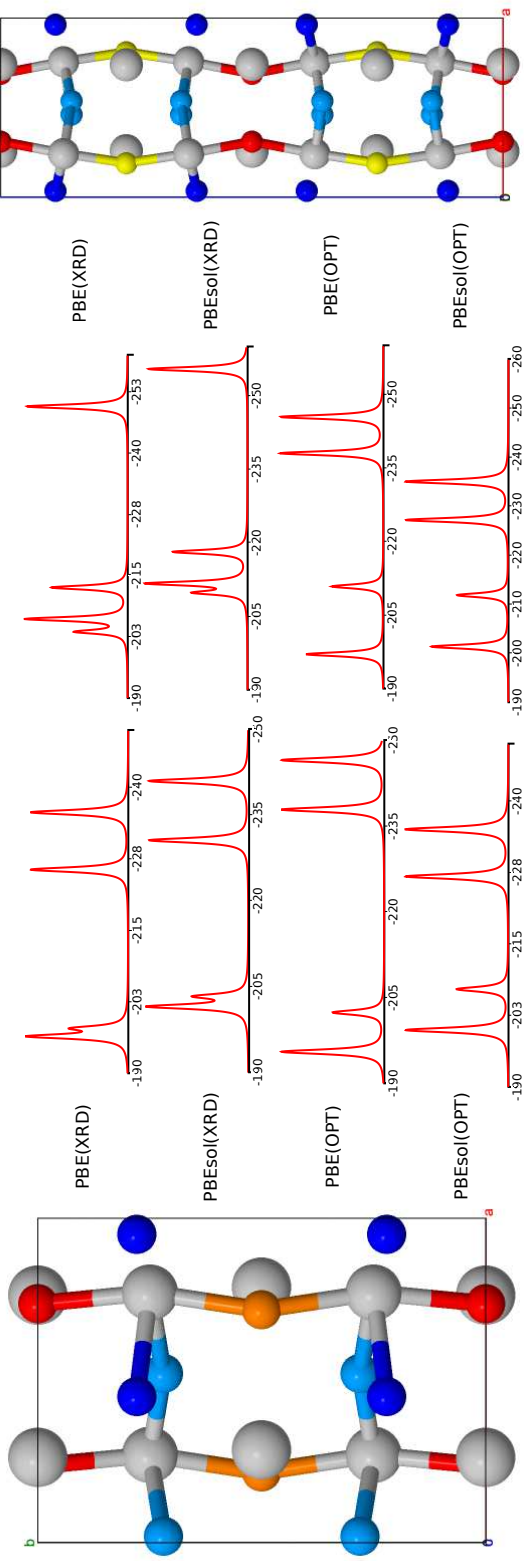

Figure 5.7: The ^{17}O isotropic magnetic shielding as simulated spectra in both studied $NaNbO_3$ polymorphs. The σ_{iso} values have been broadened with a Lorentzian of width 0.5 ppm. Only magnetic shieldings have been taken into account in these line-shapes—i.e. there is no quadrupolar broadening. σ_{iso} has been converged to within ±1 ppm. The oxygen atoms in the structures are shaded according to the value of σ_{iso}: red corresponds to the least negative σ_{iso} in each structure and dark blue to the most negative σ_{iso} values. The spectra and shaded images have been made using MagresView [119].

a. ^{93}Nb—$NaNbO_3$ Pbcm

Structure	σ_{iso}/ppm	δ_{iso}/ppm	ζ/ppm	η	$\lvert C_Q\rvert$/MHz	η_Q	$\lvert P_Q\rvert$/MHz
Exp [83]	430.2(5)	-1078.3(5)	-	-	19.6(2)	0.7(1)	21.2(2)
Exp [105]	430(10)	-1078(10)	-60(10)	0.3(1)	19.5(7)	0.7(1)	21.1(4)
Calc(XRD[118]) [105]	422.7	-1070.8	31.2	0.38	45.1	0.80	49.7
Calc(OPT[118]) [105]	408.0	-1056.1	-75.5	0.14	26.4	0.98	30.3
Calc(XRD[83]) [105]	440.9	-1089.0	-46.9	0.48	14.8	0.96	16.9
Calc(OPT[83]) [105]	409.8	-1057.9	-78.4	0.17	27.0	0.99	31.1
PBE(XRD)	446.7	-1094.8	67.1	0.51	19.6	0.23	19.7
PBEsol(XRD)	426.4	-1074.5	70.1	0.47	19.7	0.22	19.8
PBE(OPT)	395.4	-1043.5	108.4	0.20	24.3	0.91	27.4
PBEsol(OPT)	418.9	-1067.0	88.1	0.34	16.8	0.82	18.6

b. ^{93}Nb—$NaNbO_3$ $P2_1ma$

Structure	σ_{iso}/ppm	δ_{iso}/ppm	ζ/ppm	η	$\lvert C_Q\rvert$/MHz	η_Q	$\lvert P_Q\rvert$/MHz
Exp [105]	430(10)	-1078(10)	-90(10)	0.5(1)	20.3(7)	0.7(1)	21.5(6)
Calc(XRD[117]) [105]	429.2	-1077.3	-58.8	0.23	15.1	0.27	15.3
Calc(OPT[117]) [105]	406.9	-1055.0	-72.9	0.11	25.2	0.91	28.5
Calc(XRD[83]) [105]	442.3	-1090.4	-72.9	0.27	19.3	0.53	20.2
Calc(OPT[83]) [105]	407.3	-1055.4	-74.6	0.08	26.5	0.92	30.0
PBE(XRD)	425.8	-1073.9	88.8	0.22	14.6	0.28	14.8
PBEsol(XRD)	406.3	-1054.4	88.9	0.21	14.6	0.29	14.8
PBE(OPT)	394.5	-1042.6	114.4	0.08	25.6	0.98	29.4
PBEsol(OPT)	415.6	-1063.7	91.7	0.29	17.8	0.75	19.4

Table 5.8: ^{93}Nb NMR parameters for the $NaNbO_3$ *Pbcm* (**a.**) and $P2_1ma$ structures (**b.**). 'Exp' entries are experimental data from the literature; the brackets give the uncertainty in the measurements. 'Calc' entries correspond to CASTEP calculations in the literature, all using the PBE functional. 'PBE/PBEsol' entries are my CASTEP calculations. 'XRD' and 'OPT' refer to whether the structure used was from experiment or relaxed/optimised respectively. The sources of the initial structures are referenced where appropriate. The signs of the calculated ζ values have been reversed so that they may be compared to experiment in accordance with the procedure by Johnston *et al.* [105].

NMR parameters in $LiNbO_3$

Table 5.9 shows the calculated NMR parameters for ^{7}Li, ^{93}Nb and ^{17}O in $LiNbO_3$ $R3c$, alongside experimental measurements from the literature. It can be seen that there is a single chemical environment each for Li, Nb and O. The range of σ_{iso} values for ^{17}O and ^{93}Nb indicate that these nuclei are relatively sensitive to changes in geometry and the functional used for the calculations, as was the case for $NaNbO_3$. By contrast, the σ_{iso} values for

^{7}Li are relatively insensitive to changes in geometry and functional. For the Li and Nb nuclei, $\eta_Q = 0$ indicating that these nuclei are in a cylindrical environment with respect to the electric field gradient. The C_Q values for ^{7}Li are small—of the order of kHz, compared to MHz for the other nuclei.

Structural relaxation appears to significantly improve the ^{93}Nb C_Q values with respect to experiment. This could be related to the relatively high forces on the O nuclei prior to structural relaxation (table 5.2). The oxygen octahedral arrangements would therefore alter significantly during geometry optimisation calculations, thus changing the electric field gradient experienced by the niobium nuclei. In the case of Nb and O, ζ is of the order of a few hundreds of ppm, implying that the electronic environment around the oxygen octahedra is far from isotropic.

NMR parameters in $KNbO_3$

Two subtly different unit cells for the $KNbO_3$ $Amm2$ structure are reported in the literature from X-ray diffraction data [114, 126]. The Kawamura cell is approximately the primitive cell of the Shuvaeva cell and also includes fractional occupancy of the Nb atoms. Both cells upon relaxation have similar NMR parameters, for example the σ_{iso} values across all the nuclei differ by no more than 2 ppm. Cycling through the four possible permutations for the positions of the Nb atoms in the Shuvaeva cell produces at most a 0.1 ppm change in the ^{93}Nb σ_{iso} value and corresponds to a 0.040 Å change in the position of the Nb atom along the **a**-axis. The cell measured by Shuvaeva *et al.* has been chosen for all subsequent calculations so that the structure can be easily compared to the supercells for the disordered $Na_xK_{1-x}NbO_3$ structures later in this chapter.

a. ^{7}Li—$LiNbO_3$

Structure	σ_{iso}/ppm	ζ/ppm	η	$\lvert C_Q\rvert$/MHz	η_Q	$\lvert P_Q\rvert$/MHz
Exp1 [120]	-	-	-	0.0552(4)	0	-
Exp2 [121, 122]	-	-	-	0.054(1)	0	-
PBE(XRD)	88.78	-2.28	0.19	0.0365	0.00	0.04
PBEsol(XRD)	88.29	-2.31	0.19	0.0351	0.00	0.04
PBE(OPT)	89.17	-0.27	0.02	0.0165	0.00	0.02
PBEsol(OPT)	88.42	-0.66	0.09	0.0080	0.00	0.0080

b. ^{93}Nb—$LiNbO_3$

Structure	σ_{iso}/ppm	ζ/ppm	η	$\lvert C_Q\rvert$/MHz	η_Q	$\lvert P_Q\rvert$/MHz
Exp1 [123]	-	-	-	22.02(4)	0	-
Exp2 [124]	-	-	-	-	-	22.1(5)
PBE(XRD)	370.52	-117.79	0.00	7.060	0.00	7.06
PBEsol(XRD)	354.19	-119.60	0.00	7.272	0.00	7.27
PBE(OPT)	341.11	-174.43	0.00	22.34	0.00	22.34
PBEsol(OPT)	370.54	-168.98	0.00	20.94	0.00	20.94

c. ^{17}O—$LiNbO_3$

Structure	σ_{iso}/ppm	ζ/ppm	η	$\lvert C_Q\rvert$/MHz	η_Q	$\lvert P_Q\rvert$/MHz
Exp1 [125]	-	-	-	3.4	-	-
PBE(XRD)	-219.7	393.8	0.19	1.043	0.87	1.17
PBEsol(XRD)	-224.9	387.6	0.19	0.9623	0.96	1.10
PBE(OPT)	-224.4	437.8	0.36	1.193	0.96	1.36
PBEsol(OPT)	-216.3	409.1	0.33	1.130	0.74	1.23

Table 5.9: ^{7}Li, ^{93}Nb and ^{17}O NMR parameters for the $LiNbO_3$ $R3c$ structure. For ^{7}Li, the σ_{iso} values have been converged to within ± 0.2 ppm and C_Q to within ± 0.005 MHz. For ^{93}Nb, the σ_{iso} values have been converged to within ± 1 ppm and the C_Q values to within ± 0.01 MHz. For ^{17}O, the σ_{iso} values have been converged to within ± 0.7 ppm and C_Q to within ± 0.01 MHz. All η_Q values have been converged to within ± 0.005.

Table 5.10 shows the results of my NMR calculations for ^{39}K, ^{93}Nb and ^{17}O. In general, there is an absence of suitable experimental NMR data in the literature to compare my results to. Nevertheless, the calculations reveal some interesting trends. There is a single environment each for the K and Nb nuclei, but two distinct environments for the three oxygen sites. The single ^{39}K environment is relatively isotropic, as indicated by the small ζ values and C_Q of the order of tens of kHz. The Nb and O environments are more anisotropic, particularly in the case of the oxygen sites which have ζ values twice as large as σ_{iso}. The C_Q values for the oxygen sites are around 1 MHz. The Nb C_Q values are higher, at 20–35 MHz. Note that the relaxed PBEsol structure has a ^{93}Nb C_Q value that is considerably closer to experiment than that for the relaxed PBE structure.

5.2.3 The effect of functional on calculated NMR parameters: PBE versus PBEsol

When investigating the NMR parameters for a given system, the structure should first be relaxed before the NMR parameters are calculated. The choice of functional can therefore indirectly affect the NMR parameters through its effect on structural distortions, in addition to directly affecting the NMR parameters via the NMR calculation. This section examines both of these effects by investigating the changes in σ_{iso} across the pure $NaNbO_3$, $LiNbO_3$ and $KNbO_3$ structures discussed above.

The effect of geometry optimisations using PBE or PBEsol on σ_{iso}

How does the choice of functional for a geometry optimisation indirectly affect the relaxed structure's NMR parameters? By way of example, figure 5.8 shows the difference in σ_{iso} between structures relaxed with either PBE

a. ^{39}K—$KNbO_3$

Structure	σ_{iso}/ppm	ζ/ppm	η	$\lvert C_Q\rvert$/MHz	η_Q	$\lvert P_Q\rvert$/MHz
PBE(XRD)	1161.0	-7.9	0.97	0.0173	0.72	0.0188
PBEsol(XRD)	1150.0	-8.4	0.97	0.0161	0.81	0.0178
PBE(OPT)	1171.3	-10.8	0.90	0.0419	0.59	0.0443
PBEsol(OPT)	1146.9	-7.1	0.88	0.0402	0.73	0.0436

b. ^{93}Nb—$KNbO_3$

Structure	σ_{iso}/ppm	ζ/ppm	η	$\lvert C_Q\rvert$/MHz	η_Q	$\lvert P_Q\rvert$/MHz
Exp [127]	-	-	-	23.1	0.80	-
PBE(XRD)	390.2	93.5	0.70	23.46	0.79	25.79
PBEsol(XRD)	371.8	93.1	0.71	23.14	0.83	25.66
PBE(OPT)	361.8	99.3	0.77	34.18	0.65	36.51
PBEsol(OPT)	370.3	81.4	0.63	19.50	0.78	21.39

c. ^{17}O—$KNbO_3$

Structure	σ_{iso}/ppm	ζ/ppm	η	$\lvert C_Q\rvert$/MHz	η_Q	$\lvert P_Q\rvert$/MHz
A PBE(XRD)	-241.3	412.7	0.18	1.373	0.02	1.373
B PBE(XRD)	-276.2	478.1	0.20	0.787	0.24	0.795
A PBEsol(XRD)	-247.7	405.4	0.18	1.249	0.03	1.249
B PBEsol(XRD)	-282.5	470.9	0.21	0.679	0.28	0.688
A PBE(OPT)	-241.4	413.4	0.23	1.623	0.02	1.623
B PBE(OPT)	-289.5	497.6	0.23	0.918	0.20	0.924
A PBEsol(OPT)	-255.4	414.0	0.14	1.111	0.05	1.111
B PBEsol(OPT)	-282.4	464.3	0.17	0.663	0.23	0.669

Table 5.10: ^{39}K, ^{93}Nb and ^{17}O (in two different environments—'A' and 'B') NMR parameters for the $KNbO_3$ $Amm2$ structure. For ^{39}K, the σ_{iso} values have been converged to within ± 0.1 ppm, C_Q to within ± 0.001 MHz and η_Q to within at least ± 0.1. For ^{93}Nb, the σ_{iso} values have been converged to within ± 1 ppm, C_Q to within ± 0.01 MHz and η_Q to within ± 0.005. For ^{17}O, the σ_{iso} values have been converged to within ± 1 ppm, C_Q to within ± 0.005 MHz and η_Q to within ± 0.01.

or PBEsol ('OPT') and the initial experimental structure ('XRD'). In order to directly compare the structural effect on σ_{iso}, the NMR calculation has been performed using PBEsol irrespective of whether the structure has been relaxed with PBEsol or PBE or not at all. The ^{93}Nb and ^{17}O σ_{iso} values are particularly sensitive to structural relaxation. Furthermore, the change in σ_{iso} as a result of relaxing with PBEsol is much smaller than that

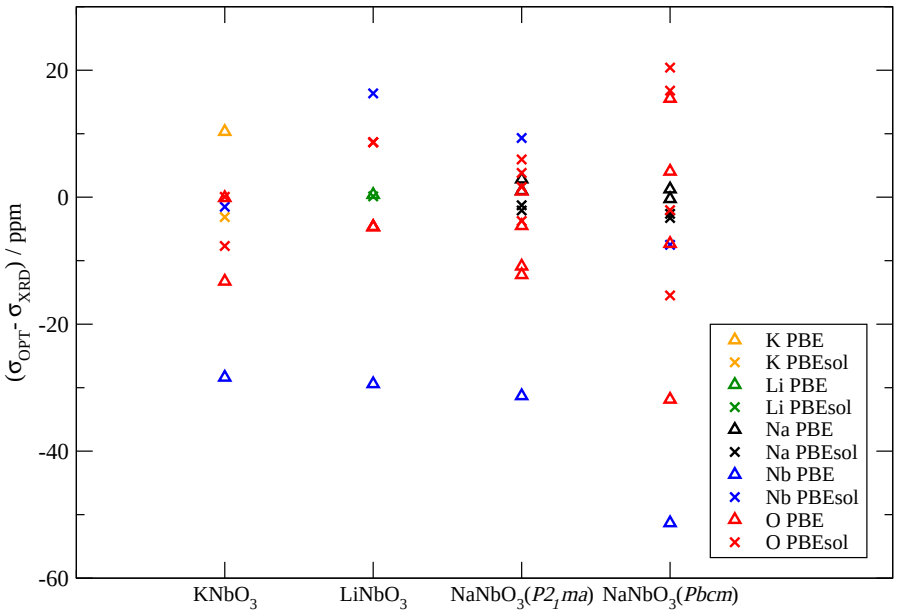

Figure 5.8: The difference between σ_{iso} for a relaxed ('OPT') structure and the initial experimental ('XRD') structure. Triangles denote relaxations using PBE, crosses—relaxations using PBEsol. All σ_{iso} values shown have been calculated using PBEsol. Orange denotes potassium nuclei, green—lithium, black—sodium, blue—niobium and red—oxygen.

when relaxing with PBE. In the most extreme case, the ^{93}Nb σ_{iso} value deviates by 51 ppm between the PBE-relaxed and the initial XRD structure. By contrast, the equivalent deviation for the PBEsol-relaxed structure is only -7.5 ppm. This implies that PBEsol more accurately represents the experimental structures, and that therefore NMR parameters calculated on structures which have been optimised using PBEsol will be more consistent with experiment, particularly for ^{93}Nb nuclei.

The effect of using PBE or PBEsol to calculate σ_{iso} for a given structure

How does the choice of functional directly affect the calculated NMR parameters for a given structure? Figure 5.9 shows the difference between the calculated σ_{iso} values obtained using PBE and PBEsol for the same structure i.e. for the initial experimental structures ('XRD'), the PBE-relaxed ('PBE(OPT)') structures and the PBEsol-relaxed ('PBEsol(OPT)') structures.

The σ_{iso} values for the group I cations are relatively insensitive to the choice of functional when compared to a range of experimental chemical shifts of suitable compounds. The ^{7}Li σ_{iso} values are changed by approximately 0.5 ppm with respect to functional, compared to a general chemical shift range of ∼4 ppm over a range of lithium-containing compounds [94, p. 630–1]. The ^{23}Na values are changed by up to 2 ppm with functional, compared to an experimental chemical shift range of ∼5 ppm for the $NaNbO_3$ structures (from tables 5.5 and 5.6) and ∼20 ppm over a range of other Na-containing compounds [94, p. 403-11]. The ^{39}K σ_{iso} values differ by ∼11 ppm with respect to functional. In the absence of any experimental ^{39}K NMR measurements, this can only be placed in the context of a σ_{iso} range of other potassium-containing compounds which extend over ∼160 ppm [94, p. 497].

The ^{17}O σ_{iso} values are also relatively insensitive to the choice of functional. ^{17}O σ_{iso} values are changed by up to 7 ppm with respect to functional, relative to a chemical shift range of ∼59 ppm across two measured ^{17}O chemical shifts in $LiNbO_3$ ([94, p. 357–8] after [125]). In the context of the overall chemical shift range for ^{17}O, which is greater than 1000 ppm over

a range of compounds, the effect of functional is diminished even further [94, p. 357–8].

Finally, the ^{93}Nb σ_{iso} values are affected by up to ∼20 ppm depending on the functional, however the range of chemical shifts across $LiNbO_3$, $NaNbO_3$ and $KNbO_3$ is ∼69 ppm so the relative effect of the choice of functional is not as great as it might seem when considering absolute values [94, p. 665].[4]

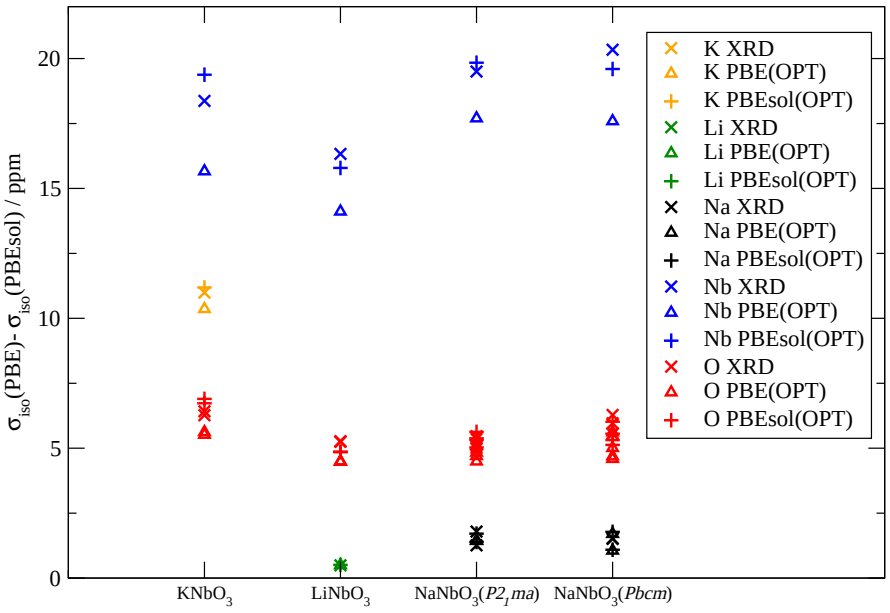

Figure 5.9: The difference between σ_{iso} calculated using PBE and PBEsol for a given structure. Crosses denote structures before relaxation ('XRD'), triangles denote structures which have been relaxed using PBE ('PBE(OPT)') and plusses denote structures which have been relaxed using PBEsol ('PBEsol(OPT)'). Orange denotes potassium nuclei, green—lithium, black—sodium, blue—niobium and red—oxygen.

This change in the calculated σ_{iso} as a result of changing the functional

[4]The experimental ^{93}Nb chemical shifts relative to $NbCl_5$ in acetonitrile are -1004 ppm [124] or -1009 ppm [123] for $LiNbO_3$, -1073 ppm for $NaNbO_3$ (polymorph unspecified) [124, 123] and -1050 ppm for $KNbO_3$ [127, 123] as given by Mackenzie and Smith [94, p. 665].

could originate from either the core electrons, the valence electrons or a combination of both. Table 5.11 shows that the contribution to σ_{iso} from the core electrons is hardly affected by functional. Therefore the functional must predominantly affect the valence electrons (shown for completeness in figure 5.10).

Nucleus	Core with PBE (ppm)	Core with PBEsol (ppm)	PBE-PBEsol (ppm)
^{17}O	271.08	270.50	0.57
^{93}Nb	3782.13	3780.74	1.39
^{39}K	1193.41	1192.38	1.03
^{7}Li	0.00	0.00	0.00
^{23}Na	377.27	376.66	0.61

Table 5.11: Core contributions to the magnetic shielding tensor when using PBE and PBEsol. All of these core magnetic shielding tensors are isotropic.

Overall, the effect of the functional on the NMR calculations has a smaller effect on the final σ_{iso} values than the initial geometry optimisation, as can be seen by comparing the absolute magnitudes of the change in σ_{iso} for graphs 5.8 and 5.9. The σ_{iso} deviations range from ∼-30—20 ppm in the case of altering the geometry (with the PBE ^{93}Nb value for $NaNbO_3$ *Pbcm* being an outlier at -51 ppm). In the case of altering the functional used for the NMR calculations for a given geometry, σ_{iso} values ranged only from 0—20 ppm.

In all cases, whether the functional was changed for the geometry optimisations or for the NMR calculations, the ^{93}Nb σ_{iso} values were the most sensitive.

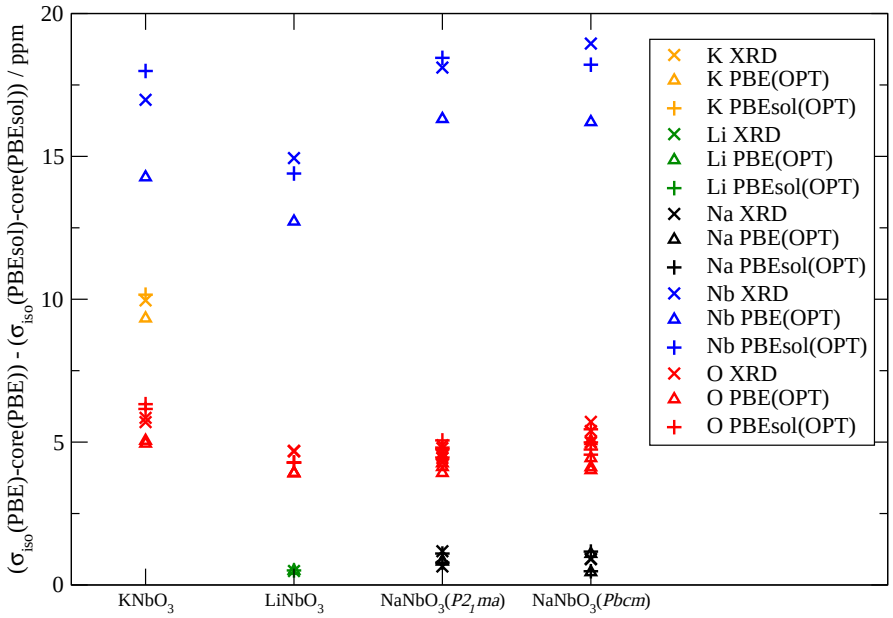

Figure 5.10: The difference between the valence contribution to σ_{iso} calculated using PBE and PBEsol for each of the experimental (XRD) and PBE/PBEsol-relaxed (PBE(OPT)/PBEsol(OPT)) structures. This is obtained by subtracting the relevant core contribution to σ_{iso} (shown in table 5.11) from σ_{iso}. Crosses denote structures before relaxation, triangles denote structures which have been relaxed using PBE and plusses denote structures which have been relaxed using PBEsol. Orange denotes potassium nuclei, green—lithium, black—sodium, blue—niobium and red—oxygen.

5.2.4 The effect of octahedral distortions on ^{93}Nb C_Q

As discussed above, the choice of functional has a greater effect on the calculated magnetic shielding tensor through its effect on geometry optimisations than directly through the NMR calculations. Out of all the nuclei studied, the ^{93}Nb are the most sensitive. A similar sensitivity could be expected for the electric field gradient tensor, as has been alluded to in section 5.2.2, again particularly in the case of the ^{93}Nb nuclei. To a first approximation, it could be assumed that the ^{93}Nb C_Q values are most affected by the Nb nucleus's nearest neighbours. In this case, these are six oxygen atoms which, if not evenly spaced around the Nb atom, will produce an electric field gradient which in turn will interact with the quadrupole moment of the ^{93}Nb nucleus. Investigating the correlation between ^{93}Nb C_Q values and oxygen octahedral distortions provides insight into how the ^{93}Nb nuclei are affected by the arrangement of their nearest neighbours. This in turn provides valuable information for predicting and interpreting experimental ^{93}Nb NMR spectra.

Figure 5.11 shows ^{93}Nb C_Q plotted against the longitudinal and shear strain parameters—defined by equations 5.2 and 5.1—across the range of pure $LiNbO_3$, $NaNbO_3$ and $KNbO_3$ perovskite structures. The correlation between the longitudinal strain and ^{93}Nb C_Q values is positive and reasonably strong. By contrast, the correlation between the shear strain and ^{93}Nb C_Q values is much weaker, though it appears to be positive if each compound is considered separately.

Similar plots by Johnston *et al.* across a range of $NaNbO_3$ perovskite space groups display much weaker positive correlations [105]. This could be

due to the use of PBE instead of PBEsol for their structural relaxations. For the octahedral site in aluminosilicates, Ghose and Tsang have found that there is a strong positive correlation between ^{27}Al C_Qs and longitudinal strain, but that the correlation with shear strain is 'very poor' [93]. Similarly, the correlation between ^{25}Mg and shear strain has been shown to be poor, but that there is a reasonably strong positive correlation with longitudinal strain [128]. The correlation between ^{45}Sc and shear strain has also been shown to be poor [129]. Conversely, the correlation for ^{49}Ti has been shown to be poor with respect to longitudinal strain but reasonably strong and positive with respect to shear strain [130]. Owing to the extreme sensitivity of the octahedral arrangements to the parameters employed when optimising my niobate structures and the subsequent sensitivity of the ^{93}Nb C_Q values, it is likely that similar trends would be exhibited in the C_Q of other nuclei surrounded by oxygen octahedra. A degree of caution should therefore be taken in assigning too much validity to favourable comparisons between older results in the literature and up-to-date calculations.

Note too the range of octahedral strains calculated as a function of relaxation. This provides an indication of how much the geometry of the oxygen octahedra is changed as a result of structural relaxation and functional. The difference between the octahedral strains for the relaxed structures and the experimental structure is smaller when using PBEsol than PBE. Again this implies that PBEsol provides a better representation of the structure than PBE.

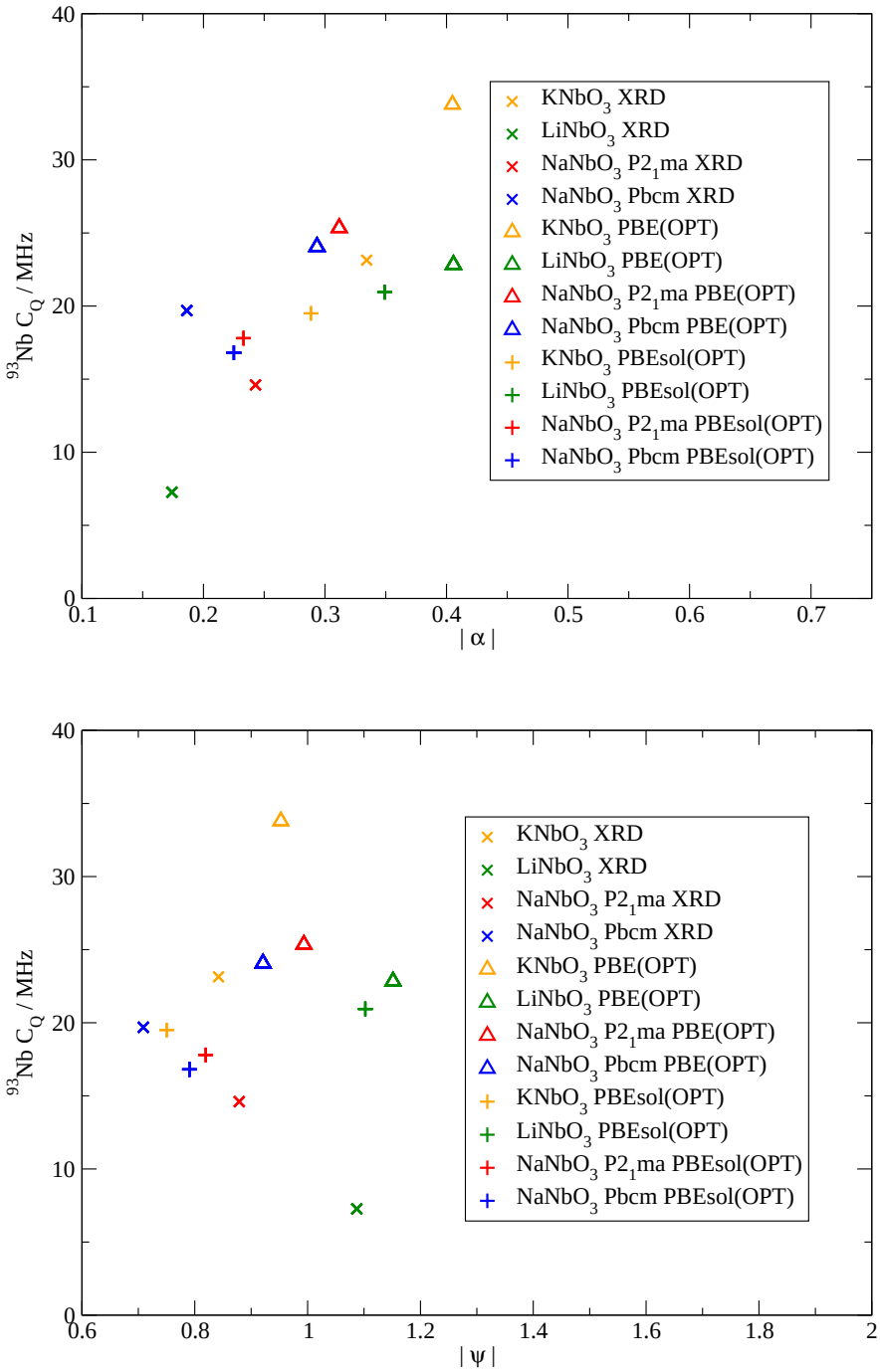

Figure 5.11: Plots of C_Q against the longitudinal strain $|\alpha|$ (top) and the shear strain $|\psi|$ (bottom). The C_Q values have all been calculated using PBEsol. Crosses denote the experimental structures (XRD), triangles—relaxations using PBE (PBE(OPT)), and plusses—relaxations using PBEsol (PBEsol(OPT)). Orange denotes $KNbO_3$, green—$LiNbO_3$, red—$NaNbO_3$ $P2_1ma$, and blue—$NaNbO_3$ $Pbcm$.

5.2.5 Conclusions for the pure perovskite structures

My calculations on the pure $NaNbO_3$, $LiNbO_3$ and $KNbO_3$ perovskite structures have shown that the NMR parameters for the ^{93}Nb nuclei are particularly sensitive to structural distortions, with the ^{17}O NMR parameters being the second most sensitive. The forces on the Nb and, to a lesser extent, the O atoms in the XRD structures were particularly large, and therefore the geometry optimisation calculations were dominated by subtle structural reconfigurations in the vicinity of the oxygen octahedra and the niobium atoms inside these octahedra. By examining both the geometries and the NMR parameters of the relaxed structures, it was found that PBEsol produced geometries which were closer to experiment than those produced using PBE. The calculated NMR parameters were correspondingly closer to experiment when using PBEsol than with PBE, particularly in the case of ^{93}Nb C_Q in $KNbO_3$ which was calculated as 34.2 MHz using PBE and 19.5 MHz with PBEsol compared to an experimentally measured value of 23.1 MHz. The trends in the calculated ^{23}Na δ_{iso} values across the two $NaNbO_3$ polymorphs were also closer to experiment when using PBEsol instead of PBE.

By examining the trends in σ_{iso} across the five nuclei in the XRD and PBE/PBEsol optimised structures, it was found that the differences in the calculated magnetic shielding between using PBE or PBEsol were more significantly affected by the initial changes in geometry due to relaxation than from the actual NMR calculation itself. Again, it was evident that the PBEsol functional produced more subtle geometrical changes when the structures were relaxed which resulted in smaller deviations in σ_{iso} from the σ_{iso} values calculated for the XRD structures.

Finally, the relationship between the ^{93}Nb C_Q values and the geometrical arrangements of the surrounding oxygen atoms was investigated. There is a fairly strong correlation with a positive gradient between ^{93}Nb C_Q and the longitudinal strain in the oxygen octahedra, however the correlation with shear strain is much weaker (still with a positive gradient). This implies that the electric field gradient experienced by a ^{93}Nb nucleus in these perovskites is strongly affected by the relative distances of the surrounding nearest neighbour oxygen atoms, but that any effects from torsions within the oxygen octahedra are much weaker or of longer range.

5.3 Calculations on disordered structures

Substituting an impurity atom into the pure ordered perovskite structures introduces a degree of disorder. In this section we investigate the relationship between this disorder and the structure's NMR parameters. The disordered systems investigated are a set of solid solutions related to the pure perovskites previously discussed: $Na_xK_{1-x}NbO_3$, $K_xNa_{1-x}NbO_3$ and $Li_xNa_{1-x}NbO_3$. In cases where the main structure is $NaNbO_3$, the *Pbcm* polymorph has been used. Having concluded that the PBEsol functional produces better representations of the pure perovskite structures than those produced with PBE, and that the agreement of the calculated ^{93}Nb NMR parameters (which are extremely sensitive to geometrical distortions) to measured values is much improved, all calculations in this section have been performed with the PBEsol functional.

Models of solid solutions with differing concentrations have been constructed using a range of supercell sizes formed from the PBEsol-optimised pure unit cells studied above. The impurity atom was then substituted onto

a suitable Na/K site and the structure relaxed before calculating the NMR parameters. All calculations were performed with a planewave cut-off of 800 eV, and a **k**-point spacing of $0.04\times2\pi$Å^{-1}. The tolerances employed for structural relaxation were the same as those used for the pure structures.

Figure 5.12 shows an example relaxed supercell structure, in this case a 2×2×2 $KNbO_3$ supercell in which the K atom closest to the origin has been replaced with a Na atom. Table 5.12 lists the different structures studied in this section alongside their equivalent molar concentrations.

Supercell size	No. 'A' sites	Molar conc./%
1Na-$KNbO_3$		
primitive	1	100
1×1×1	2	50
2×1×1	4	25
2×2×1	8	12.5
2×2×2	16	6.25
3×2×2	24	4.17
2Na-$KNbO_3$		
2×2×2	16	12.5
1K-$NaNbO_3$ and 1Li-$NaNbO_3$ (*Pbcm*)		
1×1×1	8	12.5
1×2×1	16	6.25
2×2×1	32	3.13
2×3×1	48	2.08

Table 5.12: Summary of the supercell structures investigated and their corresponding impurity concentrations.

5.3.1 $KNbO_3$ with one Na substituted for one K (1Na-$KNbO_3$)

The 1Na-$KNbO_3$ supercells were constructed by substituting a Na atom onto the K site closest to the origin as shown in figure 5.12.

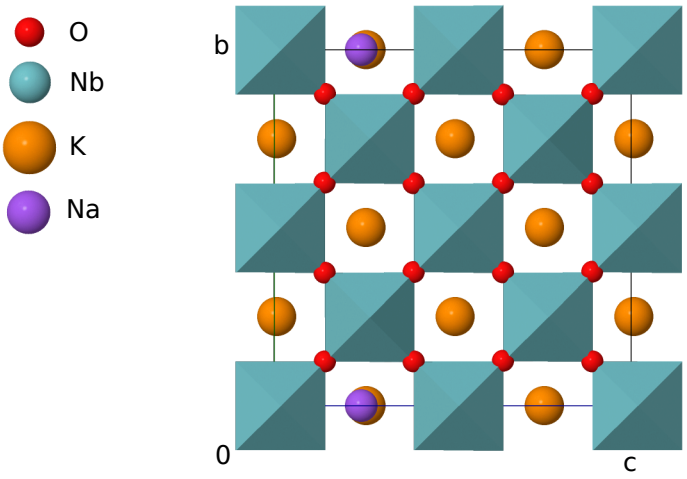

Figure 5.12: The PBEsol-relaxed structure for the 2×2×2 1Na-$KNbO_3$ supercell.

Behaviour of ^{23}Na

The ^{23}Na isotropic magnetic shielding, σ_{iso}, varies by only 0.7 ppm across the supercell sizes investigated, as shown in table 5.13. This indicates that ^{23}Na σ_{iso} is relatively insensitive to the separation between Na atoms and implies that ^{23}Na NMR is not a good probe of the level of Na doping in $KNbO_3$. However, the ^{23}Na σ_{iso} value of 577 ppm differs by 10–15 ppm from the equivalent ^{23}Na resonances in the pure $NaNbO_3$ polymorphs.[5] This implies that, whilst ^{23}Na NMR cannot be used to finely measure the Na concentration, it can be used to investigate whether the Na concentration is low enough that the overall structure is based on $KNbO_3$.

The ^{23}Na C_Q values are small, of the order of tens of kHz, in contrast to ^{23}Na C_Q in the pure $NaNbO_3$ polymorphs which were generally of the order of MHz. However, in comparison to the ^{39}K C_Q values in pure $KNbO_3$ the ^{23}Na values are generally an order of magnitude larger.

[5]For comparison, the PBEsol ^{23}Na σ_{iso} values for $NaNbO_3$ *Pbcm* are 562.5 ppm and 566.5 ppm, and for $P2_1ma$ 562.7 ppm and 567.2 ppm.

Note also the entries for the 'primitive' cell in table 5.13. This cell has only one Na, one Nb and three O nuclei. The cell therefore contains no K nuclei but it still exhibits a pure $KNbO_3$ structure. The value of ^{23}Na σ_{iso} for the relaxed primitive cell is the same as that for the supercells (i.e. 577 ppm), implying that the magnetic shielding for Na is not affected by the presence of K nuclei.

Supercell size	^{23}Na σ_{iso}/ppm	^{23}Na $\lvert C_Q\rvert$/MHz	η_Q	Na–Na separation/Å
primitive	577.4	0.32	0.38	3.91
1×1×1	577.1	0.41	0.37	3.94
2×1×1	577.8	0.39	0.29	5.66
2×2×1	577.8	0.09	0.17	5.69
2×2×2	577.5	0.18	0.88	7.93
3×2×2	577.3	0.22	0.62	11.34

Table 5.13: Table showing the calculated ^{23}Na isotropic magnetic shielding, σ_{iso}, with nearest neighbour Na-Na separation in 1Na-$KNbO_3$. All structures were relaxed with PBEsol before σ_{iso} was calculated, also with PBEsol.

Behaviour of ^{39}K, ^{93}Nb and ^{17}O

Figures 5.13 and 5.14 show values of σ_{iso} for ^{39}K, ^{93}Nb and ^{17}O as a function of distance from the Na impurity. As the separation between the K/Nb/O and Na nuclei increases, the σ_{iso} values tend to the equivalent values for pure $KNbO_3$. 'Pure' σ_{iso} values are observed to within ∼3 ppm at separations of at least 6.5 Å. A similar trend is also observed with the ^{93}Nb C_Q values, shown in figure 5.14. However the decay to the 'pure' value is not as rapid as it is for σ_{iso}, with there still being a reasonable spread in C_Q values at the largest separation.

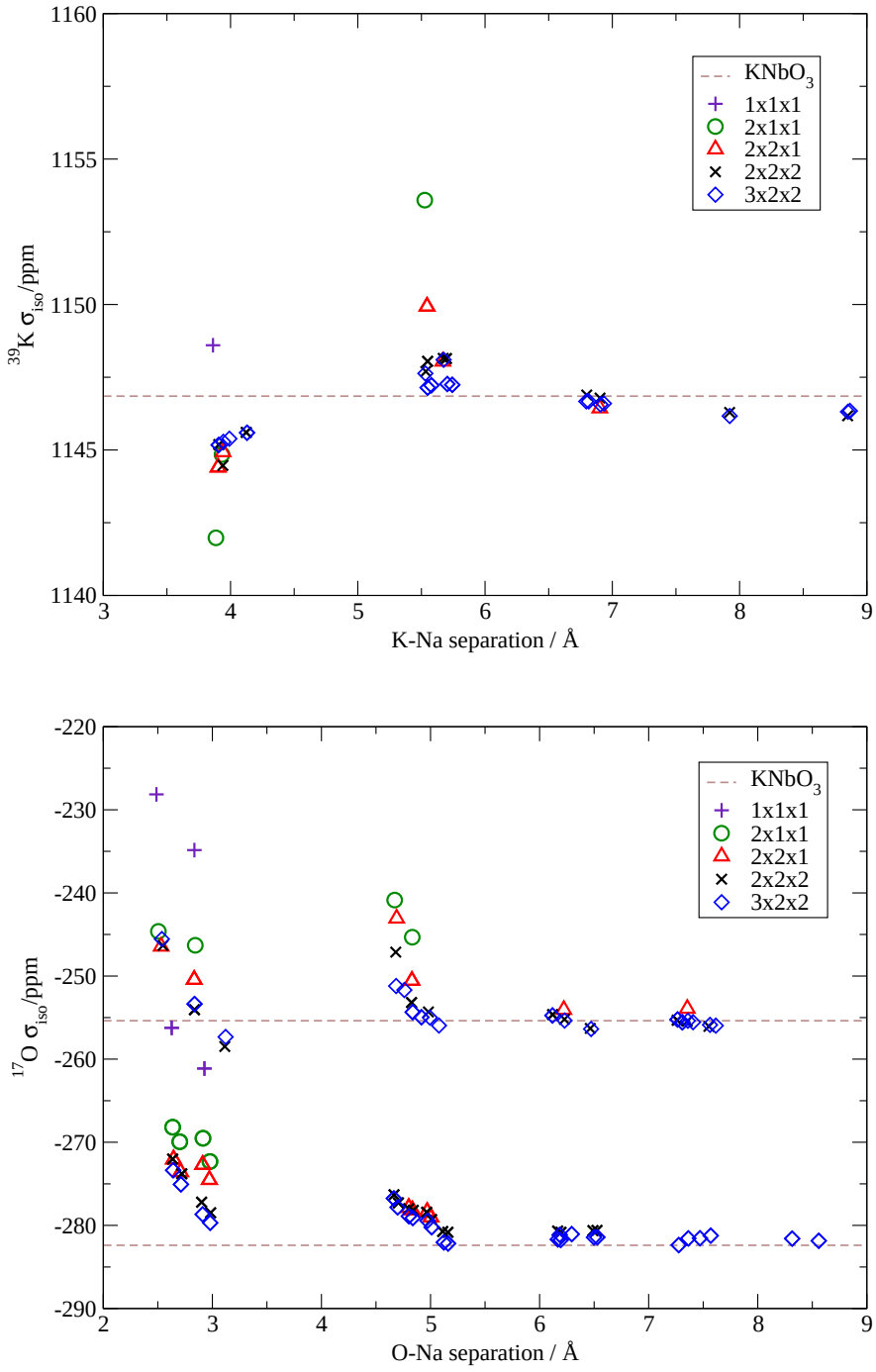

Figure 5.13: The value of ^{39}K σ_{iso} (top) and ^{17}O σ_{iso} (bottom) as a function of separation from the Na impurity for the set of relaxed 1Na-$KNbO_3$ supercells. The dotted lines denote equivalent ^{39}K and ^{17}O σ_{iso} values in pure relaxed $KNbO_3$ (top and bottom figures respectively).

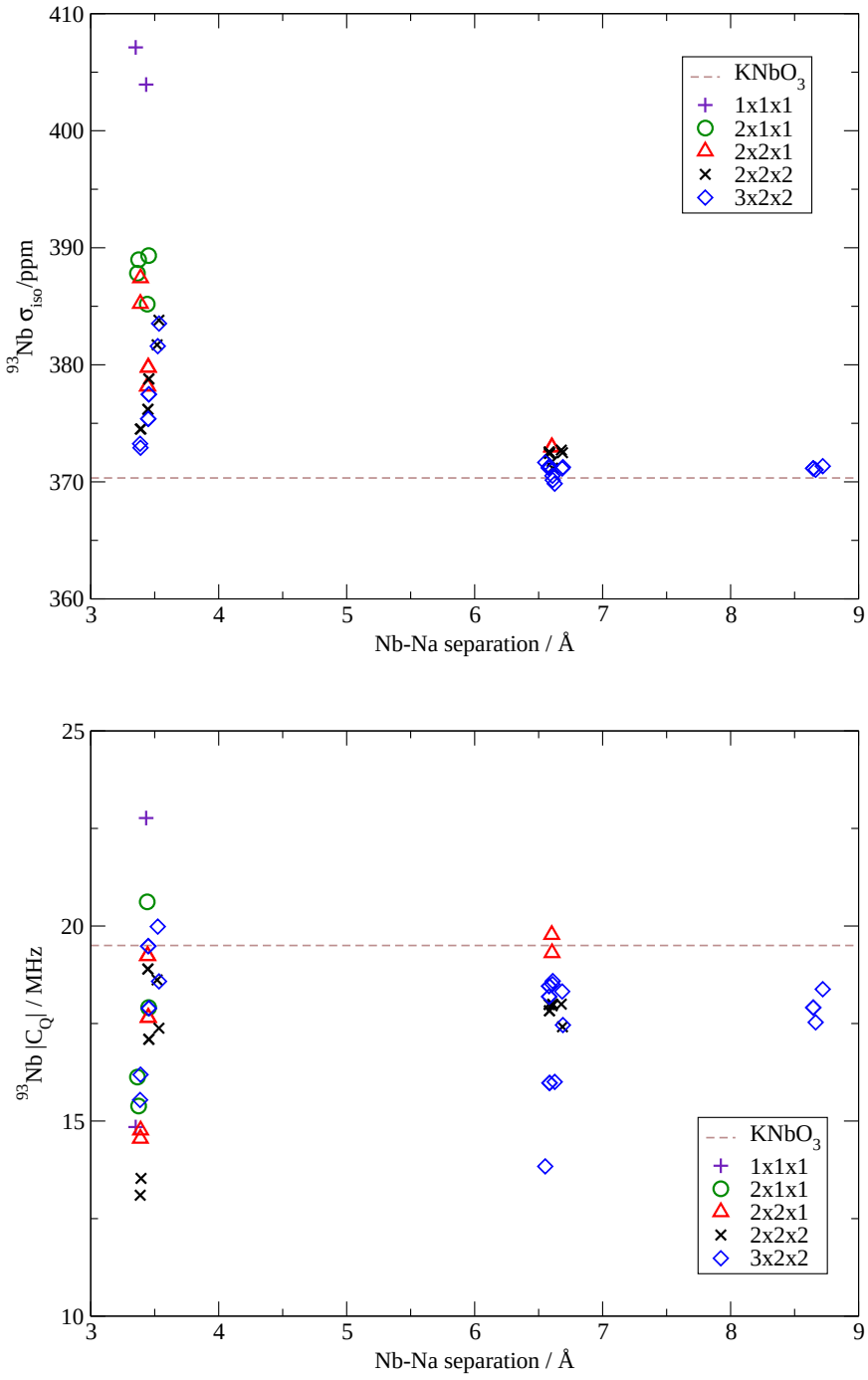

Figure 5.14: The value of ^{93}Nb σ_{iso} (top) and ^{93}Nb $|C_Q|$ (bottom) as a function of separation from the Na impurity for the set of relaxed 1Na-$KNbO_3$ supercells. The dotted lines denote equivalent ^{93}Nb σ_{iso} and $|C_Q|$ values in pure relaxed $KNbO_3$ (top and bottom figures respectively).

The effect of oxygen octahedral distortions on Nb

As was the case for the pure $KNbO_3$, $NaNbO_3$ and $LiNbO_3$ structures, the ^{93}Nb C_Q values in the 1Na-$KNbO_3$ supercells will be affected by the subtle structural distortions of the surrounding oxygen atoms. Figure 5.15 shows the correlations between ^{93}Nb C_Q and the longitudinal and shear strains in the surrounding oxygen octahedra. For small supercells (i.e. those with a high Na concentration), the correlation between C_Q and the longitudinal strain is negative. Supercells with a Na concentration below 6.25% (i.e. the 2×2×2 and 3×2×2 supercells) display a positive correlation, as was also observed for the pure structures in section 5.2.4. The correlations between C_Q and the shear strain are negative across all supercells, although for the largest supercell the line of best fit is almost horizontal. By contrast, the correlations for the shear strain in the pure structures were positive, albeit fairly weak. It can also be seen that there is considerable scatter about the lines of best fit in both figures.

These trends can be explained if the distortion parameters are considered as a function of distance from the impurity Na atom, as shown in figure 5.16. Both $|\alpha|$ and $|\psi|$ tend to their equivalent values in pure $KNbO_3$ with increasing Na–Nb separation. The scatter about the lines of best fit in figure 5.15 can therefore be explained by the increasing number of environments in which the Nb nuclei are situated as the supercell size increases. The increasing number of Nb nuclei in a comparatively 'pure' $KNbO_3$ environment with increasing supercell size also explains why the correlations of C_Q with $|\alpha|$ and $|\psi|$ tend towards those of 'pure' $KNbO_3$ with increasing supercell size (although this trend is less pronounced for $|\psi|$).

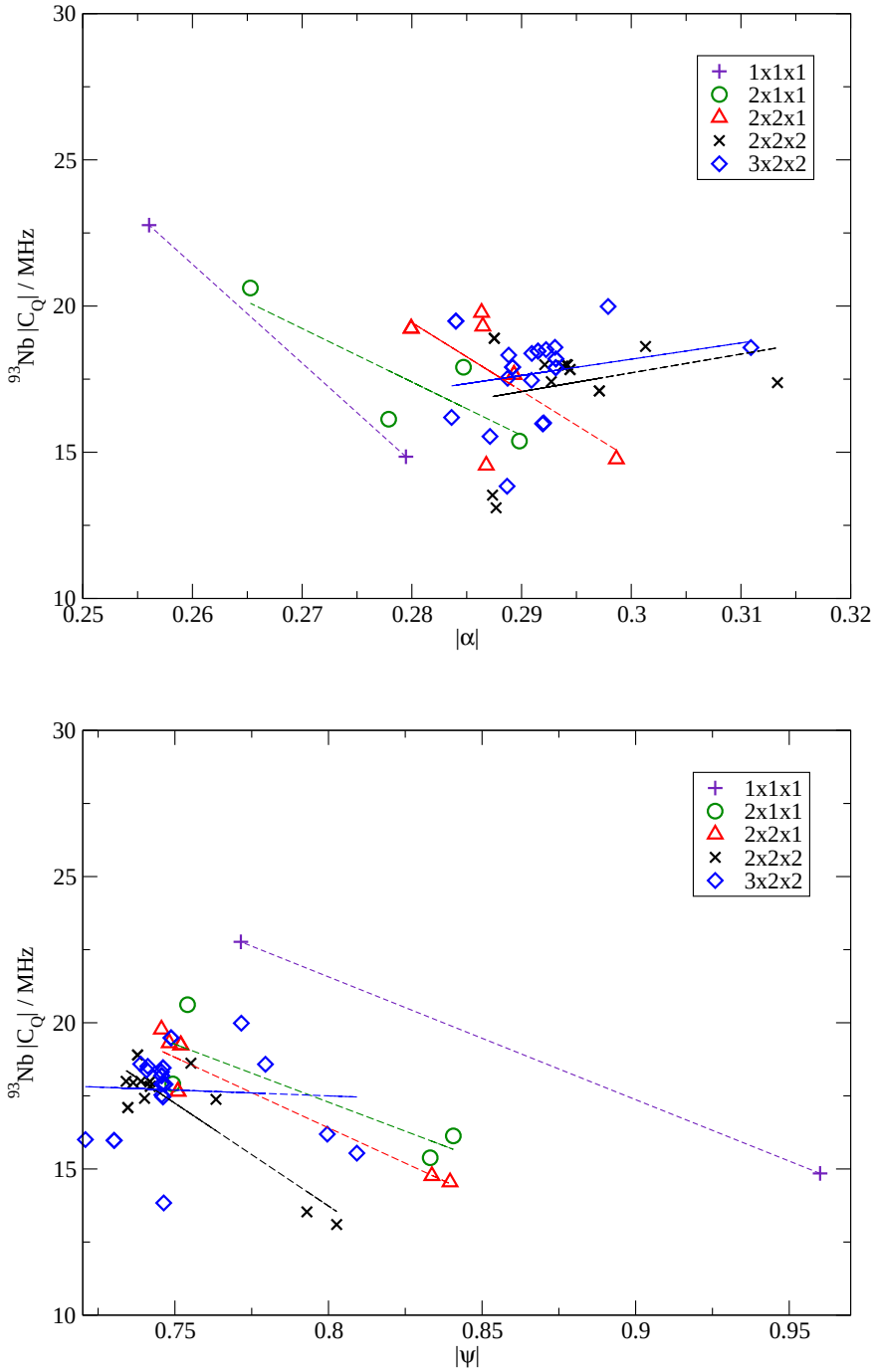

Figure 5.15: The correlation between ^{93}Nb $|C_Q|$ and the longitudinal strain $|\alpha|$ (top) and the shear strain $|\psi|$ (bottom) of the oxygen octahedra in the relaxed 1Na-$KNbO_3$ supercells. The straight lines are lines of best fit.

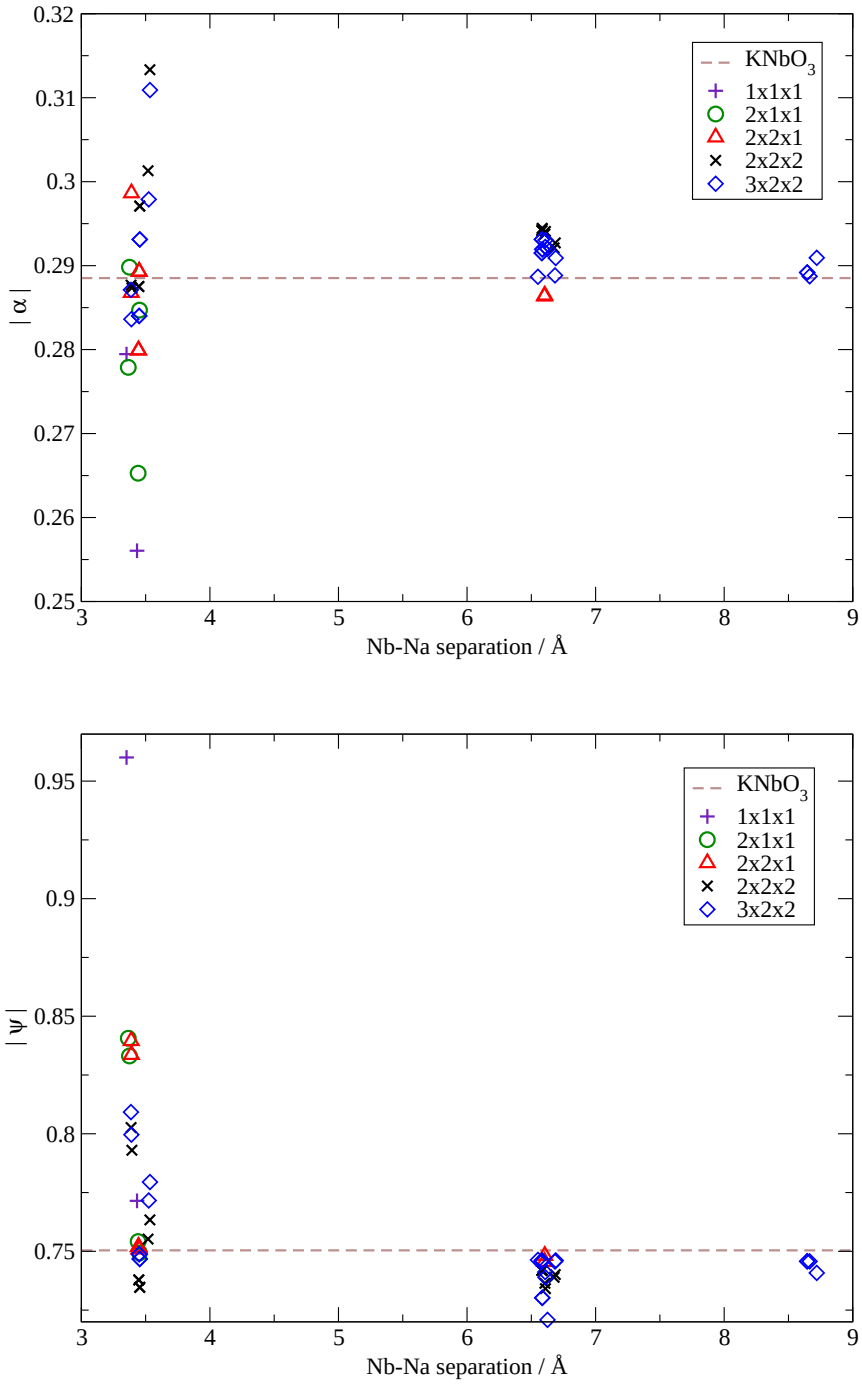

Figure 5.16: The longitudinal strain $|\alpha|$ (top) and the shear strain $|\psi|$ (bottom) of the oxygen octahedra as a function of distance between the Nb atom inside the oxygen octahedron and the impurity Na atom for the 1Na-$KNbO_3$ supercells. The dotted lines show the equivalent $|\alpha|$ and $|\psi|$ values in pure $KNbO_3$ (top and bottom figures respectively).

5.3.2 $KNbO_3$ with two Na atoms substituted for two K atoms (2Na-$KNbO_3$)

The 1Na-$KNbO_3$ structures simulate a solid-solution in which the impurity Na atoms are uniformly distributed throughout the structure. In reality this will not be the case. A second Na atom was therefore substituted into the 2×2×2 1Na-$KNbO_3$ supercell on a variety of K sites in order to simulate a degree of non-uniformity. These structures were then relaxed using PBEsol, a planewave cut-off of 800 eV and a **k**-point sampling of $0.04\times2\pi$Å^{-1}. The resulting set of relaxed structures, denoted 'a'–'g', is shown in figure 5.17.

Figures 5.18, 5.19 and 5.20 show the change in NMR parameters as a function of distance from the nearest neighbour Na atom.[6] The 2×2×1 1Na-$KNbO_3$ supercell contains the same 12.5% molar Na concentration as the 2Na-$KNbO_3$ structures. The relevant 1Na-$KNbO_3$ NMR parameters have therefore been included in the 2Na-$KNbO_3$ figures. Structure 'f' contains the same arrangement of Na atoms as the 2×2×1 1Na-$KNbO_3$ structure, however with twice as many atoms in the unit cell. Having relaxed the structures, a degree of periodicity is therefore removed from structure 'f' as a result of there being two 1Na-$KNbO_3$ unit cells in the supercell. Nevertheless the σ_{iso} values for ^{39}K, ^{17}O, and ^{93}Nb coincide quite well between the 1Na-$KNbO_3$ 2×2×1 and 'f' structures. The only notable discrepancy is in the ^{93}Nb C_Q values at ∼6.6 Å where there is a difference of ∼3 MHz. The overall decay of values with increasing separation is similar to that for the 1Na-$KNbO_3$ supercells. By a separation of 6.5 Å the σ_{iso} values for ^{39}K are within ∼1 ppm of the pure $KNbO_3$ value, for ^{93}Nb they are within ∼6 ppm and for

[6] There are two possible Na–K/O/Nb/Na separations per K/O/Nb/Na atom because there are two Na atoms per unit cell. The larger separation has therefore been neglected even in the cases where the K/O/Nb atom is approximately equidistant from both Na atoms.

^{17}O they are within ∼2.5 ppm. The ^{93}Nb C_Q values decay more slowly, as also observed for the 1Na-$KNbO_3$ supercells, and are within ∼5 MHz by a separation of 6.5 Å.

The range of ^{23}Na σ_{iso} values, shown in figure 5.18, is greater than in 1Na-$KNbO_3$. Whereas the range across the 1Na-$KNbO_3$ structures was 0.7 ppm, in the case of the 2Na-$KNbO_3$ structures, the range is ∼2.2 ppm.

Figure 5.21 shows the ^{93}Nb C_Q values as a function of longitudinal and shear strains in the surrounding oxygen octahedra. The equivalent values for the 1Na-$KNbO_3$ 2×2×1 supercell are also included. These values do not coincide with the equivalent values for structure 'f'. This implies that the reduced periodicity in structure 'f' compared to in the 1Na-$KNbO_3$ 2×2×1 structure increases the allowed range of octahedral distortions in the structure. The correlations are also much weaker for the 2Na-$KNbO_3$ structures in comparison to the 1Na-$KNbO_3$ structures. The correlation with respect to shear strain is negative, whilst the equivalent for longitudinal strain is weakly positive in most structures.

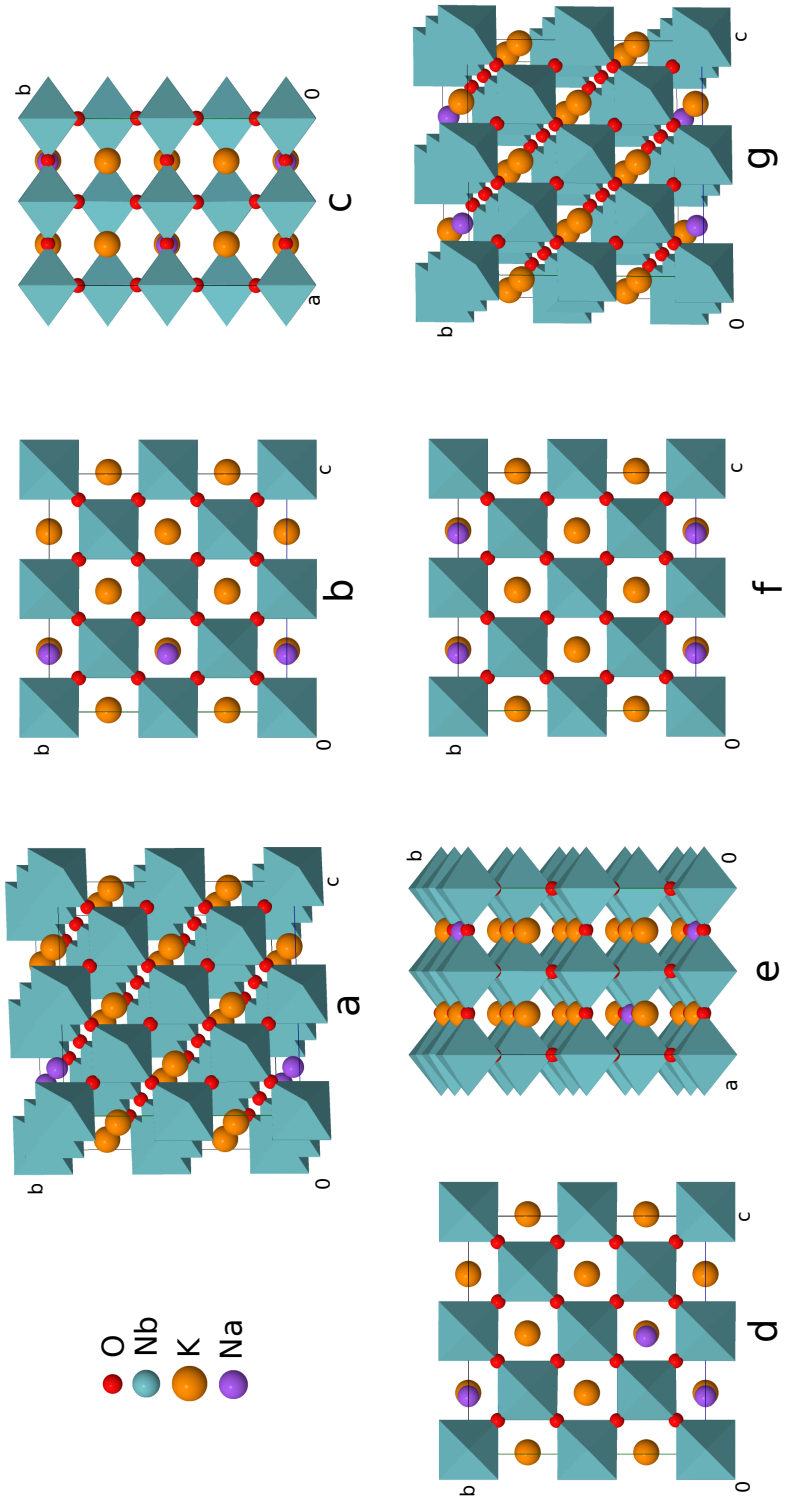

Figure 5.17: The PBEsol relaxed set of 2Na-$KNbO_3$ structures, labelled a–g.

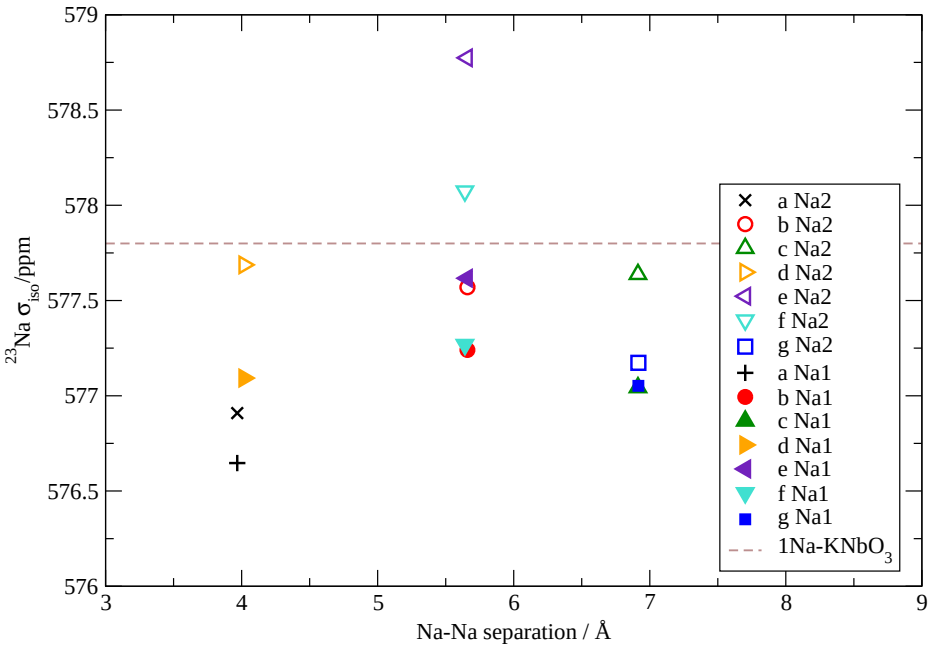

Figure 5.18: ^{23}Na σ_{iso} as a function of Na–Na separation in the 2Na-$KNbO_3$ supercells. The brown dotted line shows the equivalent ^{23}Na σ_{iso} value in the 1Na-$KNbO_3$ 2×2×1 supercell.

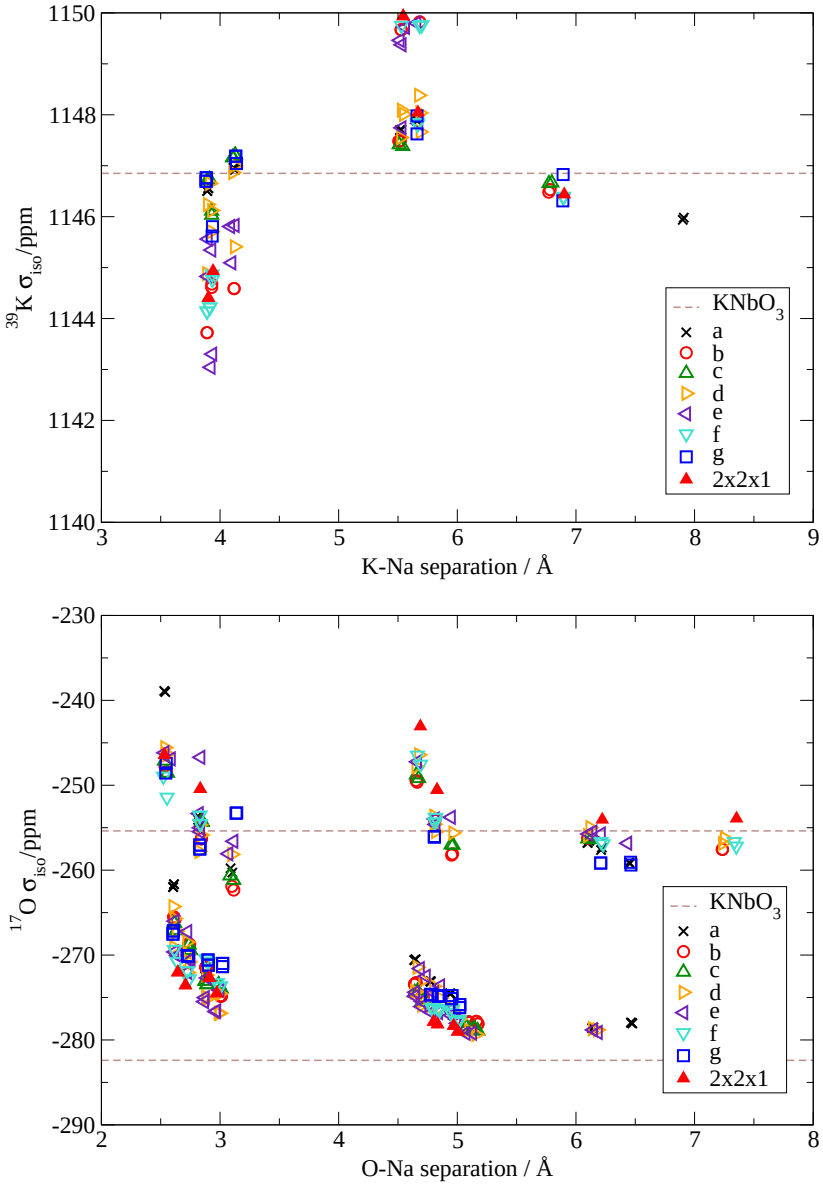

Figure 5.19: ^{39}K σ_{iso} (top) and ^{17}O σ_{iso} (bottom) as a function of Na–Na separation in the 2Na-$KNbO_3$ supercells. The brown dotted lines show the equivalent ^{39}K σ_{iso} and ^{17}O σ_{iso} values in pure $KNbO_3$ (top and bottom figures respectively) and the filled red triangles show the equivalent data for the 1Na-$KNbO_3$ 2×2×1 supercell.

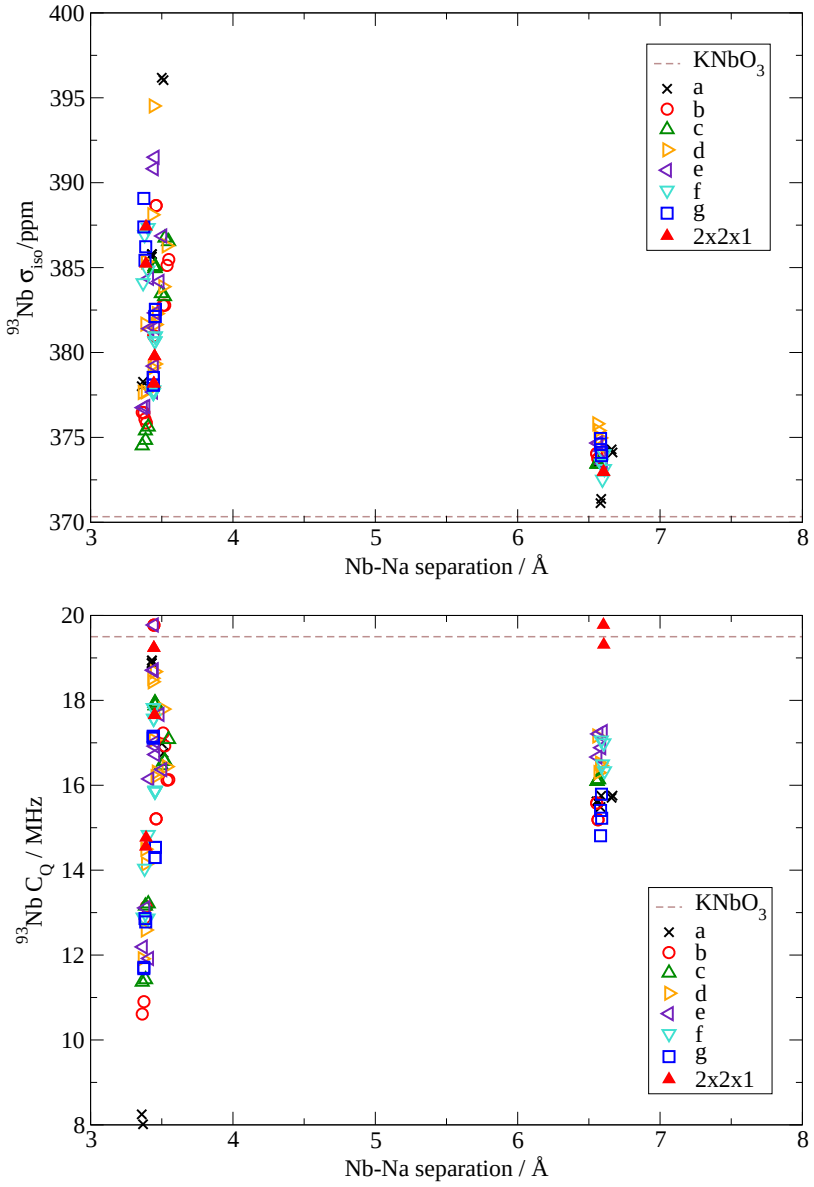

Figure 5.20: ^{93}Nb σ_{iso} (top) and $|C_Q|$ (bottom) as a function of Nb–Na separation in the 2Na-KNbO$_3$ supercells. The brown dotted lines shows the equivalent ^{93}Nb σ_{iso} and $|C_Q|$ values (top and bottom figures respectively) in pure KNbO$_3$ and the filled red triangles show the equivalent data for the 1Na-KNbO$_3$ 2×2×1 supercell.

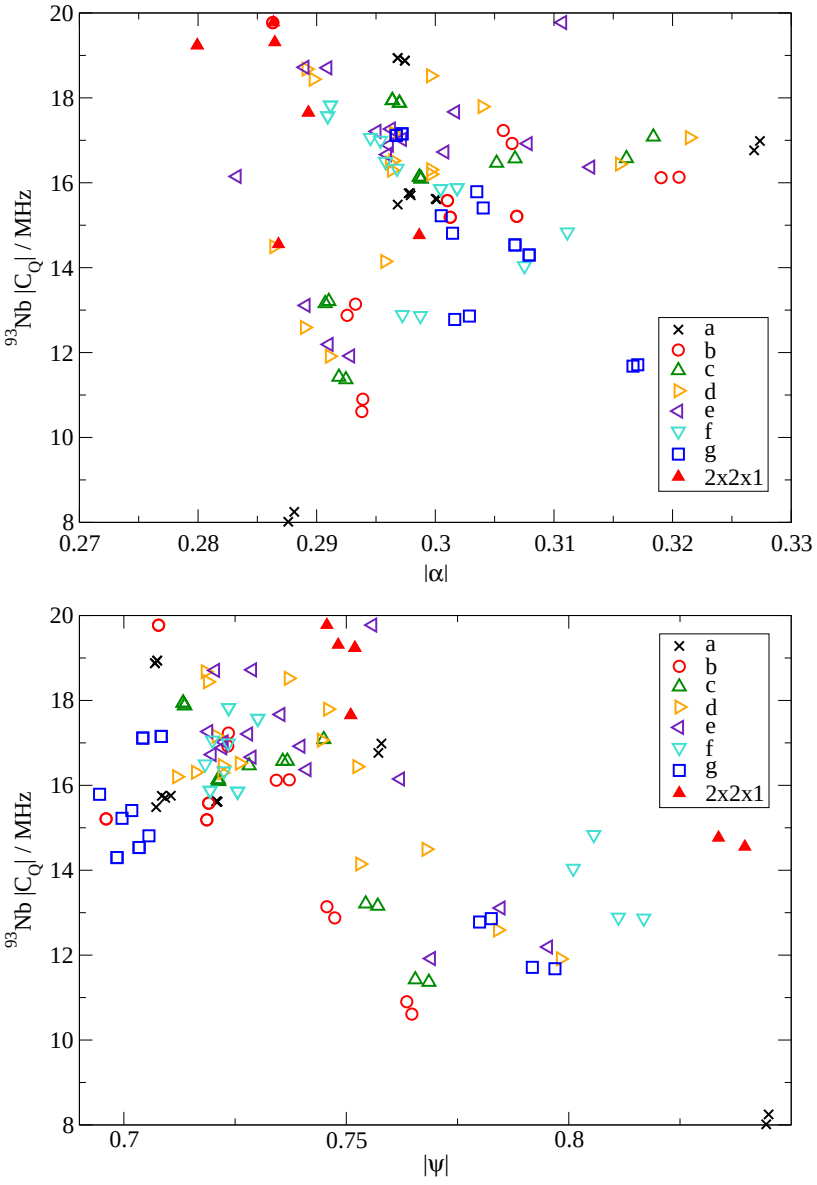

Figure 5.21: ^{93}Nb C_Q as a function of longitudinal strain $|\alpha|$ (top) and shear strain $|\psi|$ (bottom) of the surrounding oxygen octahedra in the 2Na-$KNbO_3$ supercells. The filled red triangles show the equivalent 1Na-$KNbO_3$ 2×2×1 values for comparison.

5.3.3 1K-$NaNbO_3$-*Pbcm* and 1Li-$NaNbO_3$-*Pbcm*

Previous investigations of $K_xNa_{1-x}NbO_3$ and $Li_xNa_{1-x}NbO_3$ in the literature have already been outlined in section 5.1.2. It was found that doping *Pbcm*-$NaNbO_3$ with more than 2% Li or K produced a $P2_1ma$ structure. I have therefore substituted Li and K atoms into supercells of *Pbcm*-$NaNbO_3$ across a concentration range of 2.1%–12.5% as outlined in table 5.12.

From section 5.2.2, it can be seen that there are two Na atomic environments, therefore the effect of substituting a Li or K atom for a Na atom is expected to be dependent on the substitution site. Figure 5.22 shows the substitution of a K atom in four different places: two in one chemical environment, two in another. Table 5.15 shows the ^{39}K σ_{iso} and C_Q values for each of these four sites. As expected, the 'A' and 'B' sites are almost equivalent, and the same is true for the 'C' and 'D' sites. For simplicity, all subsequent structures in this section involve the K or Li impurity atom being substituted onto the 'A' site. In the supercells this corresponds to the 'A' site that is closest to the origin.

Geometry optimisations

Upon relaxation with PBEsol, none of the structures became $P2_1ma$ in contrast to experimental observations. The degree of structural distortion in the oxygen octahedra could however be seen to increase, particularly in the vicinity of the impurity atom. The supercells also all became slightly monoclinic upon relaxation. In the 1K-$NaNbO_3$ structures, the angle α decreased from 90° upon relaxation, whereas in the 1Li-$NaNbO_3$ structures α became larger than 90°. The change in α ranged from 89.87° in the 1×1×1 1K-$NaNbO_3$ structure to 90.34° in the 1×1×1 1Li-$NaNbO_3$ structure. The

degree of distortion was greatest in the 1×1×1 unit cells and decreased with increasing supercell size. Experimentally, monoclinic phases have been observed in $K_xNa_{1-x}NbO_3$ solid solutions for concentrations of K up to 30% [109].

NMR parameters

The ^{17}O σ_{iso} values appear to tend towards their pure $NaNbO_3$ *Pbcm* equivalents with increasing separation from the impurity atom, as shown in figures 5.23 and 5.26. A similar trend is observed for the ^{93}Nb σ_{iso} and C_Q values (figures 5.24 and 5.27), although ^{93}Nb σ_{iso} may be tending towards a value approximately 2.5 ppm lower than that in pure $NaNbO_3$ with increasing Nb-K separation. Larger supercells would be required to investigate this further.

In the 1K-$NaNbO_3$ structures, the ^{23}Na σ_{iso} values appear to be tending towards values that are 0.7–0.9 ppm lower than the pure $NaNbO_3$ values (figure 5.23). In the 1Li-$NaNbO_3$ structures the effect is even more noticeable, with ^{23}Na σ_{iso} values being 1.5–1.8 ppm below the pure equivalent (figure 5.26). This suggests that doping *Pbcm* $NaNbO_3$ with Li and K has an experimentally measurable effect on ^{23}Na NMR spectra. Table 5.14 shows the ^{23}Na experimental chemical shifts for a pure $NaNbO_3$ sample and a solid solution of $Li_{0.3}Na_{0.7}NbO_3$, both assigned as phase $P2_1ma$. The difference in the chemical shifts between the Na sites with similar quadrupolar products (P_Q) is 0.5–0.8 ppm (±1 ppm if experimental errors are taken into account). The shift in the calculated ^{23}Na σ_{iso} values in 1Li-$NaNbO_3$, albeit in the context of a *Pbcm* structure, may be linked to this experimental observation.

Whilst the ^{23}Na NMR parameters in 1Na-$KNbO_3$ were independent of

Sample		δ_{iso}/ppm	P_Q/MHz
Exp2 *Pbcm* [83]	Na1	-0.5(5)	2.1(1)
Exp2 *Pbcm* [83]	Na2	-4.2(5)	1.2(2)
Exp2 $P2_1ma$ [83]	Na1	-1.4(5)	2.4(1)
Exp2 $P2_1ma$ [83]	Na2	-5.1(5)	1.2(2)
$Li_{0.3}Na_{0.7}NbO_3$ $P2_1ma$ [102]	Na1	-4.6(5)	1.1(1)
$Li_{0.3}Na_{0.7}NbO_3$ $P2_1ma$ [102]	Na2	-0.6(5)	2.3(1)

Table 5.14: Experimental ^{23}Na chemical shifts for a pure mixed-phase $NaNbO_3$ sample and a 3% Li-$NaNbO_3$ sample of phase $P2_1ma$. The pure $NaNbO_3$ measurements are the same as presented in tables 5.5 and 5.6, and labelled 'Exp2'. All chemical shifts have been measured with respect to 1 M $NaCl_{(aq)}$ and a secondary reference of $NaCl_{(s)}$ (with $\delta_{iso} = 7.8$ ppm).

supercell size, this is not the case for K in *Pbcm*-$NaNbO_3$, where ^{39}K σ_{iso} varies by up to 7.9 ppm (shown in table 5.16). In the case of Li in *Pbcm* $NaNbO_3$, ^{7}Li σ_{iso} varies across a smaller range of 1.1 ppm across the supercells studied (shown in table 5.17). These changes in σ_{iso} may be experimentally measurable, implying that ^{39}K, and to a lesser extent ^{7}Li, are potential probes for $NaNbO_3$ doping.

The correlations between ^{93}Nb C_Q values and the octahedral strains all have a firmly positive gradient (figures 5.25 and 5.28). By contrast, the shear strains for the disordered $KNbO_3$ structures have a generally negative gradient whilst those for the pure structures were positive. The greater the concentration of impurity atoms, the greater the deviation from the trends identified in the pure structure. The *Pbcm* $NaNbO_3$ has eight oxygen octahedra in the 1×1×1 unit cell, whereas the $KNbO_3$ 1×1×1 unit cell has only two. Therefore the disordered *Pbcm* $NaNbO_3$ supercells studied generally contain lower impurity concentrations than the 1Na-$KNbO_3$ supercells. It is therefore not surprising that the 1Li-$NaNbO_3$ and 1K-$NaNbO_3$ $|C_Q|$–strain correlations are closer to the pure structure correlations than those of the

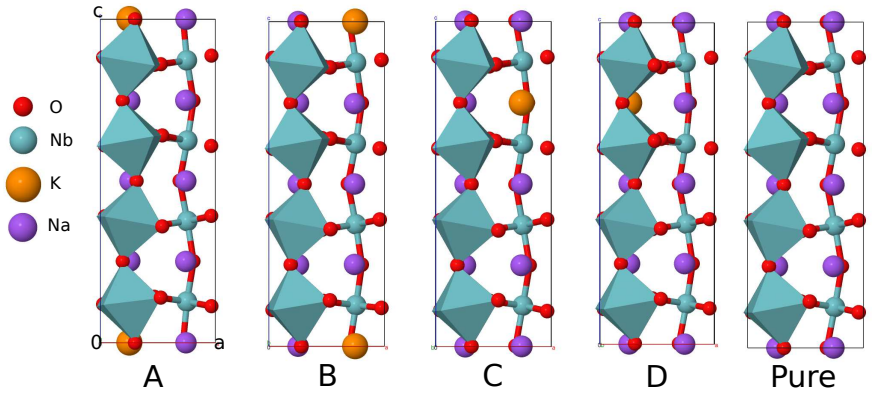

Figure 5.22: Four 1K-$NaNbO_3$ *Pbcm* structures in which the K atom is substituted onto four different sites. The pure $NaNbO_3$ *Pbcm* structure is included for comparison. All structures have been relaxed with PBEsol.

K position	σ_{iso}/ppm	$\lvert C_Q \rvert$/MHz
A	1123.1	1.740
B	1122.9	1.740
C	1128.4	0.982
D	1128.5	1.005

Table 5.15: The ^{39}K σ_{iso} and $\lvert C_Q \rvert$ values for one K substituted in turn onto a different Na site in 1K-$NaNbO_3$ *Pbcm* as shown in figure 5.22.

1Na-$KNbO_3$ structures.

Nevertheless, as was the case for the pure perovskites and disordered $KNbO_3$ structures, the correlations with longitudinal strain are stronger than those with shear strain, implying that the longitudinal distortions in the oxygen octahedra have a greater effect on the EFG experienced by the ^{93}Nb nuclei than the shear strains do. The equivalent C_Q–strain values for pure *Pbcm* $NaNbO_3$ also lie on, or very close to, the lines of best fit.

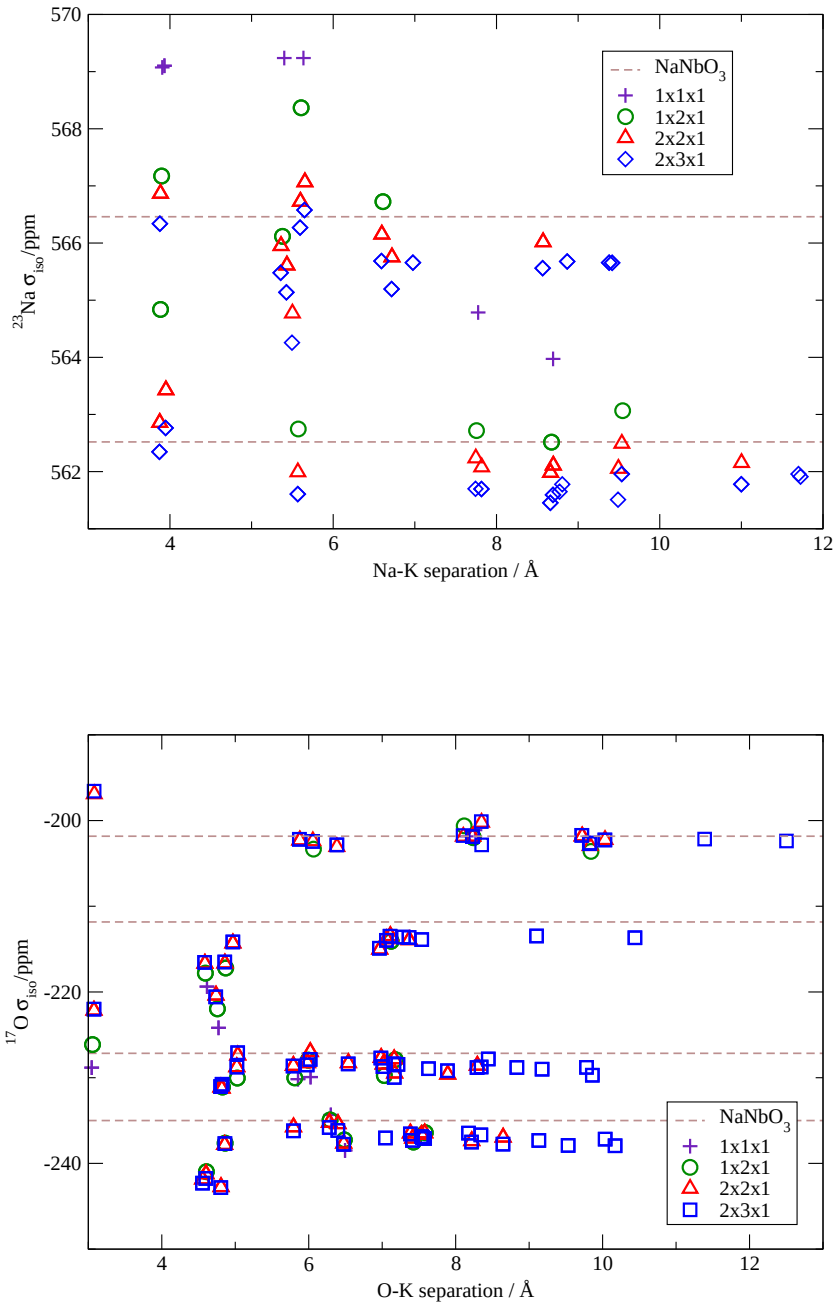

Figure 5.23: ^{23}Na σ_{iso} (top) and ^{17}O σ_{iso} (bottom) as a function of separation from the impurity K atom in the 1K-$NaNbO_3$ supercells. The brown dotted lines show the equivalent σ_{iso} values in pure *Pbcm* $NaNbO_3$.

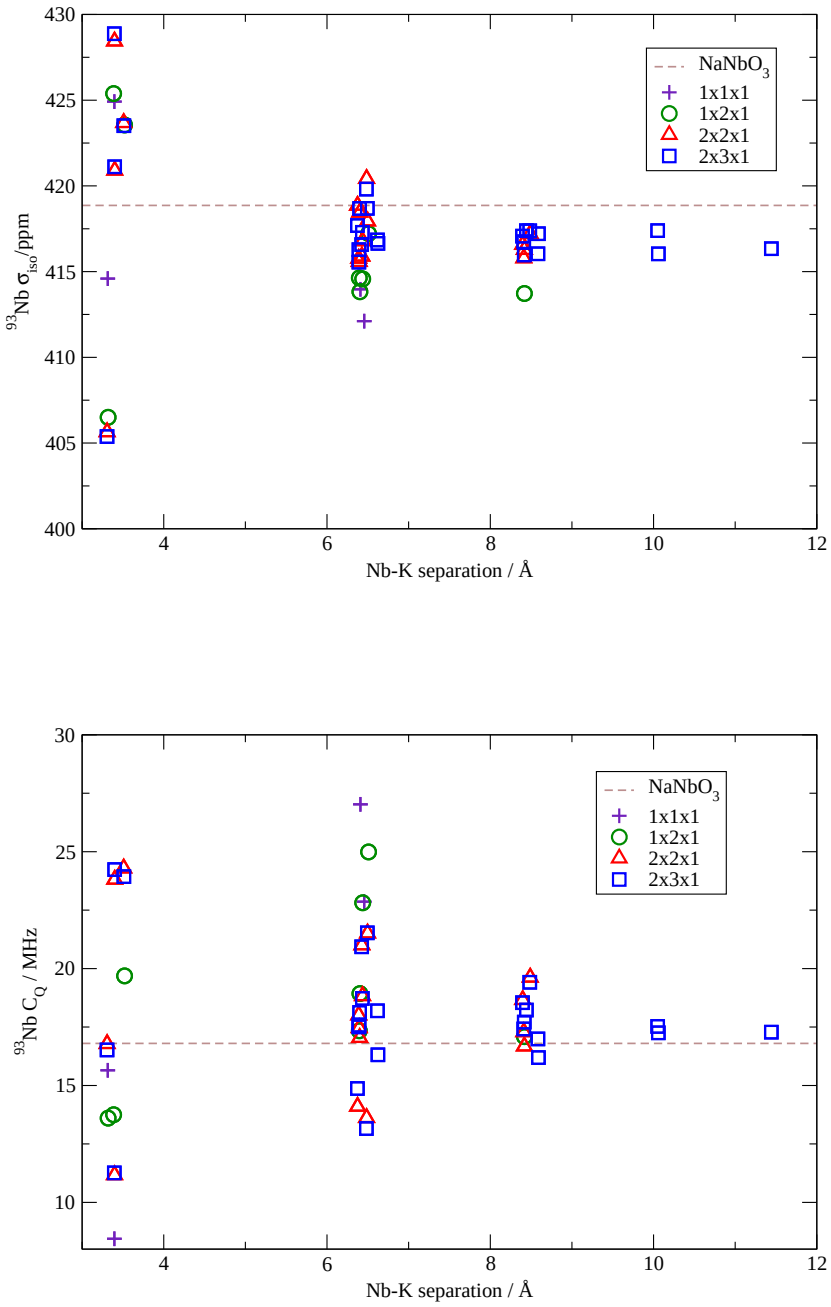

Figure 5.24: ^{93}Nb σ_{iso} (top) and $|C_Q|$ (bottom) as a function of Nb–K separation in the 1K-$NaNbO_3$ supercells. The brown dotted lines show the equivalent ^{93}Nb values in pure *Pbcm* $NaNbO_3$.

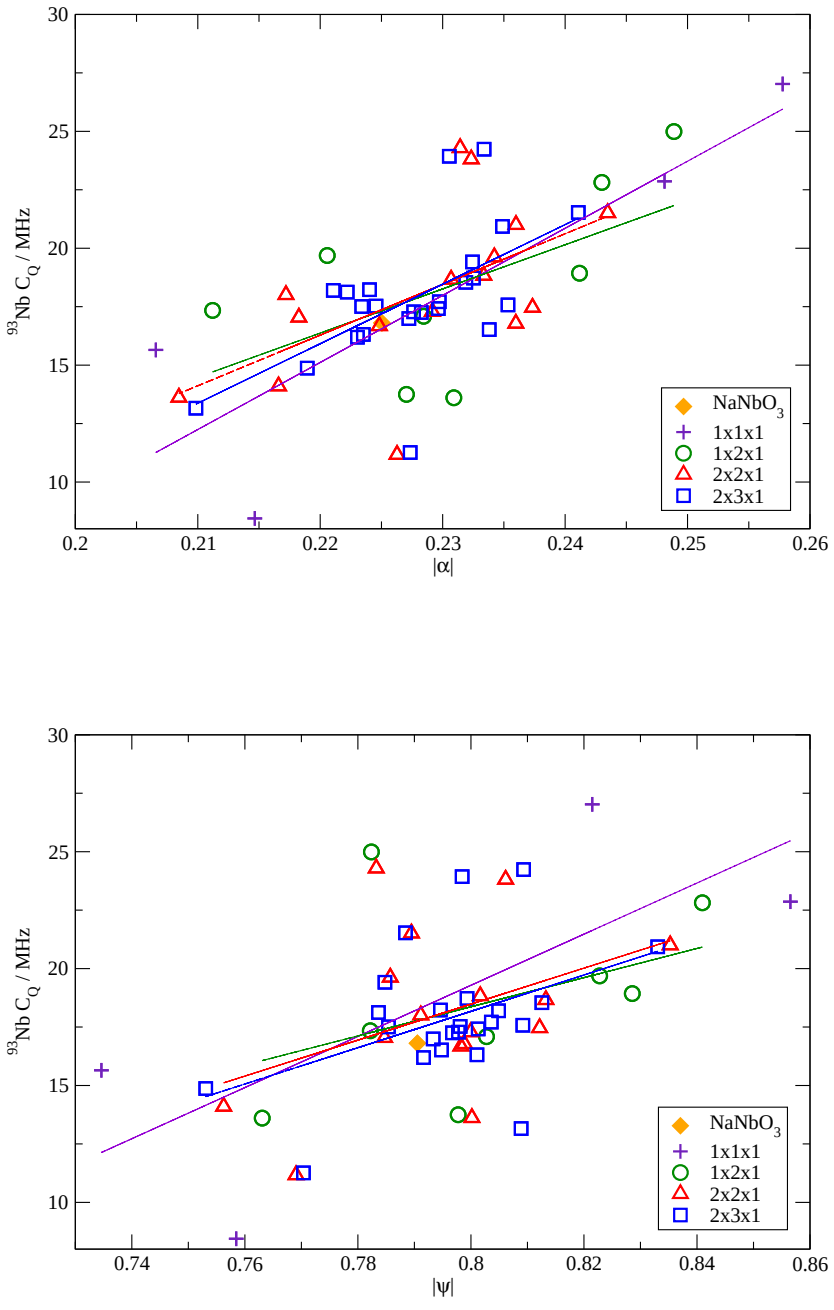

Figure 5.25: ^{93}Nb $|C_Q|$ as a function of longitudinal strain $|\alpha|$ (top) and shear strain $|\psi|$ (bottom) of the oxygen octahedra in the 1K-$NaNbO_3$ supercells. The orange diamonds show the equivalent ^{93}Nb values in pure *Pbcm* $NaNbO_3$ and the straight lines are lines of best fit.

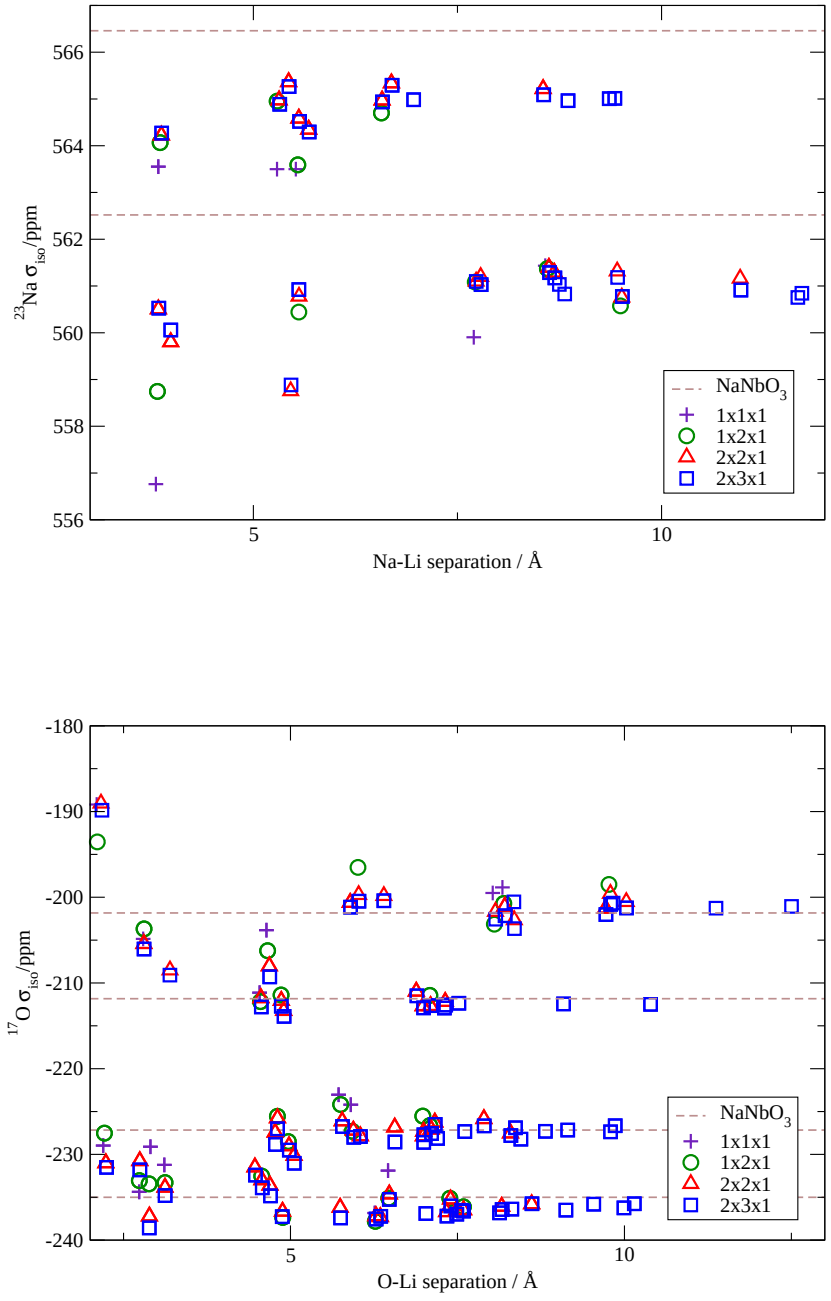

Figure 5.26: ^{23}Na σ_{iso} (top) and ^{17}O σ_{iso} (bottom) as a function of separation from the impurity Li atom in the 1Li-$NaNbO_3$ supercells. The brown dotted lines show the equivalent σ_{iso} values in pure *Pbcm* $NaNbO_3$.

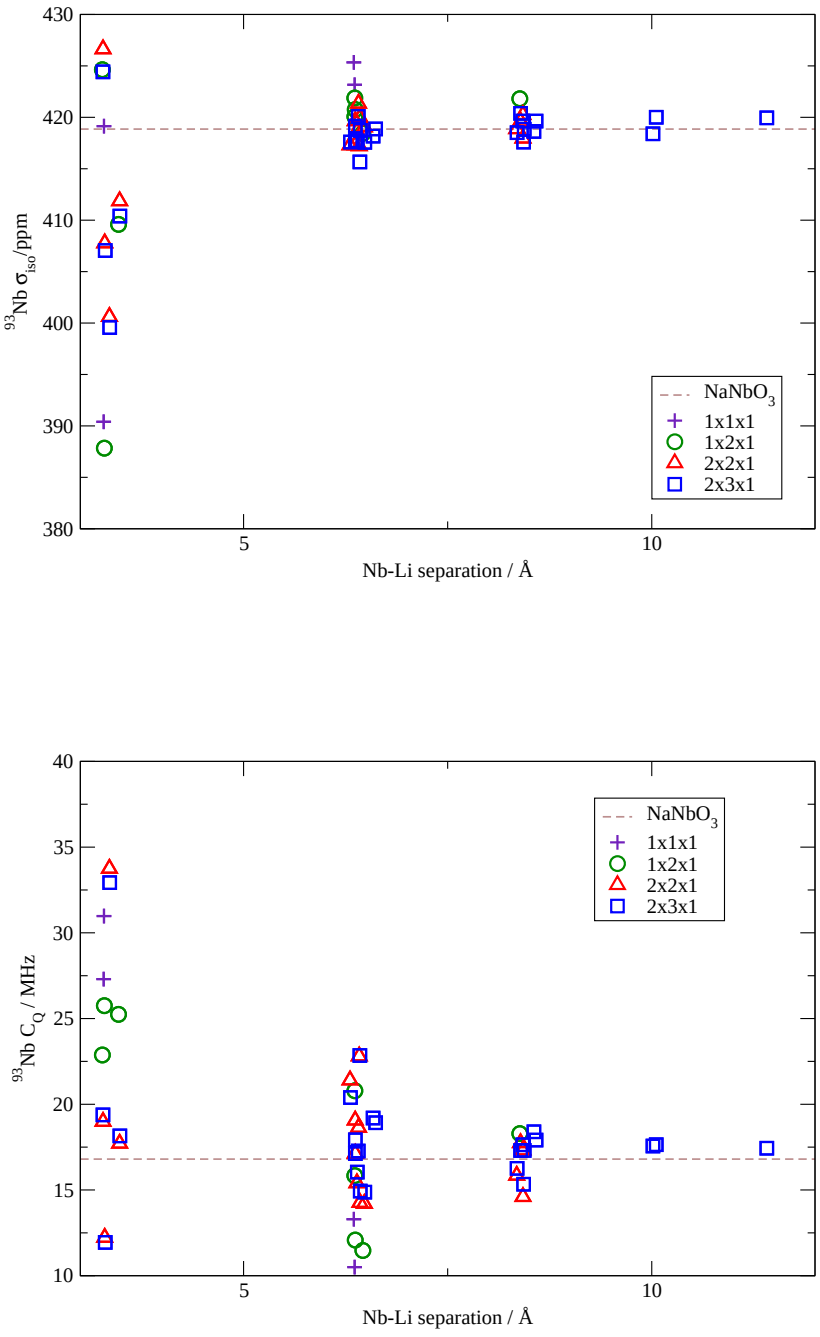

Figure 5.27: ^{93}Nb σ_{iso} (top) and $|C_Q|$ (bottom) as a function of Nb–Li separation in the 1Li-$NaNbO_3$ supercells. The brown dotted lines show the equivalent ^{93}Nb values in pure *Pbcm* $NaNbO_3$.

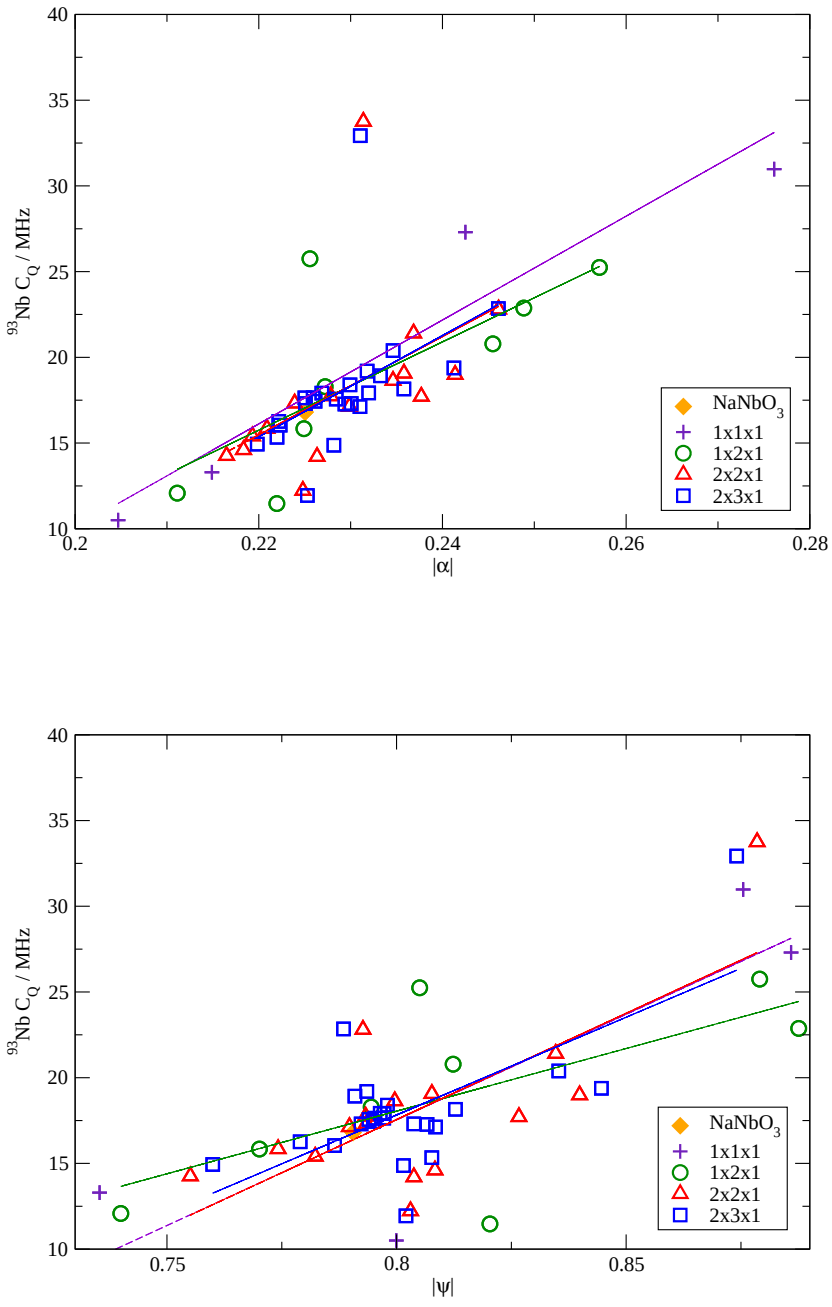

Figure 5.28: ^{93}Nb $|C_Q|$ as a function of longitudinal strain $|\alpha|$ (top) and shear strain $|\psi|$ (bottom) of the oxygen octahedra in the 1Li-$NaNbO_3$ supercells. The orange diamonds show the equivalent ^{93}Nb values in pure *Pbcm* $NaNbO_3$ and the straight lines are lines of best fit.

Supercell	σ_{iso}/ppm	C_Q/MHz	η_Q	K–K separation/Å
1×1×1	1123.1	1.740	0.16	5.53
1×2×1	1121.4	1.898	0.15	5.51
2×2×1	1116.1	2.031	0.15	11.01
2×3×1	1115.2	2.042	0.16	11.00

Table 5.16: The NMR parameters for ^{39}K in 1K-$NaNbO_3$ *Pbcm* with increasing K–K separation.

Supercell	σ_{iso}/ppm	C_Q/MHz	η_Q	Li–Li separation/Å
1×1×1	89.5	0.177	0.10	5.46
1×2×1	88.9	0.158	0.17	5.47
2×2×1	88.7	0.156	0.22	10.97
2×3×1	88.4	0.151	0.21	10.98

Table 5.17: The NMR parameters for ^{7}Li in 1Li-$NaNbO_3$ *Pbcm* with increasing Li–Li separation.

5.3.4 Conclusions for the disordered perovskite structures

The NMR parameters for the 1Na-$KNbO_3$, 2Na-$KNbO_3$, 1K-$NaNbO_3$ and 1Li-$NaNbO_3$ structures have been analysed as a function of distance from the impurity atoms and in terms of strain parameters which quantify the subtle distortions within the oxygen octahedra.

The σ_{iso} values of individual nuclei generally tend towards their equivalent values in the pure perovskites as the distance from the impurity atom increases. σ_{iso} values are close to their pure equivalents by a separation of 6.5 Å in the case of the disordered $KNbO_3$ structures, and by up to 9.5–11 Å for the disordered $NaNbO_3$ structures.[7] In order to assess these trends in the disordered $NaNbO_3$ structures more thoroughly, the $P2_1ma$ structure should be investigated. A range of other disordered and pure $NaNbO_3$ polymorphs could be investigated using the ab initio random structure searching (AIRSS) technique [131].

The strength of the correlations between ^{93}Nb $|C_Q|$ and octahedral strains were found to be linked to the degree of disorder within the structure. The greater the range of environments in which the ^{93}Nb were situated, the weaker the correlations—as shown by the plots of octahedral strains as a function of distance from the impurity Na atom in the 1Na-$KNbO_3$ supercells, and from the study of 2Na-$KNbO_3$ supercells. Structures with lower impurity concentrations were found to exhibit positive-gradient $|C_Q|$–strain correlations that were close to that for pure perovskites. An increase in impurity concentration was correspondingly accompanied by an increasing deviation from the trends observed for the pure structures. This was most

[7] In the case of Nb in the disordered $NaNbO_3$ structures, the decay appears to be still slower than this, though larger supercells would be required to investigate this further.

notable in the 1Na-$KNbO_3$ structures (for which the correlations ranged from a negative to positive gradient), the supercells of which extended to higher impurity concentrations than examined in the 1Li-$NaNbO_3$ and 1K-$NaNbO_3$ structures (for which the correlations all had a positive gradient). The strength of the ^{93}Nb $|C_Q|$ correlations with longitudinal strain were stronger than those with shear strain, implying that the electric field gradient experienced by the ^{93}Nb nuclei is affected more by the Nb–O bond lengths than their angular orientation.

5.4 Overall conclusions

In this chapter I have presented calculated NMR parameters for the perovskite structures for pure $NaNbO_3$, $LiNbO_3$ and $KNbO_3$, and the solid solutions of $Na_xK_{1-x}NbO_3$, $K_xNa_{1-x}NbO_3$ and $Li_xNa_{1-x}NbO_3$ across a range of compositions. It was found that the NMR parameters were very sensitive to structural distortions, particularly in the case of the Nb and O nuclei due to their complex octahedral arrangements. When relaxing the initial experimental structures, PBEsol was found to give a better representation of the structures than the commonly-used PBE functional. The choice of functional for the initial geometry optimisation was found to have a greater effect on the calculated NMR parameters than the choice of functional for the NMR calculation itself. Therefore calculations using PBEsol were found to produce calculated NMR parameters which were closer to experiment than those using PBE, particularly in the case of ^{93}Nb C_Q values. By extension, these investigations highlight the importance of performing careful geometry optimisations for any material before calculating NMR parameters.

My investigations of ^{23}Na σ_{iso} values indicate that ^{23}Na can be used to

infer whether a $Na_xK_{1-x}NbO_3$ sample is based on the pure $KNbO_3$ or *Pbcm* $NaNbO_3$ structures. In the case of structures based on $KNbO_3$, which are likely to contain low Na concentrations, ^{23}Na NMR cannot be used to obtain a definitive measurement of the Na concentration. In the case of structures based on *Pbcm* $NaNbO_3$ however, the ^{23}Na σ_{iso} values are much more sensitive to Na concentration and it may be possible to use them to accurately measure the Na concentrations. In the case of the $Li_xNa_{1-x}NbO_3$ system, figure 5.26 implies that the two experimental ^{23}Na peaks will shift by approximately 1–4 ppm (from σ_{iso} =∼561 ppm to σ_{iso} =∼557–560 ppm) and ∼1.5 ppm (from σ_{iso} =∼565 ppm to σ_{iso} =∼563.5 ppm) respectively as the Li impurity concentration is increased from 2% to 12.5%. In the case of the $K_xNa_{1-x}NbO_3$ system, figure 5.23 implies that the two experimental ^{23}Na peaks will shift by ∼3.5 ppm (from σ_{iso} =∼565.5 ppm to σ_{iso} =∼569 ppm) and by 2.5–3.5 ppm (from σ_{iso} =∼561.5 ppm to σ_{iso} =∼564–565 ppm) respectively as the K impurity concentration increases from 2% to 12.5%. The spread of ^{23}Na σ_{iso} values in figures 5.23 and 5.26 further implies that the degree of broadening will increase with increasing impurity concentrations, however such an effect may be experimentally obscured by large amounts of quadrupolar broadening.

The correlation between ^{93}Nb C_Q values and the octahedral distortions in the surrounding arrangement of nearest neighbour oxygens has also been investigated. It was found that the correlations were linked to the degree of disorder in the structure. The degree of disorder can be examined in terms of the range of environments within a structure (linked to the range of separations between the ^{93}Nb nuclei and the impurity atom), the impurity concentration and the strain within a given oxygen octahedron. The range

of environments was found to affect the strength of the ^{93}Nb C_Q–strain correlations: the greater the number of ^{93}Nb environments, the weaker the correlation. The impurity concentration affected whether the correlation had a positive (as it was for the pure structures) or negative gradient: structures with high impurity concentrations tended towards negative gradients (i.e. the correlations deviated most from the trends exhibited by the pure structures). The change in the gradient of the C_Q–strain correlations may be experimentally observable as a change in the degree of quadrupolar broadening. A correlation with an almost flat gradient could lead to only small amounts of quadrupolar broadening.

By analysing the octahedral strains as a function of Nb–impurity separation in the 1Na-$KNbO_3$ supercells, I was able to show that the octahedral strains tended to their values in the pure $KNbO_3$ structure with increasing separation and within a separation of ∼8.5 Å. The $|C_Q|$–longitudinal strain correlations were stronger than those with shear strain, implying that the distribution in the lengths of the Nb–O bonds has a more direct effect on the ^{93}Nb C_Q values than the angles between the Nb–O bonds.

When analysing the correlation between the strain in a given octahedron and the ^{93}Nb C_Q values, a greater strain correlated to a greater ^{93}Nb $|C_Q|$ in the pure perovskite structures. This implies that an increased octahedral strain led to an increased V_{zz} component in the electric field gradient and resulted in higher ^{93}Nb $|C_Q|$ values. However introducing a high impurity concentration could result in negative ^{93}Nb $|C_Q|$–strain correlations. The change in the electric field gradients (and therefore ^{93}Nb $|C_Q|$ values) could arise from a combination of two effects. First, the effect of the octahedral distortions arising from the presence of the impurity atom (as alluded to

in the discussions above)—i.e. an indirect effect from the impurity atom. Second, the direct effect of the impurity atom on the electric field gradient. The relative strengths of these two effects could be investigated further. The oxygen octahedra could be distorted manually in order to investigate the effect of octahedral distortions on ^{93}Nb $|C_Q|$. Furthermore, the direct effect of the impurity atoms could be investigated by manually distorting their positions or hybridising all the group I nuclei via the virtual crystal approximation.

This level of structural analysis and attention to their correlations with NMR parameters highlights the value of calculating NMR parameters from first-principles. NMR experiments measure the aggregate response of nuclei in the same atomic environment, and there is no direct indication of where these atomic environments are located within the structure. By contrast, it is possible from calculations to obtain the magnetic response for each individual nucleus. Such calculations can then be used to interpret existing experiments and inform the creation of new ones.

Chapter 6

The Knight shift in bulk platinum, palladium and rhodium

Platinum, palladium and rhodium have long been prized as catalysts, being commonly used in catalytic converters, fuel cells and in the petroleum industry. Their chemical inertness and low toxicity to humans have led them to being used in a variety of medical applications, whilst their low electrical resistance has made them favourable materials for electrical contacts and, in the case of Pt and Pd, as thermocouples.

The measurement of the Knight shift in the NMR spectra of metals potentially provides valuable information on local electronic environments, which in the case of Pt, Pd and Rh is used to tailor their catalytic efficiency. Most of the existing experimental research on the Knight shift in Pt, Pd and Rh concerns Pt particles which may be coated in Pd or Rh, or the interaction of adsorbates on the catalyst's surface.

To date, there has been very little research on the calculation of the Knight shift from first-principles. The linear response approach for calculating Knight shifts was developed by d'Avezac *et al.* and tested on Al,

Li and Cu [3]. Laskowski and Blaha used the finite field approach to calculate the Knight shift in a range of metals up to Ag [132]. In addition to the particularly fine **k**-point grids required for the calculation of NMR parameters in metals, and the slow convergence with respect to smearing (section 4.3), the authors also discuss the difficulty of modelling core polarisation. D'Avezac *et al.* used a planewave-pseudopotential approach which does not include the effects of core polarisation. They however mention that previous studies by Gaspari *et al.* indicate that core polarisation may not significantly contribute to the Knight shift—the core polarisation in Li was estimated as being only ∼5% of the total Knight shift [133]. By contrast, the calculations of Laskowski and Blaha used an all-electron methodology which was automatically capable of including core polarisation. In the experimental literature, it is assumed that the effect of core polarisation on the Knight shift is significant, as will be discussed in section 6.1.

In this chapter and the next I present the first first-principles calculations of the Knight shift in Pt, Pd and Rh. This chapter focusses on the bulk structures and how their calculated Knight shifts are affected by **k**-point sampling and smearing widths. The assumption in the experimental literature that core polarisation has a major effect on the Knight shift is also preliminarily assessed. In the next chapter I shall discuss the Knight shift in infinite slabs of the same metals with an eye to furthering the existing research on catalytic efficiency.

A note on nomenclature and sign conventions: The 'Knight shift', K, is experimentally defined as the ratio of the additional magnetic field experienced by a nucleus in a metallic material (ΔB_{met}) compared to that

which is experienced in an equivalent diamagnetic material (B_{dia}):

$$K = -\frac{\Delta B_{met}}{B_{dia}}. \tag{6.1}$$

In the absence of spin-orbit coupling, the Knight shift can be decomposed into a contribution from the electron spin interacting with the nucleus (i.e. a hyperfine interaction) and from the orbital electron currents interacting with the nucleus (i.e. a magnetic shielding component).

In experimental NMR papers, the 'total' Knight shift, as expressed in equation 6.1, is often referred to as the 'Knight shift' or sometimes the 'metallic shift'. However, papers with a more theoretical focus often reserve the term 'Knight shift' to express the spin component. For the sake of clarity I shall refer to the total Knight shift as the 'metallic shift', the spin component as the 'Knight shift', and the orbital component as the 'orbital shift'.

By convention, the sign of the metallic shift is the opposite to that of the chemical shift. A negative metallic shift therefore corresponds to a magnetic shielding, $\mathbf{B_s}$, that is parallel to the applied magnetic field $\mathbf{B_0}$.

6.1 Experimental Knight shifts

The value of the metallic shift will differ depending upon the reference compound chosen and the temperature at which the measurements are taken. In order to present values that are more readily comparable to other studies, the measurements are therefore extrapolated to 0 K and presented with respect to a diamagnetic reference compound. The methodologies used to estimate this 'true metallic shift', irrespective of temperature or reference compound, are briefly outlined below so that the values reported in the

literature can be placed in an appropriate context.

6.1.1 Extrapolation to 0 K

The methodology to extrapolate metallic shifts to 0 K was developed by Jaccarino *et al.* in the 1960s [134] for *d*-band superconductors, and subsequently employed for ^{195}Pt, ^{105}Pd and ^{103}Rh [135, 136, 137].

The methodology is founded on the assumption that the Knight shift could be considered as arising from non-interacting contributions from the *s*-band and *d*-band electrons and that these contributions are directly proportional to their respective densities of states (or partial densities of states—PDOS).

The metallic shift (or total 'Knight shift'), K, is decomposed into a sum of three contributions:

- the (Fermi-)contact interaction arising from the *s*-band electrons at the Fermi level (K_s),
- the effect of *d*-band electrons at the Fermi level inducing a core polarisation on the inner *s* electrons (K_d),
- the orbital paramagnetism of the *d*-band electrons (K_{orb}),

such that[1]

$$K = K_s + K_d + K_{orb}. \tag{6.2}$$

Likewise, the total susceptibility χ is expressed as

$$\chi = \chi_s + \chi_d + \chi_{orb}, \tag{6.3}$$

[1] In some cases (e.g. [138]) a further diamagnetic contribution is included (δK_{dia}), but this is considered to be negligible.

where χ_s and χ_d are the magnetic spin susceptibilities for s-band and d-band electrons respectively, and χ_{orb} is the paramagnetic orbital magnetic susceptibility.

Each component i of the susceptibility is taken to be proportional to the equivalent Knight shift component according to

$$K_i = \alpha_i \chi_i, \tag{6.4}$$

where α_i is a fitted parameter.

The components of K corresponding to a contact interaction are correlated to the spin-lattice relaxation time, T_1, and the temperature, θ, through the Korringa relation:

$$K^2 = \frac{a}{T_1 \theta}, \tag{6.5}$$

where a is a constant [139, 140].

The temperature dependence of the Knight shift is assumed to arise from the temperature dependence of the d-like DOS. By contrast, it is assumed that the s-like DOS is temperature-independent [141, 140]. Since the Knight shift can arise only from s-like electrons, it is assumed that the d-like electrons must polarise the core s-electrons, leading to a temperature dependence in the Knight shift. The orbital component of the metallic shift is also considered to be temperature-dependent.

In this way, K_d is deduced by plotting K against the susceptibility χ with temperature as the implicit parameter (often referred to as K-χ analysis) and by measuring the temperature dependence of the spin-lattice relaxation time T_1. K_{orb} is deduced by a combination of K-χ analysis and atomic Hartree-Fock calculations of $\langle r^{-3} \rangle$. K_s is obtained by estimating the s-like DOS at the Fermi surface, often by empirical methods based on experimental

electronic specific heat coefficients.

6.1.2 Reference compounds

The choice of reference compound is of paramount importance because it determines the 'zero point' of the experimental Knight shift scale. Ideally, the reference compound should be wholly diamagnetic, and its chemical shift should only contain orbital components as expressed in equation 4.1. As discussed by van der Klink and Brom [142], it can be useful to separate the chemical shift of the reference compound into the sum of the diamagnetic contribution of the core electrons, the diamagnetic contribution of the valence electrons and a paramagnetic contribution of the electrons as a whole. The diamagnetic contribution of the core electrons can be accurately approximated to that of an isolated atom (the 'frozen core approximation' discussed in section 3.3.4). The diamagnetic contribution from the valence electrons is considered to be small compared to the paramagnetic contribution by the same electrons. The compound with the smallest paramagnetic contribution is then chosen as the reference so that the full effect of the paramagnetic orbital contribution in the elemental metal can be measured [143]. In some studies, any remaining paramagnetic contribution in the reference compound is estimated and removed from the measured metallic shift (for example, in Drain's estimate of the metallic shift in Pt [144]). An evaluation of different reference compounds is presented by van der Klink and Brom in their comprehensive review paper of metallic NMR [142].

Chloroplatinic acid (H_2PtCl_6) is a common reference compound for Pt [145], or in some cases iodoplatinic acid (H_2PtI_6) [142].[2] There has been

[2] It has been pointed out by Clogston *et al.* that there is still some degree of paramagnetic contribution from the *d*-shell in H_2PtCl_6 [135].

some difficulty finding suitable diamagnetic compounds containing Rh or Pd. In the case of Rh, $RhSn_2$ was originally selected by Seichik *et al.* in the first measurement of this Knight shift [137], however Brown and Green suggested that $HRh(Ph_3P)_3CO$ contained a smaller paramagnetic contribution [143]. Finding a Pd-containing diamagnetic compound has been a particular problem. Through analogy to Pt, hexachloropalladate has been used, with an attempt at 'zeroing' the scale by taking into account the resonance behaviours of Pt and Rh hexachloro complexes [142]. In the earliest Pd Knight shift study, Seitchik *et al.* investigated several candidate compounds, however all were found to be unsuitable due to large quadrupolar broadening [136].

6.1.3 Experimental values

Tables 6.1, 6.2 and 6.3 show the measured metallic shifts of Pt, Pd and Rh respectively, along with their estimated K_i components where applicable. In order to provide a meaningful comparison to my DFT calculations only measurements taken close to or extrapolated to 0 K have been presented.[3] I have included an additional column for the sum of K_s and K_d which gives a total estimated Knight shift. This will be discussed in the context of my calculations later in this chapter.

It can be seen from table 6.1 that the Pt data are relatively numerous and consistent with each other. ^{195}Pt is a relatively straightforward nucleus to measure, with a reasonably high gyromagnetic ratio and no quadrupolar broadening. As discussed in section 6.1.2, the choice of reference compound

[3] The ^{103}Rh measurement by Brown and Green was taken at room temperature, however given the difficulty with finding a suitable reference compound and the estimations made to correct for this, I have included it nevertheless.

is well established.

By contrast, there is a greater range of values for Pd and Rh, and fewer measurements. The small number of studies could be due to the difficulty in taking NMR measurements for these nuclei. The ^{103}Rh nucleus, whilst 100% naturally abundant, is not particularly sensitive (approximately one hundred times less so than ^{195}Pt) and has a long relaxation rate (three hundred times slower than ^{195}Pt) [146]. By the mid 1980s, techniques for detecting ^{103}Rh had however improved [147]. ^{105}Pd has a large quadrupole moment and its spectra therefore exhibit large amounts of quadrupolar broadening. The range of values could be attributed to at least three causes. First and foremost is the considerable difficulty finding suitable reference compounds for Pd and Rh, as discussed in section 6.1.2. Of particular note is the ^{103}Rh measurement by Brown and Green. They chose $HRh(Ph_3P)_3CO$ as a reference, in comparison to the earlier use of $RhSn_2$ by Seitchik *et al.*, and estimated the remaining paramagnetic contribution. Their total metallic shift of $0.04 \pm 0.05\%$ is an order of magnitude smaller than other measurements before and after. Second, there has been difficulty in measuring the magnetic moments of these nuclei to a sufficient degree of accuracy. This was a notable problem in the papers of Seitchik *et al.* in the 1960s [136, 137]. Third, some of the assumptions underlying the methodologies may not hold true for Rh and Pd. In the case of Rh, the validity of K-χ analysis has been doubted because it is not clear that the temperature dependence of χ depends only on the *d*-spin susceptibility [148].[4] In the case of Pd, it has been noted that there may be non-negligible exchange interactions between the

[4]Furthermore, Burnet *et al.* report that the Knight shift in Rh is almost independent with respect to temperature up to 100 K.

electrons which could invalidate the assumption that there is no interaction between s-band and d-band electrons [142].

Reference [Authors,Year]	K_s	K_d	$K_s + K_d$	K_{orb}	Total K	Experimental
Butterworth, 1962 [139]						-3.68±0.010
Drain, 1963 [144]						-3.3
Clogston *et al.*, 1964 [135, 149]	1.02	-4.65	-3.63	0.26		
Yafet and Jaccarino, 1964 [141, 149]	0.99	-1.76	-0.77			
Narath and Weaver, 1968 [150]						-4.04±0.05
Shaham *et al.*, 1978 [140, 149]	0.788	-4.61	-3.822	0.38		-3.4
Bucher and van der Klink, 1988 [151, 149]	0.72	-4.38	-3.66	0.21		
Fraissard, 1999 [145]						-3.4
van der Klink and Brom, 2000 [142]	0.78	-4.42	-3.64	0.2	-3.44	-3.44

Table 6.1: Table of ^{195}Pt metallic shifts in the literature, quoted in percent. $K_s + K_d$ gives the total Knight shift arising from spin magnetic moments. 'Total K' corresponds to the sum of K_s, K_d and K_{orb}. Values have been quoted to the same level of accuracy presented in the literature.

Reference [Authors, Year]	K_s	K_d	$K_s + K_d$	K_{orb}	Total K	Experimental
Seitchik *et al.*, 1964 [136]	0.36	-4.38	-4.02	0.36		
Takigawa *et al.*, 1982 [152, 142]	0.12	-4.50	-4.38	0.36		
van der Klink and Brom, 2000 [142] (after Bucher, PhD thesis, 1988)	0.59	-4.55	-3.96	0.36		
van der Klink and Brom, 2000 [142] (after [136, 152])	0.62	-4.41	-3.79	0.36	-3.44	
van der Klink, 2000 [142]						-2.7 to -3.5

Table 6.2: Table of ^{105}Pd metallic shifts in the literature, quoted in percent. $K_s + K_d$ gives the total Knight shift arising from spin magnetic moments. 'Total K' corresponds to the sum of K_s, K_d and K_{orb}. Values have been quoted to the same level of accuracy presented in the literature. The accuracy of the data is likely to increase in order of year published (down the table). Seitchik *et al.* were not able to find a suitable reference compound with which to zero their data. Takigawa *et al.* assumed that χ_d for Pd was the same as that for Pt. Van der Klink and Brom amalgamated these two data sets in their review paper published in 2000 [142]. Taking into account possible corrections for reference compounds, they conclude that the 'true' value for the metallic shift is likely to lie within -2.7% to -3.5%.

Reference [Authors,Year]	K_s	K_d	$K_s + K_d$	K_{orb}	Total K	Experimental
Seitchik *et al.*, 1965 [137]	0.36	-0.25	0.11	0.32	0.34–0.43	
Brown and Green, 1970 [143]						0.04±0.05
Burnet *et al.*, 2002 [153]	0.06	-0.525	-0.465	0.842	0.376	0.375–0.43

Table 6.3: Table of ^{103}Rh metallic shifts in the literature, quoted in percent. $K_s + K_d$ gives the total Knight shift arising from spin magnetic moments. 'Total K' corresponds to the sum of K_s, K_d and K_{orb}. Values have been quoted to the same level of accuracy presented in the literature.

6.2 Initial DFT calculations

Calculations were performed using the PBE functional, and ultrasoft pseudopotentials from the 'OTFG9' $\Delta = 0.5\,\text{meV}$ set [49]. Initial FCC structures were relaxed taking the lattice parameters from the Δ gauge paper of Lejaeghere *et al.* [49]. The planewave cut-off and **k**-point spacings were converged so that the relaxed lattice parameters were within $\pm 0.001\,\text{Å}$ for Rh, $\pm 0.005\,\text{Å}$ for Pd and $\pm 0.001\,\text{Å}$ for Pt. The tolerances placed on the geometry optimisations were the same as those placed on the perovskite structures in chapter 5: the forces between atoms had to be less than $2.5 \times 10^{-2}\,\text{eV/Å}$, the stress on the unit cell was less than $0.05\,\text{GPa}$, the change in the free energy per atom between successive iterations was within $1 \times 10^{-5}\,\text{eV}$ and the change in atomic displacement between successive iterations was less than $5 \times 10^{-4}\,\text{Å}$.

The resulting lattice constants were benchmarked against those quoted in the impressively comprehensive paper by Lejaeghere *et al.* from 2016 which compared the accuracy and precision of structural calculations performed using 15 DFT codes [49]. Compared to these lattice constants quoted for 'OTFG9' in the Δ gauge paper [49], the Pt lattice parameter expanded by 0.06%, the Pd lattice parameter by 0.31% and the Rh lattice parameter contracted by a tiny 0.008%. The reason for relaxing the structures in the first place was to maintain consistency with the energy cut-off and **k**-point parameters converged for the total energy. The input benchmark lattice constants had been obtained by Lejaeghere *et al.* using extremely fine parameters that would not be computationally reasonable to use for further study for, for example, calculating band structures or densities of states.

The benchmark calculation parameters included an energy cut-off of 700 eV and **k**-point spacings of at most $0.0125\times2\pi$Å^{-1}. By way of comparison, the equivalent values used for my calculations were an energy cut-off of at most 650 eV and a **k**-point spacing of $0.04\times2\pi$Å^{-1}.

6.2.1 Band structures and densities of states (DOS)

The band structures and densities of states (DOS) for bulk Pt, Pd and Rh are typical of transition metals and indicate that these structures have similar electronic characteristics to one another (figures 6.1 and 6.2). The valence s electrons display high degrees of delocalisation, as indicated by the parabolic bands in the band structures in figure 6.1. A number of flatter bands are situated near the Fermi energy (E_f). These are predominantly d-like with a small p-like contribution, as indicated by their projected densities of states (PDOS) in figure 6.2. At the lowest energies in the valence bands (around -7 to -5 eV below the Fermi energy) the electronic character is entirely s-like and corresponds to the parabolic band located about Γ in the band structures. The main difference between the structures is the position of the Fermi level (E_f).

Since the Knight shift originates from the behaviour of electrons at E_f, it makes sense to note the electronic characteristics in this region. The band structures of Pt and Pd reveal the presence of flattened bands that lie almost at E_f, whereas in Rh these flat bands lie approximately 0.5–0.8 eV above E_f. The DOS of Pt and Pd show a corresponding peak of strong d-like character at E_f whereas in Rh this peak is situated 0.5eV above E_f. For all three structures, the s-like contribution at E_f is very small. The narrow d-like peak and the almost flat s-like band in the PDOS at E_f has also

been noted by Rao *et al.* in their investigations of the Knight shift of ^{100}Rh in very dilute *Pd*-Rh alloys [138] and Shaham *et al.* in their Knight shift measurements of Pt [140].[5] DOS calculations for Pt have been conducted by Fradin *et al.* [154] and Andersen [155].

[5]Technically Shaham mentions it as a general point over all energies—i.e. no energy scale is mentioned.

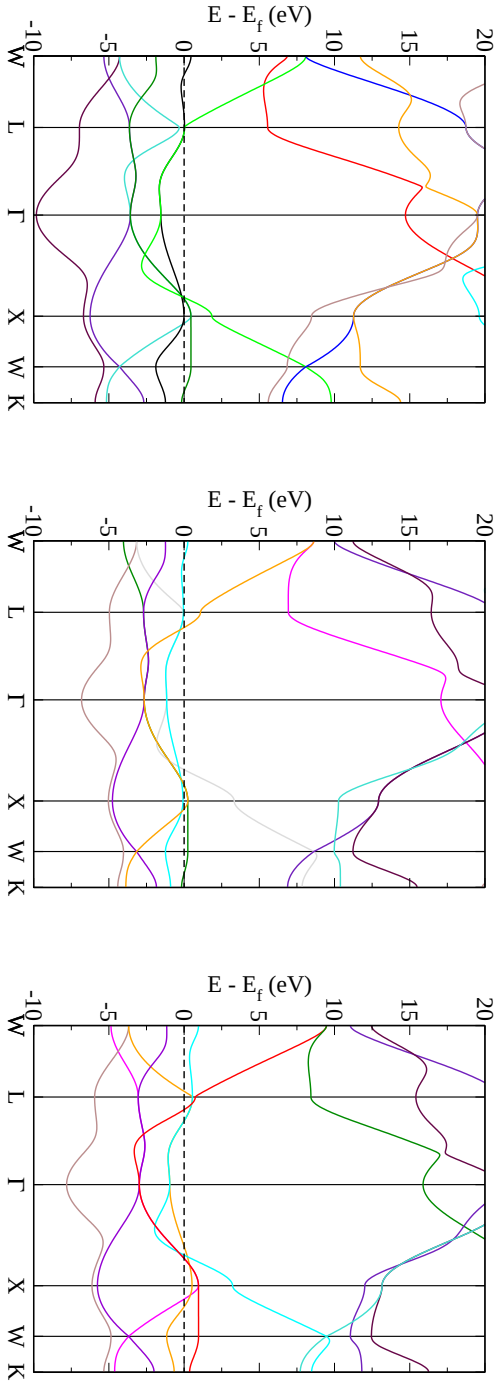

(a) Bulk Pt.

(b) Bulk Pd.

(c) Bulk Rh.

Figure 6.1: Band structures for bulk (a) Pt, (b) Pd and (c) Rh, using PBE.

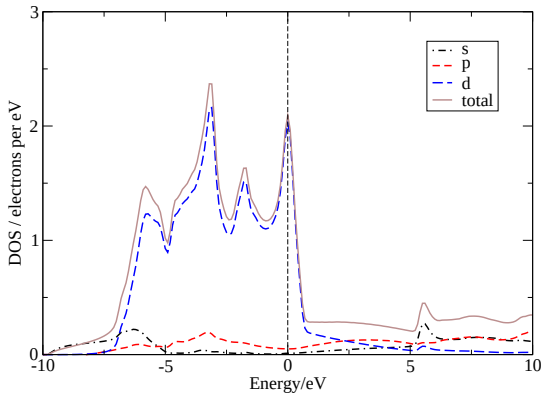

(a) Bulk Pt.

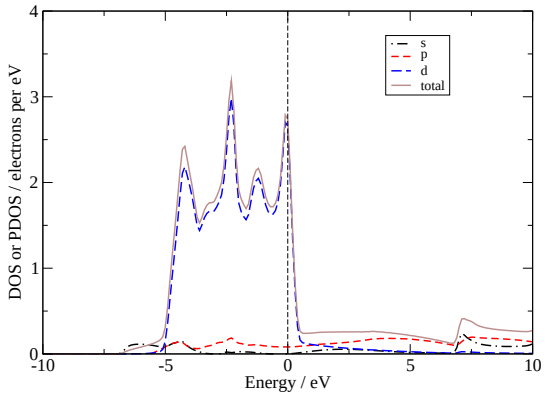

(b) Bulk Pd.

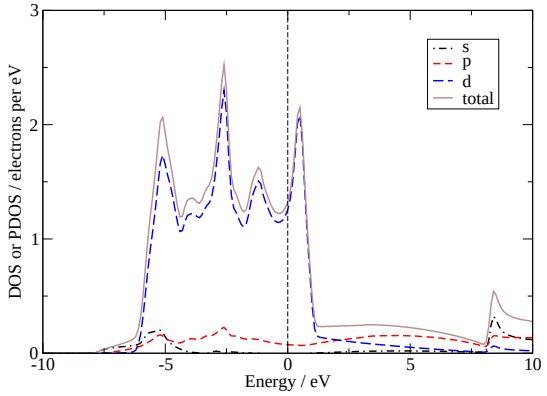

(c) Bulk Rh.

Figure 6.2: DOS and angular PDOS for bulk (a) Pt, (b) Pd and (c) Rh.

6.3 DFT calculations of the Knight shift and the orbital shift

6.3.1 Calculation details

The methodology for calculating the Knight shift from first-principles has been discussed in the previous chapter, and was implemented into the CASTEP code by Dr. Bi-Ching Shih at the Department of Materials, University of Oxford. In contrast to the band structure and DOS calculations discussed above, calculations of the Knight shift (the shift due to spin) and orbital shift were performed with norm-conserving pseudopotentials because methodologies involving ultrasoft pseudopotentials had not been fully implemented at the time of writing. The pseudopotentials were from the CASTEP 9.0 set of norm-conserving pseudopotentials with Δ =1.1 meV per atom. All calculated Knight shift and orbital shift values are quoted in ppm with respect to the equivalent bare nucleus.

The Knight shift and orbital components were first converged with respect to energy cut-off to within at least 0.4%.[6] The effect of **k**-points and smearing widths on the spin and orbital contributions to the metallic shift was then investigated. Figures 6.3, 6.4 and 6.5 display these results on the spin component of the Knight shift for Pd, Pt and Rh respectively. Figure 6.6 shows the equivalent investigation for the orbital component of the Knight shift for Pt. It was not possible to calculate the orbital contributions for Pd and Rh because the methodology for correctly handling the pseudopotential projectors had not been worked out and implemented at

[6] The Knight shift values for Pt are within 2 ppm (or 0.005%) using a cut-off of 550 eV. Pd is within 15 ppm (0.3%) with a cut-off of 800 eV and Rh is within 10 ppm (0.4%) with a cut-off of 650 eV. The orbital shift for Pt is within 40 ppm (0.06%) with a cut-off of 550 eV.

the time of writing.

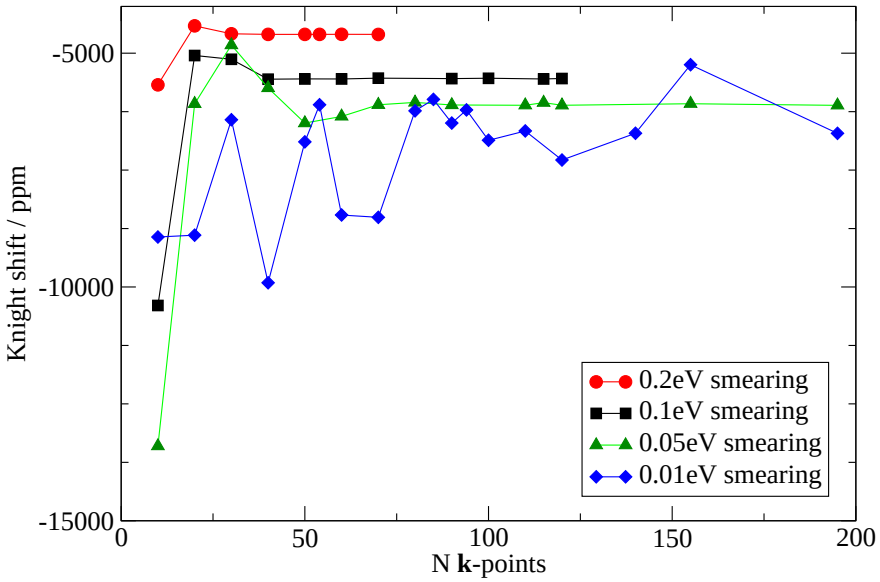

Figure 6.3: Convergence of the Knight shift in bulk Pd with respect to **k**-points and Gaussian smearings. The **k**-points were distributed in a regular N×N×N grid. All calculations were conducted using a planewave cut-off of 800 eV, with the exception of the calculations with 0.01 eV smearing which were conducted using a planewave cut-off of 650 eV.

6.3.2 Convergence with respect to k-points

It can be seen from figures 6.3, 6.4, 6.5 and 6.6 that a large number of **k**-points is required to obtain converged values for the Knight shift. For example, in the case of Rh, at least 60×60×60 **k**-points were required, using a smearing of 0.2 eV, to converge the Knight shift to within a 0.1% precision. This corresponds to a **k**-point spacing of $0.0075\times 2\pi$Å^{-1}. When using a smearing of 0.05 eV at least 155×155×155 **k**-points were required to converge the Knight shift to within 1.6%, corresponding to a **k**-point spacing of $0.0029\times 2\pi$Å^{-1}. By contrast, a spacing of $0.05\times 2\pi$Å^{-1} would be regarded as

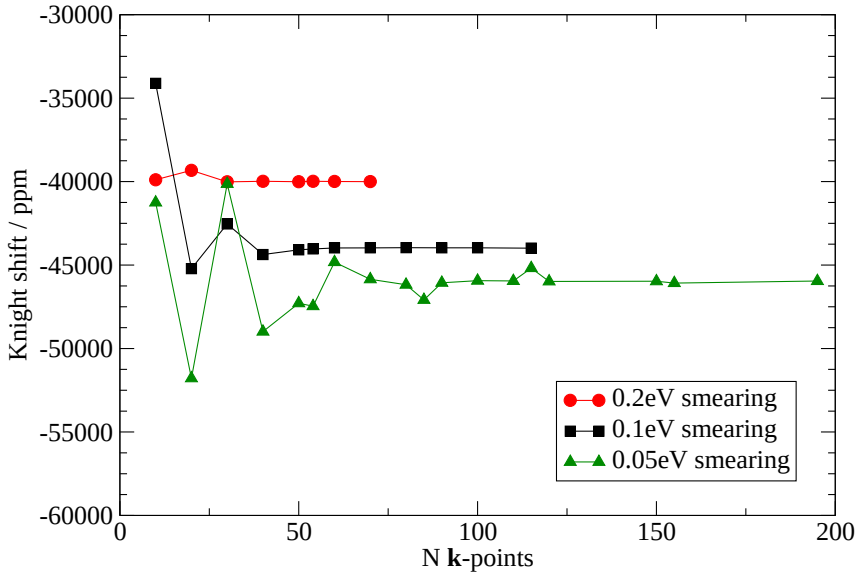

Figure 6.4: Convergence of the Knight shift in bulk Pt with respect to **k**-points and Gaussian smearings. The **k**-points were distributed in a regular N×N×N grid.

typical for a highly converged NMR calculation of a diamagnetic material. It can also be seen that decreasing the smearing width increases the number of **k**-points required to obtain a converged value and that the magnitude of these converged values increases with decreasing smearing width.

6.3.3 Convergence with respect to smearing width

The graphs also show that the Knight shift converges slowly with respect to smearing width, as also noted by d'Avezac *et al.* for their Knight shift calculations on Li, Al and Cu [3]. This raises the question of how feasible it can be to obtain a single precise value for the Knight shift within current methodologies and the limits on computing resources. In my Knight shift calculations for Pd, I decided to investigate whether a tiny smearing

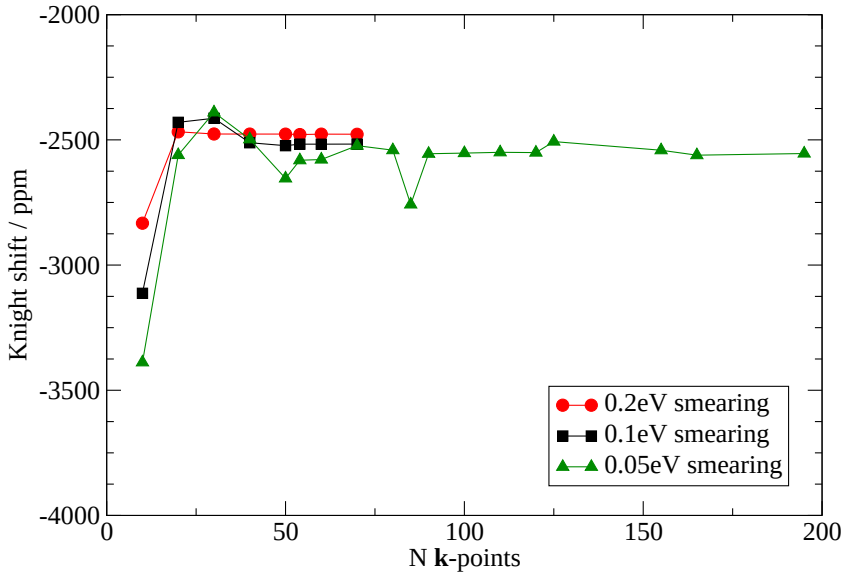

Figure 6.5: Convergence of the Knight shift in bulk Rh with respect to **k**-points and Gaussian smearings. The **k**-points were distributed in a regular N×N×N grid.

of 0.01 eV would produce a converged result (see figure 6.3). Even at a **k**-point sampling of 195×195×195 the value of the Knight shift using a 0.01 eV smearing width had not converged. It is, of course, possible that the value would have converged had I been able to use an increasingly finer **k**-point grid. Either way, the graph clearly shows that the rate of convergence using a 0.01 eV smearing width is significantly slower than that for 0.05 eV. D'Avezac *et al.* note that there is a correlation between the rate of convergence of a property and the property's dependence on the precision with which the Fermi surface is represented [3]. In their case, these properties are the spin susceptibility, the orbital susceptibility, the Knight shift and the orbital shift. Their calculations show that the orbital susceptibility is the slowest to converge, and they mention that this is consistent with the

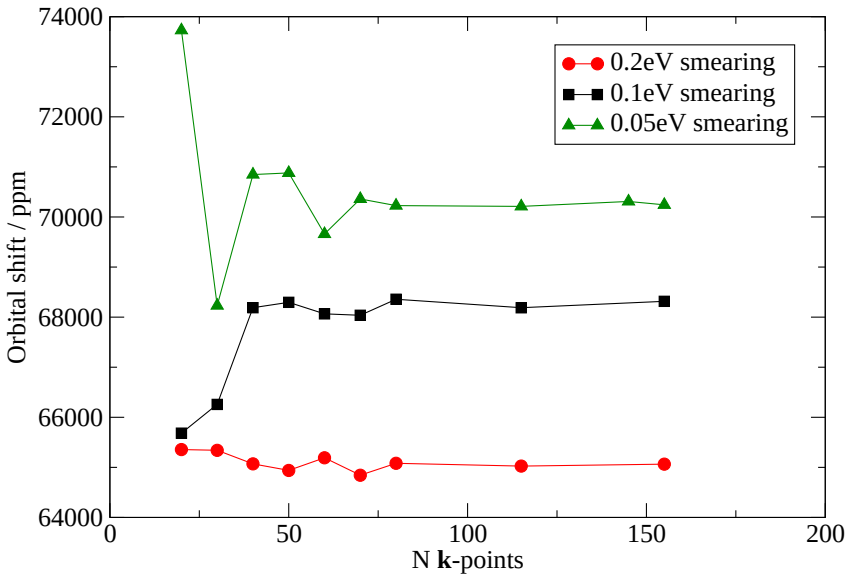

Figure 6.6: Convergence of the orbital shift for bulk Pt with respect to **k**-points and Gaussian smearings. The **k**-points were distributed in a regular N×N×N grid.

orbital susceptibility being a second derivative of the total energy. Likewise the orbital shift is slow to converge. The spin susceptibility, by contrast, converges relatively quickly because it depends on the average of the spin density over the whole unit cell; there is a similar trend for the Knight shift.

6.3.4 Precision of 'converged' values

Table 6.4 shows the converged values of the Knight shift for Pt, Pd and Rh, and the orbital shift for Pt. A conservative estimate of the degree of precision with respect to **k**-point convergence has also been given. This estimate has been obtained by considering the range of values at high numbers of **k**-points. Similar **k**-point grids from 10×10×10 to 195×195×195 were used for all structures. The precision of the Knight shift for Pt is much higher

than for Pd and Rh, implying that the Knight shift converged most readily for Pt with respect to **k**-points. If you consider the precision with respect to smearing widths, it can be seen that the Knight shift values obtained using a 0.2 eV smearing width are the most precise—within 0.03% for Pt, 0.11% for Pd and 0.20% for Rh—and become less precise with decreasing smearing widths.

Smearing	Pt	Pd	Rh
0.2 eV spin	-40000±10 (0.03%)	-4597±5 (0.11%)	-2480±5 (0.20%)
0.1 eV spin	-44000±30 (0.07%)	-5540±15 (0.27%)	-2520±5 (0.20%)
0.05 eV spin	-46000±150 (0.33%)	-6100±35(0.57%)	-2550±40 (1.57%)
0.2 eV orbital	65000±100 (0.15%)		
0.1 eV orbital	68200±200 (0.29%)		
0.05 eV orbital	70300±200 (0.28%)		

Table 6.4: Converged values of the Knight (spin) shift for Pt, Pd and Rh metals, and the orbital shift for Pt. All shifts are given in ppm. The error estimates were obtained by considering the convergence of the values with respect to the number of **k**-points.

An overall estimate of precision can be obtained by adding on the estimated errors arising from the pseudopotential (i.e. from the planewave convergences). To reiterate from section 6.3.1, these were 2 ppm, 15 ppm and 10 ppm for the Knight shift in Pt, Pd and Rh respectively, and 40 ppm for the orbital shift in Pt. The calculated Knight shift and orbital shifts with the total estimated errors in precision are given in table 6.5.

The calculated Knight shifts for Pt, Pd and Rh are all negative, indicating a paramagnetic electronic response in all three metals. The Knight shift for Pt is an order of magnitude greater than that for Pd or Rh. This can be explained by noting that the highest occupied state in atomic Pt extends further from the nucleus than those in Pd or Rh, and is therefore more readily polarised. The orbital shift for Pt is also shown to be very

Smearing	Pt	Pd	Rh
0.2 eV spin	-40000±12	-4597±20	-2480±15
0.1 eV spin	-44000±32	-5540±30	-2520±15
0.05 eV spin	-46000±152	-6100±50	-2550±50
0.2 eV orbital	65000±140		
0.1 eV orbital	68200±240		
0.05 eV orbital	70300±240		

Table 6.5: Converged values of the Knight (spin) shift for Pt, Pd and Rh metals, and the orbital shift for Pt. All shifts are given in ppm. The error estimates were obtained by considering the convergence of the values with respect to the number of **k**-points and the planewave energy cut-offs.

large and of the same magnitude as the equivalent Knight shift, but with the opposite sign. Since the Knight shift and chemical shift have opposite signs by convention, the orbital shift is also due to a paramagnetic electronic response.

6.3.5 Sensitivity of the Knight shift to structural changes

Since NMR parameters are very sensitive to atomic position, it would be interesting to briefly investigate how sensitive the Knight shift is in this respect. The primitive cells for Pd and Rh were reduced by 11%. This corresponds to a hydrostatic pressure of 153 GPa in Pd and of 217 GPa in Rh. Table 6.6 shows the change in lattice parameter and resulting change in Knight shift. The magnitude of the Knight shift for Pd decreased by 23% (with respect to the Knight shift for the original structure) as a result of applying pressure to the structure. The equivalent Knight shift for Rh decreased by only 5%. This indicates that the Knight shift of Pd is much more sensitive to structural changes than Rh.

	Pres.	Non-pres.	Pres.−Non-pres.	% change
Pd lattice parameter/Å	2.481	2.796	-0.315	-11%
Pd Knight shift/ppm	-3542	-4597	1055	-23%
Rh lattice parameter/Å	2.411	2.707	-0.296	-11%
Rh Knight shift/ppm	-2344	-2480	136	-5%

Table 6.6: Lattice parameters for the primitive FCC cell and for Pd and Rh for the original and pressurised structures alongside the corresponding calculated Knight shifts. The percentage change between the original and pressurised structures is quoted with respect to the values for the original structure. The Knight shifts were calculated using a smearing width of 0.2 eV. The precision estimates for both sets of Knight shifts remain the same as those quoted in table 6.5.

6.3.6 Contributions to the Knight shift as a function of energy

As mentioned earlier in this chapter, it is assumed in the experimental literature[7] that core polarisation has a significant effect on the measured Knight shift and that this originates from the *d*-band electrons polarising the inner *s* electrons. To date, first-principles calculations have not been able to fully assess the validity of this approximation [3, 132]. It therefore remains unknown whether core polarisation is important for the calculation of the Knight shift, though early theoretical estimates indicate that it may have only a small effect, at least for Li [133]. In order to further these investigations, I have calculated the relative Knight shift contributions of the semi-core and valence electrons—i.e. from the electrons contained in the pseudopotential. This has been done by calculating the Knight shift contributions as a function of the number of bands and as a function of energy.[8]

The norm-conserving pseudopotentials for Rh and Pd included the 4*s*,

[7] For example the early papers of Clogston, Seichik *et al.* [134, 135, 136, 137].

[8] This functionality was implemented into the CASTEP code by Dr. Bi-Ching Shih.

$4p$, $4d$ and $5s$ atomic electrons as valence, whilst the norm-conserving pseudopotential for Pt included the $5p$, $5d$ and $6s$ atomic electrons as valence. All calculations were conducted on the relaxed structures with a Gaussian smearing of 0.2 eV and correspondingly converged **k**-point sampling.[9]

Table 6.7 shows the isotropic Knight shift (Fermi-contact) contribution summed over a given number of bands for Rh and Pd. Primitive unit cells were used and therefore the first band corresponds to the contribution from the semi-core $4s$ states. The sum up to and including the tenth band corresponds to the Knight shift contribution from the whole pseudopotential (including the $5s$ states). The values for the isotropic Knight shift, dipolar and spin-susceptibility summed over all bands are also included to show that the isotropic Knight shift is the dominant component in the total Knight shift. It can be seen that the contribution from the $4s$ states is negligible. By comparing the summed contributions up to the ninth and the tenth bands ('Band #' 9 and 10 in table 6.7), it can be seen that the majority of the Knight shift originates from the highest energy band (a hybridised $4d$–$5s$ band).

Figure 6.7 plots the Knight shift integrated up to a given energy for the Rh, Pd and Pt structures. The Knight shift becomes increasingly paramagnetic and tends to the total Knight shift value (orange dotted lines) as the summed energy increases. The greatest increase in the Knight shift occurs close to the Fermi energy (brown dotted lines). The overall trends will be due to the Gaussian smearing included in the calculations.

Overall, the variation of the Knight shift as a function of number of

[9] The converged **k**-point samplings were 60×60×60 for Pd and Rh, and 70×70×70 for Pt.

bands and energy indicates that the greatest contribution to the Knight shift originates from the electrons at the Fermi surface. There is a minimal contribution from energies below the Fermi energy. This does not rule out the possibility that there is a core polarisation within the electrons not included in the pseudopotential, however my investigations show that there is unlikely to be any polarisation within the semi-core $4s$ states in Pd and Rh.

	Pd				Rh			
Band #	1($4s$)	8	9	10	1($4s$)	8	9	10
Partial FC/ppm	0.46	550	311	-4473	-0.03	-132	-1342	-2419
Total FC/ppm	-	-	-	-4473	-	-	-	-2419
Total K/ppm	-	-	-	-4596	-	-	-	-2477
Dipolar/ppm	-	-	-	0	-	-	-	0
Spin χ/ppm	-	-	-	-123	-	-	-	-58

Table 6.7: The isotropic Knight shift contribution ('Partial FC') summed up to a specified valence band ('Band #'), using a 0.2 eV smearing width and converged 60×60×60 **k**-point grids. The isotropic Knight shift ('Total FC'), dipolar and spin susceptibility contributions to the total Knight shift ('total K') are also included. Each metal contains a total of 10 valence bands.

6.3.7 Comparison to experiment

Before making a direct comparison between experimental values and my calculated values, it is important to acknowledge the approximations and assumptions employed by the various methodologies. These include differences in the references used (i.e. a range of supposed diamagnetic compounds for the experimental studies, and a bare nucleus for my calculations), temperature effects, inherent errors in experimental apparatus, and the numerical approximations used in first-principles calculations (smearing widths, pseudopotentials, limits to planewave cut-off and so on, as discussed in chapter 3). To a certain extent the Knight shifts given by $K_s + K_d$ in experimental

papers could be compared to my calculated Knight shifts—they both originate from spin—however the values for $K_s + K_d$ have been obtained via semi-empirical means.

In the case of Pt, the K_{orb} values in the literature are an order of magnitude smaller than $K_s + K_d$, and it might therefore be reasonable to compare the experimental, or estimated $K_s + K_d$, values to my calculated Knight shift. The experimental and $K_s + K_d$ values (table 6.1) lie in the range of -3.30 – -4.65%. My calculated values of -4.0 – -4.6% are consistent with this. This implies that the assumptions used to estimate the experimental spin-Knight shift, and the approximations used for my first-principles calculations are reasonable (at worst there is a cancellation of errors within each methodology). In particular, my calculations do not include the potential effects of core polarisation because the core states are modelled using the PAW methodology. The reasonably close agreement between calculated and experimental values further indicate that core polarisation may not have a significant effect on the Knight shift in Pt.

In the case of Pd and Rh, the values in the literature differ greatly from one another due to the difficulty in finding suitable reference compounds and subsequently extracting the spin-only component of the metallic shift. Any comparisons between the literature and my calculated values should therefore be taken with care. My calculated Rh Knight shift of approximately -0.25% (taking into account differences in smearing width) is of the same order of magnitude as the $K_s + K_d$ values (table 6.3). For Pd, the calculated value of -0.46 to -0.61% (depending on smearing width) is an order of magnitude smaller than the $K_s + K_d$ values of -3.8 to -4.4%, though still of the same sign (table 6.2). However, given the difficulties of obtaining

experimental Knight shifts for Rh and Pd, these calculated values may be able to assist future experimental studies.

The calculated orbital shift for Pt of approximately 6.5 to 7.0% should not be compared with the semi-experimental K_{orb} values of 0.2 to 0.4%. In addition to considering the validity of semi-empirical methodologies versus those obtained from first-principles, K_{orb} is supposed to be the paramagnetic orbital contribution to the metallic shift, having removed the diamagnetic orbital contribution by zeroing against a diamagnetic reference compound. The calculated orbital shift has a completely different reference—that of a bare nucleus.

6.3.8 Conclusions

In this chapter I have presented the first first-principles calculations of the Knight shift for Pt, Pd and Rh, and the orbital shift for Pt. These calculations converge slowly with respect to **k**-point sampling and, in particular, with respect to smearing width. As the smearing width decreases, the convergence rate with respect to **k**-points also decreases. The Knight shift of Pd and Rh was found to be sensitive to structural changes, particularly in the case of Pd where contracting the lattice parameter by 11% resulted in a decrease in the Knight shift of 23%.

The relative Knight shift contributions across the valence states have also been investigated. It was found that almost all of the Knight shift originated from states close to the Fermi surface. Whilst this does not rule out the possibility of core polarisation having an effect on the Knight shift, it does indicate that the $4s$ semi-core states in Pd and Rh have a negligible effect on the Knight shift. Furthermore, the agreement between the experimental

and calculated Pt Knight shifts suggests that core polarisation has only a very small effect on the Pt Knight shift.

In the next chapter we shall discuss the Knight shift in Pt, Pd and Rh surface structures.

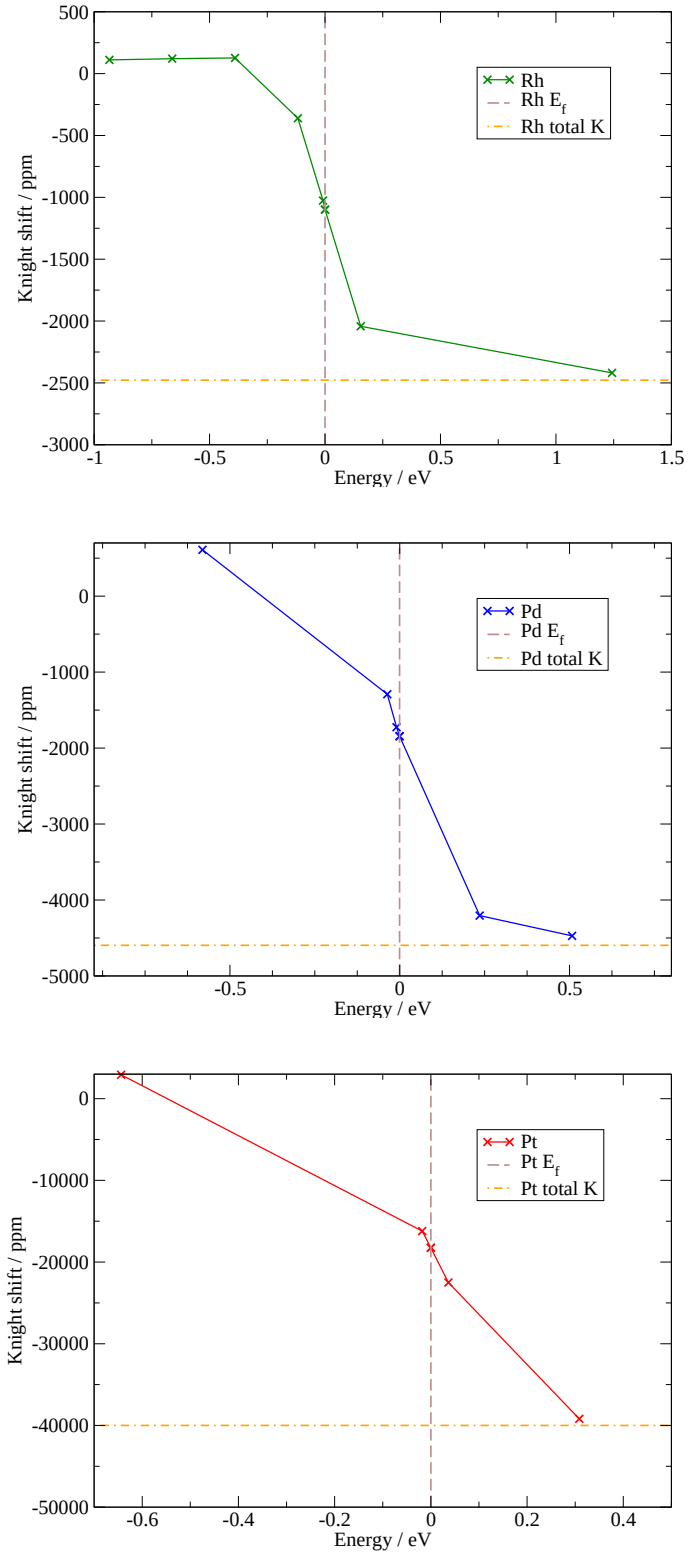

Figure 6.7: The Knight shift integrated up to a given energy (in eV) for Rh (top), Pd (middle) and Pt (bottom). The relevant full Knight shift values and the Fermi energies for each structure are also given.

Chapter 7

The Knight shift of Pt, Pd and Rh surfaces

7.1 Introduction

Having calculated the Knight shift in the Pt, Pd and Rh bulk structures, we are now well equipped to investigate the Knight shift in structures more comparable to those used in catalysts. The most important structural property for a catalyst is that it has a large surface area upon which the reactions to be catalysed can take place. As such, surfaces coated with nanoparticles are commonly used.

Much of the motivation for studying the catalytic efficiency in these nanoparticles comes from trying to gain a better understanding of the reactions taking place on the catalyst surface. NMR is an important tool for doing this. In particular, many experimental NMR studies on Pt particles are concerned with the chemisorption of CO which is known to significantly reduce their catalytic efficiency. There are two possible focusses for NMR study: one can measure either the resonance of the catalyst nuclei or the nuclei of the adsorbant molecules. In the case of Pt chemisorbed with CO, both ^{195}Pt and ^{13}C NMR exhibit a Knight shift which provides information

on the bonding environment. The Knight shift is taken to be an experimental probe of the local density of states (LDOS)—i.e. the DOS relating to a particular region of the structure, usually an atomic site or layer.

To date, the interpretation of experimental spectra of particles is placed in the context of the conclusions drawn by Clogston, Jaccarino *et al.* for bulk metals, as previously discussed in section 6.1. To recap, they argue that the Knight shift can be decomposed into separate contributions from the s-band valence electrons and the core polarisation of inner s electrons by valence d-band electrons. My calculations on bulk structures in chapter 6 provide strong evidence that this decomposition may not be entirely accurate. Furthermore, the existing analyses of experimental particle spectra are based on comparisons with other experimental spectra and fitted empirical models. In this chapter I shall first review these existing analyses before presenting my own first-principles calculations of the Knight shifts in surface structures. These calculations—the first of their kind—provide valuable insight on the validity of these existing empirical approaches.

7.2 Review of literature

7.2.1 Experimental studies

Experimental NMR on surfaces have to be conducted on samples with a large surface-area-to-volume ratio. This is because NMR is a relatively insensitive technique that requires a large number of nuclei in the same environment before a resonance can be measured with sufficient intensity. Samples of particles are therefore well suited for such studies.

^{195}Pt NMR in Pt particles

The experimental ^{195}Pt NMR spectrum for Pt particles is widely accepted to consist of two peaks: one at 1.138 G/kHz corresponding to the expected position of Pt nuclei in a bulk environment and another at approximately 1.100 G/kHz which is attributed to nuclei on the surface—see figure 7.1 for an example set of spectra. In samples consisting of Pt particles with diameters greater than approximately 1 nm, the intensity of this surface peak is shown to be significantly reduced, but that it reappears (i.e. it is significantly enhanced) when the particles are coated in adsorbates [156, 151, 157]. This observation is the reason for the assignment of the peak at 1.100 G/kHz to the resonance of the surface nuclei. Furthermore, this 'surface peak' is also at the same resonance as Pt in non-metallic compounds such as PtO_2, leading to the ubiquitous conclusion that the surface exhibits zero Knight shift [157].

There is a significant amount of broadening on these peaks due to nuclei in a range of subsurface layers which are neither in a surface environment nor yet bulk. The range in particle sizes in each sample, though kept to a minimum, further contributes to the broadening. Recording spectra using samples over a range of diameters show that the intensity of the surface peak increases whilst the bulk peak decreases with decreasing particle size. This is to be expected because as the particle size decreases the proportion of nuclei on the surface compared to those in the interior increases. The area under a peak is proportional to the number of nuclei in the corresponding chemical environment. NMR spectra produced by Rice *et al.* and Tong *et al.* clearly show this trend across three samples with average diameters of

8.8 nm, 2.5 nm and 2.0 nm [158, 159].[1]

Yu *et al.* also conducted an early NMR study of Pt particles for diameters 3.3 nm to 10 nm as a function of temperature, diameter and magnetic field strength. They found that the broadening of the bulk peak increased with an increase in magnetic field and decreasing particle diameter, but that it was independent of temperature [161].

The layer-analysis model of Pt particles

Since it is not possible to selectively measure the NMR signal from the separate concentric layers inside a particle, the relative contributions have been estimated using a layer model, as first outlined by Bucher *et al.* [157]. This 'layer analysis' assumes that a particle can be modelled as an ideal cuboctahedron consisting of layers built up about a central nucleus, that the NMR signal from each layer can be modelled as a Gaussian and that the Knight shift for each layer tends exponentially back to its bulk value from the surface towards the centre. In this way the Knight shift K_n for the n^{th} layer (counting in from the surface where the surface layer is taken to be $n = 0$) is described as

$$K_n = K_\infty + (K_0 - K_\infty)\exp(-n/m), \tag{7.1}$$

where K_∞ is the bulk Knight shift, K_0 is the surface Knight shift, and m is the number of layers required before the Knight shift is 63% bulk-like [162]. A set of these Gaussians, one for each layer, is then fitted to the

[1] Both spectra are measured at 80 K, with samples cleaned in 0.5 M H_2SO_4 and of diameters 8.8 nm, 2.5 nm and 2.0 nm (figure 2 in [158], figure 1 in [159]). Babu *et al.* report spectra for 2.8 nm and 6 nm diameter particle samples in which the surface peak is evident, but much suppressed, and the bulk peak is shifted from the bulk 1.138 G/kHz to 1.322 G/kHz in the 6nm sample and 1.1306 G/kHz in the 2.8 nm sample [160]. They attribute this to the interior of the particle interacting with the particle surface, i.e. that the particles are so small that they are not quite bulk-like.

experimental data. The area under each Gaussian is either considered to be a 'freely fittable parameter' (in the case of Bucher *et al.* [157]) or is taken to be proportional to the number of atoms in that layer (in the case of Tong *et al.* and Yano *et al.* [162, 163]). Figure 7.1 is an example of one of these many 'layer analysis' procedures [163]. The Knight shift is shown to tend from the bulk value (taken as -3.49% using H_2PtI_6 as a reference) in the centre to K_0 at the surface.

In terms of the number of layers required for the material to become sufficiently bulk-like, Tong *et al.* obtain a value of $m = 2$ for a 2.5 nm diameter Pt sample in which the surfaces have first been electrochemically cleaned (see figure 7.2) [159]. Bucher *et al.* state that they have set $m = 1.35$ for a sample of 1.6–2.7 nm diameter particles (using a gaseous sample for NMR measurements) [157]. Yano *et al.* obtain values of $m = 3.7$, 3.1 and 1.8 for samples of diameter 1.6 nm, 2.6 nm and 4.8 nm respectively [163]. These values of m can be converted into an equivalent 'healing length'. This is the distance from the particle surface at which the Knight shift becomes 63% bulk-like. It is calculated by multiplying m by the interlayer distance. In the literature, the interlayer distance for Pt is taken to be 0.229 nm [157, 159]. The healing length for Pt particles is therefore 0.31–0.85 nm in the above studies [157, 159, 163]. Note that, in the case of the smallest particle studied by Yano *et al.*, the healing length is 0.85nm for a particle of diameter 1.6 nm; this indicates that the centre of this particle can only be 63% bulk-like at most.

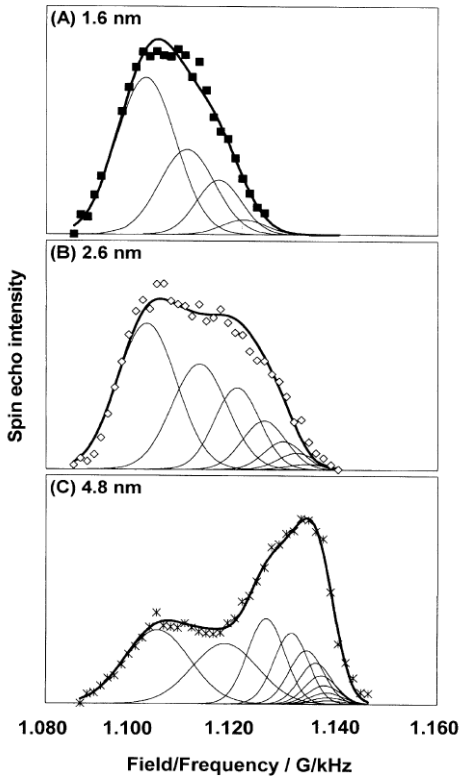

Figure 7.1: Experimental ^{195}Pt NMR spectra (points) using Pt particle samples of average diameter 1.6 nm (A), 2.6 nm (B) and 4.8 nm (C). Field/frequency ratios are expressed with respect to H_2PtI_6. The samples were electrochemically cleaned prior to measurement. The thin solid lines are the separate Gaussians used to model the NMR contribution from each layer in accordance with layer-analysis. The thick solid line shows the sum of these Gaussians. [Reproduced from [163] with permission of the PCCP Owner Societies. http://dx.doi.org/10.1039/B610573D]

Adsorbates on Pt particle surfaces

The most commonly studied adsorbant molecule is CO as it is well known for its 'poisoning' effect on Pt catalysts [159, 160, 164, 165, 166, 167, 168, 169]. Both ^{13}C and ^{195}Pt NMR are employed in these studies. It has been found that alloying Pt with Ru significantly reduces the CO poisoning effect [160].

In terms of ^{195}Pt NMR, Tong *et al.* have also conducted a study of the

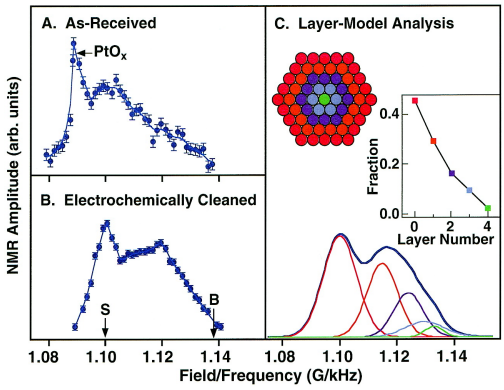

Figure 7.2: ^{195}Pt NMR spectra before and after electrochemical cleaning (parts A and B respectively). Part C shows the layer-model analysis for spectrum B, including a cross-section of the (111) plane through the ideal five-layer cuboctahedron used to model the Pt particle. The inset in part C shows the fraction of particles in each layer where layer number 0 is the surface. [Reprinted (adapted) with permission from [159]. Copyright 1999 American Chemical Society.]

effect of a range of other adsorbates—including H, Ru, CN^-, O and S (from a Na_2S solution) [162]. In all cases, the bulk-like peak which they observed at 1.131 G/kHz did not change position, indicating that the adsorbate had only short range effects on the Pt atoms. Using layer-model analysis, they concluded that this effect did not extend beyond the third layer from the surface.

In terms of ^{13}C NMR spectra, it is widely noted that when CO is adsorbed onto a Pt surface, the resonance peaks corresponding to the usually non-metallic carbon nuclei exhibit a Knight shift [159, 160, 164, 165, 166, 167, 168]. This ^{13}C Knight shift is taken to be an indication of the interaction between the CO molecule and the Pt surface. The reasoning for this stems from the Knight shift being proportional to the density of states of the bonding orbital and the square of the wavefunction of the bonding orbital [170]. The origin of this ^{13}C Knight shift is taken to be due to the

interaction between the molecule's 5σ and $2\pi^*$ orbitals ('frontier orbitals') and the Pt's d-band. There is also a correlation between this Knight shift and the value of the local density of states at the Fermi energy (E_f-LDOS) of the particle's surface [159].

7.2.2 Experimental NMR for Pd and Rh particles

Whilst studies on Pt particles are abundant, there are few existing studies on Pd and Rh particles. This is due to the relative difficulty in obtaining NMR spectra for ^{105}Pd and ^{103}Rh nuclei.

There are a few cases of Pd or Rh being alloyed with Pt or of Pd decorating a Pt surface, but the measured nuclei in these cases are still ^{195}Pt [164, 171, 168]. A small number of studies of Pd particles exist but the NMR is for ^{17}O and ^{13}C and concerns the chemisorption of CO onto the Pd surface [172, 173]. In a similar fashion to CO with Pt, these ^{13}C spectra also exhibit a Knight shift.

Vuissoz *et al.* and Burnet *et al.* have both recorded ^{103}Rh NMR spectra for Rh particles [153, 146]. Figure 7.3 shows the spectra of Vuissoz *et al.* Both studies show that there is no marked surface peak like that observed for Pt particles, but that the spectra broaden fairly uniformly about the bulk resonance of 7.4425 G/kHz as the particle size decreases. Vuissoz *et al.* observe that the 'centres of gravity' of their spectra lie at slightly lower field/frequency ratios than those in bulk, and that this shifts to even lower values when the particle size is decreased. This could be an indication of a measurable surface peak, however it is hard to draw a satisfactory conclusion because both samples contained a range of sizes (around 1.5 nm–3 nm) which the authors note could have affected the spectra [146]. The presence of

adsorbates on the particles' surfaces has also not been ruled out.

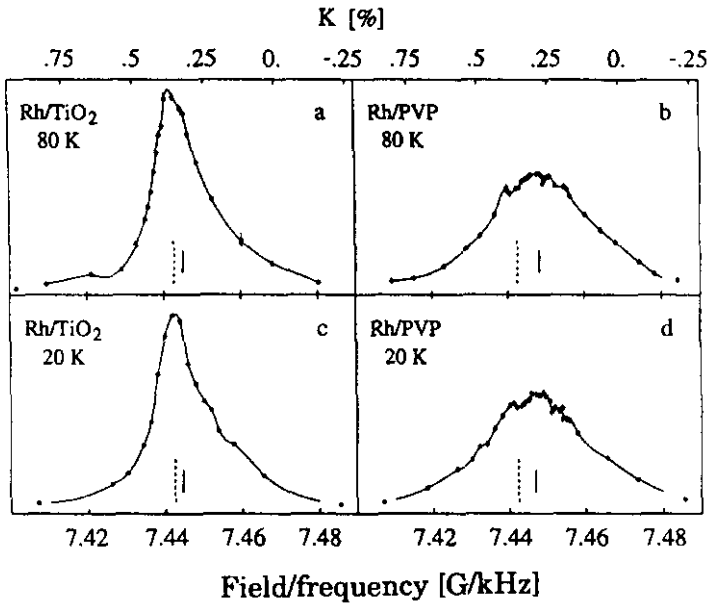

Figure 7.3: Experimental ^{103}Rh spectra for Rh particles at 80 K (a and b) and at 20 K (c and d). Parts a and c correspond to the sample in which the mode diameter was approximately 2.2 nm. In parts b and d the mode particle diameter was around 2.5 nm, but there were also a significant number of particles with diameters around 1.7 nm. The short vertical lines correspond to the 'centres of gravity of the spectra', the longer dashed lines to the Rh bulk resonance of 7.4425 G/kHz. [Reprinted from [146], Copyright 1997, with permission from Elsevier. http://www.sciencedirect.com/science/journal/00092614]

7.2.3 Theoretical Pt surface Knight shift calculations

Weinert and Freeman calculated the Knight shift in a 5-layer (001) infinite Pt slab using DFT within the local density approximation and using scalar relativistic corrections [174]. This study has been commonly cited by the experimental papers discussed above. The Knight shift was calculated by placing a range of external magnetic fields across the structure. They calculated the Knight shift for the central layer as being -4.1% which

they compared to an experimental value of -3.4%. The Knight shift for the sublayer was calculated as -2.6% and for the surface it was -0.6%. Note the trend that the surface was calculated as having a more positive Knight shift than the inner layers, a trend which the authors also noted was consistent with experiments by Rhodes *et al.* (see section 7.2.1) [156]. At this stage it is important to note that the core and valence contributions were calculated separately, in accordance with the common belief that core polarisation had a major effect on the Knight shift as discussed by Clogston *et al.* and Shaham *et al.* [135, 140] (see chapter 6). By contrast, my calculations from chapter 6 indicate that the core polarisation has a negligible effect on the Knight shift. Subsequently, the founding assumptions of Weinert and Freeman's study may need to be revised.

Alternative theoretical studies have been conducted by Efetov and Prigodin using empirical mesoscopic methods [175], Fritschij *et al.* by extending these methodologies for bulk methodologies [176], and by Pastawski and Gascón using a tight-binding methodology [177]. Further background information on the experimental NMR of metallic particles, and associated analytic methodologies, is given in the review papers of van der Klink and Brom [142] and Fraissard [145]. For further information specifically on metal surfaces, see the review paper by Slichter [178], and for an additional discussion of experimental NMR of Pt particles, see my review paper [26].

7.3 First-principles calculations

In order to calculate the Knight shift for Pt, Pd and Rh surfaces so that it might be compared to the existing literature, there are two candidate structures. The first is an infinite slab similar to that used by Weinert and

Freeman [174], the second a spherical particle or cuboctahedron similar to that used in layer-analysis (section 7.2.1). In the context of first-principles calculations involving planewaves, the latter would be extremely computationally expensive. It would require large amounts of vacuum in all three dimensions in order to ensure that there was no interaction between the periodic images.[2] Furthermore, the number of atoms required to create a structure with a suitable number of layers would need to be extremely large. A 2.0 nm sized cuboctahedron with only 5 layers would require ∼300 atoms, whilst a 8.8 nm cuboctahedron with approximately 20 layers would require ∼29000 atoms [158]. In order for my calculations to be computationally viable, I have therefore chosen to use slab structures, infinite in two directions and bounded by sections of vacuum in the other. The surfaces were (001) and without any surface reconstruction.

There is one question to bear in mind at this stage: how representative is a simple slab structure to an experimental surface or nanoparticle? If the Knight shift at the surface can be shown to be distinct from its inner layers it would be possible to gain some insight into the trends in the Knight shift at a surface compared to that in bulk. The small m values of approximately 2 layers indicate that this might not be an unreasonable prediction.

The (001) surfaces of Pt, Pd, Rh were constructed with thicknesses of 5 and 7 atomic layers using the relaxed bulk structures as a starting point. By way of example, figure 7.4 shows the 5-layer Pt structure. These structures were then relaxed within the constraints of symmetry, fixing both the angles between cell axes and the magnitude of the [001] cell axis. The

[2]The tight-binding calculations mentioned in section 7.2.3 and any first-principles calculations using Gaussian orbitals as the basis set would not require periodic images and therefore also no vacuum.

structures were relaxed until the forces between the atoms were less than 2.5×10^{-2} eV/Å, the stress on the unit cell was less than 0.05 GPa, the change in the total energy per atom between successive iterations was within 1×10^{-5} eV and the change in atomic displacement between successive iterations was less than 5×10^{-4} Å. This resulted in a total of 12 structures: the relaxed and non-relaxed versions of 5- and 7-layer surfaces for each of the three metals. For convenience, I shall refer to the initial non-relaxed structures as structures 'A', and the relaxed ones as structures 'B'.

The pseudopotentials used for the calculations reported in sections 7.3.1 and 7.3.2 were the same ultrasoft pseudopotentials used for the equivalent calculations on bulk metals reported in section 6.2. Likewise, the PBE functional was used for all calculations. In addition to the usual convergence tests for planewave cut-off and **k**-point sampling, the vacuum spacing between the layers also had to be converged so that there was no interaction between the periodic images. This was carefully checked each time a different parameter was calculated. 15 Å was determined to be a very reasonable vacuum spacing in all cases.

A note on symmetry: the values of all properties calculated below are the same for atoms in equivalent positions above and below the central layer. This is true for all the layered structures considered here, whether relaxed or not. Therefore only the properties corresponding to one set of layers (one of the two possible surfaces to the centre) will be shown here.

7.3.1 Structural distortion

For the relaxation calculations, the length of the **c**-axis and the angles between all axes were held constant. The length of the **a**- and **b**-axes and

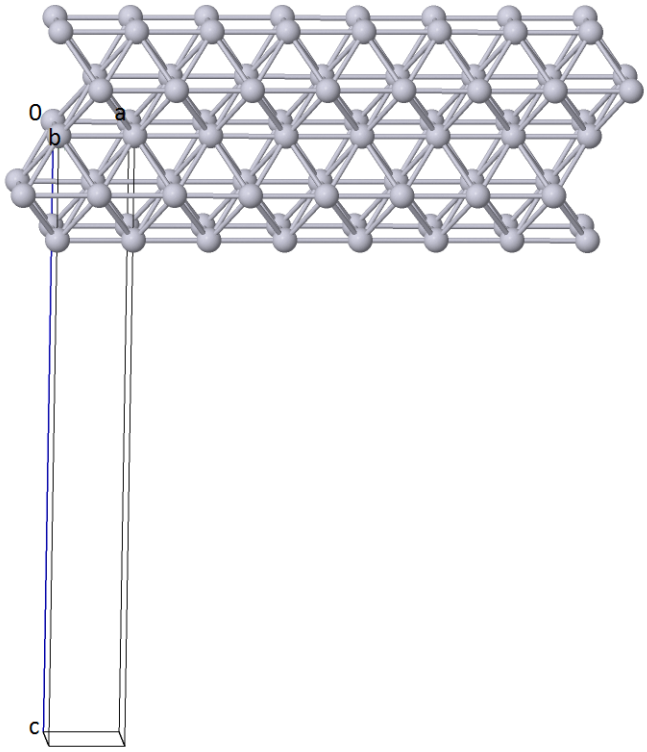

Figure 7.4: The Pt 5-layer 'A' structure. This shows 8×2×1 unit cells. The unit cell is shown with the **a**-axis pointing to the right, the **b**-axis out of the page and the **c**-axis pointing down.

the positions of the atoms were allowed to move within the constraints of symmetry. The **a** and **b** lattice parameters of all six 'A' structures (Pt, Pd, Rh for 5 and 7 layers) contracted upon relaxation as shown in table 7.1.

The relaxed bond lengths across all structures were within 2.65–2.85 Å, with Rh having the smallest bond lengths and Pt the largest. This is a similar trend to the relaxed bulk structures where the relaxed bond lengths were 2.71 Å, 2.80 Å and 2.81 Å for Rh, Pd and Pt respectively.

Upon relaxation, the outer layers moved apart in the case of the Pt surfaces, but contracted in the case of Pd and Rh. An indication of this can be seen from the changes in the surface-to-subsurface bond lengths shown in table 7.2, but it is also shown by an analysis of the change in atomic positions parallel to the **c**-axis. Table 7.2 also shows that the degree of structural distortion within the inner layers is less than that nearer to the surface.

	Initial 'A'/Å	Final 'B'/Å	% change from 'A' to 'B'
Pt 5-layer	2.808	2.739	-2.47
Pt 7-layer	2.808	2.753	-1.98
Pd 5-layer	2.796	2.755	-1.46
Pd 7-layer	2.796	2.769	-0.96
Rh 5-layer	2.707	2.676	-1.16
Rh 7-layer	2.707	2.687	-0.74

Table 7.1: The initial **a**-axis lattice parameter and the corresponding lattice parameter upon relaxation. The **a**- and **b**-axis lengths are the same due to symmetry. The precision in the lattice parameters is to within at least 0.005 Å. Percentages are presented with respect to the initial 'A' lattice parameter.

	Surface-subsurface	Subsurface-subsubsurface	Sub(sub)surface-centre
Pt 5-layer	0.52	-	0.47
Pt 7-layer	0.66	0.84	0.45
Pd 5-layer	-0.87	-	-0.79
Pd 7-layer	-1.20	-1.03	0.31
Rh 5-layer	-2.04	-	0.11
Rh 7-layer	-1.39	-0.46	-0.17

Table 7.2: The change in bond lengths upon structural relaxation, presented as a percentage of the non-relaxed 'A' structure bond length. The bond lengths investigated are those between atoms in adjacent layers.

7.3.2 Densities of states (DOS)

A set of carefully converged DOS for the structures was constructed with all energies zeroed at the Fermi energy, E_f. As expected, the DOS contain similar features over all structures. Figures 7.5a, 7.5b and 7.5c show the total DOS and the DOS projected onto s, p and d angular momentum channels (PDOS) for the 5-layer 'B' structures of Pt, Pd and Rh respectively. As expected, all contain broad, low-lying bands for s- and p-like channels, and large peaked d-like states grouped around the Fermi level. The features are very similar to their bulk equivalents in the previous chapter including the energy ranges for the d-band which is approximately 5 eV in width for Pd compared to 7 eV for Pt and Rh. Also, the highest energy d-like peak for Rh is approximately 0.5 eV above E_f, compared to Pt and Pd where it is situated at E_f, as in the bulk cases.

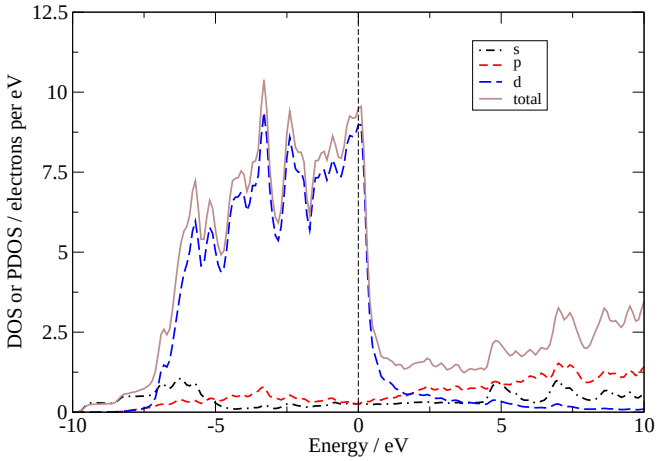

(a) Pt(001) 5-layer 'B' structure.

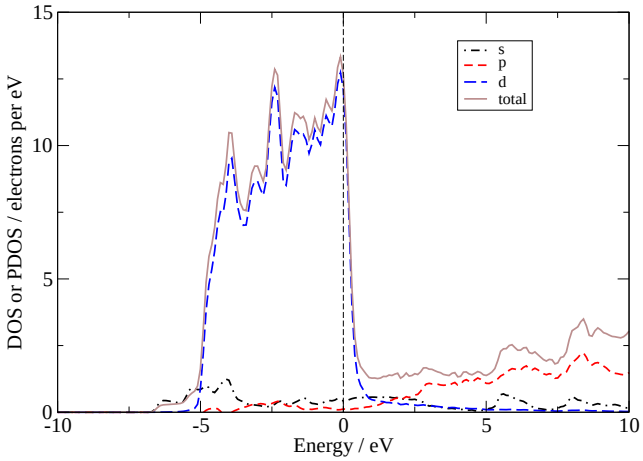

(b) Pd(001) 5-layer 'B' structure.

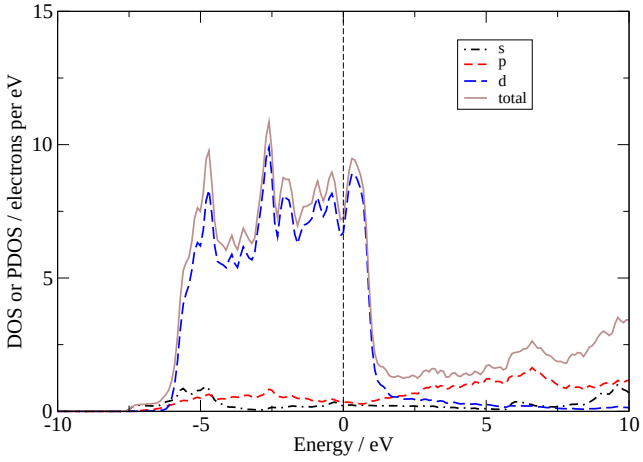

(c) Rh(001) 5-layer 'B' structure.

Figure 7.5: DOS and angular PDOS for the 5-layer 'B' structures for (a) Pt, (b) Pd and (c) Rh.

The local density of states for each layer (LDOS), as in the case of the total DOS, exhibit similar features across all the structures. Figure 7.6 shows the LDOS across the Pt 5-layer 'B' structure, from which it can be seen that the electron energies in the surface layer are slightly higher than in the subsurface layers.

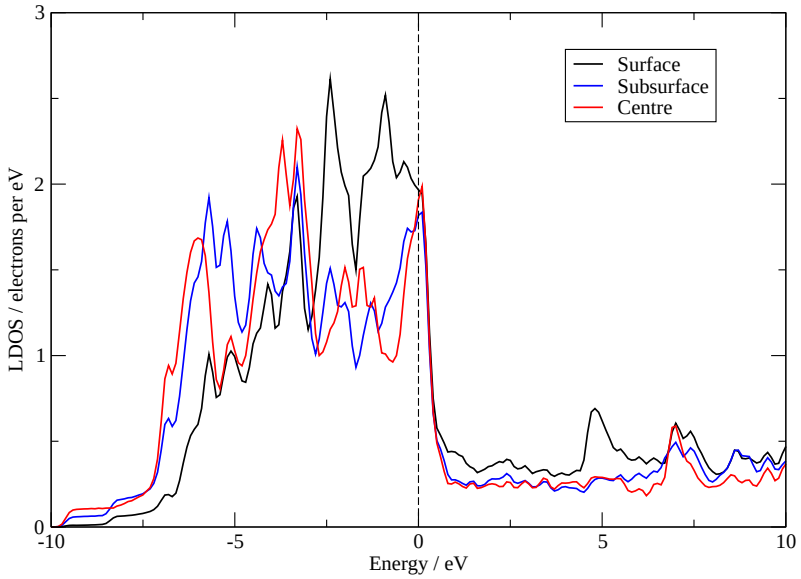

Figure 7.6: LDOS across the Pt(001) 5-layer 'B' structure.

Given that the total DOS appear to be similar to the DOS for the bulk structures, it makes sense to compare the LDOS of the central layer to the bulk total DOS. Figure 7.7 shows the comparison between the central layer of all four Pt surfaces with that of the bulk. It is clear that the LDOS of the central layers are very similar to that of the bulk, with the four main peaks below and at E_f lining up well across all structures. The shift in the LDOS across the different layers in figure 7.6 indicates that the outer layers are not as bulk-like as the central layer.

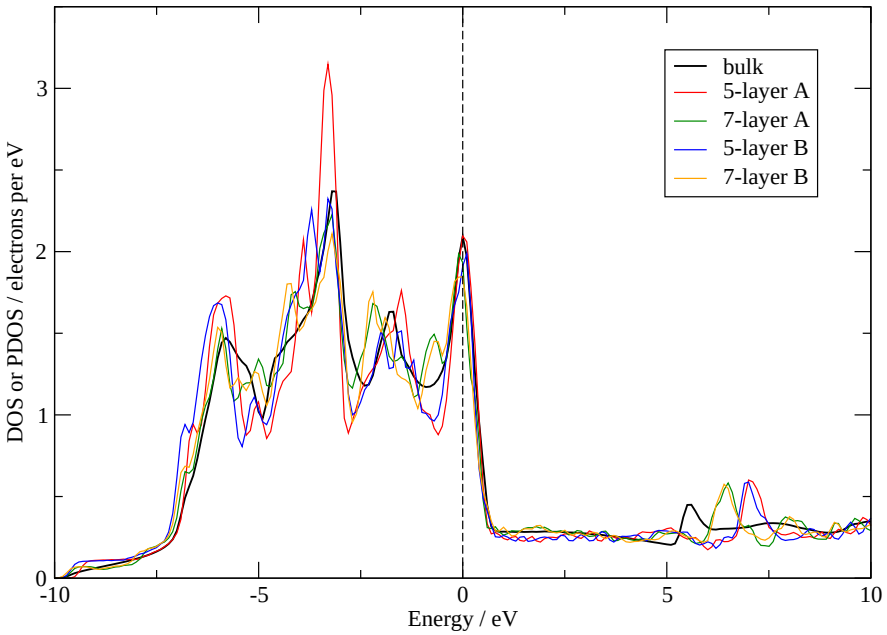

Figure 7.7: LDOS for the central layer in all four Pt(001) structures, with the DOS for Pt bulk included for comparison.

The Knight shift is often approximated by the s-like densities of states at E_f of each atom. The validity of this approximation will be tested later in this chapter. Figures 7.8a, 7.8b and 7.8c show the s-LDOS, and for completeness the d-LDOS, for 5-layer 'B' structures for Pt, Pd and Rh respectively. It can be seen that the s-like DOS for the surface atom (black line) is much larger than that for the underlying layers, implying that the Knight shift could be of greatest magnitude at the surface. This marked difference in the behaviour of the surface layer is also exhibited by the d-LDOS. The surface d-LDOS is skewed towards a higher energy compared to the underlying layers.

The s-LDOS at E_f across all atoms in all twelve structures is shown

in figure 7.9 alongside the equivalent s-like PDOS for the bulk Pt, Pd and Rh structures. Note that the DOS in this section are for the acquisition of qualitative trends only with the intention of then comparing these to the trends exhibited by the Knight shift. The total DOS, though converged carefully, had to be converged by eye because the intensity of fine details are extremely sensitive to computational parameters. Since the DOS are dominated by large d-like peaks, the tiny, by comparison, s-like contributions will be subject to a degree of numerical noise. Figure 7.9 is therefore insufficiently converged for the extraction of quantitative relationships, but will suffice for noting qualitative trends. Figure 7.9 shows a clear decrease in the s-LDOS from the surface atom to the central layer for all structures. By one layer in from the surface, all Pt and Rh structures have s-LDOS that are close to bulk. By contrast, for Pd it requires two layers before the s-LDOS is close to bulk. For all three metals, this implies that material properties decay quickly to bulk, within at most two layers—a trend which is likely to be exhibited by the Knight shift. Finally, it can be seen that structural changes between the 'A' and 'B' structures do not greatly affect the s-LDOS, implying that the Knight shift might be similarly insensitive.

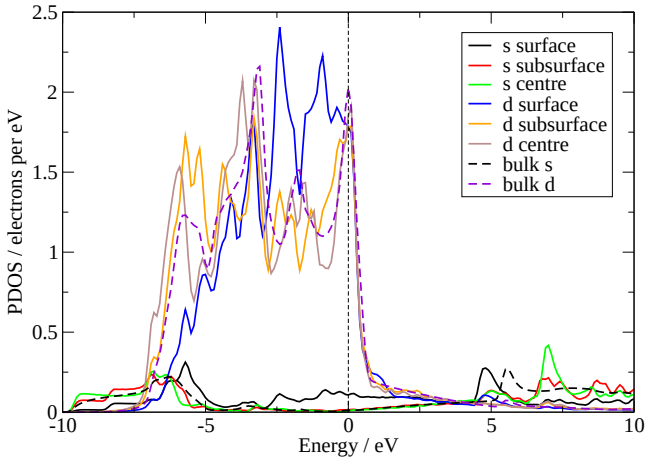

(a) Pt(001) 5-layer 'B' structure.

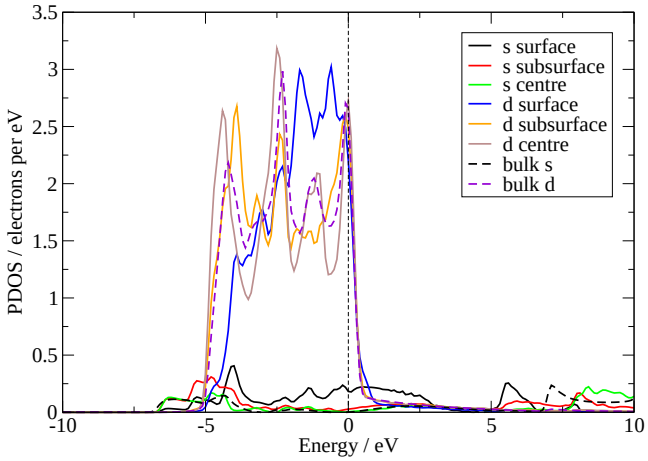

(b) Pd(001) 5-layer 'B' structure.

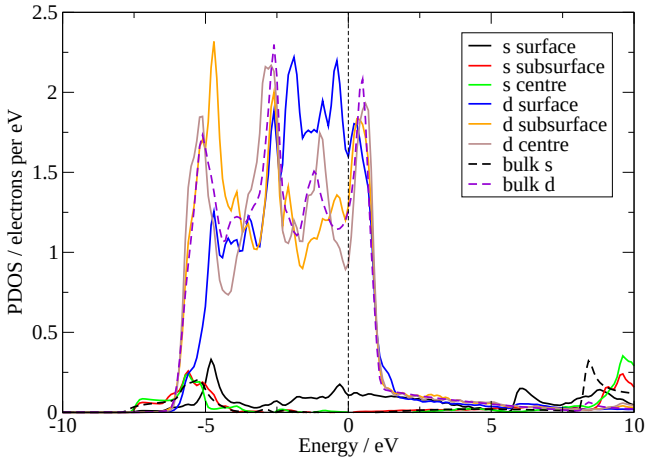

(c) Rh(001) 5-layer 'B' structure.

Figure 7.8: *s*-LDOS and *d*-LDOS across the (a) Pt, (b) Pd and (c) Rh 5-layer 'B' structures, with the equivalent bulk *s*-PDOS and *d*-PDOS included for comparison.

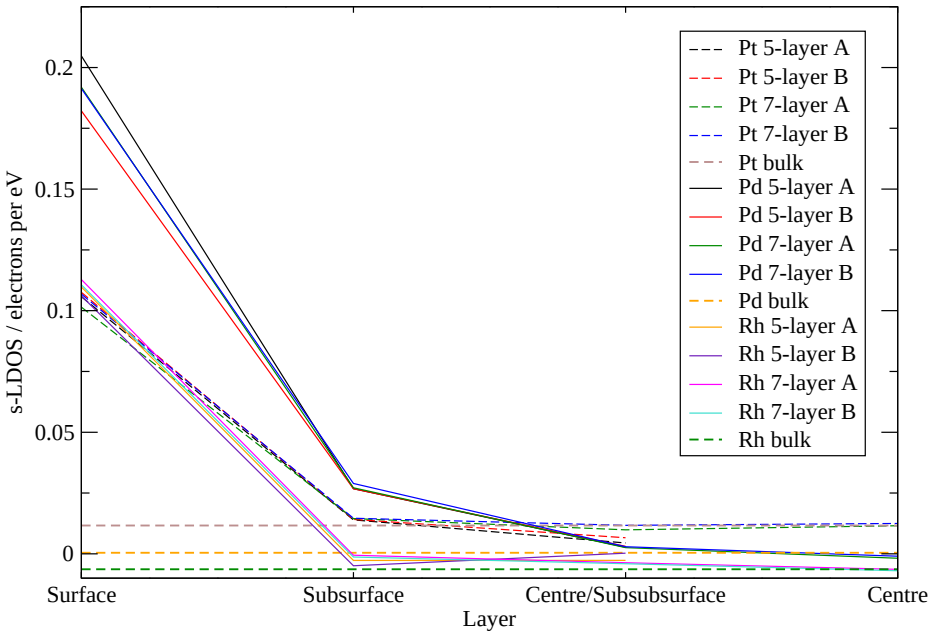

Figure 7.9: The s-LDOS values at E_f across all layers, from the surface to the centre, and across all structures investigated. Equivalent s-PDOS values for the bulk structures have also been included. Note that values here cannot be strictly converged; the instances of small negative DOS for example will be due to this. The plot is for obtaining qualitative trends only.

7.4 First-principles calculations of the Knight shift

Having discussed trends in the LDOS across the structures, we shall see if the Knight shift follows similar trends. The pseudopotentials used for the calculation of the Knight shift were the same norm-conserving ones used for the equivalent calculations on bulk metals (section 6.3). Note that since the structures investigated in this chapter are anisotropic, so too are the tensors representing the Knight shift. The Knight shifts obtained from my calculations are therefore reported in this section as a third of the trace of

the Knight shift tensor.

7.4.1 Convergence with respect to vacuum spacing, k-points and smearing

Increasing the vacuum spacing from 15 Å to 25 Å was found to have only a very small systematic effect on the Knight shift. Figure 7.10 clearly shows this for the Pd 5-layer 'A' structure over several **k**-point grids and smearing widths. Using a vacuum spacing of 15 Å therefore produced a converged set of Knight shifts to within 20 ppm for Pt, Pd and Rh.

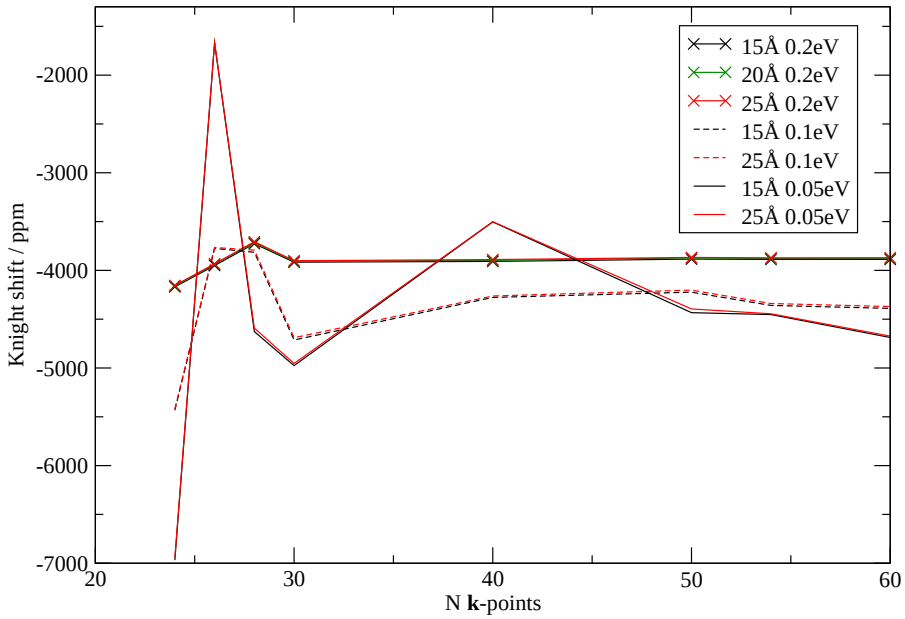

Figure 7.10: Convergence of the Knight shift over several vacuum spacings and smearing widths for the central layer in the 5-layer Pd structure 'A'. The Knight shift has also been converged with respect to the number of **k**-points on a regular N×N×1 grid (as shown on the horizontal axis).

The convergence of the Knight shift with respect to smearing width and **k**-points was also investigated. A regular N×N×1 **k**-point grid was

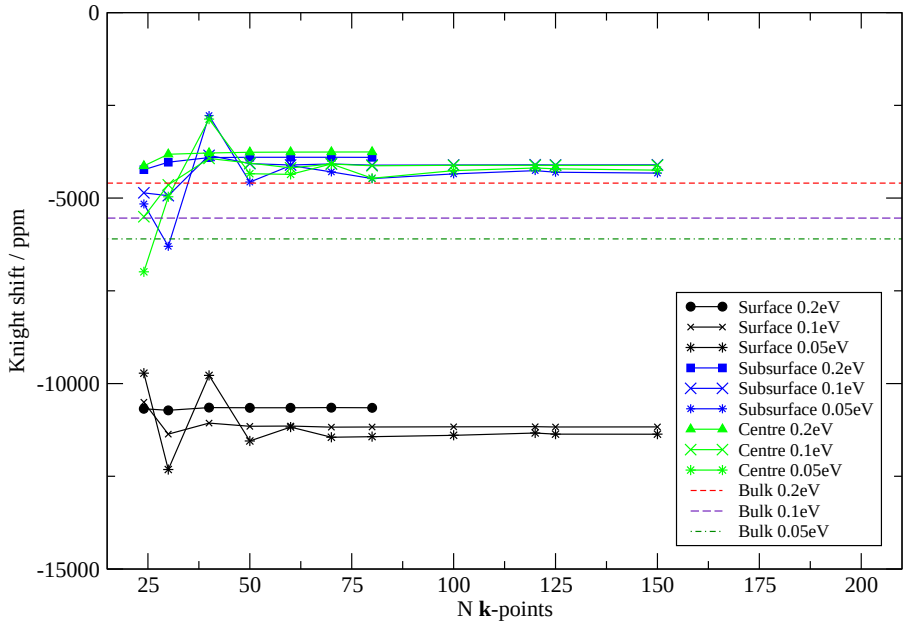

Figure 7.11: Convergence of the Knight shift across different atoms in the 5-layer Pd 'B' (relaxed) structure. The Knight shift has been converged with respect to the number of **k**-points on a regular N×N×1 grid (as shown on the horizontal axis), and over different smearing widths. The converged bulk Pd values from table 6.5 have also been included.

used. Since there is a large amount of vacuum along [001], only one **k**-point was needed to precisely sample the charge density in this direction. The **k**-points were placed $^1/_4$ along the **c***-axis for computational efficiency. Figures 7.11 and 7.12 show the convergence of the Knight shift with respect to **k**-points and smearing widths for the Pd 'B' structures. Similar trends were observed for the other structures. As was observed for the bulk structures in section 6.3, the Knight shift converges slowly with respect to **k**-points and smearing width; the smaller the smearing width, the slower the convergence with respect to **k**-points. A smearing width of 0.2 eV typically required a **k**-point grid of approximately 70×70×1 to obtain Knight shift values that were

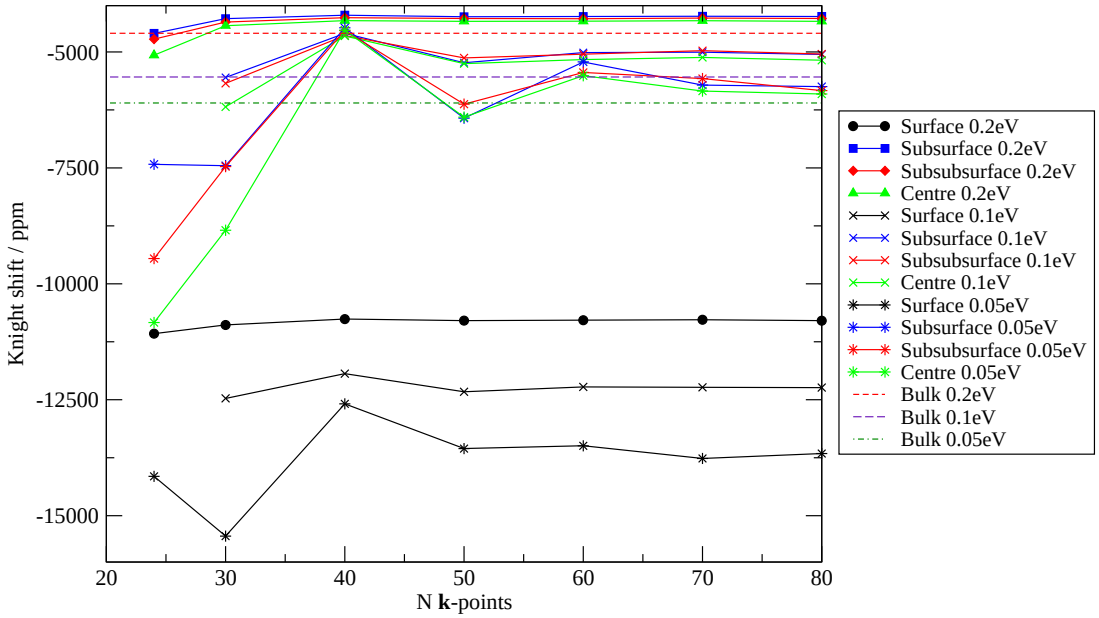

Figure 7.12: Convergence of the Knight shift across different atoms in the 7-layer Pd 'B' (relaxed) structure. The Knight shift has been converged with respect to the number of **k**-points on a regular N×N×1 grid (as shown on the horizontal axis), and over different smearing widths. The converged bulk Pd values from table 6.5 have also been included.

converged to within 0.1%, for 0.1 eV the grid was approximately 150×150×1 to obtain Knight shifts within 0.5%, and a 0.05 eV smearing required a grid of 180×180×1 for Knight shifts within 3%.

The qualitative differences noted above can be quantified more readily from single values of the Knight shift converged with respect to **k**-points. Tables 7.3, 7.4 and 7.5 show these Knight shifts for each layer, structure and smearing width. A conservative estimate of the precision of the Knight shift with respect to **k**-points has been given. This estimate has been obtained by considering the range of the Knight shift values at high numbers of **k**-points—the same procedure used when obtaining equivalent values for the

bulk structures in chapter 6. It is readily apparent that the Pt structures exhibit absolute Knight shifts that are an order of magnitude greater than the Pd and Rh structures, as was the case for the bulk structures in chapter 6. Furthermore, the surface Knight shift is also markedly larger than that of the inner layers as will be discussed later.

	Surface	Subsurface	Subsubsurface	Centre
Pt 5-layer A 0.2 eV	-133100±100	-41100±200	-	-28200±100
Pt 5-layer B 0.2 eV	-146990±20	-45230±10	-	-35010±10
Pt 5-layer B 0.1 eV	-147280±20	-50110±20	-	-35070±10
Pt 7-layer A 0.2 eV	-133700±200	-42400±200	-37000±200	-38900±200
Pt 7-layer B 0.2 eV	-146100±100	-44000±100	-41200±100	-43400±100
Pt 7-layer B 0.1 eV	-161100±100	-50400±200	-48200±200	-52200±200

Table 7.3: Converged Knight shifts (in ppm) for all Pt surface structures. Conservative estimates of the precision have also been given. Further calculations on the 'A' structures with smearing widths of 0.1 eV and 0.05 eV have not been included because I determined that the results were not sufficiently converged to extract a meaningful value.

	Surface	Subsurface	Subsubsurface	Centre
Pd 5-layer A 0.2 eV	-10910±10	-4010±10	-	-3890±10
Pd 5-layer B 0.2 eV	-10650±10	-3900±10	-	-3760±10
Pd 5-layer B 0.1 eV	-11170±10	-4100±10	-	-4120±10
Pd 5-layer B 0.05 eV	-11360±30	-4330±50	-	-4250±50
Pd 7-layer A 0.2 eV	-11190±10	-4330±10	-4320±10	-4270±10
Pd 7-layer B 0.2 eV	-10800±30	-4230±10	-4270±20	-4340±30
Pd 7-layer B 0.1 eV	-12230±20	-5050±50	-5000±100	-5200±100

Table 7.4: Converged Knight shifts (in ppm) for all Pd surface structures. Conservative estimates of the precision have also been given. Further calculations on the 'A' structures with smearing widths of 0.1 eV and 0.05 eV have not been included because I determined that the results were not sufficiently converged to extract a meaningful value.

As can be seen from figures 7.11 and 7.12 and tables 7.3, 7.4 and 7.5, changes in smearing width have a significant effect on the Knight shift. This

	Surface	Subsurface	Subsubsurface	Centre
Rh 5-layer A 0.2 eV	-8910±10	-2990±20	-	-2050±10
Rh 5-layer B 0.2 eV	-8120±10	-2740±10	-	-1940±10
Rh 5-layer B 0.1 eV	-7380±10	-2590±10	-	-1870±10
Rh 7-layer A 0.2 eV	-9080±10	-2730±10	-2030±10	-2700±10
Rh 7-layer B 0.2 eV	-8670±10	-2650±10	-1970±10	-2690±10

Table 7.5: Converged Knight shifts (in ppm) for all Rh surface structures. Conservative estimates of the precision have also been given. Further calculations on the 'A' structures with smearing widths of 0.1 eV and 0.05 eV have not been included because I determined that the results were not sufficiently converged to extract a meaningful value.

is particularly apparent for the 7-layer Pd 'B' structure in figure 7.12, where the Knight shifts corresponding to the inner layers (subsurface, subsubsurface and central) for a given smearing width are tightly grouped together and distinct from the Knight shift of the inner layers for another smearing width. Furthermore, figures 7.11 and 7.12 show that a decrease in smearing width corresponds to a more negative Knight shift, i.e. a larger paramagnetic response by the conduction electrons. The surface layer is particularly sensitive to smearing width. As was the case for the bulk structures in section 6.3, the Knight shift can therefore not be considered to be fully converged with respect to smearing width.

In practice, does the slow convergence of the Knight shift with respect to smearing width affect our ability to draw meaningful trends from the calculations? Figure 7.13 shows the difference between the Knight shift of the surface and the central layers in the Pt 7-layer 'A' structure for a set of smearing widths (red lines). It can be seen that this difference is not the same for each smearing width—the red lines do not lie on top of one another. As alluded to in the discussion on smearing width for figures

7.11 and 7.12, the change in Knight shift with respect to smearing width is greater for the surface layer than the inner layers. This provides the reason for the sensitivity of the change in the Knight shift from surface to centre over different smearings. Despite this difference in Knight shift not being equal across different smearings, the red lines in figure 7.13 are closer together than those for the surface (black) and central layers (green) which indicates that the difference in the Knight shift between the surface and centre is not as sensitive to smearing as the Knight shift for only the surface or central layer. Figure 7.14 shows this quantitatively for all three metals. The figure shows the difference in the surface-to-centre Knight shift between different smearings as a function of the surface Knight shift between the same smearings. All but one point lies below the line where these quantities would be equal (the dotted line), implying that the surface-to-centre Knight shift is less sensitive to smearing than the surface Knight shift. In most cases, the Knight shift of the inner layers is less sensitive still.

7.4.2 Variation of the Knight shift with respect to atomic position

The Knight shift in the surface structures rapidly decays to close to the bulk value, often within one layer, as indicated by figures 7.11 and 7.12 (the dotted lines are the bulk values). The magnitude of the surface Knight shift is markedly larger than all the inner layers. Both these features are also seen in the s-LDOS at E_f in figure 7.9.

Figures 7.15 and 7.16 show that there is a strong correlation between the Knight shift of a given layer and the E_f-s-LDOS. An increase in the magnitude of the Knight shift coincides with an increase in the corresponding s-LDOS. This could indicate that calculating the s-LDOS for a given

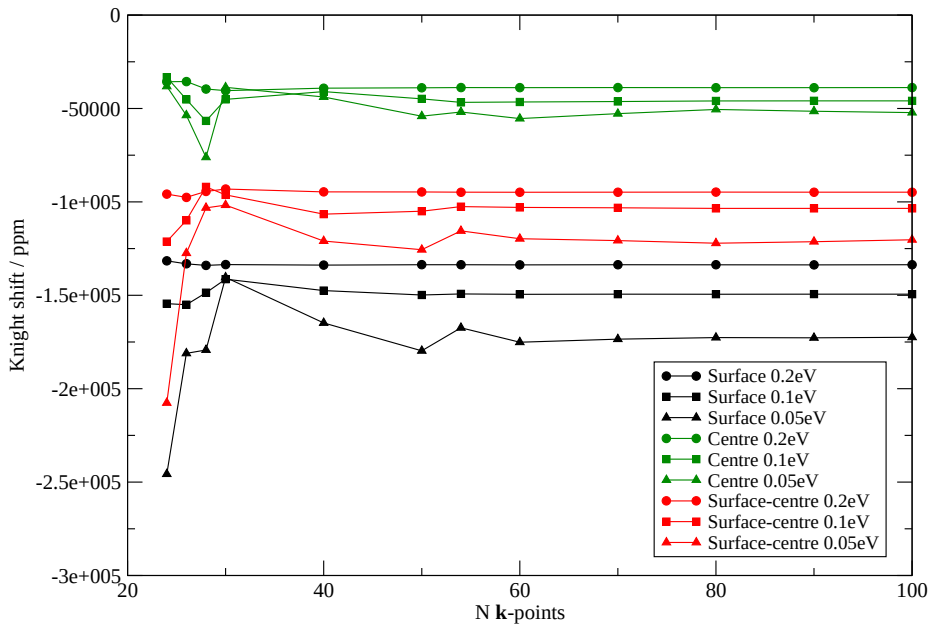

Figure 7.13: The Knight shift of the central and surface layers in the Pt 7-layer 'A' structure (with a vacuum spacing of 25 Å), and the difference between these values for each smearing width. The horizontal axis denotes the N number of **k**-points used in a regular N×N×1 grid.

structure is sufficient to extract broad trends on the behaviour of the Knight shift. However, the strength of the correlation has yet to be fully determined owing to the slow convergence of the DOS and Knight shift calculations, as discussed in sections 7.3.2 and 7.4.1 respectively. Furthermore, the correlation could be affected by the choice of pseudopotential used for the DOS calculations, owing to the sensitivity of the calculated DOS to the basis set.

Figures 7.15 and 7.16 are also useful for highlighting trends in the Knight shift across structures. The points corresponding to the surface layers are situated towards higher *s*-LDOS values and greater absolute Knight shifts, and are distinct from the inner layers (also shown in figures 7.11 and 7.12). There is a considerable spread in the Knight shift and *s*-LDOS values for

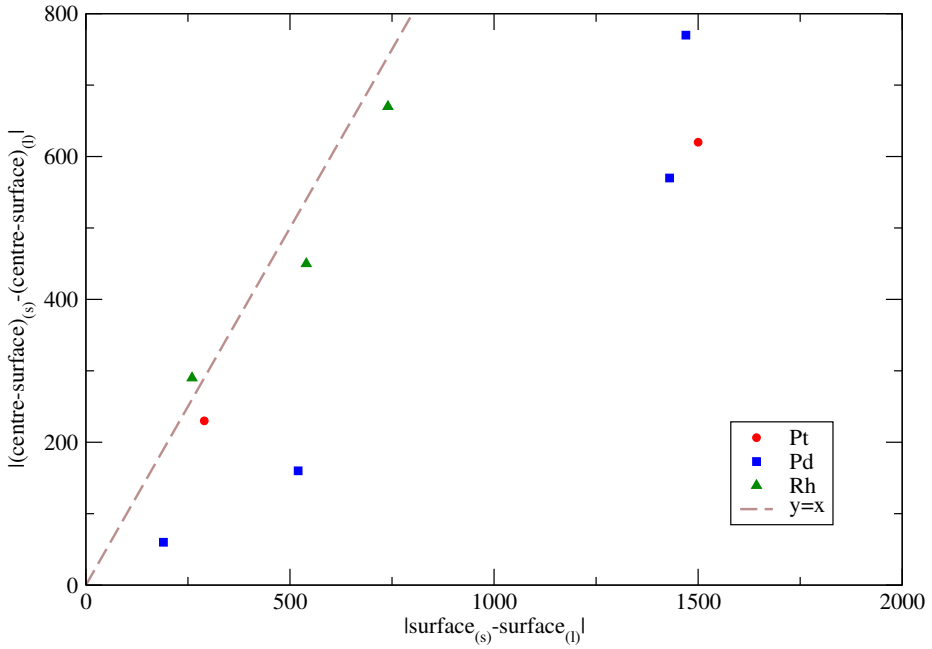

Figure 7.14: The difference in the surface-to-centre Knight shift between successive smearings (i.e. from 0.2 eV to 0.1 eV, or 0.1 eV to 0.05 eV) as a function of the surface Knight shift between successive smearings. Successive smearings are denoted by subscripts 's' and 'l'. The dotted line denotes where these values would be equal. The Pt point at (1500, 620) has been divided by 10 so that it fits neatly within the plot—i.e. its true value is (15000, 6200). The figure uses the converged values from tables 7.3, 7.4 and 7.5 to calculate the differences between the Knight shifts.

these surface layers across the range of structures (element, number of layers, 'A' or 'B' structures and smearing widths) in comparison to those for the inner layers. This implies that the Knight shift and *s*-LDOS are particularly sensitive to changes in structural distortion and numerical parameters such as smearing width. Furthermore, the surface layers corresponding to the Rh structures are not quite so distinct from the inner layers compared to those in the Pd and Pt structures, implying that there is a smaller change in the electronic structure at the surface of Rh structures than there is in Pd and Pt.

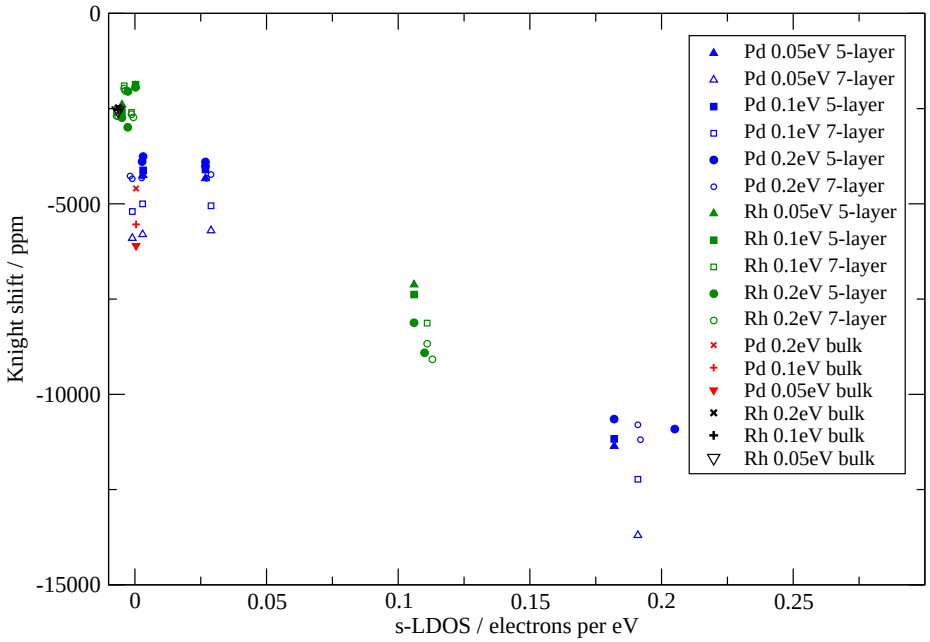

Figure 7.15: Plot to show the correlation between the Knight shift for each layer in the Pd and Rh structures against the corresponding s-LDOS at E_f. Pd layer structures are in blue, Rh layer structures in green. Smearing widths of 0.05 eV, 0.1 eV and 0.2 eV are denoted by upwards triangles, squares and circles respectively. 5-layer and 7-layer structures are denoted by filled and unfilled symbols respectively. Both 'A' and 'B' structures have been included, but have not been distinguished from one another. For comparision, the bulk Pd (red) and bulk Rh (black) points have also been included (smearing widths are denoted using different symbols to those used for the layers for clarity).

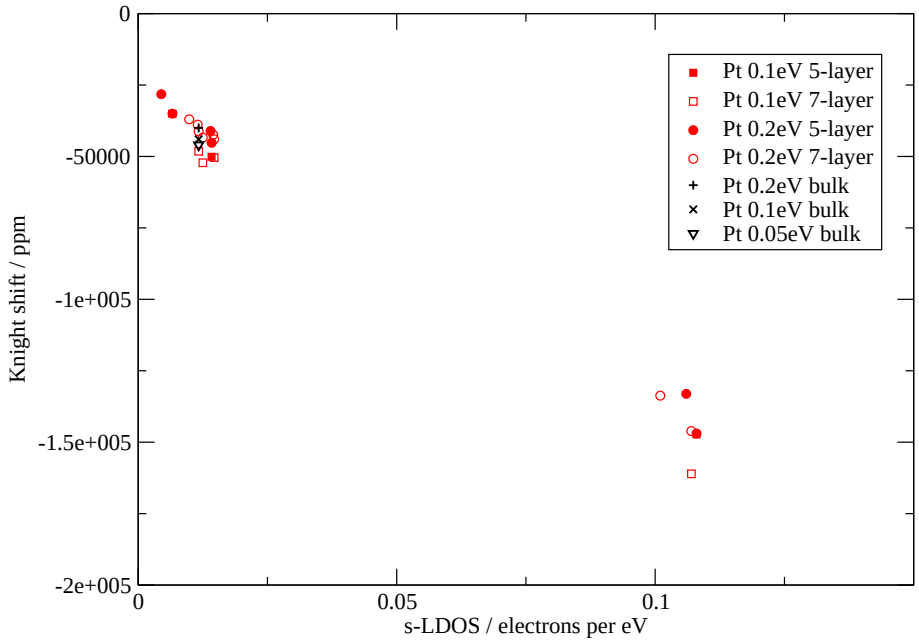

Figure 7.16: Plot to show the correlation between the Knight shift for each layer in the Pt structures against the corresponding s-LDOS at E_f. Squares and circles denote smearing widths of 0.1 eV and 0.2 eV respectively, filled and unfilled symbols denote 5- and 7-layer structures respectively. Both 'A' and 'B' structures have been included, but have not been distinguished from one another. Points for bulk have also been included for comparison (black, and using a different symbol scheme to those for the layers for clarity).

7.4.3 Comparison between the Knight shift of the central layer and bulk

Another question to address is how bulk-like the central layer is in terms of the Knight shift. Figure 7.17 shows how much the Knight shift of the central layer for each structure differs from that in bulk. I have defined the deviation as

$$deviation = \frac{(K_{bulk} - K_{centre})}{K_{bulk}} \times 100, \tag{7.2}$$

so that negative values correspond to central layer Knight shifts which are less negative than that for bulk i.e. they lie above the bulk line in plots such as figures 7.11 and 7.12.

In general, the central layer of the 7-layer structures is closer to the equivalent bulk value than the central layer of the 5-layer structures. This is to be expected as the central layer is further from the surface as the number of layers in the structure increases. Furthermore, it is only 7-layer structures that exhibit negative deviations from the bulk, meaning that the central layer has a less negative Knight shift than in the bulk. There is no clear trend for whether the structures of a different metal (Pt, Pd or Rh) tend closer to bulk, nor can any reliable conclusion be drawn on the effect of smearing width. Regarding differences between the initial 'A' structures and the relaxed 'B' structures, some preliminary patterns can be noted. Upon relaxing the Pd structures the central layer becomes less bulk-like, whilst the Rh structures exhibit more positive deviations and the Pt structures more negative deviations.

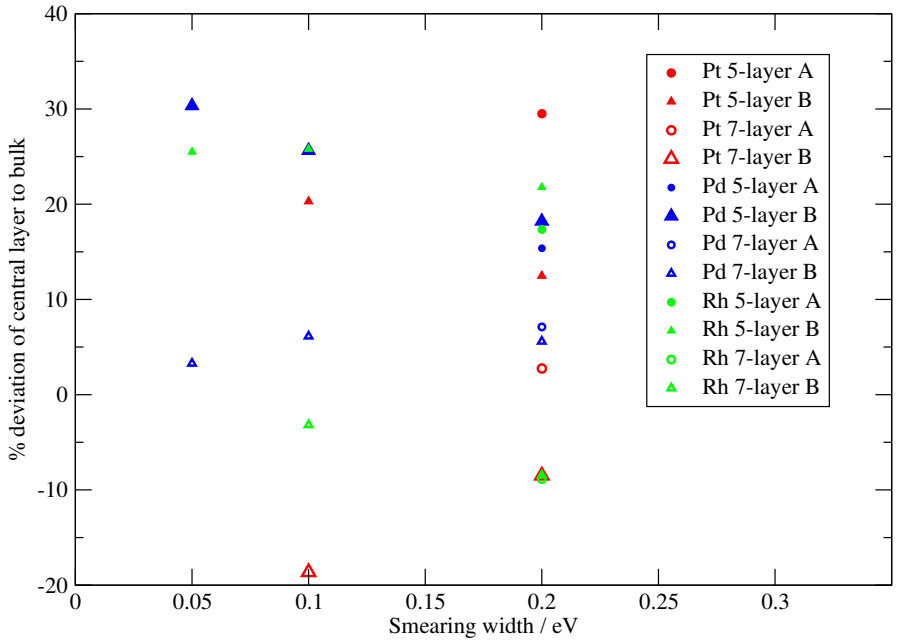

Figure 7.17: Plot to show how the Knight shift of the central layer differs to that in bulk. Values are presented as percentages of the bulk Knight shift and as a function of smearing width. Circles correspond to 'A' structures, triangles to 'B' structures, filled symbols to 5-layer structures, unfilled to 7-layer structures. Red is used for Pt, blue for Pd and green for Rh. A negative percentage means that the Knight shift of the central layer is less negative than that for bulk i.e. that the Knight shift for the central layer would be situated above the bulk (in contrast to the surface Knight shift which is always below that of the bulk).

7.4.4 Sensitivity of the Knight shift to structural changes

This leads us on to consider how the Knight shift differs from 'A' to 'B' structures, which in turn gives us an indication of the effect that structural changes have on the Knight shift. It has already been seen from chapter 6 that the bulk Knight shifts are extremely sensitive to structural distortions—in the most extreme case, a change in the Pd bulk lattice parameter of 11% corresponded to a change in the Knight shift of 23%. Figure 7.18 shows an

example **k**-point convergence for the Rh 5-layer 'A' and 'B' structures. The variations in the Knight shift over different **k**-point samplings are almost identical across 'A' and 'B' structures, but translated to less negative values upon relaxation.

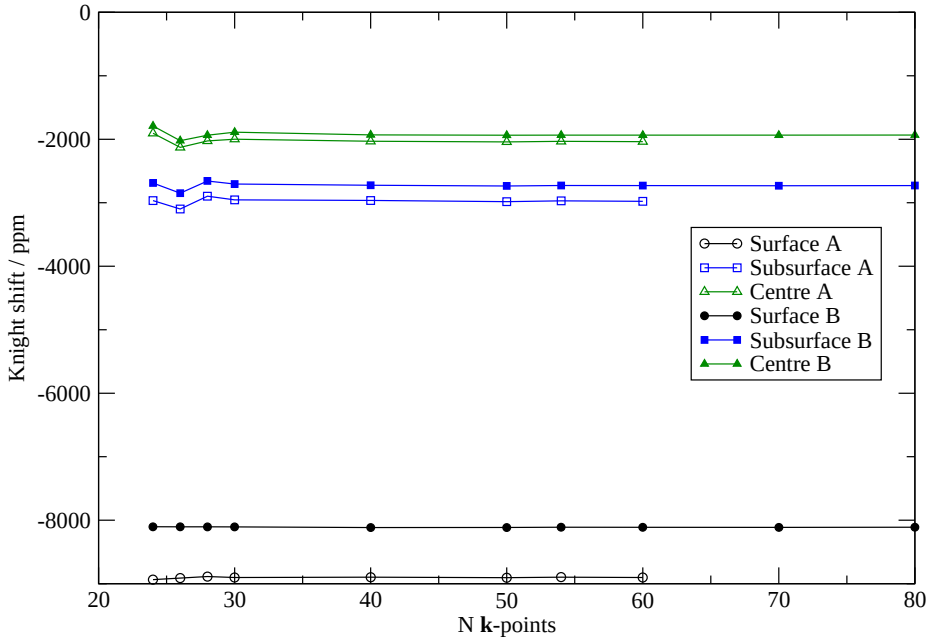

Figure 7.18: The change in the Knight shift between structures 'A' and 'B' for 5-layer Rh using a 0.2 eV smearing width and 25 Å vacuum spacing. The horizontal axis denotes N **k**-points on a regular N×N×1 grid.

Figure 7.19 shows that, for all structures, the Knight shift of the surface layer tends to be the most sensitive to structural changes and the central layer the least sensitive. We should consider why this should be the case. Figures 7.20 and 7.21 show that there is a reasonably strong correlation between the change in the Knight shift for an atom in a given layer and the bond length between the atom in this layer and the atom in the adjacent inner layer. Both figures—the figure for the Pd and Rh structures

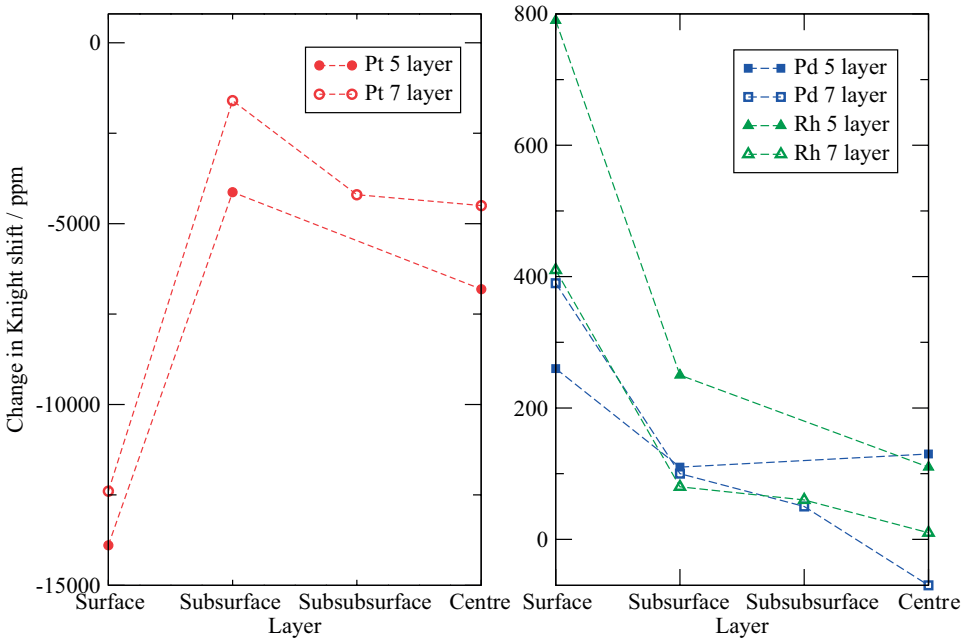

Figure 7.19: The change in the Knight shift between structures 'A' and 'B' across all layers in all 5-layer and 7-layer structures of Pt, Pd and Rh. The Knight shift values are for a 0.2 eV smearing width.

in particular—show that the greater the magnitude of the change in the bond length, the greater the change in the magnitude of the Knight shift. In the case of Pd and Rh, the bond lengths contracted upon relaxation and the negative (paramagnetic) Knight shift became less negative, leading to a positive change in the Knight shift upon relaxation. In the case of Pt, the structure expanded upon relaxation and the Knight shift became more negative. The correlation is weaker for Pt however due to the slight irregularity in the initial bond lengths of the 'A' structures—note the 'outlier' corresponding to the subsurface in the 7-layer structures. This is likely to be linked to the substantial structural movement in this layer between the 'A' and 'B' structures. In conclusion, the reason for the greater change in surface Knight shifts on moving from structure 'A' to 'B' compared to that in the inner layers is that the change in the Knight shift is linked to structural changes and these changes are greatest at the surface.

Finally, it should be noted that the Knight shift's sensitivity to structural distortion is not markedly greater for any particular metal. One might think that Pt is most sensitive, however when these changes are weighted by the equivalent bulk Knight shift values Pt is no more sensitive than Pd or Rh.

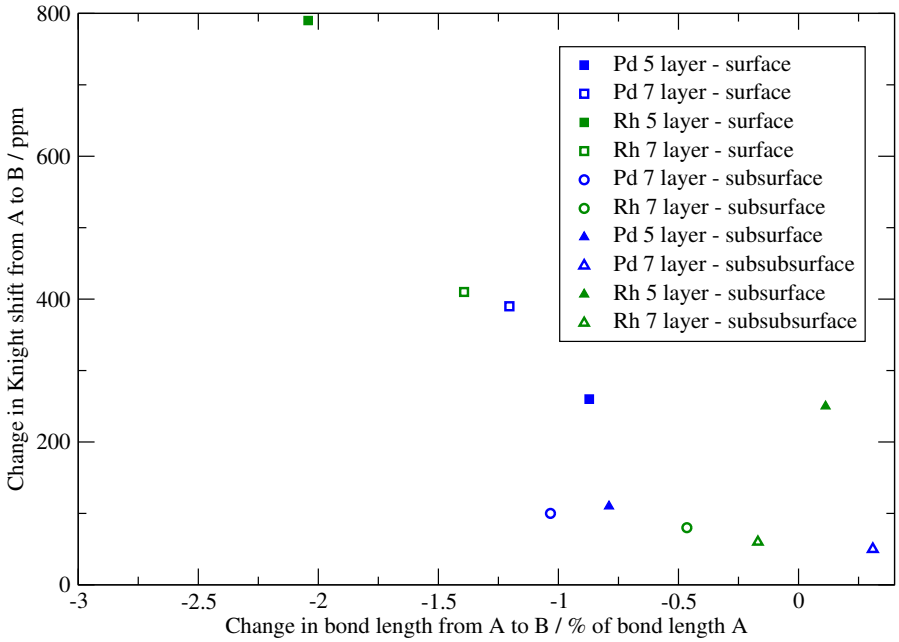

Figure 7.20: The correlation between the change in the Knight shift between structures 'A' and 'B' and the corresponding change in bond length. The change in bond length is presented as a percentage change with respect to the original 'A' bond length. The change in Knight shift for a given layer has been plotted against the bond length between this layer and the adjacent inner layer, e.g. the surface Knight shift has been plotted against the surface-subsurface bond length. The Knight shift values all correspond to a 0.2 eV smearing width. Pd and Rh are presented in blue and green respectively. Surface layers are represented with squares, the layer adjacent to the centre (subsurface for 5-layers, subsubsurface for 7-layers) with triangles, and the layer in between—in the case of 7-layer structures—with circles. These symbols are filled and unfilled for 5-layer and 7-layer structures respectively.

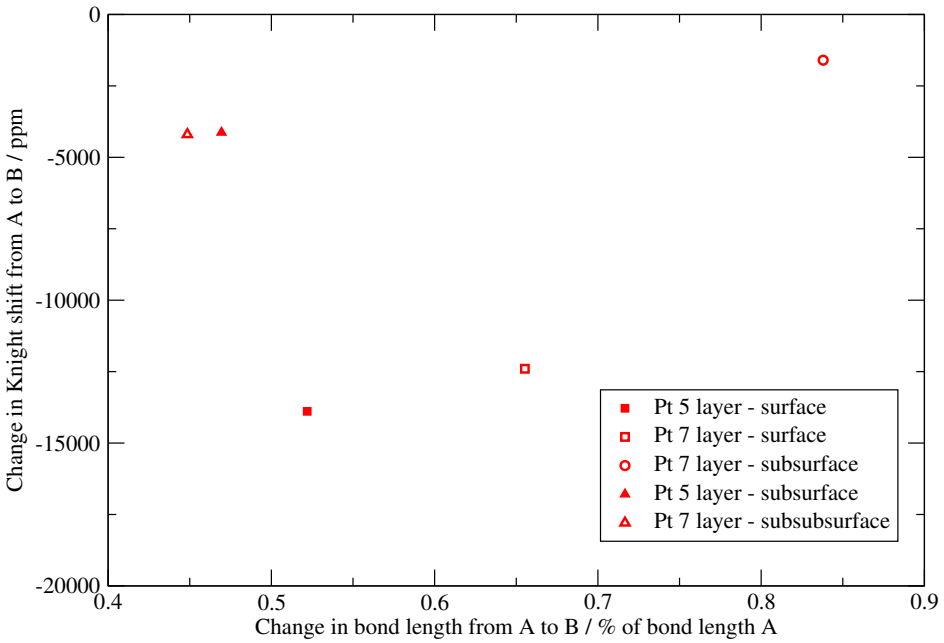

Figure 7.21: The correlation between the change in the Knight shift between structures 'A' and 'B' and the corresponding change in bond length for Pt structures. The change in bond length is presented as a percentage change with respect to the original 'A' bond length. The change in Knight shift for a given layer has been plotted against the bond length between this layer and the adjacent inner layer, e.g. the surface Knight shift has been plotted against the surface-subsurface bond length. The Knight shift values all correspond to a 0.2 eV smearing width. Surface layers are represented with squares, the layer adjacent to the centre (subsurface for 5-layers, subsubsurface for 7-layers) with triangles, and the layer in between—in the case of 7-layer structures—with circles. These symbols are filled and unfilled for 5-layer and 7-layer structures respectively.

7.4.5 Physical origin of the surface Knight shift

As discussed in this chapter so far, the calculated surface Knight shifts are much larger in magnitude than those of the inner layers. Furthermore, the Knight shifts rapidly decay towards their equivalent bulk values, within one to two layers of the surface. In order to understand the physical origin for this, the total induced spin density has been calculated by incorporating the spin response to an external magnetic field into the Hamiltonian. This is in accordance with the finite field approach for calculating the Knight shift as outlined in section 4.3.

Figure 7.22 shows the charge and spin densities through the (010) plane across the Pt 7-layer 'B' structure in the presence of a 100 T field.[3] There is little difference between the charge density in the vicinity of the surface atoms compared to that around the inner atoms. The spin density around the inner atoms is strongly localised, which provides an explanation for why the Knight shift does not vary much between the inner layers. There is a greater spin density around the surface atoms than those in the inner layer. This can also be seen from figure 7.23 which shows the spin density summed across planes perpendicular to the **c**-axis. However, the calculation for figures 7.22 and 7.23 was performed using pseudised wavefunctions and therefore the spin density shown close to the nucleus in this case is non-physical.

The real induced spin density at each nuclear site was also calculated and was found to be significantly greater for the surface atoms than for the

[3]Several magnitudes of magnetic field were tested, from 10 T to 1000 T, and across several **k**-point grids. A smearing width of 0.2 eV was used for all the calculations. The same charge and spin density trends were observed in all cases, with the total spin density increasing linearly with increasing magnetic field.

inner atoms.[4] This explains why the magnitude of the surface Knight shift is greater than the Knight shift of the inner layers.

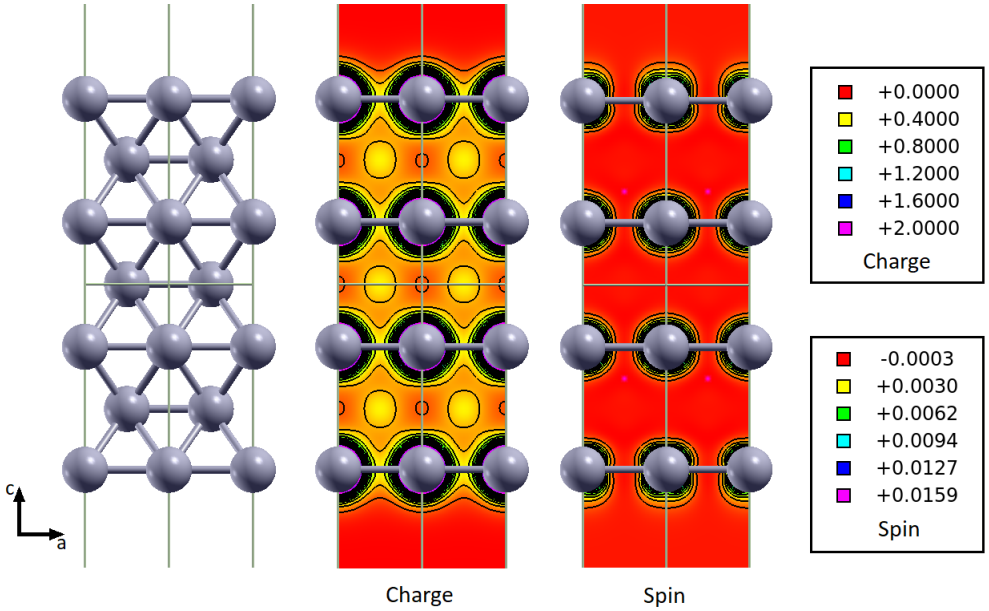

Figure 7.22: Charge and spin density plots through the (010) plane in the Pt 7-layer 'B' (relaxed) structure. The centre plot shows the charge density; the right plot shows the spin density. The left image is a projection of the structure as viewed along the **b**-axis; the second, fourth and sixth layers are situated behind the plane of the charge and spin density plots. The colour scales to the far right are expressed in $e/\text{Å}^3$ and $\hbar/\text{Å}^3$ for the charge and spin densities respectively.

The increased spin density at the Pt surface could be explained by the presence of Friedel-like oscillations in the spin density of the conduction electrons.[5] This hypothesis is backed up by the DFT calculations of Kautz and Schwartz in which a jellium model was used to simulate the behaviour of conduction electrons in a metal surface [180]. In the presence of a magnetic field, they found that the spin susceptibility was enhanced at the metal

[4]The spin density at the nucleus was also found to increase linearly with increasing magnetic field.

[5]Friedel oscillations are oscillations in the electronic charge density due to a localised perturbation in the electronic environment. The RKKY interaction between spins results in an equivalent oscillation in the electronic spin density [179, p. 157].

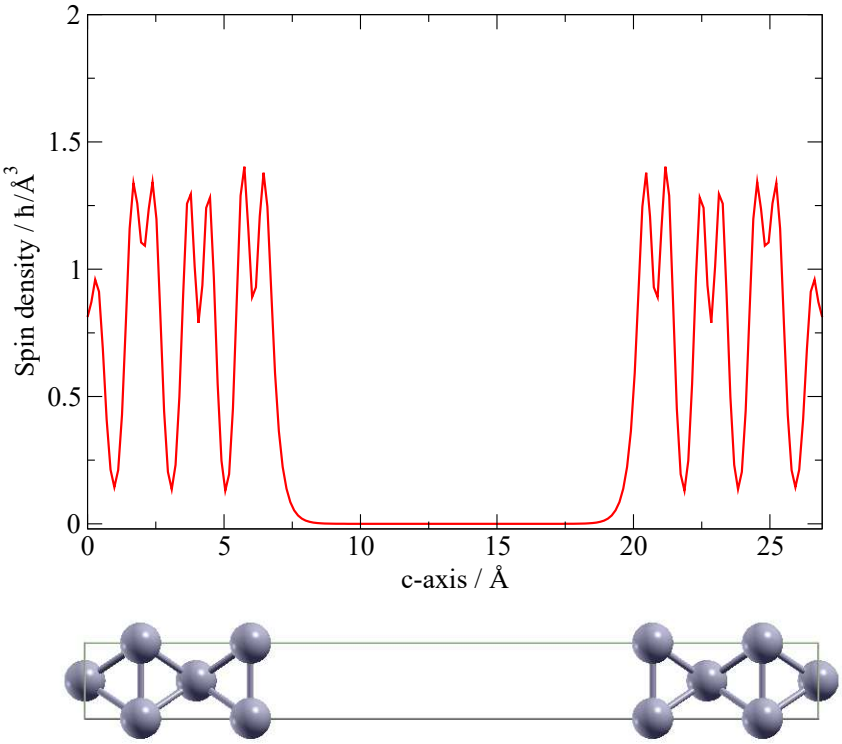

Figure 7.23: Spin density summed across the plane perpendicular to the **c**-axis and plotted as a function of distance along the **c**-axis. The Pt unit cell has been included for comparison. The decrease in spin density in the centre of each atom is a result of using the pseudised wavefunction for the calculation.

surface and decayed to the bulk susceptibility of a uniform electron gas with increasing distance from the surface. Furthermore, the spin susceptibility oscillated with a wavelength of $^{\pi}/_{k_F}$, where k_F is the Fermi wavevector. However, in the case of this model, the interaction between the electrons and nuclei was not included. When electron-nuclear interactions are taken into account, the manifestation of Friedel-like oscillations could therefore depend on the atomic species and the atomic packing at the surface.

If the Fermi surface for the Pt 7-layer structure is approximated as a

sphere, the Fermi wavevector is $\sim 7.39 \times 10^9\,\mathrm{m}^{-1}$ and the period of spatial oscillation is therefore $\sim 4.25\,\text{Å}$. Given that the Pt slab is 12.1 Å thick, this results in approximately 3 periods of Friedel-like oscillation across the thickness of the slab. The calculated Knight shift values for the Pt structures in table 7.3 appear to correlate qualitatively with this approximation. However, in order to investigate this correlation further, the Knight shift should be calculated for a set of Pt slab structures of increasing thickness and of differing surface planes—for example (111). It should be noted that oscillations in the Knight shift have been used to explain the broadening of experimental Knight shifts in Pt alloys [181] and Pt particles [156, 182, 183].

7.5 Calculations of the orbital shift

The orbital shift in the Pt structures was also investigated, again with the same norm-conserving pseudopotential used for bulk Pt (section 6.3). Table 7.6 shows the orbital shifts for the Pt 5- and 7-layer, 'A' and 'B' structures converged with respect to **k**-points. These values are converged to within 1%. The **k**-point convergence was slower for the orbital shift calculations compared to those for the Knight shift. **k**-point grids of up to $195 \times 195 \times 1$ were required to converge the orbital shift to within 500 ppm, as seen in table 7.6, whereas grids of at most $120 \times 120 \times 1$ were required to converge the Knight shift to within 100–200 ppm.

Following a similar trend to that with the Knight shift, the orbital shift rapidly tends to the bulk orbital values of 65000 ppm and 68200 ppm for smearing widths of 0.2 eV and 0.1 eV respectively. The variation in the orbital shift across the layers is however much less than that for the Knight shift. Whereas the Knight shift for the surface layer is typically around

350% of the bulk value (the central layer having a Knight shift close to the bulk value), the surface layer orbital shift is only around 90% of the bulk (i.e. it differs by around 10% of the bulk value). The orbital shift is also less sensitive to structural changes than the Knight shift, with the values differing by only a few 100 ppm between structures 'A' and 'B'. These differences are so small that they are very close to the estimated convergence errors. As a result, it would not be meaningful to consider correlations between structural changes and the changes in the orbital shift.

	Surface	Subsurface	Subsubsurface	Centre
Pt 5-layer A 0.2 eV	59200±500	63300±200	-	65200±400
Pt 5-layer A 0.1 eV	63700±200	67300±200	-	68000±500
Pt 5-layer B 0.2 eV	59800±200	63400±100	-	66500±200
Pt 5-layer B 0.1 eV	63800±200	67200±200	-	69400±200
Pt 7-layer A 0.2 eV	57400±300	63300±600	64900±300	63900±100
Pt 7-layer A 0.1 eV	62400±500	67100±500	67400±200	67600±500
Pt 7-layer B 0.2 eV	58400±200	63200±200	65700±100	64000±200
Pt 7-layer B 0.1 eV	62900±200	66800±100	68100±300	67500±300

Table 7.6: Converged orbital shifts (in ppm) for all Pt surface structures. Conservative estimates of the precision have also been given.

7.6 Conclusions and further work

7.6.1 General trends

I have presented the first set of fully *ab initio* calculations on the Knight shift in surface structures. These have shown that the Knight shift is extremely sensitive to changes in atomic environment, as indicated by the large difference between the Knight shifts of the surface and central layers, and the large change in the Knight shift upon structural relaxation. By comparison, the orbital shift is much less sensitive. The surface Knight shifts are

found to be much larger in magnitude than the Knight shifts of the inner layers, which can be explained by the higher induced spin density present at the surface. Both the Knight and orbital shifts rapidly decay to their bulk values—within two or three layers into the structure.

The **k**-point convergence of the Knight and orbital shifts is slower for layered structures compared to that in bulk. For example, the coarsest grid used for the bulk calculations corresponded to a spacing of $0.0075\times2\pi\text{Å}^{-1}$ (in the case of the Knight shift being converged to within 0.1% for Rh bulk) compared to $0.0062\times2\pi\text{Å}^{-1}$ for the layered structures (in the case of the Knight shift for the 5-layer Rh structure being converged to within 0.12%). Furthermore, as also seen in the bulk study, this convergence is slower for the orbital shift than the Knight shift. As with the bulk structures, smearing width has a large effect on the Knight and orbital shifts for the surface structures, so it is not possible to obtain definitive values which can be compared with experiment. The difference in the Knight shift between the surface and central layers is however less sensitive to smearing width than the values for the individual layers and can more readily be used as a guide for experiments. Furthermore, the qualitative trends across the layers should serve as a useful guide for experiments.

7.6.2 Comparison with literature and further work

Finally, we return to the main questions raised towards the beginning of this chapter:

1. Does the *s*-LDOS at the Fermi energy provide an adequate indication of the Knight shift?

2. How representative is an infinite slab model of real-life particles, and

can my results therefore be compared to experimental results?

The relationship between the Knight shift and the *s*-LDOS

Figures 7.15 and 7.16 show that an increase in the s-LDOS at E_f correlates with an increase in the magnitude of the Knight shift. As discussed however in section 7.4.2, it is currently not clear exactly how strong this correlation is due to the slow convergence of the DOS and Knight shift calculations, and because the effect of different pseudopotentials has yet to be investigated. Care should still be taken when interpreting experimental Knight shifts in terms of LDOS.

Relevance to experimental NMR of nanoparticles

In order to assess how representative a slab structure is to a spherical nanoparticle, we need to examine the rate at which the surface Knight shift decays to bulk and its sensitivity to structural changes. My results have shown that in 5-layer structures the Knight shift of the central layers differs at most by 30% to that in bulk, meaning that the Knight shift is at least 70% bulk-like within two layers of the surface. This correlates well with the estimated values of m =1.35–3.7 obtained via layer analysis in the literature (discussed in section 7.2.1).[6] By the third layer in from the surface (i.e. the central layer of the 7-layer structures) this increases to being at least 80% bulk-like (in all but the 7-layer Pt 'B' structure the central layer was at least 90% bulk-like). There are however cases for the 7-layer structures where the most bulk-like layer is not the central one, but the one adjacent to it. As

[6] In the case of Pt, the interlayer spacings in my structures were in the range 0.193–0.205 nm, compared to the value of 0.229 nm used in the literature [157, 159]. Using the calculated interlayer spacings for the 5-layer Pt structures, and $m = 2$, the estimated healing lengths are 0.388–0.408 nm, which is again within the range estimated in the literature.

discussed in section 7.4.5, this could be due to Friedel-like oscillations in the electron spin density. Investigating slab structures with a greater number of layers than those used here could provide further insight on oscillating Knight shift values and the number of layers required before a several-layer region of near bulk-like material is achieved.

My results have also shown that the Knight shift is extremely sensitive to structural environment. The most sensitive case was for the surface of the Pt 7-layer structure (0.2 eV) for which a change in the Knight shift of -12400 ppm (a 9% change with respect to the surface Knight shift of the corresponding 'A' structure) corresponded to a 0.02 Å change in bond length. It could therefore be the case that the surface Knight shift is highly sensitive to surface reconstructions, different planes and surface defects—all of which could be present on a particle's surface. These structural differences could somewhat account for the discrepency between my calculated surface Knight shift for Pt (which was shown to be large and negative) and the experimentally measured ^{195}Pt surface Knight shift which was close to zero. The presence of adsorbates, such as oxygen, could also explain why the experimental surface Knight shift is zero instead of being large and negative; for example, PtO_2 also exhibits no Knight shift [157]. The lack of a clear surface peak in the experimental ^{103}Rh spectra (section 7.2.2), in which there could also be some broadening towards higher field/frequency ratios, could indicate that there may be a surface Knight shift for Rh particles that is more negative than bulk in accordance with my calculations.

To investigate surface Knight shifts in more detail, further calculations could be conducted using different planes (for example (111)) and surface reconstructions (for example the 5×20 Pt reconstruction mentioned by Wein-

ert and Freeman [174]). The effect of adsorbates on the surface Knight shift could also be investigated. Overall, the results obtained provide a strong foundation on which to further investigate the Knight shift in nanoparticles.

Chapter 8

Calculating hyperfine interactions

As discussed in section 4.3.1, core polarisation can have a significant effect on the calculation of hyperfine parameters in paramagnetic systems. It is particularly important for systems which exhibit ground-state hyperfine interactions (i.e. in Curie paramagnets). In the cases where the hyperfine interaction is induced, such as in the Knight shift and J-coupling, core polarisation is expected to have little effect. In the case of J-coupling, this is well-supported by the good agreement between J-couplings calculated using the planewave-pseudopotential methodology, and those obtained via quantum chemical methodologies and experiment [56, 35, 1, 184]. In the case of the Knight shift, my calculations in chapter 6 also support this. However, it would be useful to have a robust approach for incorporating core polarisation so that its effect could be systematically tested.

When calculating ground-state hyperfine parameters for paramagnetic systems, it has been shown that the perturbative method developed by Bahramy *et al.* results in a significant improvement in the calculated values of hyperfine parameters [74, 75]. However, a perturbative approach cannot

be used for perturbed situations such as the calculation of J-couplings and Knight shifts. By contrast, it is well accepted that core polarisation does not affect interactions in diamagnetic systems, and therefore in these cases the core states can be safely replaced with those of an isolated atom.

In this chapter I investigate a novel method for including the effects of core polarisation which can be used in all ground-state and perturbed situations. Instead of treating the effect of core polarisation as a perturbation to the hyperfine interaction of the valence electrons, the interaction between the core and valence electrons is included holistically by treating the core electrons in the pseudopotential as valence to form an 'all-electron pseudopotential' (AE-PSP). The effect of replacing the pseudopotential with a Coulomb potential has also been investigated.

8.1 All-electron pseudopotentials (AE-PSPs)

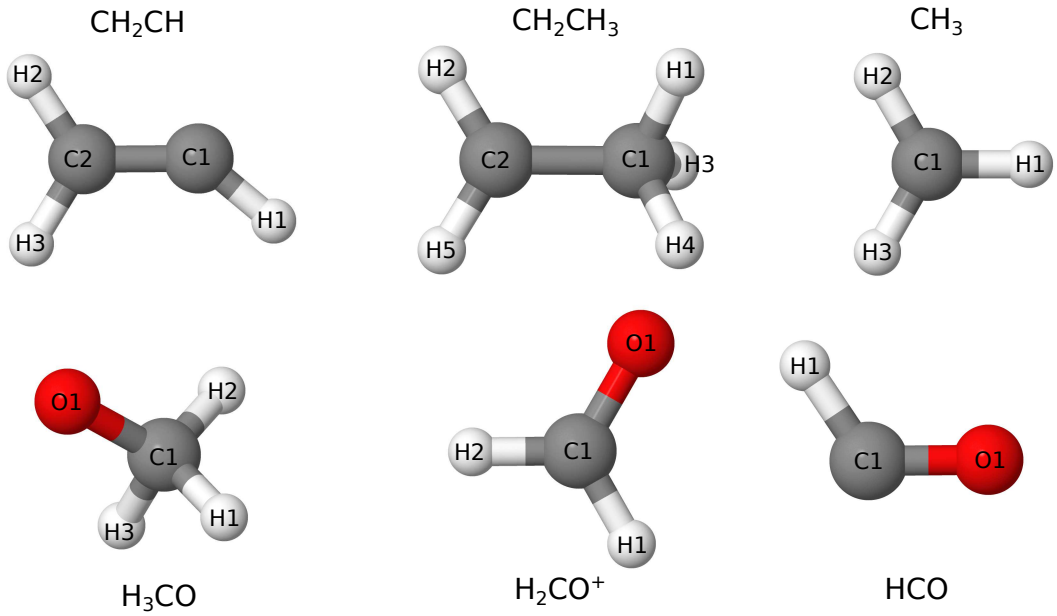

Figure 8.1: The set of radicals investigated. The carbon, hydrogen and oxygen atoms are labelled in accordance with the following discussion.

The accuracy of using all-electron pseudopotentials for calculating the Fermi-contact interaction has been tested on the set of small organic radicals shown in figure 8.1. Previously, Filidou *et al.* used the same set of structures to evaluate the accuracy of the perturbative approach when calculating the isotropic hyperfine interaction. The geometries used for my calculations were provided by Filidou *et al.* so that these methodologies could be directly compared.

A variety of carbon AE-PSPs were investigated: the number of projectors used to describe the electron wavefunctions were changed, as were the relative energies of these projectors and the cut-off radius for the pseudopotential. The AE-PSPs converged easily with respect to the planewave cut-off and the sampling of the augmentation charge. A planewave cut-off of 1100 eV was easily sufficient to give converged results with all AE-PSPs. Furthermore, increasing the density of the fine grid upon which the augmentation charge is stored did not alter the Fermi-contact values.[1] Overall, the reliable convergences confirmed that the AE-PSPs were accurate pseudopotentials. Each molecule was placed in a cubic supercell with sides of length 35 a.u. ($\sim$18.5 Å) to ensure that there was no interaction between images. A single **k**-point placed at $(\frac{1}{4}, \frac{1}{4}, \frac{1}{4})$ was used for each calculation. The PBE functional was used for all calculations.

Figure 8.2 shows the Fermi-contact terms for the carbon nuclei in the set of organic molecules, as calculated using a candidate all-electron pseudopotential (red crosses) and a conventional valence-only carbon pseudopotential set as the default in CASTEP (blue crosses). These are compared to the calculations of Filidou *et al.* and a set of experimental data previously ref-

[1] In general, the fine grid sampling was set to 3, compared to the default of 1.75.

erenced in their paper [14].[2]

The default CASTEP carbon pseudopotential was the same as presented in the 'OTFG7' (i.e. 'C7') set in the paper by Lejaeghere *et al.* [49]. Only the $2s$ and $2p$ wavefunctions are included in this pseudopotential and each are represented by a single projector function. The results presented for this pseudopotential have been well-converged using a planewave cut-off of 950 eV. Both pseudopotentials have the same cut-off radius, r_c, of 1.4 a.u.

In the all-electron pseudopotential, $1s$ electrons were modelled with a single projector, the $2s$ with two projectors and the $2p$ with two projectors (this can be referred to in the CASTEP pseudopotential string as '10U:20UU:21UU').

The calculations by Filidou *et al.* consist of calculations involving no core polarisation (blue plusses) and a set of calculations which modelled core polarisation using perturbation theory (red plusses). Both of these sets of calculations were performed using the QUANTUM-ESPRESSO software package [191]. The authors also performed a set of all-electron (AE) calculations (black diamonds) using the GAUSSIAN 09 software package [42].

8.1.1 Comparison of core polarisation methodologies

Figure 8.2 shows the carbon Fermi-contact terms as evaluated by the different methodologies discussed above. Figure 8.3 shows the corresponding values for the hydrogen Fermi-contact terms.

Comparing the Fermi-contact terms in figure 8.2 to the structures in figure 8.1 shows that the Fermi-contact terms for the carbons with fully occupied states (C2 in $CHCH_2$, C1 in CH_3CH_2, and the carbons in H_3CO

[2]For completeness, the experimental references for each of the molecules are: $CHCH_2$ and CH_3CH_2 [185, 186], CH_3 [187], H_3CO [188, 189], HCO [190] and H_2CO^+ [189].

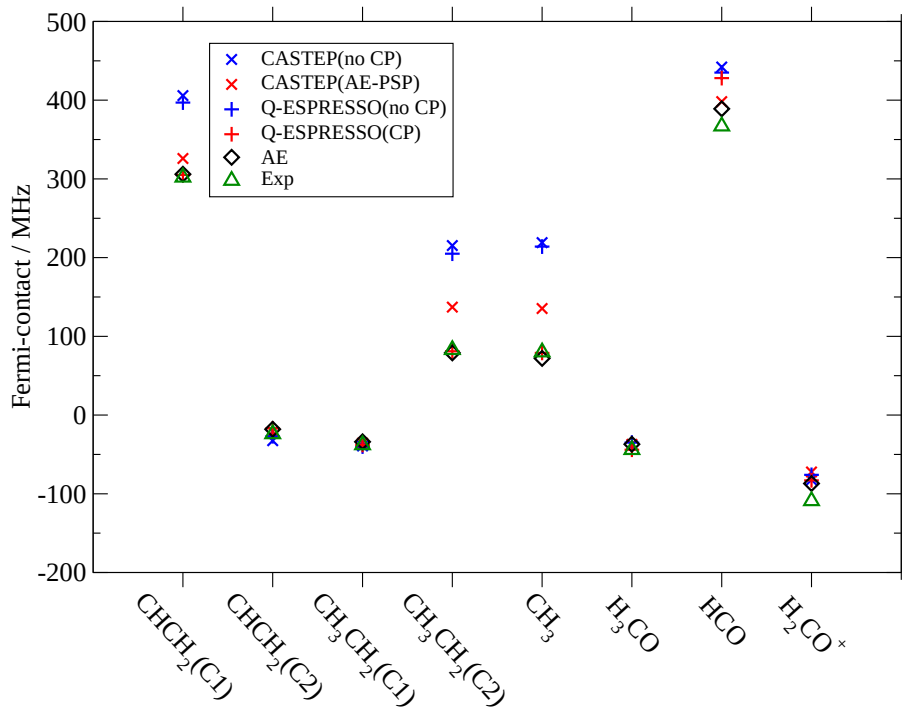

Figure 8.2: Comparison of the methodologies used to evaluate the Fermi-contact interaction for carbon nuclei in a set of small molecules. My CASTEP calculations are shown with crosses and compared against existing QUANTUM-ESPRESSO (plusses) and AE (diamonds, using GAUSSIAN 09) calculations by Filidou *et al.* [14]. The experimental data are individually referenced in the main discussion. CASTEP and QUANTUM-ESPRESSO calculations which do not include corrections for core polarisation (CP) are shown in blue, and those which incorporate corrections for core polarisation are shown in red. (See discussion for further details.)

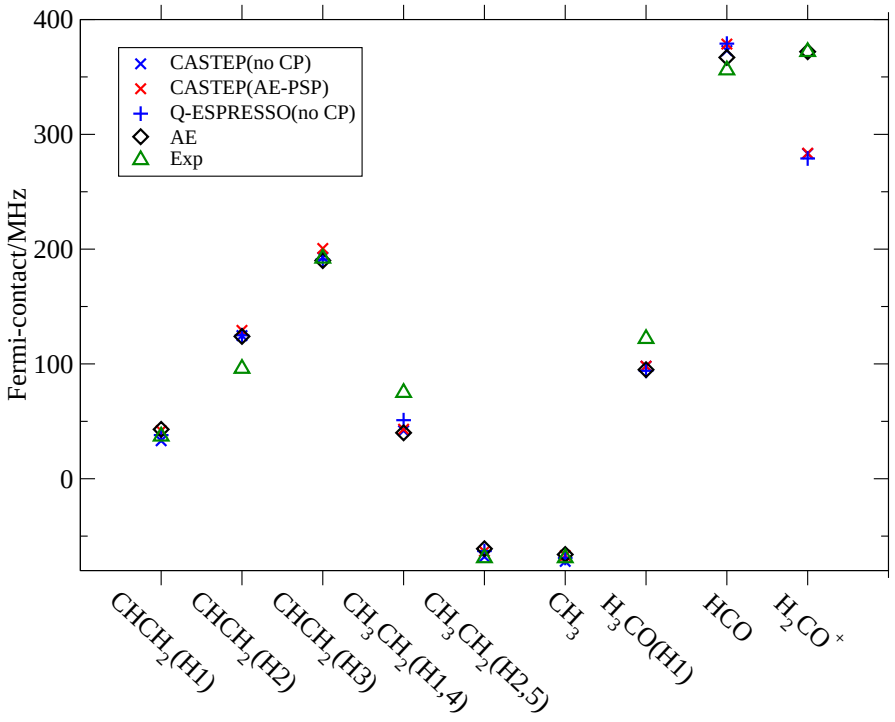

Figure 8.3: Comparison of the Fermi-contact interactions for hydrogen nuclei as a result of using different approaches to evaluate the Fermi-contact interaction in the carbon nuclei (figure 8.2). My CASTEP calculations are shown with crosses, QUANTUM-ESPRESSO and AE calculations by Filidou *et al.* with plusses and diamonds respectively [14] and experimental data with triangles. Methods incorporating core polarisation in the carbon nuclei are shown in red, and those without in blue. (See discussion for further details.)

and H_2CO^+) are not greatly affected by core polarisation. By contrast, core polarisation has a significant effect on the carbons which possess a lone electron (C1 in $CHCH_2$, C2 in CH_3CH_2, and the carbons in CH_3 and HCO).[3] In these cases, the all-electron pseudopotential results in a substantial improvement in the accuracy of the Fermi-contact terms compared to the calculations which do not include core polarisation (both CASTEP and QUANTUM-ESPRESSO calculations). However, the perturbative approach to including core polarisation ('Q-ESPRESSO with CP') is more accurate still. The difference in the calculations incorporating core polarisation will predominantly be due to the differences in the AE-PSP and pertubative approaches, and not due to differences in the codes. This can be inferred from noting that the calculations involving no core polarisation produce very similar values.

The Fermi-contact terms for each hydrogen are not significantly altered by the modelling methods for the carbon nuclei as shown in figure 8.3.[4] The AE-PSP Fermi-contact terms are fairly consistent with the other QUANTUM ESPRESSO and AE calculations, further validating the accuracy of the carbon AE-PSPs. In the case of the HCO and H_2CO^+ radicals the AE calculations agree well with experiment, but the pseudopotential calculations agree less favourably with experiment. This implies that in the HCO and H_2CO^+ radicals there is a degree of polarisation which has not been accurately modelled by the carbon pseudopotentials. In other cases the AE and pseudopotential calculations agree well with one another, but

[3]The sign indicates whether the spin density is predominantly 'up' or 'down'. The change in sign across carbons in the same molecule indicates that there must be a node in the charge density at some point between the carbon nuclei.

[4]Note that hydrogen atoms cannot have a core polarisation because each atom has only one electron. They can however be affected by interactions with the electrons associated with neighbouring nuclei.

not with experiment. In part, this could be due to the sensitivity of the hyperfine interaction to geometries. The calculated molecules are frozen in a particular orientation. This results in a degree of variation in the calculated hydrogen Fermi-contact terms which in practice would be averaged out due to bond rotations. For example, experimentally it would be expected that the Fermi-contact terms for the hydrogen nuclei in the methyl group in CH_2CH_3 would be the same. In my CASTEP calculations, which use a fixed CH_2CH_3 geometry, the H1 and H4 have almost equal values but the H3 value (omitted from the figures due to lack of a comparative AE value) is over four times larger.

8.1.2 Investigation of alternative all-electron pseudopotentials

A large number of carbon all-electron pseudopotentials were investigated. None of them produced a significant improvement on those used in figures 8.2 and 8.3. By way of example, figure 8.4 shows the Fermi-contact term calculated for C1 in the $CHCH_2$ radical across a range of pseudopotentials with different numbers of projectors and cut-off radii. The Fermi-contact term only varied by $\sim$16 MHz with respect to changing the AE-PSP compared to a $\sim$80 MHz difference between using the standard 'OTFG7' CASTEP pseudopotential and the all-electron pseudopotentials. The effect of changing the energy of the second $1s$ projector was also investigated however this had an even weaker effect on the Fermi-contact term. Changing the energy over a range of 0.1–10 Ha changed the Fermi contact term by only 1.6 MHz.

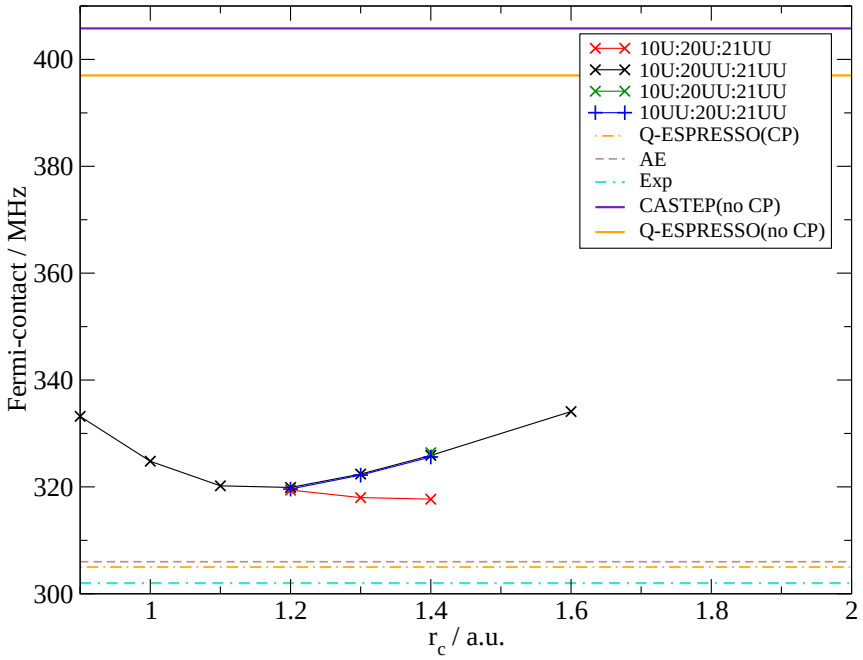

Figure 8.4: The calculation of the Fermi-contact interaction for C1 in the $CHCH_2$ radical using different all-electron pseudopotentials. Pseudopotentials using different cut-off radii, r_c, and different numbers of projectors are shown in red, black, green and blue. By way of comparison, the QUANTUM-ESPRESSO calculations with and without core polarisation, the AE calculations, my own CASTEP calculations with no core polarisation and experimental values have also been included [14, 185, 186].

8.2 Using a Coulomb potential

The effect of replacing the pseudopotential with a simple Coulomb potential was investigated. Figure 8.5 shows the Fermi-contact term for a single hydrogen atom in a $7\times7\times7$ a.u.^{3} box converging with respect to the planewave cut-off. The values obtained using the default hydrogen ultrasoft pseudopotential from the 'OTFG7' set are shown in red, the values using the Coulomb potential in black. It is immediately apparent that convergence when using the Coulomb potential is extremely slow—the Fermi-contact term hasn't even converged with a planewave energy of 10000 eV!

By contrast, a planewave energy of 600 eV using the pseudopotential has converged the Fermi-contact to within 5 MHz (0.3%) of the equivalent value at 10000 eV.

The carbon pseudopotential was replaced with a Coulomb potential to investigate how this modelled the effects of core polarisation. Figure 8.6 shows how the Fermi-contact term converges with respect to the planewave cut-off for the CH_3 radical in a $10\times10\times10$ a.u.^{3} box. As expected, the rate of convergence is even slower than for hydrogen.

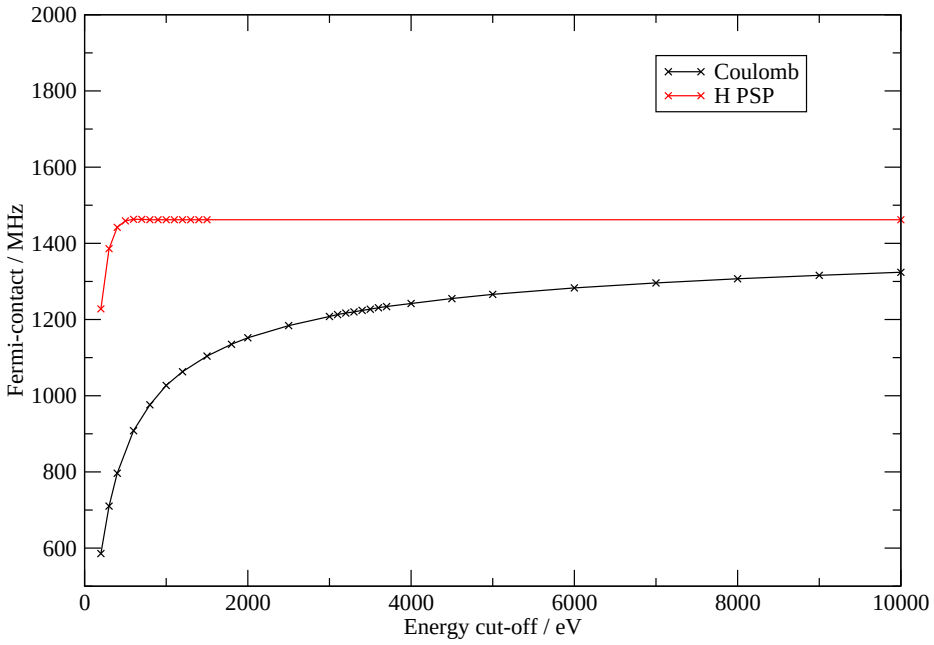

Figure 8.5: The Fermi-contact term for a single hydrogen atom calculated using a hydrogen Coulomb potential (black) and the default ultrasoft pseudopotential (red).

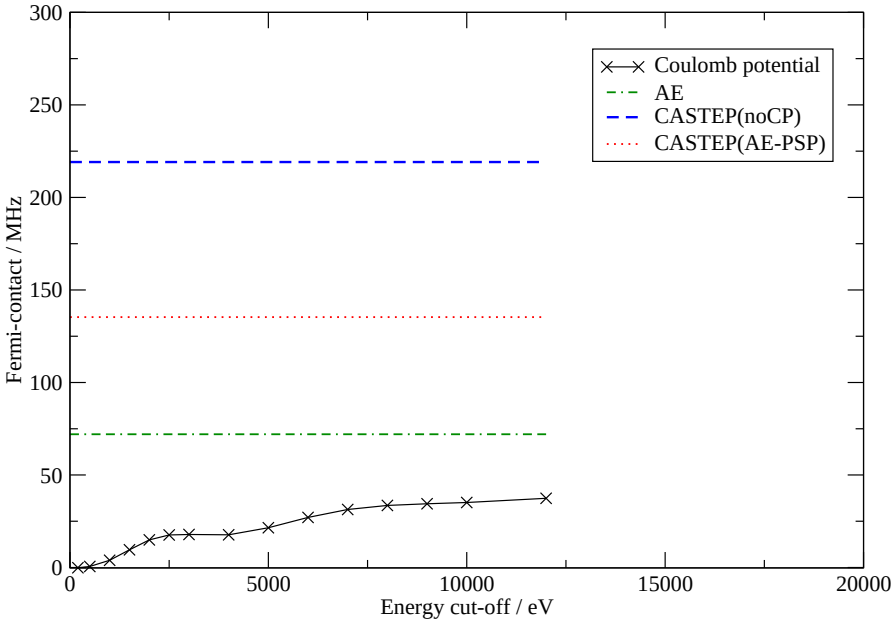

Figure 8.6: The Fermi-contact term for carbon in CH_3 using a carbon Coulomb potential (black crosses). The AE and CASTEP pseudopotential and AE-PSP values from figure 8.2 have been included for comparison.

8.3 Conclusions

The use of a Coulomb potential leads to an extremely slow convergence of the isotropic hyperfine interaction with respect to the planewave cut-off and is therefore not a computationally realistic method for modelling core polarisation. By contrast, all-electron pseudopotentials converge rapidly with respect to planewave cut-off however they can only partially model the effects of core polarisation. The AE-PSP results also remained relatively stable with respect to a range of pseudopotential parameters. This behaviour implies that some part of fundamental physics is missed when modelling the system with AE-PSPs such as the augmentation charge not fully describing

the exchange-correlation interactions of the electrons. Evaluating this could form the basis for further research.

For ground-state properties, all-electron methods remain the best methodology for including the effects of core polarisation. However, there is still no robust methodology for including the effects of core polarisation on response properties such as in J-coupling and Knight shifts.

Chapter 9

Conclusions and further work

In this thesis I have presented two studies which illustrate the power of first-principles calculations for predicting the NMR parameters for materials applications. The first study (chapter 5) used well-established first-principles methodologies for diamagnetic materials in order to calculate the NMR parameters for the pure $NaNbO_3$, $KNbO_3$ and $LiNbO_3$ perovskite structures and related solid solutions. The aim was to investigate potential correlations between structural disorder and NMR parameters, in order to aid the interpretation of future NMR experiments. The second study involved the use of relatively new methodologies to calculate the Knight shift in platinum, palladium and rhodium. This started with an investigation of the bulk systems (chapter 6) which identified the computational considerations required for Knight shift calculations and investigated the subsequent accuracy of the calculated Knight shifts in comparison to experiment. The findings from the bulk systems were then used to inform the study of a set of surface structures (chapter 7), which in turn identified correlations between the Knight shift on a particular atomic site or layer and structural environment. An

overview of the main conclusions and potential avenues for further enquiry are as follows.

9.1 Chapter 5—NMR parameters of group I niobate perovskite structures

The NMR parameters for pure $NaNbO_3$, $KNbO_3$ and $LiNbO_3$ perovskite structures were calculated prior to investigating sets of related disordered structures containing impurities. By analysing the NMR parameters as a function of distance from the impurity atoms, I was able to show that the NMR parameters were significantly affected by the presence of the impurity atoms. In general, these parameters tended towards their equivalent pure structure values with increasing separation from the impurity atom.

The NMR parameters were found to be extremely sensitive to structural distortions, particularly in the case of the ^{93}Nb nuclei which are surrounded by an octahedral configuration of oxygen atoms. For pure compounds and those with a small concentration of impurities, there was a positive gradient to the correlation between the ^{93}Nb C_Q values and the strains within the oxygen octahedra. This tended to a negative gradient for high concentrations. There are two possible reasons for this: the C_Q values could be affected by the structural distortions in the octahedra (the geometries of which are influenced by the impurity atom) or the C_Q could be directly affected by the impurity atom. This is an area that could be researched further, through manually distorting either the octahedra or the position of the impurities in order to decouple their effects on the ^{93}Nb C_Q values. Experimentally, the trends in ^{93}Nb C_Q values will lead to the degree of quadrupolar broadening decreasing with increasing impurity concentration as the gradient of

the C_Q–strain correlation flattens. Beyond a certain impurity concentration, the broadening will however increase as the gradient becomes increasingly negative. This highlights the difficulty in interpreting experimental spectra and the consequential necessity of a computational model.

It was found that ^{23}Na NMR can be used experimentally to determine whether they are situated in a *Pbcm* $NaNbO_3$ environment with small amounts of Li or K doping, or whether they are situated in an *Amm*2 $KNbO_3$ environment as dopants. In the case of Na in a *Pbcm* $NaNbO_3$ environment, ^{23}Na σ_{iso} can be used to measure the concentration of Li or K doping. In the case of the $Li_xNa_{1-x}NbO_3$ system, it is predicted that the two experimental ^{23}Na peaks will shift by approximately 1–4 ppm (from σ_{iso} =∼561 ppm to σ_{iso} =∼557–560 ppm) and approximately 1.5 ppm (from σ_{iso} =∼565 ppm to σ_{iso} =∼563.5 ppm) as the Li impurity concentration is increased from 2% to 12.5%. In the case of the $K_xNa_{1-x}NbO_3$ system, the two experimental ^{23}Na peaks will shift by ∼3.5 ppm (from σ_{iso} =∼565.5 ppm to σ_{iso} =∼569 ppm) and by 2.5–3.5 ppm (from σ_{iso} =∼561.5 ppm to σ_{iso} =∼564–565 ppm) as the K impurity concentration increases from 2% to 12.5%. The degree of broadening arising from the range of magnetic shielding environments is also expected to increase with increasing impurity concentrations, though it may not be possible to experimentally extract this from the overwhelming presence of other broadening mechanisms such as quadrupolar broadening. In the case of Na in a $KNbO_3$ structure, ^{23}Na σ_{iso} was found to be fairly insensitive to Na concentration, with values only changing by 0.7 ppm with no correlation to concentration. Aside from determining the main crystal structure, this implies that ^{23}Na NMR would not assist with measuring the amount of Na doping.

In terms of the details of the perovskite calculations, I found that relaxing the structures with PBEsol led to calculated NMR parameters that were significantly closer to experiment than those calculated with the more commonly used PBE functional. The increase in accuracy was predominantly driven by PBEsol producing a better representation of the structure, which in turn influenced the NMR parameters. This suggests that, in the future, researchers calculating the NMR parameters of diamagnetic materials would do well to investigate the effect of PBEsol on their structures.

9.2 Chapters 6 and 7—The Knight shifts of Pt, Pd and Rh bulk and surface structures

The Knight shift was calculated for platinum, palladium and rhodium in their bulk forms and in a set of surface structures. The key challenge faced when calculating the properties of metals is the accurate sampling of the Fermi surface. As a result, the Knight shift converged slowly with respect to the number of **k**-points and smearing width. However, in the case of the surface structures, the effects of this slow convergence could be reduced by considering the difference between the Knight shift of the surface and the central layer.

Previously, the Knight shift in surfaces has been taken to be a probe of the *s*-like densities of states localised on the surface and internal layers (*s*-LDOS). I have shown that there is a reasonably strong correlation between the Knight shift and the *s*-LDOS at the Fermi energy. Nevertheless, these correlations should still be treated with care due to the slow convergence of the DOS and the Knight shifts, and because the correlation could be affected by changes in pseudopotential.

As was the case for the NMR parameters in the perovskites, the Knight shift in platinum, palladium and rhodium surface structures was found to be extremely sensitive to structural environment—for example, upon structural relaxation the surface Knight shift of the Pt 7-layer structure changed by 9%. The magnitudes of the surface Knight shifts were found to be much larger than those of the inner layers and can be explained by the higher induced spin density at the surface compared to that in the inner layers. The Knight shift was found to tend towards the bulk value with increasing distance from the surface. Within two layers of the surface, the Knight shift was within ∼30% of the bulk value, implying that surface effects are strongly localised to the surface. This implies that infinite slabs could be used to predict experimental Knight shift measurements, not only for surfaces, but also for nanoparticles. However, given the sensitivity of the Knight shift to structural distortions, and the existence of surface reconstructions which were not taken into account in my investigation, further research should be conducted on a wider range of structures and surface reconstructions before trends in the Knight shift are systematically compared to experimental systems. The effect of adsorbates on the calculated Knight shift could also be investigated.

The relative contributions of the valence electrons to the Knight shift in the bulk structures was investigated as a function of energy. It was shown that the conduction electrons near the Fermi surface made the most significant contribution. By summing the Knight shift contribution over a set number of bands it was found that the semi-core $4s$ states in Pd and Rh did not significantly contribute to the Knight shift. This implies that the $4s$ electrons are not polarised by the higher energy conduction bands.

In the literature, it is assumed that core polarisation has a significant effect on the Knight shift. I have shown that this is not the case at least for the semi-core 4*s* states in Pd and Rh. Furthermore, the reasonable agreement of my calculated Pt Knight shift value to the experimental values (both ∼-4%) suggest that core polarisation, which is not yet taken into account computationally, has a minimal effect on the Knight shift.

9.3 Chapter 8—Calculating hyperfine interactions

A systematic methodology for including core polarisation in the NMR calculations of paramagnetic materials has yet to be developed. When calculating parameters that involve Pauli paramagnetism, such as the Knight shift, core polarisation appears not to have a significant effect. However, if the calculation involves Curie paramagnetism, the inclusion of core polarisation becomes much more important, for example when calculating a ground-state hyperfine interaction. In the latter case, core polarisation can be included for isolated systems using all-electron methods, or to a certain extent for periodic systems by including perturbation theory with pseudopotential methodologies. There is, however, no robust method for including core polarisation in the calculation of response properties such as the Knight shift or *J*-coupling. Chapter 8 investigated a potential method for solving this through the use of an all-electron pseudopotential (AE-PSP). This meant that the core electrons were treated as valence electrons. Whilst the AE-PSPs improved upon the capabilities of standard pseudopotentials to model core polarisation in a set of small molecules, they were still not able to fully model core polarisation. Furthermore, altering the pseudopotential parameters did not significantly improve their accuracy in modelling

core polarisation. As demonstrated by my thesis, it is clear that developing methodologies for accurately modelling core polarisation is a major area for further research.

Bibliography

[1] C. Bonhomme, C. Gervais, F. Babonneau, C. Coelho, F. Pourpoint, T. Azaïs, S. E. Ashbrook, J. M. Griffin, J. R. Yates, F. Mauri, and C. J. Pickard. First-Principles Calculation of NMR Parameters Using the Gauge Including Projector Augmented Wave Method: A Chemists Point of View. *Chemical Reviews*, 112(11):5733–5779, 2012.

[2] W. D. Knight. Nuclear Magnetic Resonance Shift in Metals. *Phys. Rev.*, 76:1259–1260, Oct 1949.

[3] M. d'Avezac, N. Marzari, and F. Mauri. Spin and orbital magnetic response in metals: Susceptibility and NMR shifts. *Physical Review B*, 76(16):165122, October 2007.

[4] S. J. Clark, M. D. Segall, C. J. Pickard, P. J. Hasnip, M. J. Probert, K. Refson, and M. C. Payne. First principles methods using CASTEP. *Z. Kristall.*, 220(5-6):567–570, 2005.

[5] D. C. Apperley, R. K. Harris, and P. Hodgkinson. *Solid State NMR: Basic Principles & Practice*. Momentum Press, New York, NY, 2012.

[6] J. T. Arnold, S. S. Dharmatti, and M. E. Packard. Chemical Effects on Nuclear Induction Signals from Organic Compounds. *The Journal of Chemical Physics*, 19(4):507–507, 1951.

[7] P. J. Hore. *Oxford Chemistry Primers - Nuclear Magnetic Resonance*. Oxford University Press, Oxford, 1995.

[8] C. Bonhomme, C. Gervais, C. Coelho, F. Pourpoint, T. Azaïs, L. Bonhomme-Coury, F. Babonneau, G. Jacob, M. Ferrari, D. Canet, J. R. Yates, C. J. Pickard, S. A. Joyce, F. Mauri, and D. Massiot. New perspectives in the PAW/GIPAW approach: JP-O-Si coupling constants, antisymmetric parts of shift tensors and NQR predictions. *Magnetic Resonance in Chemistry*, 48(S1):S86–S102, 2010.

[9] F. A. Anet, D. J. O'Leary, C. G. Wade, and R. D. Johnson. NMR relaxation by the antisymmetric component of the shielding tensor: a longer transverse than longitudinal relaxation time. *Chemical Physics Letters*, 171(5):401 – 405, 1990.

[10] D. Massiot, F. Fayon, M. Capron, I. King, S. Le Calvé, B. Alonso, J.-O. Durand, B. Bujoli, Z. Gan, and G. Hoatson. Modelling one- and two-dimensional solid-state NMR spectra. *Magnetic Resonance in Chemistry*, 40(1):70–76, 2002.

[11] C. J. Foot. *Atomic Physics*. Oxford University Press, Oxford, 2011.

[12] F. Neese. Metal and ligand hyperfine couplings in transition metal complexes: The effect of spinorbit coupling as studied by coupled perturbed KohnSham theory. *The Journal of Chemical Physics*, 118(9):3939–3948, 2003.

[13] A. V. Arbuznikov, J. Vaara, and M. Kaupp. Relativistic spin-orbit effects on hyperfine coupling tensors by density-functional theory. *The Journal of Chemical Physics*, 120(5):2127–2139, 2004.

[14] V. Filidou, D. Ceresoli, J. J. L. Morton, and F. Giustino. First-principles investigation of hyperfine interactions for nuclear spin entanglement in photoexcited fullerenes. *Physical Review B*, 85(11):115430, 2012.

[15] P. Atkins and R. Friedman. *Molecular Quantum Mechanics*. Oxford University Press, Oxford, 2005.

[16] C. Kittel. *Introduction to Solid State Physics*. John Wiley & Sons, Inc., New York, 1986.

[17] A. Abragam. *Principles of Nuclear Magnetism*. Oxford University Press, New York, NY, 1961.

[18] E. R. Andrew, A. Bradbury, and R. G. Eades. Nuclear Magnetic Resonance Spectra from a Crystal rotated at High Speed. *Nature*, 182(4650):1659–1659, Dec 1958.

[19] I. J. Lowe. Free Induction Decays of Rotating Solids. *Phys. Rev. Lett.*, 2:285–287, Apr 1959.

[20] Y. Q. Ye, M. Malon, C. Martineau, F. Taulelle, and Y. Nishiyama. Rapid measurement of multidimensional ^{1}H solid-state NMR spectra at ultra-fast MAS frequencies . *Journal of Magnetic Resonance*, 239(0):75 – 80, 2014.

[21] F. Giustino. *Materials Modelling using Density Functional Theory: Properties and Predictions*. Oxford University Press, Oxford, 2014.

[22] R. M. Martin. *Electronic Structure: Basic Theory and Practical Methods*. Cambridge University Press, Cambridge, 2010.

[23] W. Koch and M. C. Holthausen. *A Chemist's Guide to Density Functional Theory*. WILEY-VCH, Weinheim, 2000.

[24] P. Hohenberg and W. Kohn. Inhomogeneous Electron Gas. *Physical Review B*, 136(3B):B864, 1964.

[25] W. Kohn and L. J. Sham. Self-Consistent Equations Including Exchange and Correlation Effects. *Physical Review*, 140(4A):1133, 1965.

[26] C. I. Lynch. An overview of first-principles calculations of NMR parameters for paramagnetic materials. *Materials Science and Technology*, 32(2):181–194, 2016.

[27] D. M. Ceperley and B. J. Alder. Ground State of the electron gas by a stochastic method. *Physical Review Letters*, 45(7):566–569, 1980.

[28] J. P. Perdew and A. Zunger. Self-Interaction correction to density functional approximations for many-electron systems. *Physical Review B*, 23(10):5048–5079, 1981.

[29] P. Haas, F. Tran, P. Blaha, K. Schwarz, and R. Laskowski. Insight into the performance of GGA functionals for solid-state calculations. *Phys. Rev. B*, 80:195109, Nov 2009.

[30] J. P. Perdew, K. Burke, and M. Ernzerhof. Generalized Gradient Approximation Made Simple. *Physical Review Letters*, 77:3865–3868, 1996.

[31] J. P. Perdew, A. Ruzsinszky, G. I. Csonka, O. A. Vydrov, G. E. Scuseria, L. A. Constantin, X. Zhou, and K. Burke. Restoring the Density-

Gradient Expansion for Exchange in Solids and Surfaces. *Phys. Rev. Lett.*, 100:136406, Apr 2008.

[32] R. Dovesi, R. Orlando, B. Civalleri, C. Roetti, V. R. Saunders, and C. M. Zicovich-Wilson. CRYSTAL: a computational tool for the ab initio study of the electronic properties of crystals. *Zeitschrift für Kristallographie*, 220(5-6):571–573, 2005.

[33] R. Dovesi, R. Orlando, A. Erba, C. M. Zicovich-Wilson, B. Civalleri, S. Casassa, L. Maschio, M. Ferrabone, M. De La Pierre, P. D'Arco, Y. Noël, M. Causà, M. Rérat, and B. Kirtman. CRYSTAL14: A program for the ab initio investigation of crystalline solids. *International Journal of Quantum Chemistry*, 114(19):1287–1317, 2014.

[34] J. M. Soler, E. Artacho, J. D. Gale, A. García, J. Junquera, P. Ordejón, and D. Sánchez-Portal. The SIESTA method for ab initio order- N materials simulation. *Journal of Physics: Condensed Matter*, 14(11):2745–2779, March 2002.

[35] J. R. Yates. Prediction of NMR J-coupling in solids with the planewave pseudopotential approach. *Magnetic Resonance in Chemistry*, 48(S1):S23–S31, 2010.

[36] H. J. Monkhorst and J. D. Pack. Special Points for Brillouin-zone integration. *Physical Review B*, 13:5188, 1976.

[37] N. Troullier and J. L. Martins. Efficient pseudopotentials for plane-wave calculations. *Phys. Rev. B*, 43:1993–2006, Jan 1991.

[38] D. Vanderbilt. Soft self-consistent pseudopotentials in a generalized eigenvalue formalism. *Phys. Rev. B*, 41:7892–7895, Apr 1990.

[39] T. Gregor, F. Mauri, and R. Car. A comparison of methods for the calculation of NMR chemical shifts. *The Journal of Chemical Physics*, 111(5):1815–1822, 1999.

[40] C. G. V. de Walle and P. E. Blöchl. 1st-Principles Calculations of Hyperfine Parameters. *Physical Review B*, 47(8):4244–4255, 1993.

[41] P. E. Blöchl. Projector augmented-wave method. *Phys. Rev. B*, 50:17953–17979, Dec 1994.

[42] M. J. Frisch, G. W. Trucks, H. B. Schlegel, G. E. Scuseria, M. A. Robb, J. R. Cheeseman, G. Scalmani, V. Barone, G. A. Petersson, H. Nakatsuji, X. Li, M. Caricato, A. Marenich, J. Bloino, B. G. Janesko, R. Gomperts, B. Mennucci, H. P. Hratchian, J. V. Ortiz, A. F. Izmaylov, J. L. Sonnenberg, D. Williams-Young, F. Ding, F. Lipparini, F. Egidi, J. Goings, B. Peng, A. Petrone, T. Henderson, D. Ranasinghe, V. G. Zakrzewski, J. Gao, N. Rega, G. Zheng, W. Liang, M. Hada, M. Ehara, K. Toyota, R. Fukuda, J. Hasegawa, M. Ishida, T. Nakajima, Y. Honda, O. Kitao, H. Nakai, T. Vreven, K. Throssell, J. A. M. Jr., J. E. Peralta, F. Ogliaro, M. Bearpark, J. J. Heyd, E. Brothers, K. N. Kudin, V. N. Staroverov, T. Keith, R. Kobayashi, J. Normand, K. Raghavachari, A. Rendell, J. C. Burant, S. S. Iyengar, J. Tomasi, M. Cossi, J. M. Millam, M. Klene, C. Adamo, R. Cammi, J. W. Ochterski, R. L. Martin, K. Morokuma, O. Farkas, J. B. Foresman, and D. J. Fox. Gaussian09 Revision A.1. Gaussian Inc. Wallingford CT 2009.

[43] J. Kohanoff. *Electronic Structure Calculations for Solids and*

Molecules: Theory and Computational Methods. Cambridge University Press, New York, 2006.

[44] M. Methfessel and A. Paxton. High-precision sampling for Brillouin-zone integration in metals. *Physical Review B*, 40(6):3616–3621, August 1989.

[45] S. de Gironcoli. Lattice dynamics of metals from density-functional perturbation theory. *Phys. Rev. B*, 51:6773–6776, Mar 1995.

[46] C. L. Fu and K. M. Ho. First-principles calculation of the equilibrium ground-state properties of transition metals: Applications to Nb and Mo. *Phys. Rev. B*, 28:5480–5486, Nov 1983.

[47] B. G. Pfrommer, M. Côté, S. G. Louie, and M. L. Cohen. Relaxation of Crystals with the Quasi-Newton Method. *Journal of Computational Physics*, 131(1):233 – 240, 1997.

[48] K. Lejaeghere, V. V. Speybroeck, G. V. Oost, and S. Cottenier. Error Estimates for Solid-State Density-Functional Theory Predictions: An Overview by Means of the Ground-State Elemental Crystals. *Critical Reviews in Solid State and Materials Sciences*, 39(1):1–24, 2014.

[49] K. Lejaeghere, G. Bihlmayer, T. Björkman, P. Blaha, S. Blügel, V. Blum, D. Caliste, I. E. Castelli, S. J. Clark, A. Dal Corso, S. de Gironcoli, T. Deutsch, J. K. Dewhurst, I. Di Marco, C. Draxl, M. Dułak, O. Eriksson, J. A. Flores-Livas, K. F. Garrity, L. Genovese, P. Giannozzi, M. Giantomassi, S. Goedecker, X. Gonze, O. Grånäs, E. K. U. Gross, A. Gulans, F. Gygi, D. R. Hamann, P. J. Hasnip, N. A. W. Holzwarth, D. Iuşan, D. B. Jochym, F. Jollet, D. Jones,

G. Kresse, K. Koepernik, E. Küçükbenli, Y. O. Kvashnin, I. L. M. Locht, S. Lubeck, M. Marsman, N. Marzari, U. Nitzsche, L. Nordström, T. Ozaki, L. Paulatto, C. J. Pickard, W. Poelmans, M. I. J. Probert, K. Refson, M. Richter, G.-M. Rignanese, S. Saha, M. Scheffler, M. Schlipf, K. Schwarz, S. Sharma, F. Tavazza, P. Thunström, A. Tkatchenko, M. Torrent, D. Vanderbilt, M. J. van Setten, V. Van Speybroeck, J. M. Wills, J. R. Yates, G.-X. Zhang, and S. Cottenier. Reproducibility in density functional theory calculations of solids. *Science*, 351(6280), 2016.

[50] N. Ramsey. The Internal Diamagnetic Field Correction in Measurements of the Proton Magnetic Moment. *Physical Review*, 77(4):567–567, February 1950.

[51] N. Ramsey. Magnetic Shielding of Nuclei in Molecules. *Physical Review*, 78(6):699–703, June 1950.

[52] N. Ramsey. Electron Coupled Interactions between Nuclear Spins in Molecules. *Physical Review*, 91(2):303–307, July 1953.

[53] C. J. Pickard and F. Mauri. All-electron magnetic response with pseudopotentials: NMR chemical shifts. *Physical Review B*, 63(24):245101, 2001.

[54] J. R. Yates, C. J. Pickard, and F. Mauri. Calculation of NMR chemical shifts for extended systems using ultrasoft pseudopotentials. *Physical Review B*, 76(2):024401, 2007.

[55] M. Profeta, F. Mauri, and C. J. Pickard. Accurate First Principles Prediction of ^{17}O NMR Parameters in SiO_2: Assignment of the Zeo-

lite Ferrierite Spectrum. *Journal of the American Chemical Society*, 125(2):541–548, 2003. PMID: 12517169.

[56] S. A. Joyce, J. R. Yates, C. J. Pickard, and F. Mauri. A first principles theory of nuclear magnetic resonance J-coupling in solid-state systems. *Journal of Chemical Physics*, 127(20):204107–204107, 2007.

[57] H. Heise, F. H. Köhler, F. Mota, J. J. Novoa, and J. Veciana. Determination of the Spin Distribution in Nitronylnitroxides by Solid-State ^{1}H, ^{2}H, and ^{13}C NMR Spectroscopy. *Journal of the American Chemical Society*, 121(41):9659–9667, 1999.

[58] G. Maruta, S. Takeda, R. Imachi, T. Ishida, T. Nogami, and K. Yamaguchi. Solid-State High-Resolution ^{1}H and ^{2}D NMR Study of the Electron Spin Density Distribution of the Hydrogen-Bonded Organic Ferromagnetic Compound 4-Hydroxyimino-TEMPO. *Journal of the American Chemical Society*, 121(2):424–431, January 1999.

[59] C. Köhler, G. Seifert, U. Gerstmann, M. Elstner, H. Overhof, and T. Frauenheim. Approximate density-functional calculations of spin densities in large molecular systems and complex solids. *Physical Chemistry Chemical Physics*, 3(23):5109–5114, November 2001.

[60] D. Carlier, M. Ménétrier, C. P. Grey, C. Delmas, and G. Ceder. Understanding the NMR shifts in paramagnetic transition metal oxides using density functional theory calculations. *Physical Review B*, 67(17):174103, 2003.

[61] F. Ban, K. N. Rankin, J. W. Gauld, and R. J. Boyd. Recent applications of density functional theory calculations to biomolecules. *Theoretical Chemistry Accounts*, 108(1):1–11, 2002.

[62] F. Neese. Quantum chemical calculations of spectroscopic properties of metalloproteins and model compounds: EPR and Mössbauer properties . *Current Opinion in Chemical Biology*, 7(1):125 – 135, 2003.

[63] M. Kaupp and F. H. Köhler. Combining NMR spectroscopy and quantum chemistry as tools to quantify spin density distributions in molecular magnetic compounds . *Coordination Chemistry Reviews*, 253(1920):2376 – 2386, 2009. Deutsche Forschungsgemeinschaft Molecular Magnetism Research Report.

[64] T. Helgaker, M. Jaszuński, and K. Ruud. Ab Initio Methods for the Calculation of NMR Shielding and Indirect SpinSpin Coupling Constants. *Chemical Reviews*, 99(1):293–352, 1999. PMID: 11848983.

[65] W. Kutzelnigg, U. Fleischer, and M. Schindler. *The IGLO-Method: Ab-initio Calculation and Interpretation of NMR Chemical Shifts and Magnetic Susceptibilities*, pages 165–262. Springer Berlin Heidelberg, Berlin, Heidelberg, 1991.

[66] R. Ditchfield. Self-consistent perturbation theory of diamagnetism. *Molecular Physics*, 27(4):789–807, 1974.

[67] K. Wolinski, J. F. Hinton, and P. Pulay. Efficient implementation of the gauge-independent atomic orbital method for NMR chemical shift calculations. *Journal of the American Chemical Society*, 112(23):8251–8260, 1990.

[68] F. Mauri, B. G. Pfrommer, and S. G. Louie. *Ab Initio* Theory of NMR Chemical Shifts in Solids and Liquids. *Phys. Rev. Lett.*, 77:5300–5303, Dec 1996.

[69] D. Sebastiani and M. Parrinello. A New ab-Initio Approach for NMR Chemical Shifts in Periodic Systems. *The Journal of Physical Chemistry A*, 105(10):1951–1958, 2001.

[70] D. Sebastiani. Ab-initio Calculations of NMR Parameters in Condensed Phases. *Modern Physics Letters B*, 17(25):1301–1319, 2003.

[71] J. Cuny, J. Yates, R. Gautier, E. Furet, E. Le Fur, and L. Le Pollès. Electric field gradient calculations in paramagnetic compounds using the PAW approach. Application to ^{23}Na NMR in layered vanadium phosphates. *Magnetic Resonance in Chemistry*, 48(S1):S171–S175, 2010.

[72] O. V. Yazyev, I. Tavernelli, L. Helm, and U. Rothlisberger. Core spin-polarization correction in pseudopotential-based electronic structure calculations. *Physical Review B*, 71(11):115110, 2005.

[73] R. Declerck, E. Pauwels, V. V. Speybroeck, and M. Waroquier. First-principles calculations of hyperfine parameters with the Gaussian and augmented-plane-wave method: Application to radicals embedded in a crystalline environment. *Physical Review B*, 74(24):245103, 2006.

[74] M. S. Bahramy, M. H. F. Sluiter, and Y. Kawazoe. First-principles calculations of hyperfine parameters with the all-electron mixed-basis method. *Physical Review B*, 73(4):045111, 2006.

[75] M. S. Bahramy, M. H. F. Sluiter, and Y. Kawazoe. Pseudopotential hyperfine calculations through perturbative core-level polarization. *Physical Review B*, 76(3):035124, 2007.

[76] C. Marichal, J. Hirschinger, P. Granger, M. Ménétrier, A. Rougier, and C. Delmas. ^{6}Li and ^{7}Li NMR in the $LiNi_{1-y}Co_yO_2$ Solid Solution ($0 \leq y \leq 1$). *Inorganic Chemistry*, 34(7):1773–1778, 1995.

[77] J. C. Johnston, R. J. Iuliucci, J. C. Facelli, G. Fitzgerald, and K. T. Mueller. Intermolecular shielding contributions studied by modeling the C^{13} chemical-shift tensors of organic single crystals with plane waves. *The Journal of Chemical Physics*, 131(14):144503, 2009.

[78] C. Gervais, R. Dupree, K. J. Pike, C. Bonhomme, M. Profeta, C. J. Pickard, and F. Mauri. Combined First-Principles Computational and Experimental Multinuclear Solid-State NMR Investigation of Amino Acids. *The Journal of Physical Chemistry A*, 109(31):6960–6969, 2005. PMID: 16834055.

[79] N. Lu, Y. Huang, H.-b. Li, Z. Li, and J. Yang. First principles nuclear magnetic resonance signatures of graphene oxide. *The Journal of Chemical Physics*, 133(3):034502, 2010.

[80] E. Zurek, C. J. Pickard, and J. Autschbach. A Density Functional Study of the ^{13}C NMR Chemical Shifts in Functionalized Single-Walled Carbon Nanotubes. *Journal of the American Chemical Society*, 129(14):4430–4439, 2007. PMID: 17371025.

[81] M. A. L. Marques, M. d'Avezac, and F. Mauri. Magnetic response and NMR spectra of carbon nanotubes from *ab initio* calculations. *Phys. Rev. B*, 73:125433, Mar 2006.

[82] S. E. Ashbrook, L. Le Polles, R. Gautier, C. J. Pickard, and R. I. Walton. ^{23}Na multiple-quantum MAS NMR of the perovskites $NaNbO_3$ and $NaTaO_3$. *Phys. Chem. Chem. Phys.*, 8:3423–3431, 2006.

[83] K. E. Johnston, C. C. Tang, J. E. Parker, K. S. Knight, P. Lightfoot, and S. E. Ashbrook. The Polar Phase of $NaNbO_3$: A Combined Study by Powder Diffraction, Solid-State NMR, and First-Principles Calculations. *Journal of the American Chemical Society*, 132(25):8732–8746, 2010. PMID: 20521792.

[84] S. P. Brown. Recent Advances in Solid-State MAS NMR Methodology for Probing Structure and Dynamics in Polymeric and Supramolecular Systems. *Macromolecular Rapid Communications*, 30(9-10):688–716, 2009.

[85] J.-S. Filhol, J. Deschamps, S. G. Dutremez, B. Boury, T. Barisien, L. Legrand, and M. Schott. Polymorphs and Colors of Polydiacetylenes: A First Principles Study. *Journal of the American Chemical Society*, 131(20):6976–6988, 2009. PMID: 19413321.

[86] F. Pourpoint, C. Gervais, L. Bonhomme-Coury, T. Azaïs, C. Coelho, F. Mauri, B. Alonso, F. Babonneau, and C. Bonhomme. Calcium Phosphates and Hydroxyapatite: Solid-State NMR Experiments and First-Principles Calculations. *Applied Magnetic Resonance*, 32(4):435–457, 2007.

[87] S. Cadars, B. J. Smith, J. D. Epping, S. Acharya, N. Belman, Y. Golan, and B. F. Chmelka. Atomic Positional Versus Electronic Order in Semiconducting ZnSe Nanoparticles. *Phys. Rev. Lett.*, 103:136802, Sep 2009.

[88] H. Chappell, M. Duer, N. Groom, C. Pickard, and P. Bristowe. Probing the surface structure of hydroxyapatite using NMR spectroscopy and first principles calculations. *Phys. Chem. Chem. Phys.*, 10:600–606, 2008.

[89] F. Tielens, C. Gervais, J. F. Lambert, F. Mauri, and D. Costa. Ab Initio Study of the Hydroxylated Surface of Amorphous Silica: A Representative Model. *Chemistry of Materials*, 20(10):3336–3344, 2008.

[90] M. Kibalchenko, J. R. Yates, C. Massobrio, and A. Pasquarello. Structural Composition of First-Neighbor Shells in $GeSe_2$ and $GeSe_4$ Glasses from a First-Principles Analysis of NMR Chemical Shifts. *The Journal of Physical Chemistry C*, 115(15):7755–7759, 2011.

[91] A. Pedone, T. Charpentier, and M. C. Menziani. Multinuclear NMR of $CaSiO_3$ glass: simulation from first-principles. *Phys. Chem. Chem. Phys.*, 12:6054–6066, 2010.

[92] A. M. Glazer. The classification of tilted octahedra in perovskites. *Acta Crystallographica Section B*, 28(11):3384–3392, Nov 1972.

[93] S. Ghose and T. Tsang. Structural Dependence of Quadrupole Coupling Constant e^2qQ/h for ^{27}Al and Crystal Field Parameter D for Fe^{3+} in Aluminosilicates. *American Mineralogist*, 58:748–755, 1973.

[94] K. J. D. MacKenzie and M. E. Smith. *Multinuclear Solid-State NMR of Inorganic Materials*. Elsevier Science Ltd, Oxford, 2002.

[95] Y. Saito, H. Takao, T. Tani, T. Nonoyama, K. Takatori, T. Homma, T. Nagaya, and M. Nakamura. Lead-free piezoceramics. *Nature*, 432:84–87, 2004.

[96] J. Rödel, W. Jo, K. T. P. Seifert, E.-M. Anton, T. Granzow, and D. Damjanovic. Perspective on the Development of Lead-free Piezoceramics. *Journal of the American Ceramic Society*, 92(6):1153–1177, 2009.

[97] H. D. Megaw. The seven phases of sodium niobate. *Ferroelectrics*, 7(1):87–89, 1974.

[98] I. Lefkowitz, K. Lukaszewicz, and H. D. Megaw. The High-Temperature Phases of Sodium Niobate and the Nature of Transitions in Pseudosymmetric Structures. *Acta Crystallographica*, 20:670–683, 1966.

[99] Y. Shiratori, A. Magrez, J. Dornseiffer, F.-H. Haegel, C. Pithan, and R. Waser. Polymorphism in Micro-, Submicro-, and Nanocrystalline $NaNbO_3$. *The Journal of Physical Chemistry B*, 109(43):20122–20130, 2005. PMID: 16853601.

[100] D. R. Modeshia, R. J. Darton, S. E. Ashbrook, and R. I. Walton. Control of polymorphism in $NaNbO_3$ by hydrothermal synthesis. *Chem. Commun.*, pages 68–70, 2009.

[101] M. D. Peel, S. P. Thompson, A. Daoud-Aladine, S. E. Ashbrook, and P. Lightfoot. New Twists on the Perovskite Theme: Crystal Structures

of the Elusive Phases R and S of $NaNbO_3$. *Inorganic Chemistry*, 51(12):6876–6889, 2012. PMID: 22668027.

[102] M. D. Peel, S. E. Ashbrook, and P. Lightfoot. Unusual Phase Behavior in the Piezoelectric Perovskite System, $Li_xNa_{1-x}NbO_3$. *Inorganic Chemistry*, 52(15):8872–8880, 2013. PMID: 23855830.

[103] C. Darlington and K. Knight. On the lattice parameters of sodium niobate at room temperature and above. *Physica B: Condensed Matter*, 266(4):368 – 372, 1999.

[104] Y. I. Yuzyuk, P. Simon, E. Gagarina, L. Hennet, D. Thiaudière, V. I. Torgashev, S. I. Raevskaya, I. P. Raevskii, L. A. Reznitchenko, and J. L. Sauvajol. Modulated phases in $NaNbO_3$: Raman scattering, synchrotron x-ray diffraction, and dielectric investigations. *Journal of Physics: Condensed Matter*, 17(33):4977, 2005.

[105] K. E. Johnston, J. M. Griffin, R. I. Walton, D. M. Dawson, P. Lightfoot, and S. E. Ashbrook. ^{93}Nb NMR and DFT investigation of the polymorphs of $NaNbO_3$. *Phys. Chem. Chem. Phys.*, 13:7565–7576, 2011.

[106] R. A. Shakhovoy, S. I. Raevskaya, L. A. Shakhovaya, D. V. Suzdalev, I. P. Raevski, Y. I. Yuzyuk, A. F. Semenchev, and M. El Marssi. Ferroelectric Q and antiferroelectric P phases' coexistence and local phase transitions in oxygen-deficient $NaNbO_3$ single crystal: micro-Raman, dielectric and dilatometric studies. *Journal of Raman Spectroscopy*, 43(8):1141–1145, 2012.

[107] J. V. Hanna, K. J. Pike, T. Charpentier, T. F. Kemp, M. E. Smith, B. E. G. Lucier, R. W. Schurko, and L. S. Cahill. A ^{93}Nb Solid-State NMR and Density Functional Theory Study of Four- and Six-Coordinate Niobate Systems. *Chemistry A European Journal*, 16(10):3222–3239, 2010.

[108] M. Ahtee and A. M. Glazer. Lattice parameters and tilted octahedra in sodium–potassium niobate solid solutions. *Acta Crystallographica Section A*, 32(3):434–446, May 1976.

[109] N. Zhang, A. M. Glazer, D. Baker, and P. A. Thomas. Structures of $K_{0.05}Na_{0.95}NbO_3$ (50–300K) and $K_{0.30}Na_{0.70}NbO_3$ (100–200K). *Acta Crystallographica Section B*, 65(3):291–299, Jun 2009.

[110] D. W. Baker, P. A. Thomas, N. Zhang, and A. M. Glazer. A comprehensive study of the phase diagram of $K_xNa_{1x}NbO_3$. *Applied Physics Letters*, 95(9):091903, 2009.

[111] T. Nitta. Properties of Sodium-Lithium Niobate Solid Solution Ceramics with Small Lithium Concentrations. *Journal of the American Ceramic Society*, 51(11):623–630, 1968.

[112] R. R. Zeyfang, R. M. Henson, and W. J. Maier. Temperature- and time-dependent properties of polycrystalline (Li,Na)NbO_3 solid solutions. *Journal of Applied Physics*, 48(7):3014–3017, 1977.

[113] R. Jiménez, M. L. Sanjuán, and B. Jiménez. Stabilization of the ferroelectric phase and relaxor-like behaviour in low Li content sodium niobates. *Journal of Physics: Condensed Matter*, 16(41):7493, 2004.

[114] V. Shuvaeva and M. Antipin. Structural disorder in $KNbO_3$ crystal from X-ray diffraction and EXAFS spectroscopy. *Crystallography Reports*, 40(3):466–471, 1995.

[115] E. P. Fedorova, L. A. Aleshina, N. V. Sidorov, P. G. Chufyrev, A. A. Yanichev, M. N. Palatnikov, V. M. Voskresenskii, and V. T. Kalinnikov. Stoichiometry and doping effects on cation ordering in $LiNbO_3$ crystals. *Inorganic Materials*, 46(2):206–211, 2010.

[116] A. C. Sakowski-Cowley, K. Łukaszewicz, and H. D. Megaw. The structure of sodium niobate at room temperature, and the problem of reliability in pseudosymmetric structures. *Acta Crystallographica Section B*, 25(5):851–865, May 1969.

[117] V. A. Shuvaeva, M. Y. Antipin, R. S. V. Lindeman, O. E. Fesenko, V. G. Smotrakov, and Y. T. Struchkov. Crystal structure of the electric-field induced ferroelectric phase of $NaNbO_3$. *Ferroelectrics*, 141(1):307–311, 1993.

[118] E. A. Chizhova, A. I. Klyndyuk, L. A. Bashkirov, G. S. Petrov, and L. V. Makhnach. Structural and dielectric properties of solid solutions of sodium niobate in lanthanum and neodymium niobates. *Neorganicheskie Materialy*, 40:1508–1514, 2004.

[119] S. Sturniolo, T. F. Green, R. M. Hanson, M. Zilka, K. Refson, P. Hodgkinson, S. P. Brown, and J. R. Yates. Visualization and processing of computed solid-state NMR parameters: MagresView and MagresPython. *Solid State Nuclear Magnetic Resonance*, 78:64 – 70, 2016.

[120] G. E. Peterson, P. M. Bridenbaugh, and P. Green. NMR Study of Ferroelectric $LiNbO_3$ and $LiTaO_3$. I. *The Journal of Chemical Physics*, 46(10):4009–4014, 1967.

[121] E. V. Charnaya, V. T. Gabrielyan, V. S. Kasperovich, and S. Klimko. Li^7 NMR in $LiNbO_3$ crystals with different nonstoichiometry. *Ferroelectrics*, 202(1):115–119, 1997.

[122] E. V. Charnaya, V. S. Kasperovich, and M. G. Shelyapina. Quadrupole splitting of the ^{7}Li NMR line in $LiNbO_3$ crystals. *Ferroelectrics*, 208-209(1):225–236, 1998.

[123] R. Kind, H. Gränicher, B. Derighetti, F. Waldner, and E. Brun. NMR of ^{93}Nb in ferroelectric $LiNbO_3$. *Solid State Communications*, 6(7):439 – 440, 1968.

[124] S. Prasad, P. Zhao, J. Huang, J. Fitzgerald, and J. Shore. Niobium-93 MQMAS NMR Spectroscopic Study of Alkali and Lead Niobates. *Solid State Nuclear Magnetic Resonance*, 19(1):45 – 62, 2001.

[125] T. J. Bastow, P. J. Dirken, M. E. Smith, and H. J. Whitfield. Factors Controlling the ^{17}O NMR Chemical Shift in Ionic Mixed Metal Oxides. *The Journal of Physical Chemistry*, 100(47):18539–18545, 1996.

[126] S. Kawamura, E. Magome, C. Moriyoshi, Y. Kuroiwa, N. Taniguchi, H. Tanaka, S. Maki, M. Takata, and S. Wada. Electronic polarization in $KNbO_3$ visualized by synchrotron radiation powder diffraction. *Japanese Journal of Applied Physics*, 52, 2013.

[127] J. J. Fitzgerald, S. Prasad, J. Huang, and J. S. Shore. Solid-State ^{93}Nb NMR and ^{93}Nb Nutation Studies of Polycrystalline

$Pb(Mg_{1/3}Nb_{2/3})O_3$ and (1-x)$Pb(Mg_{1/3}Nb_{2/3})O_3$/x$PbTiO_3$ Solid-Solution Relaxor Ferroelectrics. *Journal of the American Chemical Society*, 122(11):2556–2566, 2000.

[128] L. S. Cahill, J. V. Hanna, A. Wong, J. C. C. Freitas, J. R. Yates, R. K. Harris, and M. E. Smith. Natural Abundance ^{25}Mg Solid-State NMR of Mg Oxyanion Systems: A Combined Experimental and Computational Study. *Chemistry A European Journal*, 15(38):9785–9798, 2009.

[129] M. D. Alba, P. Chain, P. Florian, and D. Massiot. ^{45}Sc Spectroscopy of Solids: Interpretation of Quadrupole Interaction Parameters and Chemical Shifts. *The Journal of Physical Chemistry C*, 114(28):12125–12132, 2010.

[130] D. Padro, A. Howes, M. Smith, and R. Dupree. Determination of titanium NMR parameters of $ATiO_3$ compounds: correlations with structural distortion. *Solid State Nuclear Magnetic Resonance*, 15(4):231 – 236, 2000.

[131] C. J. Pickard and R. J. Needs. High-Pressure Phases of Silane. *Phys. Rev. Lett.*, 97:045504, Jul 2006.

[132] R. Laskowski and P. Blaha. NMR Shielding in Metals Using the Augmented Plane Wave Method. *The Journal of Physical Chemistry C*, 119(33):19390–19396, 2015. PMID: 26322148.

[133] G. D. Gaspari, W.-M. Shyu, and T. P. Das. Theory of Core-Electron Contributions to Hyperfine Interactions. *Phys. Rev.*, 134:A852–A862, May 1964.

[134] A. M. Clogston, A. C. Gossard, V. Jaccarino, and Y. Yafet. Orbital Paramagnetism and the Knight Shift of D-Band Superconductors. *Phys. Rev. Lett.*, 9:262–266, Sep 1962.

[135] A. M. Clogston, V. Jaccarino, and Y. Yafet. Interpretation of Knight Shifts and Susceptibilities of Transition Metals: Platinum. *Phys. Rev.*, 134:A650–A661, May 1964.

[136] J. Seitchik, A. Gossard, and V. Jaccarino. Knight Shifts and Susceptibilities of Transition Metals: Palladium. *Physical Review*, 136(4A):A1119–A1125, 1964.

[137] J. Seitchik, V. Jaccarino, and J. Wernick. Knight Shift Studies of Transition Metals: Rhodium and Rhodium Intermetallic Compounds. *Physical Review*, 138(1A):A148–A152, 1965.

[138] G. N. Rao, E. Matthias, and D. A. Shirley. Localized Moments on Rhodium in *Pd*-Rh Alloys. *Phys. Rev.*, 184:325–333, Aug 1969.

[139] J. Butterworth. Nuclear Magnetic Relaxation and Shift in Platinum. *Phys. Rev. Lett.*, 8:423–424, Jun 1962.

[140] M. Shaham, U. El-Hanany, and D. Zamir. NMR study of platinum at high temperature. *Phys. Rev. B*, 17:3513–3517, May 1978.

[141] Y. Yafet and V. Jaccarino. Nuclear Spin Relaxation in Transition Metals; Core Polarization. *Phys. Rev.*, 133:A1630–A1637, Mar 1964.

[142] J. J. van der Klink and H. B. Brom. NMR in metals, metal particles and metal cluster compounds. *Progress in Nuclear Magnetic Resonance Spectroscopy*, 36(2):89 – 201, 2000.

[143] T. Brown and P. Green. New reference compounds for the knight shifts in ^{55}Mn and ^{103}Rh. *Physics Letters A*, 31(3):148 – 149, 1970.

[144] L. Drain. Nuclear magnetic resonance in platinum. *Journal of Physics and Chemistry of Solids*, 24(3):379 – 382, 1963.

[145] J. Fraissard. NMR studies of supported metal catalysts. *Catalysis Today*, 51(34):481 – 499, 1999.

[146] P.-A. Vuissoz, T. Yonezawa, D. Yang, J. Kiwi, and J. van der Klink. ^{103}Rh NMR in small rhodium particles. *Chemical Physics Letters*, 264(3):366 – 370, 1997.

[147] J. M. Ernsting, S. Gaemers, and C. J. Elsevier. ^{103}Rh NMR spectroscopy and its application to rhodium chemistry. *Magnetic Resonance in Chemistry*, 42(9):721–736, 2004.

[148] A. Narath, A. T. J. Fromhold, and E. D. Jones. Nuclear Spin Relaxation in Metals: Rhodium, Palladium, and Silver. *Physical Review*, 144(2):428–435, 1966.

[149] J. J. van der Klink. A local-density formulation for NMR parameters in metals. *Journal of Physics: Condensed Matter*, 8(11):1845, 1996.

[150] A. Narath and H. Weaver. Nuclear magnetic resonance and relaxation of ^{195}Pt in platinum-palladium alloys. *Solid State Communications*, 6(6):413–415, 1968.

[151] J. P. Bucher and J. J. van der Klink. Electronic properties of small supported Pt particles: NMR study of ^{195}Pt hyperfine parameters. *Phys. Rev. B*, 38:11038–11047, Dec 1988.

[152] M. Takigawa and H. Yasuoka. Nuclear Magnetic Relaxation in Palladium. *Journal of the Physical Society of Japan*, 51(3):787–793, 1982.

[153] S. Burnet, T. Yonezawa, and J. J. van der Klink. Magnetism of small supported rhodium particles studied by means of ^{103}Rh nuclear magnetic resonance. *Journal of Physics: Condensed Matter*, 14(30):7135, 2002.

[154] F. Y. Fradin, D. D. Koelling, A. J. Freeman, and T. J. Watson-Yang. Calculation of the electronic structure and related physical properties of platinum. *Phys. Rev. B*, 12:5570–5574, Dec 1975.

[155] O. K. Andersen. Electronic Structure of the FCC Transition Metals Ir, Rh, Pt, and Pd. *Phys. Rev. B*, 2:883–906, Aug 1970.

[156] H. E. Rhodes, P.-K. Wang, H. T. Stokes, C. P. Slichter, and J. H. Sinfelt. NMR of platinum catalysts. I. Line shapes. *Phys. Rev. B*, 26:3559–3568, Oct 1982.

[157] J. P. Bucher, J. Buttet, J. J. van der Klink, and M. Graetzel. Electronic properties and local densities of states in clean and hydrogen covered Pt particles. *Surface Science*, 214(3):347 – 357, 1989.

[158] C. Rice, Y. Tong, E. Oldfield, and A. Wieckowski. Cyclic voltammetry and ^{195}Pt nuclear magnetic resonance characterization of graphite-supported commercial fuel cell grade platinum electrocatalysts. *Electrochimica Acta*, 43(1920):2825 – 2830, 1998.

[159] Y. Tong, C. Rice, N. Godbout, A. Wieckowski, and E. Oldfield. Correlation between the Knight Shift of Chemisorbed CO and the Fermi

Level Local Density of States at Clean Platinum Catalyst Surfaces. *Journal of the American Chemical Society*, 121(13):2996–3003, 1999.

[160] P. K. Babu, H. S. Kim, E. Oldfield, and A. Wieckowski. Electronic Alterations Caused by Ruthenium in Pt-Ru Alloy Nanoparticles as Revealed by Electrochemical NMR. *The Journal of Physical Chemistry B*, 107(31):7595–7600, 2003.

[161] I. Yu, A. A. V. Gibson, E. R. Hunt, and W. P. Halperin. Observation of Conduction-Electron Density Oscillations at the Surface of Platinum Particles. *Phys. Rev. Lett.*, 44:348–351, Feb 1980.

[162] Y. Tong, C. Rice, A. Wieckowski, and E. Oldfield. 195-Pt NMR of Platinum Electrocatalysts: Friedel-Heine Invariance and Correlations between Platinum Knight Shifts, Healing Length, and Adsorbate Electronegativity. *Journal of the American Chemical Society*, 122(48):11921–11924, December 2000.

[163] H. Yano, J. Inukai, H. Uchida, M. Watanabe, P. K. Babu, T. Kobayashi, J. H. Chung, E. Oldfield, and A. Wieckowski. Particle-size effect of nanoscale platinum catalysts in oxygen reduction reaction: an electrochemical and ^{195}Pt EC-NMR study. *Physical Chemistry Chemical Physics : PCCP*, 8(42):4932–9, November 2006.

[164] P. K. Babu, H. S. Kim, J. H. Chung, E. Oldfield, and A. Wieckowski. Bonding and Motional Aspects of CO Adsorbed on the Surface of Pt Nanoparticles Decorated with Pd. *The Journal of Physical Chemistry B*, 108(52):20228–20232, December 2004.

[165] P. K. Babu, H. S. Kim, S. T. Kuk, J. H. Chung, E. Oldfield, A. Wieckowski, and E. S. Smotkin. Activation of nanoparticle Pt-Ru fuel cell catalysts by heat treatment: a ^{195}Pt NMR and electrochemical study. *The Journal of Physical Chemistry. B*, 109(36):17192–6, September 2005.

[166] T. Kobayashi, P. Babu, J. Chung, E. Oldfield, and A. Wieckowski. Coverage Dependence of CO Surface Diffusion on Pt Nanoparticles: An EC-NMR Study. *Journal of Physical Chemistry C*, 111(19):7078–7083, May 2007.

[167] P. K. Babu, J.-H. Chung, E. Oldfield, and A. Wieckowski. CO surface diffusion on platinum fuel cell catalysts by electrochemical NMR. *Electrochimica Acta*, 53(23):6672–6679, 2008.

[168] Z. Wang, J.-P. Ansermet, C. P. Slichter, and J. H. Sinfelt. Nuclear Magnetic Resonance Study of Pt-Rh Bimetallic Clusters. *Journal of the Chemical Society, Faraday Transactions*, 84(11):3785, 1988.

[169] S. Kinayyigit, P. Lara, P. Lecante, K. Philippot, and B. Chaudret. Probing the surface of platinum nanoparticles with ^{13}CO by solid-state NMR and IR spectroscopies. *Nanoscale*, 6:539–546, 2014.

[170] S. L. Rudaz, J.-P. Ansermet, P.-K. Wang, C. P. Slichter, and J. H. Sinfelt. NMR Study of the Chemisorption Bond of Carbon Monoxide on Platinum. *Phys. Rev. Lett.*, 54:71–74, Jan 1985.

[171] Y. Y. Tong, T. Yonezawa, N. Toshima, and J. J. van der Klink. ^{195}Pt NMR of Polymer-Protected Pt/Pd Bimetallic Catalysts. *The Journal of Physical Chemistry*, 100(2):730–733, 1996.

[172] S. E. Shore, J.-P. Ansermet, C. P. Slichter, and J. H. Sinfelt. Nuclear magnetic resonance study of the bonding and diffusion of CO chemisorbed on Pd. *Phys. Rev. Lett.*, 58:953–956, Mar 1987.

[173] K. W. Zilm, L. Bonneviot, D. M. Hamilton, G. G. Webb, and G. L. Haller. Carbon-13 NMR studies of supported platinum and palladium catalysts using magic angle sample spinning. *The Journal of Physical Chemistry*, 94(4):1463–1472, 1990.

[174] M. Weinert and A. J. Freeman. Relativistic spin polarization and magnetization: Knight shift of Pt(001). *Phys. Rev. B*, 28:6262–6269, Dec 1983.

[175] K. B. Efetov and V. N. Prigodin. Local density of states distribution and NMR in small metallic particles. *Phys. Rev. Lett.*, 70:1315–1318, Mar 1993.

[176] F. C. Fritschij, H. B. Brom, L. J. de Jongh, and G. Schmid. Mesoscopic Fluctuations in Small Metal Particles Studied by Nuclear Magnetic Resonance. *Phys. Rev. Lett.*, 82:2167–2170, Mar 1999.

[177] H. M. Pastawski and J. A. Gascón. NMR line shape in metallic nanoparticles: A matrix continued fractions evaluation. *Phys. Rev. B*, 56:4887–4892, Aug 1997.

[178] C. P. Slichter. Probing Phenomena at Metal Surfaces by NMR. *Annual Review of Physical Chemistry*, 37(1):25–51, 1986.

[179] S. J. Blundell. *Magnetism in Condensed Matter*. Oxford University Press, Oxford, 2001.

[180] R. L. Kautz and B. B. Schwartz. Surface of a spin-polarized electron gas. *Phys. Rev. B*, 14:2017–2031, Sep 1976.

[181] C. Froidevaux and M. Weger. Direct Measurement of the Ruderman-Kittel Interaction in Platinum Alloys. *Phys. Rev. Lett.*, 12:123–125, Feb 1964.

[182] H. T. Stokes, H. E. Rhodes, P.-K. Wang, C. P. Slichter, and J. H. Sinfelt. NMR of platinum catalysts. III. Microscopic variation of the Knight shifts. *Phys. Rev. B*, 26:3575–3581, Oct 1982.

[183] Y. Tong, C. Belrose, A. Wieckowski, and E. Oldfield. First Observation of Platinum-195 Nuclear Magnetic Resonance in Commercial Graphite-Supported Platinum Electrodes in an Electrochemical Environment. *Journal of the American Chemical Society*, 119(48):11709–11710, 1997.

[184] T. F. G. Green and J. R. Yates. Relativistic nuclear magnetic resonance J-coupling with ultrasoft pseudopotentials and the zeroth-order regular approximation. *The Journal of Chemical Physics*, 140(23):234106, 2014.

[185] R. W. Fessenden and R. H. Schuler. Electron Spin Resonance Studies of Transient Alkyl Radicals. *The Journal of Chemical Physics*, 39(9):2147–2195, 1963.

[186] R. W. Fessenden. Electron spin resonance spectra of some isotopically substituted hydrocarbon radicals. *The Journal of Physical Chemistry*, 71(1):74–83, 1967.

[187] D. M. Chipman. The spin polarization model for hyperfine coupling constants. *Theoretica chimica acta*, 82(1):93–115, 1992.

[188] T. Momose, Y. Endo, E. Hirota, and T. Shida. The submillimeter-wave spectrum of the $^{13}CH_3O$ radical. *The Journal of Chemical Physics*, 88(9):5338–5343, 1988.

[189] H. Nakatsuji and M. Izawa. Calculation of hyperfine splitting constants with Slater-type cusp basis by the symmetry adapted cluster-configuration interaction theory. *The Journal of Chemical Physics*, 91(10):6205–6214, 1989.

[190] R. W. Holmberg. ESR Study of HCO in Single Crystals of Formic Acid at 77°K. *The Journal of Chemical Physics*, 51(8):3255–3260, 1969.

[191] P. Giannozzi, S. Baroni, N. Bonini, M. Calandra, R. Car, C. Cavazzoni, D. Ceresoli, G. L. Chiarotti, M. Cococcioni, I. Dabo, A. D. Corso, S. de Gironcoli, S. Fabris, G. Fratesi, R. Gebauer, U. Gerstmann, C. Gougoussis, A. Kokalj, M. Lazzeri, L. Martin-Samos, N. Marzari, F. Mauri, R. Mazzarello, S. Paolini, A. Pasquarello, L. Paulatto, C. Sbraccia, S. Scandolo, G. Sclauzero, A. P. Seitsonen, A. Smogunov, P. Umari, and R. M. Wentzcovitch. QUANTUM ESPRESSO: a modular and open-source software project for quantum simulations of materials. *Journal of Physics: Condensed Matter*, 21(39):395502, 2009.